Magnetopause study by means of a multi-fluid approach

Roberto Manuzzo

UNIVERSITÉ FRANCO ITALIENNE

3608078

Sorbonne Université

École Doctorale Astronomie et Astrophysique d'Ile de France
Laboratoire de Physique des Plasmas

Discipline : Space Plasma

PhD Thesis

Defended on 17 December 2019 by

Roberto Manuzzo

Magnetopause study by means of a multi-fluid approach

Ms	Laurence Rezeau	(Thesis Director)
Mr	Francesco Califano	(Thesis Co-Director)
Ms	Claire Foullon	(Reviewer)
Mr	Joerg Buechner	(Reviewer)
Ms	Caterina Riconda	(Examiner)
Mr	Roberto Bruno	(Examiner)
Mr	Gerard Belmont	(Guest)

to the Roots that allowed me to grow and the Leaves will come...

Abstract

The Earth's magnetopause is the boundary between the solar wind plasma and the Earth's magnetospheric one. Across this current sheet (which is thin in comparison to the magnetosphere), the two plasmas mix in a poorly known way, controlling the exchanges of mass, energy and momentum between the two regions. Beyond the interest in understanding how these processes could impact on our lives (space weather), this system is worth studying in order to understand how two different plasma systems interact without laboratory set-up constraints.

In this thesis, new methods are presented which are able to obtain a "realistic" multi-fluid analysis of the solar wind - magnetosphere interaction. This goal is reached in three main steps: (1) the analysis of spacecraft data acquired across the magnetopause, (2) the set up of an analytical multi-fluid equilibrium model able to predict profiles consistent with observations, (3) the development of a multi-fluid code able to simulate the temporal evolution of the analytical profiles.

The analysis of spacecraft data acquired across the magnetopause is done by means of new techniques which relax most of the hypotheses usually assumed about the observed plasma structures. These techniques help in disentangling the principal causes of misunderstanding in data interpretations by discerning whether the observed variations are due to the magnetopause motion in the spacecraft frame or due to the purely temporal variations of the magnetopause structure. The new methods show consistent results but each of them demands to fix some threshold parameters. These thresholds are determined, in an objective way, by dedicated optimization techniques.

The spatial profiles obtained from the new data analysis techniques feed a new 3fluid analytical model (two ion and one electron populations) able to spatially confine the magnetospheric and magnetosheath plasmas in their own regions and letting them to partially overlap close to the contact boundary (the magnetopause). This model helps also in determining the magnetospheric and magnetosheath contributions to the total ion population where this information is not accessible analysing the distribution functions (*e.g.* in the mixing regions).

The 3fluid equilibrium computed by the analytical model is then perturbed and evolved in time by means of a new 3fluid numerical code, explicitly coded to take the 3fluid model outputs as inputs. The numerical model of the magnetopause develops a magnetic reconnection instability, in agreement to what is observed close to the analysed magnetopause crossing.

The results lead to preliminary conclusions about the temporal evolution and the spatial distribution of the mixing processes close to the magnetopause.

Résumé

La magnétopause est la frontiere entre le plasma du vent solaire et celui de la magnétosphère terrestre. A l'intérieur de cette couche de courant, qui est très fine à l'échelle de la magnétosphère, les deux plasmas se mélangent d'une façon encore mal connue mais qui contrôle les échanges de masse, de moment et d'energie entre les deux régions. Au delà de l'intérêt à comprendre comment ces phénomènes peuvent influencer notre vie (météorologie de l'espace), l'étude de ces systèmes est importante pour comprendre comment deux plasmas magnétisés différents interagissent lorsqu'ils viennent en contact, sans les limitations propres aux expériences de laboratoire.

Dans cette thèse, je présente des nouvelles méthodes qui permettent d'obtenir une analyse multi-fluide "realiste" de l'interaction vent solaire - magnétosphère. Ce but est atteint en trois étapes: (1) l'analyse des données acquises par les satellites lors de traversées de magnétopause, (2) la construction d'un modèle analytique d'équilibre donnant des profils compatibles avec les

observations, (3) la mise au point d'un code multi-fluide permettant d'étudier l'évolution temporelle de ces profils analytiques pris comme condition initiale.

L'analyse des données est réalisée grâce à de nouvelles techniques qui relachent la plupart des hypothèses le plus souvent faites pour ces analyses. Ces techniques aident à distinguer si les variations observées sont causées par les mouvements de la magnétopause ou par la modification de sa structure au cours du temps. Les nouvelles méthodes montrent des résultats cohérents entre elles, mais elles dépendent de seuils. Ces seuils sont finalement déterminés de manière objective grâce à une technique d'optimisation.

Les profils spatiaux obtenus par l'analyse des données fournissent l'information primaire pour un nouveau modèle analytique 3fluides (deux populations ioniques et une population d'électrons), qui permet de faire en sorte que la population de chaque région voit sa densité s'annuler dans la région opposée avec une région de superposition au milieu (magnétopause). Le modèle aide aussi a déterminer dans quelle proportion les populations de la magnetogaine et de la magnetosphère contribuent à la population ionique globale, même lorsque cette information n'est pas directement accessible dans les données, permettant en particulier d'expliquer la forme de la fonction de distribution ionique dans la région de superposition.

L'équilibre décrit par ces profils analytiques est ensuite perturbé et pris comme condition initiale d'un code 3fluides, qui a été développé dans ce but. Le modèle de la magnétopause montre une instabilité de reconnexion magnétique, en accord avec ce qui est observé dans les données proches du cas analysé.

Les résultats de la simulation mènent également à des conclusions préliminaires en ce qui concerne l'évolution temporelle et la distribution spatiale du mélange des deux populations à l'intérieur de la magnétopause.

Riassunto

La magnetopausa é il confine tra il il plasma del vento solare e quello della magnetosfera terrestre. All'interno di questo strato di corrente, sottile rispetto alle dimensioni caratteristiche della magnetosfera, i due plasmi sono interessati da processi di mescolamento la cui dinamica non é ancora del tutto nota ma che é responsabile degli scambi di massa, quantità di moto ed energia tra le due regioni.

Al di là dell'interesse nel comprendere come questi fenomeni possano influenzare la nostra vita (metereologia spaziale), lo studio di questo sistema é importante per capire come due diversi plasmi magnetizzati interagiscono quando entrano in contatto senza le limitazioni proprie degli esperimenti di laboratorio.

In questa tesi presento nuovi metodi che consentono di ottenere un'analisi multi-fluida "realistica" dell'interazione vento solare-magnetosfera. Questo obiettivo viene perseguito in tre tappe: (1) l'analisi dei dati acquisiti dai satelliti durante gli attraversamenti della magnetopausa, (2) la costruzione di un modello analitico di equilibrio da cui ricavare profili compatibili con le osservazioni, (3) la messa a punto di un codice numerico multi-fluido per studiare l'evoluzione temporale del sistema modellizzato con i profili analitici di cui sopra presi come condizione iniziale.

L'analisi dei dati é realizzata per mezzo di tecniche originali che permettono di eliminare la maggior parte delle ipotesi tipicamente assunte per i modelli di magnetopausa. Queste tecniche aiutano a distinguere se le variazioni osservate sono causate dai movimenti della magnetopausa o dalla modifica temporale della sua struttura. I nuovi metodi da me sviluppati mostrano risultati coerenti fra loro, ma dipendono dai valori di soglia di alcuni parametri. Le soglie sono determinate in maniera oggettiva mediante tecniche di ottimizzazione.

I profili spaziali ottenuti dall'analisi dei dati forniscono le informazioni principali per un nuovo modello analitico 3fluido che descrive un plasma composto da due popolazioni ioniche e una popolazione elettronica. Tale modello consente di descrivere correttamente le due popolazioni ioniche che sono localizzate nelle due diverse regioni, si sovrappongono nella regione all'interfaccia (magnetopausa) e si annullano nelle opposte rispettive. Il modello permette di determinare in che misura le popolazioni della magnetoguaina e della magnetosfera contribuiscono alla popolazione ionica totale, anche nel caso in cui queste informazioni non sono direttamente accessibili dai dati osservativi. In tal modo é possibile spiegare la forma delle funzioni di distribuzione ioniche nella regione di sovrapposizione.

L'equilibrio descritto dal modello analitico viene quindi perturbato e usato come condizione iniziale da un codice 3fluido, sviluppato a questo scopo. La magnetopausa riprodotta numericamente mostra lo sviluppo di una instabilità magnetica - nota come riconnessione - in accordo con quanto osservato nei dati vicino al caso analizzato.

I risultati della simulazione numerica permettono di trarre alcune conclusioni circa l'evoluzione temporale e la distribuzione spaziale del processo di mescolamento delle due popolazioni all'interno della magnetopausa.

Contents

Chapter

1 Acronyms used in this thesis

- **Paper 1**: "*Crossing of Plasma Structures by spacecraft: a path calculator*", under review at Journal of Geophysical Research (Space Physics)
- **Paper 2**: "*A multi-fluid model of the magnetopause*", under review at Annales Geophysicae
- ***Cr1***: magnetopause crossing happened on 16/10/2015, between 10:36:55 and 10:37:50 UT
- ***Cr2***: magnetopause crossing happened on 16/10/2015, between 13:05:30 and 13:05:60s UT
- **local**: attribute of magnetopause characteristics which are valid at length scales smaller than the magnetopause thickness
- **global**: attribute of magnetopause characteristics which are valid at length scales comparable to (or greater than) the magnetopause thickness
- **GSE**: Geocentric Solar Ecliptic frame
- R_E: (mean) Radius of the Earth corresponding to 6378 km
- **MMS**: NASA's Magnetospheric Multi-Scale mission
- **ACE**: Advanced Composition Explorer
- **IMF**: Interplanetary Magnetic Field
- **FPI**: Fast Particle Instrument
- **SPEDAS**: Space Physics Environment Data Analysis Software tool written in IDL for general analyses of spacecraft data
- **IDL**: Interactive Data Visualisation Solutions Software
- **GPS**: Global Positioning System
- **LHS**: Left Hand Side (term)
- **RHS**: Right Hand Side (term)
- **KHI**: Kelvin-Helmholtz instability
- **iDF**: ions Distribution Function
- $X_n(t)$: projection of the spacecraft trajectory onto the normal direction to the magnetopause
- **MHD**: Magneto-Hydrodynamics
- **CVA**: Constant Velocity Analysis
- **CTA**: Constant Thickness Approach
- **MDD**: Minimum Directional Derivative (method)
- **LNA**: Local Normal Analysis
- **STD**: Spatio-Temporal Difference (method)
- **STD$^+$**: Spatio-Temporal Difference (method) + suppression of singularities
- **SVF**: Single Variate Fit (method)
- **MVF**: Multi Variate Fit (method)
- **MFR**: Minimum Faraday-Residue (analysis)
- **MMR**: Minimum Mass-flux Residue (analysis)
- **GRA**: Generic Residue Analysis
- **MVA**: Minimum Variance Analysis
- **GDMC**: Gradient Directed Monte Carlo (approach)

- **cold/hot ion populations**: term often used to identify the magnetosheath/magnetospheric ion populations
- **ic**: cold ions
- **ih**: hot ions
- Q or $\mathbf{Q}$: a generic scalar or vectorial quantity observed by spacecraft
- L_x: length of the simulation box side parallel to the normal to the magnetopause
- L_y: length of the simulation box side perpendicular to the normal to the magnetopause
- **FGM**: Fastest Growing Mode
- **FFT**: Fast Fourier Transform
- **HPC**: High Performance Computing
- **3fluid**: analysis/analytical model/numerical code that takes into account two ion populations and one electron population
- 3 $\rightarrow$ 2**fluid**: 3fluid analysis/analytical model/numerical code where one of the two ion population is not taken into account and has no feedback on the plasma system
- **2fluid**: analysis/analytical model/numerical code that takes into account one ion population and one electron population

Part I

The interaction between the solar wind and the Earth's Magnetosphere

> *... the most important new space research discovery is probably the cellular structure of space. [...] in every region of space which is accessible to in situ measurements, there are a number of "cell walls", sheets of electric currents, which divide space into compartments with different magnetization, temperature, density, etc. [...] even outside the present reach of spacecraft, space must have a similar cellular structure ...*
>
> Hannes Alfvén, "Cosmic Plasma", 1981

Chapter

2 The Earth's Magnetopause

Chapter content

2.1 The magnetopause in the Sun - Earth context

To a first approximation, the magnetopause is a bi-dimensional current sheet sustained by the interaction between two different plasmas present in the solar system: the solar wind and the Earth's magnetospheric plasma.
The solar wind is a flow of ionised particles escaping from the Sun outwardly. There, the particles acquire enough energy to overcome the gravitational potential energy of the Sun and they can flow outwardly. This motion of the particle flow is radial and it drags the magnetic field lines, which in turn influences the solar wind motion itself. As these lines have their feet anchored in the rotating sun, it follows that their shape is an Archimedes' spiral (the Parker's spiral [11], see a simplified drawing in Figure (2.1)). To a first approximation, the large scale solar wind can be considered collisionless; therefore all non-ideal effects such as resistivity are negligible, and the magnetic field is "frozen" into the plasma flow[1]. The magnetic field and the plasma flow are therefore linked together and the dynamics of the two are tightly connected. The same mechanism justifies the existence of the magnetospheres around the solar system objects having their own magnetic field (both residual and/or actively sustained by a melted core via the dynamo process). As long as the plasma surrounding a magnetised object is frozen into the magnetic field of the object itself, this prevents any mixing of this plasma with the solar wind one. This mechanism digs into the solar wind a sort of elongated bubble filled by a hotter and less dense plasma which is itself frozen into the magnetic field of the object. This bubble (identified by the "planetary obstacle in Figure (2.1)") is what is called "*magnetosphere*". Regarding the Earth, the Earth's dynamo sustains a quasi dipolar magnetic field which fills the nearly standing (in the Earth's rest frame) plasma envelope contained in the magnetosphere (see for instance [101] for a recent review on the subject). Where the solar wind plasma meets the Earth's magnetic field, depends on the relative direction and magnitude of the magnetic fields themselves as well as on the solar wind particle features. A current sheet forms according to Maxwell-Ampère equation. This current sheet, which characterises the boundary with the associated transitions in magnetic field and in plasma density, is what we call "the magnetopause". The balance between the solar wind pressure and the Earth's magnetosphere pressure crudely determines the shape of the magnetopause. Three pressures characterise the plasma: the dynamic (mnV^2), the thermal (nK_BT) and the magnetic ones ($B^2/(2\mu_0)$), where m, n, T, V and B are the ion

[1] the "frozen-in" concept will be explained better in the next chapter (4.1)

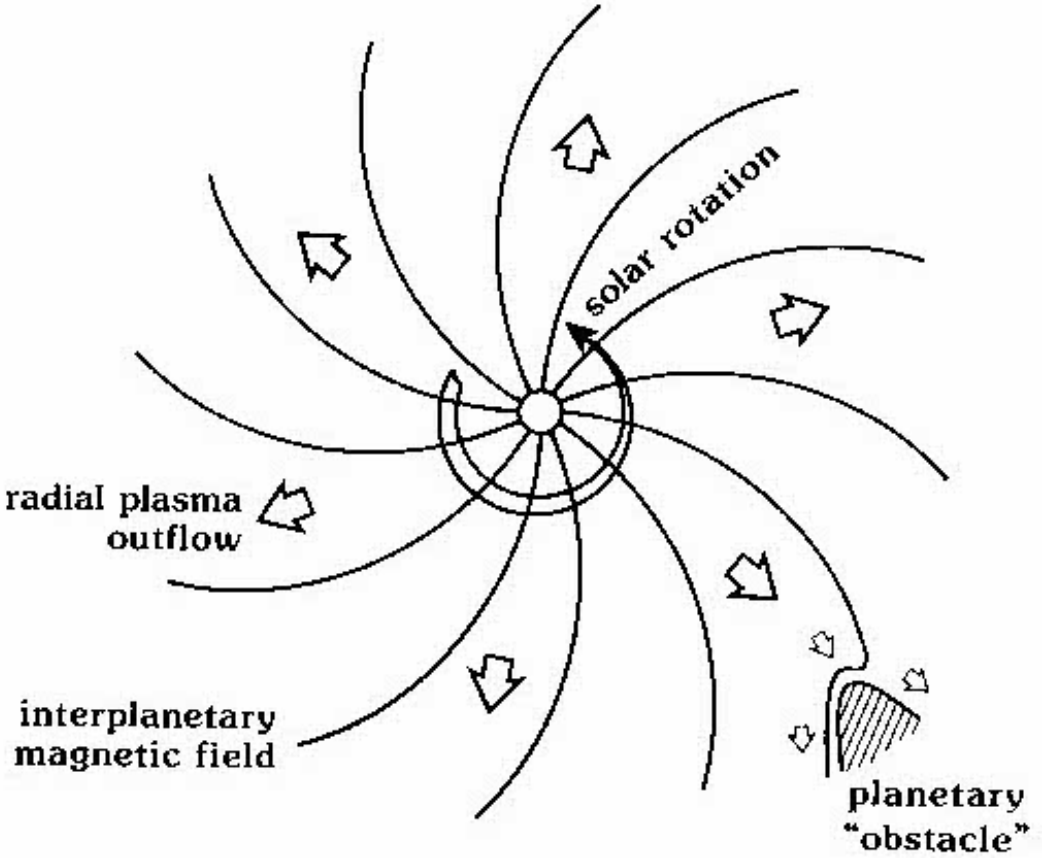

Figure 2.1: *Northward view of the Sun (at the centre) and of the escaping plasma flow from its surface. The solar wind bending trajectories are underlined by the curves departing outwardly from the Sun. During its travel, the solar wind can impact onto magnetised objects (bottom right corner of the figure).The solar wind then glides around the magnetised obstacle and a cavity is formed into the solar wind (the magnetospheres). Credits.*

mass, density, temperature, velocity and the magnetic field, respectively. While in the solar wind the main pressure is the dynamic one, in the magnetosphere the magnetic pressure is greater than the others. For this reason the shape of the magnetospheric boundary can be computed approximately as the surface where the dynamic solar wind pressure and the magnetospheric magnetic pressure are equal (for a basic treatment of this topic, see for instance [92]). The computation [37, 92] returns a parabolic shape, extremely elongated in the night-ward direction. Figure (2.2) shows a dusk-ward view of the XZ GSE (Geocentric Solar Ecliptic frame) section of the sun-ward side of the Earth's magnetosphere. The figure shows the magnetospheric side that looks at the Sun. The magnetosphere actually extends to $\sim 200R_E$ night-ward, out of Figure (2.2), even if the magnetospheric tail is not defined by clear boundaries as its sun-ward side. In the figure, the magnetopause is drawn in purple. With respect to the Earth, in the sun-ward direction, the distance of the magnetopause is approximately $10R_E$ ($R_E \simeq 6378km$), despite it's not constant due to the variation in solar wind conditions. The same can be said for the flank sides (not visible in the figure since they are out of plane), while, as said before, the magnetosphere can be distinguished from the interplanetary space up to $\sim 200R_E$ in the night-ward direction. The magnetopause current sheet has been observed statistically to be $\sim (700 \pm 300)km$ thick [25], which is very small compared to the dimensions of the magnetosphere. This justifies the view of a 2D thin boundary. Despite this, the internal structure of the magnetopause must be considered and analysed since it influences the solar wind - magnetosphere plasma exchanges. Such a current sheet is characterised by rotational and compressional variations, superposed or

not, the geometry and the dynamics of which are often oversimplified in analyses and modellings. This thesis is mainly devoted at introducing some new methods relaxing the strong assumptions often adopted.
In Figure (2.2) the solar wind comes from the left and impacts on the Earth's magnetosphere. Due to the high Alfvénic Mach number[2] of the solar wind at the Earth's distance from the Sun [11], in the sun-ward region ahead of the magnetopause, a bow shock is formed (orange curve). Compared to the solar wind, the region between the bow shock and the magnetopause is filled by a denser and hotter sheet of plasma which encases the magnetosphere and that is called "magnetosheath". Due to the "frozen-in" condition, the shocked solar wind mainly glides around the magnetosphere in the magnetosheath (violet region). The solar wind magnetic field lines are presented here directed toward south, corresponding to a "southward Interplanetary Magnetic Field" (southward IMF) condition. This boundary condition may change depending whether the Earth is below or above the heliospheric current sheet. The magnetospheric magnetic field shown in Figure (2.2) is computed with the Tsyganenko statistical model [37]. The time scales for the Earth's magnetic field to reverse are much longer and not periodic (observe for instance the Earth's magnetic polarity traces drawn in chronostratigraphic charts correlating the age of rocks to the residual magnetic field recorded within the rocks themselves [31]). In this case, the two magnetic fields on both sides of the magnetopause have different orientations, showing that the boundary is a current layer.

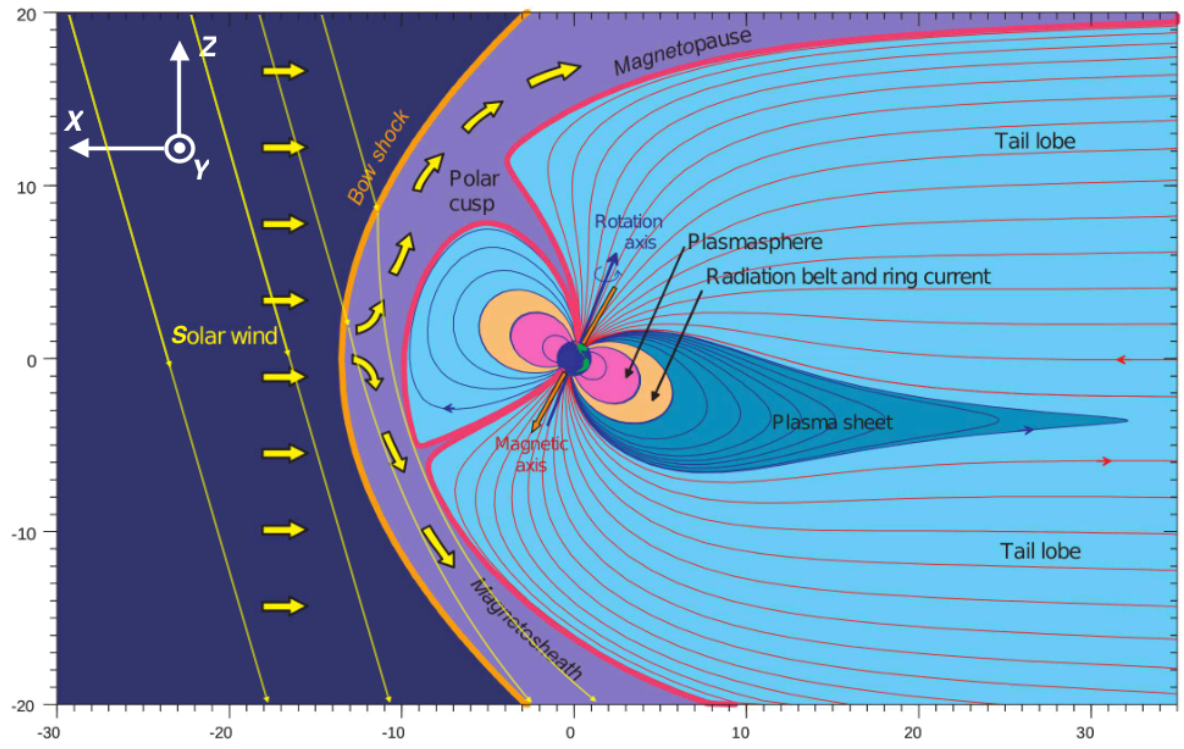

Figure 2.2: *Dusk-ward view of the Earth's magnetosphere. The units of the axes are in Earth's Radii R_E and the frame used is the Geocentric Solar Ecliptic (GSE) frame (see the white arrows on the upper left corner). The solar wind comes from the left. The orange and the purple curved lines encasing the magnetosphere are the bow shock (orange curve) and the magnetopause (purple curve). The magnetospheric magnetic field is computed with the Tsyganenko statistical model [37]. Credit: P. Robert (CETP/CNRS)*

[2] "Super Alfvénic" means the plasma fluid velocity (with respect to some stationary structure) is larger than the Alfvén velocity $V_A = \sqrt{B^2/(2\mu_0\rho)}$, where B is the modulus of the magnetic field, μ_0 is the magnetic permeability of the free space and ρ is the plasma density.

2.2 Why do we need to study the space plasmas?

From the observational point of view, such a system needs for dedicated spacecraft missions. From the numerical point of view, the simulations mimicking this system require high performance computing frameworks. Why is the scientific community so interested in the magnetopause system? The three main reasons are:

1. **Improve our understanding about plasma physics**
   The particle-magnetic system that surrounds our planet is an excellent laboratory where the plasma behaviour can be observed *in situ* and analysed in detail:

   (a) At the magnetopause, all phenomena are characterised by length scales much larger than the dimensions of the probes (*i.e.* the spacecraft size). The length scale of the finest phenomena (magnetic reconnection for instance) is of the order of 10 km whereas the spacecraft have dimensions of the order of a few meters. On the contrary, in laboratories such experimental conditions can not be reached. For this reason within the magnetopause the plasma can be probed at length scales not achievable, after re-scaling, by means of laboratory sets-ups.

   (b) the magnetopause is the nearest boundary between two astrophysical plasmas that can be measured directly with *in situ* measurements.

2. **Space Weather**
   Quasi-periodically (every $\sim$ 11 years), the frequency and magnitude of Sun surface phenomena (*e.g.* Coronal Mass Ejection, Solar Flares) reach a maximum. Near and during these periods, large amounts of particles are released (a phenomenon due to reconnection phenomena between magnetic field lines arising from the Sun surface). If released toward the Earth, these energetic particle flows (having higher energy than the standard solar wind flow) can alter the magnetosphere and enter the magnetosphere modifying the state of the magnetospheric plasma. These events can be dangerous for the life on Earth since the modification of the magnetosphere could expose the Earth's surface to high energy particles and radiations usually screened by the magnetosphere. For instance, recent studies suggest that the temporary decrease of the Earth's magnetic field (and, as a consequence, of its screening function) could have played an active role in the evolution of the humans beings [138]. The same magnetic field decrease could have caused the loss of the atmosphere of other planets. The magnetic field decrease allows the solar wind to interact directly with the atmosphere (these interactions are known as "Venus-like" interaction). In this case the top layers of the atmosphere are dragged away due to the collisional interaction with the solar wind (see for instance [99] and references therein). The study of the electromagnetic and particle coupling between the Sun and the Earth (Space Weather) is therefore fundamental to understand to what extent we can trust the natural shield constituted by the magnetosphere system which protects our lives from the Sun's moods. As a matter of fact, this shield has already demonstrated not to be strong enough to protect our tech-based life in case of violent Sun's storms (for instance the "Carrington event" on 1859 caused telegraph systems to fail all over the Europe and in the North America) and international policies have been focused on the topic [97].

3. **Fusion research**
   Though in space the measurements are local and not reproducible, many phenomena that are important in all plasmas (including far astrophysical plasmas and laboratory plasmas) can be studied in the magnetopause context (surface waves [60], Kelvin-Helmholtz and Rayleigh-Taylor instabilities [30, 35, 100], magnetic reconnection [114], turbulence [128] or inter-plays between these different phenomena ([49, 43, 76, 86, 78, 104]). Some of these phenomena are observed as well in the thermonuclear fusion plasmas where they

play often a pathological role impeding the ignition (in the magnetic fusion facilities) or the compression (in the inertial fusion facilities) of plasmas. Increasing our understanding about such phenomena can therefore be important to help reaching the targets of providing energy by means of nuclear fusion.

2.3 How is the space plasma probed?

The goal to collect data near and across the magnetopause has been carried on by single and multi spacecraft missions since the beginning of space era, i.e. the sixties of the last century. The multi-spacecraft missions, the first one being the European Cluster mission (2000), are designed to discriminate the temporal and spatial variations in the measured physical quantities. The multi-spacecraft architecture has been adopted for the successor of Cluster, the "Magnetospheric MultiScale" mission (MMS). The four MMS spacecraft are located at the vertices of a tetrahedron designed to be most regular at the apogee of the orbit, where MMS is supposed to cross the Earth's magnetopause [113]. The goal of the MMS mission is to investigate magnetic reconnection events. Such events are likely to happen mostly at the day-side magnetopause and along the magnetospheric tail. The MMS orbit is therefore designed to intersect these regions at the apogee of its orbit. Figure (2.3) shows the MMS orbits (black ellipses) in the magnetosphere context from a north-ward point of view designed to probe the magnetopause (leftward-elongated orbit) and the magnetotail (rightward-elongated orbit).

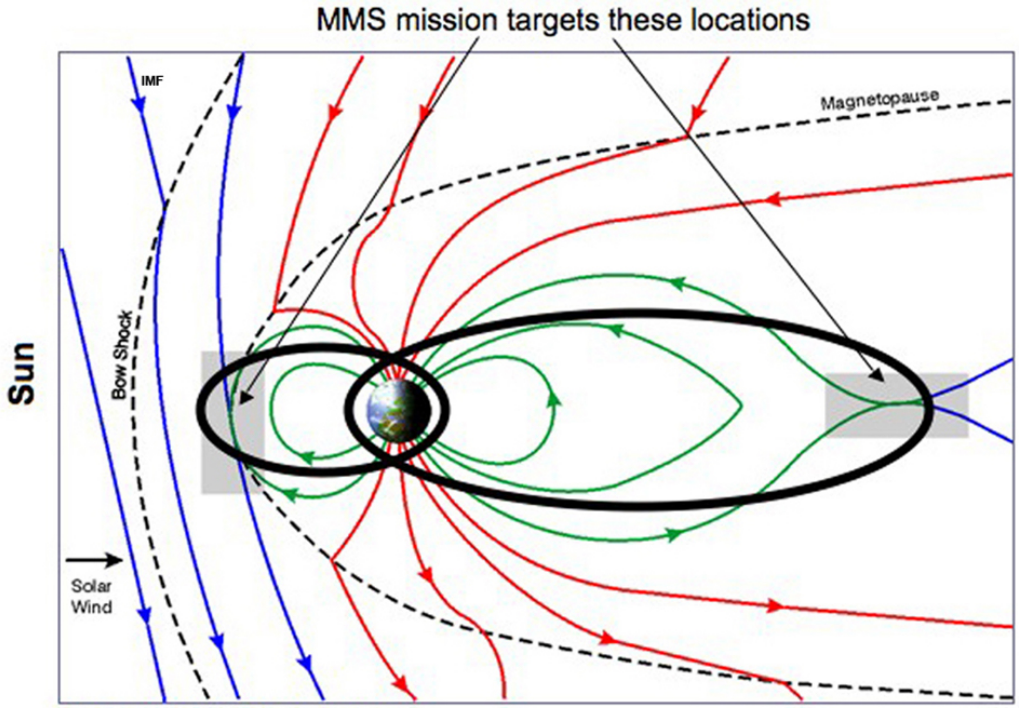

Figure 2.3: *North-ward view of the MMS orbits (black thick elliptic curves) with respect to the Earth, its magnetic field and the Magnetopause location. The two grey rectangle outline where the magnetic reconnection events are likely to happen the most. The blue, red, green magnetic field lines indicate, respectively, the solar wind, the open and the closed magnetic field lines. Credits: NASA*

The tetrahedron shape, when sufficiently regular, allows to compute the 3D spatial gradients of the measured quantities, plasma and fields [48]. It therefore allows to discriminate, in the temporal variations observed on each spacecraft, what is due to the propagation of these spatial gradients and the more intrinsic temporal variations. The choice of the size of the tetrahedron, along with the time resolution of the measurements, are based on the size of the electron and ion

diffusion regions at the magnetopause ($\sim$ 5 km and $\sim$ 200 km for electrons and ions respectively according to the densities measured, which are equal to $\sim 10^1$ cm^{-3}) and their bulk velocity ($\sim 1-100$ km/s). Following these constraints, the range of spacecraft separation available to MMS is $\sim 10-400$ km ($\sim 10-160$ km on the day-side and $\sim 30-400$ km on the night-side part of the magnetosphere). The sampling rate of the instruments depends on their positions along the orbit. In the first phase of the mission, the main scientific objective is the magnetopause and therefore the data are acquired with the highest resolution near the apogee [113]. Figure (2.4) shows a schematic view of the sampling rates used by MMS depending on the location of the spacecraft along its orbit. From the figure it can be observed that the most part of data ($\sim$ 74%) are acquired within very small intervals near the spacecraft apogee. There, magnetic fields are probed at 128 Samples per seconds (S/s) (FIELDS instrument suite [119]) whereas particle data for ions and electrons are probed respectively at $\sim 7S/s$ and $\sim 33S/s$ (Fast Particle Instrument (FPI) [117]). From MMS I got data about the plasma encountered during the magnetopause

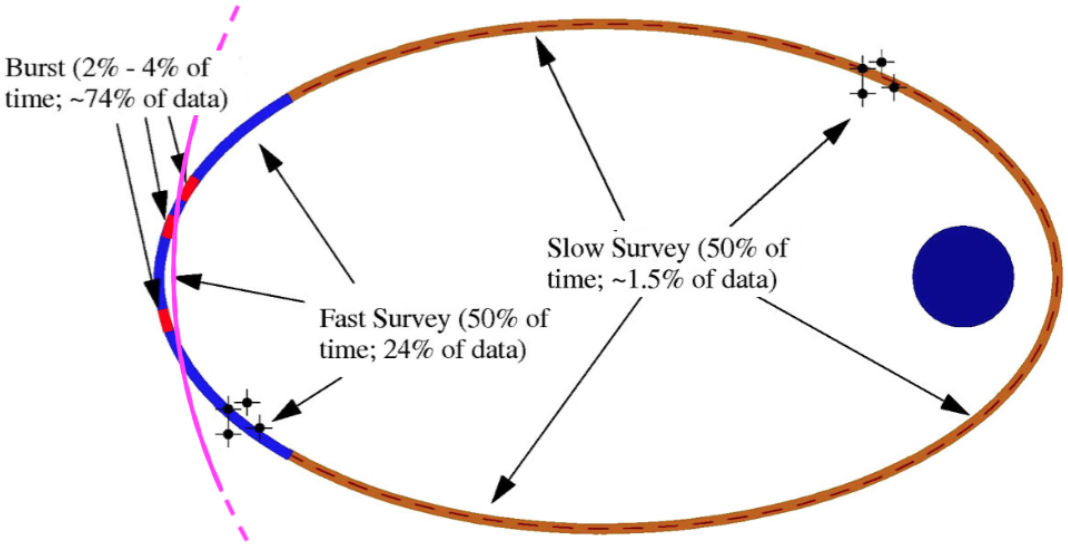

Figure 2.4: *Schematic view of the sampling rates used by MMS depending on the location of the spacecraft along its orbit (as seen from a northward point of view). The blue circle on the right is the Earth. The four black crossed points superposed twice to the orbit are the four MMS spacecraft. The magnetopause is drawn in purple. Orbit intervals of high, medium and low interest are drawn respectively in red, blue and brown. The more MMS is close to its apogee, the more it is likely to cross the magnetopause, the higher the sampling rates of instruments are. Credits: figure modified from [113].*

crossings and, in particular, I used data acquired at the nose of the magnetosphere, near the equatorial plane. MMS data are available on a standard way using the IDL framework called SPEDAS for Space Physics Environment Data Analysis Software ([132]). Some of the tools presented in this thesis are available in SPEDAS (not all). But the choice has been made to have at our disposal freeware tools to analyse the data. Therefore I have developed all the library necessary for the work presented here in Python. As will be evident in section (II), this thesis has taken full advantage from the new and peculiar features of the MMS mission since the small spacecraft distance and the high sampling rate adopted by the mission relatively to the previous multi-spacecraft missions (CLUSTER) allow to study the internal structure of the magnetopause and allowed to discriminate the pure temporal modification of the magnetopause structure from the spatial ones. Such investigations cannot be done using Cluster, the inter-spacecraft distance and the probing rates of which are respectively 100 times larger and a few times lower than that adopted for MMS. Finally, in order to find solar wind conditions far upstream from the magnetopause, I used data from the “Advanced Composition Explorer" (ACE) [57], a single spacecraft mission orbiting near the Lagrange point L1. From its position 1.5×10^6 km in front

of the Earth, ACE represents an excellent outpost where to measure the IMF and the properties of the solar wind before it impacts the Earth's magnetosphere. While its primary target is to measure the charge state composition of nuclei from H to Ni from solar wind energies to galactic cosmic ray energies, ACE also carries two experiments (the Solar Wind Electron, Proton and Alpha Monitor [52] and the MAGnetic and field experiment [55]) that provide real-time solar wind measurements.

Chapter

3 The description of the plasmas

Chapter content

3.1 The 4^{th} state of the matter

3.1.1 What is a plasma?

A plasma is a collection of charged particles of matter coupled by electromagnetic fields. A plasma behaves differently from usual solids and fluids. For this reason it is commonly known as the 4^{th} state of the matter. The coupling between Electro-Magnetic Fields (EMF) and charged matter is described on figure (3.1). Via the Lorentz force, the local values of **E** and **B** contribute to the dynamics of each individual charged particle trough the momentum and energy balance equations. Performing an average over a small volume of the positions and velocities of the many particles results in a charge density ρ and a current density **J** that are source terms in the Maxwell equations. This avoids using a full N-body description, which would be extremely heavy. One may have however to take into account the differences between **E** and **B** and their averaged values $<\mathbf{E}>$ and $<\mathbf{B}>$. This leads to corrections that are called "collisions" and that can play a role in the dynamics of the plasma, depending on the physical regime.

3.1.2 The collective interaction of plasmas

Figure (3.1) represents the coupling between charged particles and electromagnetic fields in plasmas. In gases with no ionisation at all, the red lines disappear: the particles and the electromagnetic realms are separated. In this context the particles can be considered neutrals because the charged nucleus of the atoms is completely shielded by the electrons very closely to the nucleus itself. The interaction between adjacent particles is caused by electric binary interactions happening between uncharged particles and having a $1/r^7$ spatial dependence, typical of the inter-molecular dipole induced interactions. On the other hand, when matter is ionised, the electrostatic interaction, modified by the collective reaction of the plasma, is characterised by longer space lengths $\propto 1/r^2 e^{-r/\lambda_D}$, where λ_D is the Debye length equal to $\sqrt{\frac{\epsilon_0 K_B T}{n_e e^2}}$. The notion

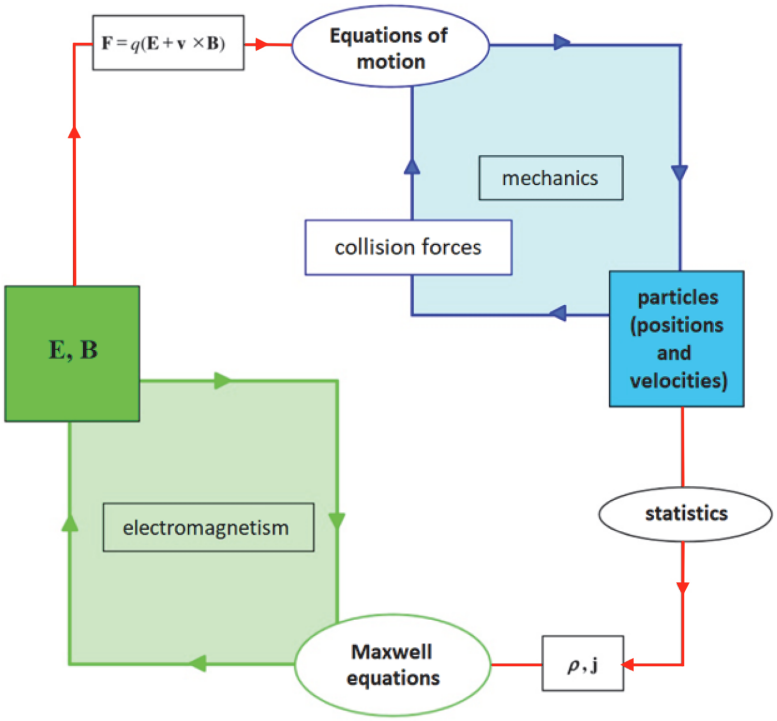

Figure 3.1: *Sketch describing the reciprocal influence of charged matter and electromagnetic fields in plasmas. Credits: modified from [133]*

of "collision" in a neutral gas or in a plasma are qualitatively different. In both cases, one can define the mean free path corresponding to this phenomenon, which is the length required for a test particle to change significantly its direction (for instance by a $\pi/2$ angle, see the bottom sketch of Figure (3.2)). But in the neutral case, each such direction change is "binary", i.e it involves only one other particle, while in the plasma case, the deviation of the test particle involves a very large number of other particles.

3.1.3 Characteristic time and length scales to define different plasma regimes

Plasmas can be found in a broad interval in temperature and density. Figure (3.3) shows the $n-T$ parameter space occupied by plasmas. It is ~ 35 orders of magnitudes width in density and ~ 10 orders of magnitude width in temperature. There is no general method (neither analytic nor numeric), which would be tractable, to describe the huge plethora of phenomena plasmas are concerned with. Plasma must be therefore studied within limited regimes that allow to simplify the equations involved.

The boundaries of these regimes are defined comparing the temporal and the spatial scale characterising the phenomenon under study to certain temporal and spatial scales characterising plasma. Indicating with β both the ions ($\beta = i$) and the electrons ($\beta = e$), the temporal and spatial scales characterising plasma can be:

- for time scales:
  - the inverse of electron plasma frequency:

$$\omega_P = \sqrt{\frac{e^2 n_e}{\epsilon_o m_e}} \tag{3.1}$$

    It represents, in a simplified and static view, the inverse of the typical time of a collective response of the electrons to any ambient charge modification.

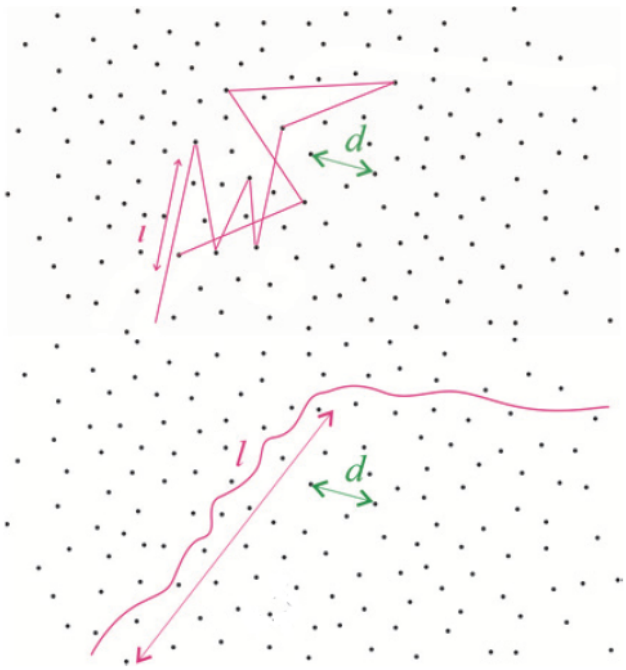

Figure 3.2: *Comparison between the particle-particle interaction in normal fluids (top sketch) and in plasmas (bottom sketch). l and d are the mean free path and the inter-particle distance. Credits: modified from [133]*

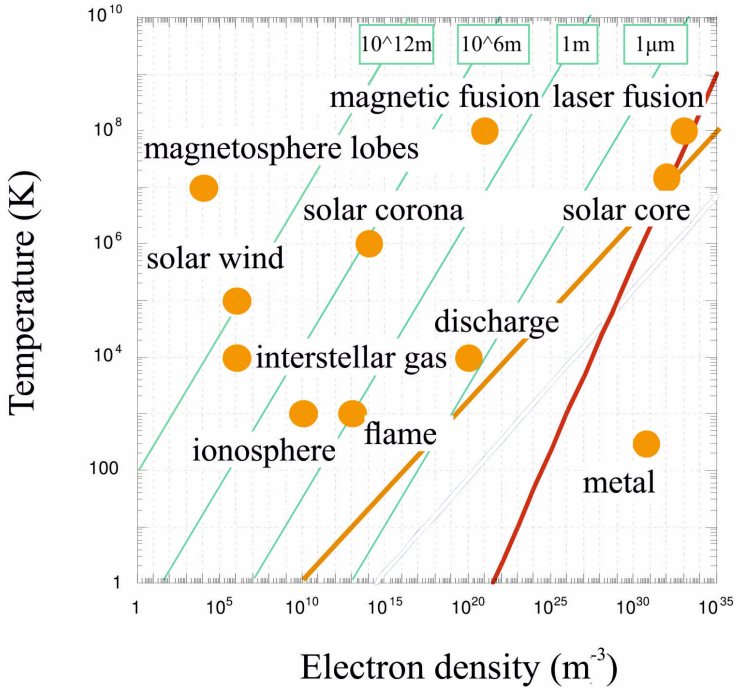

Figure 3.3: *The position in the $n - T$ parameter space of some plasmas found in nature. The green lines are four different loci defining four different mean paths. Below the red line, quantum effects have to be taken into account, above they can be neglected. Below the orange line binary interactions dominate the physics, whereas above the collective interactions are dominant. Credits: modified from [133]*

– the inverse of the cyclotron frequency:

$$\omega_{C,\beta} = \frac{q_\beta B}{m_\beta} \tag{3.2}$$

It represents the inverse of the period of the orbital motion of charged particles in magnetic fields.

- for length scales:
  - the inertial length

$$d_{I,\beta} = c\ \omega_{P,\beta}^{-1} \tag{3.3}$$

It represents the depth in a plasma to which electromagnetic radiation can penetrate ($d_{I,e}$) or the distance from a magnetic reconnection X point at which the dynamics of ions and electrons start to separate from that of the magnetic field ($d_{I,i}$ and $d_{I,e}$, respectively).

  - the Larmor radius

$$\rho_{L,\beta} = v_{th,\beta}\ \omega_{C,\beta}^{-1} \tag{3.4}$$

In the previous equations, the following definitions have been used: e is the electric charge of a proton, ϵ_0 is the electric permittivity of the free space, n_i (n_e) is the ion (electron) density, m_i (m_e) is the ion (electron) mass, B is the magnitude of the magnetic field, T_i (T_e) is the ion (electron) temperature, $v_{th} = \sqrt{\frac{3K_BT}{m}}$ is the thermal velocity where K_B is the Boltzmann's constant.

It is clear from figure (3.3) that the plasmas we are studying in this thesis, solar wind and magnetosphere plasmas, are very tenuous plasmas, almost collisionless, and dominated by collective effects. The Sun-Earth distance is about $1.5 \times 10^{11} m$ which is roughly equal to the mean free path in the solar wind.

3.2 The different descriptions of plasmas

3.2.1 The Vlasov-Maxwell equations

Plasmas visualised in the $n-T$ parameter space of figure (3.3) are composed of a huge number of charged particles, in some case including in part also neutrals. These particles belong to various populations (electrons, protons, ions). The basic method by which a plasma population can be modelled is by means of a statistical approach (see for instance [98]). The plasma population s is described by a distribution function

$$f_s(\mathbf{x}, \mathbf{v}, t) = \sum_i \delta(\mathbf{x} - \mathbf{x}_{s,i}(t))\delta(\mathbf{v} - \mathbf{v}_{s,i}(t)) \tag{3.5}$$

where $\mathbf{x}_{s,i}(t)$ and $\mathbf{v}_{s,i}(t)$ are the position and the velocity of the i^{th} particle of population s. $f_s(\mathbf{x}, \mathbf{v}, t)$ is defined in a $6D$ position - velocity ($X-V$) phase space. The evolution equation for $f_s(\mathbf{x}, \mathbf{v}, t)$ is

$$\frac{\partial f_s(\mathbf{x}, \mathbf{v}, t)}{\partial t} + \mathbf{v} \cdot \nabla_{\mathbf{x}} f_s(\mathbf{x}, \mathbf{v}, t) + < \mathbf{a} > \cdot \nabla_{\mathbf{v}} f_s(\mathbf{x}, \mathbf{v}, t) = S_s \tag{3.6}$$

The LHS term of the previous equation can be immediately identified by the $X-V$ phase space operator D/Dt applied to $f_s(\mathbf{x}(t), \mathbf{v}(t), t)$. In the right hand side (RHS) of (3.6) S_s is a source term for population s. It represents the operator accounting for collisions between the particles of the plasma. According to the form of S_s, the equation (3.6) is known with different names (for instance Boltzmann or Fokker-Planck depending on whether the collisions are modelled as hard-sphere binary interaction or if S_s has the form of a diffusion operator). When collisions can be

neglected, we assume $S_s = 0$; in this case the equation (3.6) is known as "the *Vlasov equation*". So, for each of the population s composing the plasma, the complete kinetic description is obtained by the equation (3.6) (with $S_s = 0$) coupled to the Maxwell equations. This system is known as the Vlasov-Maxwell equations.

3.2.2 The fluid equations

When the characteristics spatial L and temporal scales T of some phenomenon are larger than the spatial $\rho_{L,i}$ and temporal $1/\Omega_{C,i}$ scales of the plasma, as given by Equations (3.4) and (3.2), the plasma can most often be treated as a fluid. The fluid equations for mass, momentum and energy balance of a plasma population s can be recovered taking the p-order moment of equation (3.6), *i.e.* multiplying both the LHS and the RHS of equation (3.6) with $S_s = 0$ by $\mathbf{v}_s^p$ $(p \in N)$ and integrating the resulting equation over velocity. Assuming $< a >= F_s/m_s$ and $S_s = 0$, the first three momenta of equation (3.6) read:

$$\begin{cases} \partial_t(n_s) + \nabla \cdot (n_s \mathbf{V}_s) = 0 & \text{(3.7a)} \\ \partial_{\mathbf{t}}(n_s m_s \mathbf{V}_s) + \nabla \cdot (n_s m_s \mathbf{V}_s \mathbf{V}_s + \mathbf{P}_s) = n_s q_s (\mathbf{E} + \mathbf{V}_s \times \mathbf{B}) & \text{(3.7b)} \\ \partial_t(n_s m_s \frac{V_s^2}{2} + \frac{3}{2} P_s) + \nabla \cdot \left(\mathbf{v}_s (n_s m_s \frac{V_s^2}{2} + \frac{5}{2} P_s) + \mathbf{Q}_s \right) = n_s q_s \mathbf{V}_s \cdot \mathbf{E} & \text{(3.7c)} \end{cases}$$

where

$$n_s = \int f_s(\mathbf{x}, \mathbf{v}, t) d^3\mathbf{v} \tag{3.8}$$

is the number density,

$$n_s \mathbf{V}_s = \int \mathbf{v} f_s(\mathbf{x}, \mathbf{v}, t) d^3\mathbf{v} \tag{3.9}$$

is the bulk flow velocity,

$$\mathbf{P}_s = \int (\mathbf{v} - \mathbf{V}_s)(\mathbf{v} - \mathbf{V}_s) m_s f_s(\mathbf{x}, \mathbf{v}, t) d^3\mathbf{v} \tag{3.10}$$

is the pressure tensor and

$$\mathbf{Q}_s = \int ||(\mathbf{v} - \mathbf{V}_s)||^2 (\mathbf{v} - \mathbf{V}_s) m_s f_s(\mathbf{x}, \mathbf{v}, t) d^3\mathbf{v} \tag{3.11}$$

is the vectorial heat flux. It is worth noting that:

- all the equations of system (3.7) are in the form

$$\partial_t(quantity) + \nabla \cdot (flux) = source \tag{3.12}$$

- $\forall i$, the i^{th} moment of equation (3.6) takes into account the $(i+1)^{th}$ moment.

For the last point, the fluid description of plasmas needs a closure hypothesis about the $(i)^{th}$ moment that allows to describe the $(i)^{th}$ moment using lower order moments and excluding the contribution of the $(i+1)^{th}$ moment. This choice depends on the system under study. The system (3.7) is completed by the Maxwell equations and the definitions of charge and current sources $\rho = \sum_i^s n_i q_i$ and $\mathbf{J} = \sum_i^s n_i q_i \mathbf{V}_i$.

3.2.3 The Magneto-Hydrodynamics equations

To make a multi-fluid modelling of the plasma, one has to use the above fluid equations for each population and couple them with Maxwell equations. The ultimate simplification that can be done is to reduce this multi-fluid description to a single-fluid one. This leads to the commonly used MHD theory. We recall here briefly this description for completeness, although it will not be used in the rest of this thesis, neither in data analysis nor in numerical simulations. Anyway, the assumptions made here will help understanding the assumptions made in section (11.3). Considering the quasi-neutrality condition $n_i = n_e$ and remembering the current density $\mathbf{J} \equiv en(\mathbf{V}_i - \mathbf{V}_e)$, one can use a unique density $n = n_i = n_e$ and one unique velocity $\mathbf{U}$, which is the centre of mass velocity:

$$\mathbf{U} \equiv \frac{m_e\mathbf{V}_e + m_i\mathbf{V}_i}{m_e + m_i} \tag{3.13}$$

The equations (3.7) can be further simplified since, in this case,

$$\mathbf{V}_i = \mathbf{U} + o\left(\frac{m_e}{m_i}\right) \tag{3.14}$$

and

$$\mathbf{V}_e = \mathbf{U} - \frac{\mathbf{J}}{en} + o\left(\frac{m_e}{m_i}\right) \tag{3.15}$$

Furthermore, the pressure is assumed to be scalar and resulting from the sum of ion and electron pressures $P = P_i + P_e$.

Under these conditions, each of the equations (3.7) for ions and electrons can be summed, term by term. Using the adiabatic closure, after some algebraic reordering and simplification the resulting equations become:

$$\begin{cases} d_t(n) + n\nabla\cdot\mathbf{U} = 0 & \text{(3.16a)} \\ m_i n d_t(\mathbf{U}) + \overline{\nabla} P = \mathbf{J}\times\mathbf{B} & \text{(3.16b)} \\ d_t\left(P/\left(m_i n\right)^{(5/3)}\right) = 0 & \text{(3.16c)} \end{cases}$$

where $d_t(...) \equiv \partial_t(...) + \mathbf{U}\cdot\overline{\nabla}(...)$ and $P = P_i + P_e$ is the total pressure. System (3.16) is completed by the Maxwell's equations and the ideal Ohm's law which is derived from (3.7) and writes for large scales as:

$$\mathbf{E} + \mathbf{U}\times\mathbf{B} = 0 \tag{3.17}$$

Chapter

4 Interacting plasmas across the Magnetopause: a not simple system

Chapter content

4.1 Why do magnetospheres exist?

Consider the temporal change of the magnetic flux ψ through a loop C co-moving with the plasma, S being a surface spanning C:

$$\frac{d\psi}{dt} = \int_C \frac{\partial}{\partial t} (\mathbf{B} \cdot d\mathbf{S}) \tag{4.1}$$

The changes are due to the variations in both $\mathbf{B}$ and the surface S. The latter causes a change in the magnetic flux per unit of time equal to $\mathbf{B}\cdot\mathbf{u}\times d\mathbf{r}$. Using the curl theorem and $\partial\mathbf{B}/\partial t = -\nabla\times\mathbf{E}$, the Equation (4.1) becomes

$$\frac{d\psi}{dt} = \int_C \nabla \times (\mathbf{E} + \mathbf{u} \times \mathbf{B}) \cdot d\mathbf{S} \tag{4.2}$$

where we observe that, as long the ideal Ohm's law

$$\mathbf{E} + \mathbf{u} \times \mathbf{B} = 0 \tag{4.3}$$

is valid, the total change is $d\psi/dt = 0$ (*i.e.*: ψ =const).

Considering an infinitesimal loop and therefore an infinitesimal flux tube, this result gives sense to the notion of "field line motion". If the field line is characterised by its flux, the line "moves" in following the plasma, everywhere the ideal Ohm's law is valid. In this realm the plasma and the magnetic field move anchored to each other at $\mathbf{v}_m = \mathbf{E} \times \mathbf{B}/B^2$, which is the "frozen-in" velocity. The most general condition for the frozen-in property is actually more general than the ideal Ohm's law, since it is valid everywhere there is no parallel electric field or even more generally when the curl of the parallel electric field is zero [96]. This constraint fully derives

from the Maxwell electromagnetic properties, and they are related to plasma properties only via the existence -or not- of the ideal Ohm's law able to cancel the parallel electric field. They give the reason why the magnetopause exists: the solar wind plasma feels the encounter with the magnetosphere like an obstacle. To a first approximation, the solar and the magnetospheric magnetic field lines frozen in the two respective plasmas have to remain separated if the frozen-on condition (say $E_{\parallel} = 0$) is respected everywhere. This mechanism is the dominant one along the magnetopause: the magnetic field lines of the magnetosheath (and the plasma frozen in with them) does not reconnect to the magnetospheric magnetic field lines (and the plasma frozen in with them). In these conditions, the magnetosheath plasma glides along the magnetopause and overcomes the magnetosphere without entering it. No mixing with the magnetospheric plasma occurs.
Nevertheless, the behaviour of the two magnetic fields and plasmas can depart from this simple view as soon as the frozen-in condition is violated at some places on the magnetopause. This opens the possibility of "reconnection events" around these places. Figure (4.1) shows what happens between two magnetic field lines during a reconnection event. The first panel (panel (4.1.a)) shows on the left two field lines approaching each other: the green dotted from the right and the purple dotted from the left. Once they meet, the two fields lines start to bend (panel (4.1.b)). In case of ideal conditions (*i.e.* in case Equation (4.3) is satisfied) the two field lines would maintain their own identities: they would glide side by side and the change in topology shown in panel (4.1.c) would not occur.

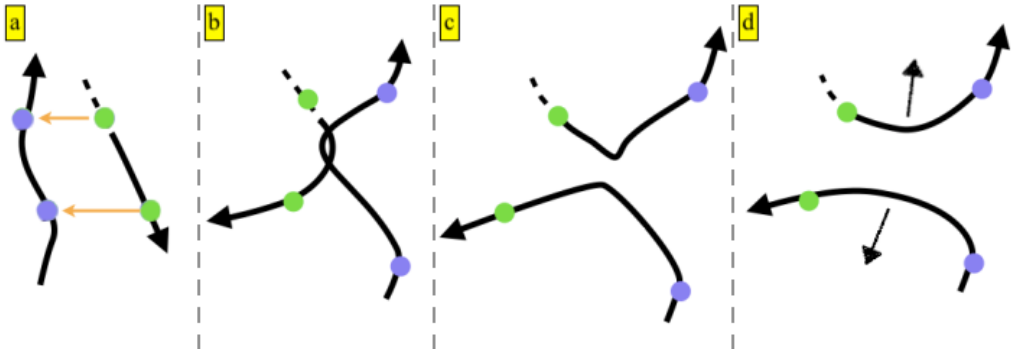

Figure 4.1: *Cartoon showing what happens to two magnetic field lines and to the associated plasma during a magnetic reconnection event. Panel (a): two magnetic field lines approach each other transported by the flow. The two field lines belong to different plasma domains. Panel (b): the two magnetic field lines gently bend. Each field line is yet identifiable. Panel (c): the ideal Ohm's Law (Equation (4.3)) becomes invalid close to an "X point", and the field lines change their connections, giving rise to strongly bent lines. Now the different plasmas are linked by the re-connected field lines. The energy accumulated in bending the field lines is released as kinetic energy and heat. Credits: after N. Aunai.*

4.2 Global and local perturbations of the magnetopause structure

In case of non-ideal conditions, *i.e.* when the generalised Ohm's law (4.3) includes terms such as resistivity or electron inertia that are non negligible at some places, the two field lines visualised in Figure (4.1) can change their topology and reconnect each other. Panel (4.1.c) shows such event: the purple and the green circles belong now to the same field line. The energy stocked in bending the field lines is so transformed and released as kinetic and thermal energy (panel (4.1.d)).

In fact, Equation (4.3) is not satisfied everywhere along the magnetopause [118]. Magnetosheath magnetic field lines reconnect to the magnetospheric ones. Direct links between the

two systems occur, plasma mixing happens and a small amount of magnetosheath mass [45], momentum [15] and energy [26] enters directly into the magnetosphere. The structure of the magnetopause is therefore severely perturbed. Changes happen at both global and local scales, where "global" and "local" refer to scales larger or smaller than the magnetopause thickness. Reconnection is called a "cross-scale phenomenon" for this reason.
Figure (4.2) shows for instance what happens to a solar wind magnetic field line (red oblique curve in panel *a*) when it impacts on the magnetosphere. From the cartoon it can be observed that due to a very localised magnetic reconnection event (localised within the star in the middle of panel *d*) the topology of the solar wind magnetic field line is severely modified (panel *e*).

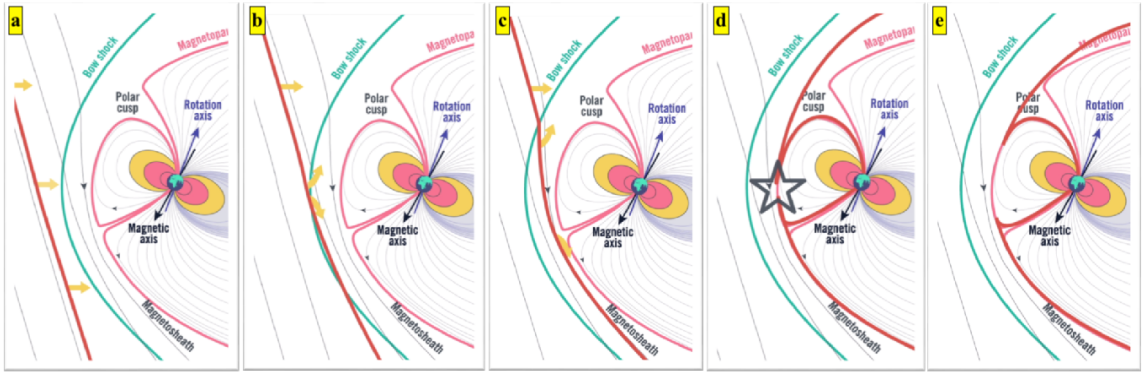

Figure 4.2: *Cartoon showing a magnetic reconnection event happening at the magnetospheric sub-solar point. A solar wind magnetic field line comes from the left dragged by the solar wind (panel a). It passes the bow shock preserving its direction (panel b) and start to bend due to accumulation onto the magnetopause forefront (panel c). Suddenly, it reconnects to the Earth's magnetic field in a very localised point (star in the middle of panel d). The magnetic field topology of both solar wind and magnetosphere magnetic fields up to global scales are therefore modified (panel e). Credits: L. Rezeau.*

Moreover, the magnetic reconnection mechanism is not only a stand-alone mechanism. Often, it is driven by primary magneto-hydrodynamic instabilities that trigger magnetic reconnection as a secondary instability and increase the amount of magnetosheath plasma that accesses the magnetosphere. For instance, Figure (4.3) shows the key steps of what is called "Doubled mid-latitude Reconnection" [104]. The phenomenon is a clear and meaningful example of the interplay between the Kelvin-Helmholtz instability (KHI) and the magnetic reconnection where the latter is induced by the former. It happens at mid-latitude, relatively far from the case studies that will be introduced in this thesis, but it is worth a few words. In Figure (4.3) some magnetic field lines of particular interest at the flank of the magnetopause have been drawn. Frame (a): the magnetospheric (blue) and the magnetosheath (red) magnetic field lines are frozen in to their own region and therefore are severely bent by the ongoing KHI. At mid-latitude in both the hemispheres the magnetospheric and magnetosheath field lines are patched close together by the twist motion of the forcing KHI ongoing at $L_z = 0d_i$ and therefore a large current sheet (the green bulk) is formed due to the large inhomogeneities in magnetic field ($\overline{J} = \overline{\nabla} \times \overline{B}$). Frame (b): at mid latitudes in the north hemisphere magnetic reconnection occurs between the magnetic field lines: a direct link between magnetosheath and magnetosphere is established. Due to the inclination of the Earth's axis rotation with respect to the ecliptic plane no reconnection have occurred yet in the south hemisphere. Panel (c): magnetic reconnection occurs between the magnetic field lines at mid latitudes in the south hemisphere too. All the plasma originally connected to the magnetic field lines between the two mid latitude points that did not managed to escape are now detached from their region of origin.

The wild interplay between magneto-hydrodynamic instabilities suggests that the magnetopause structure may be complex. The different sub-structures that compose the magnetopause discontinuity (which are theoretically predictable if they are truly 1D and stationary) are in fact

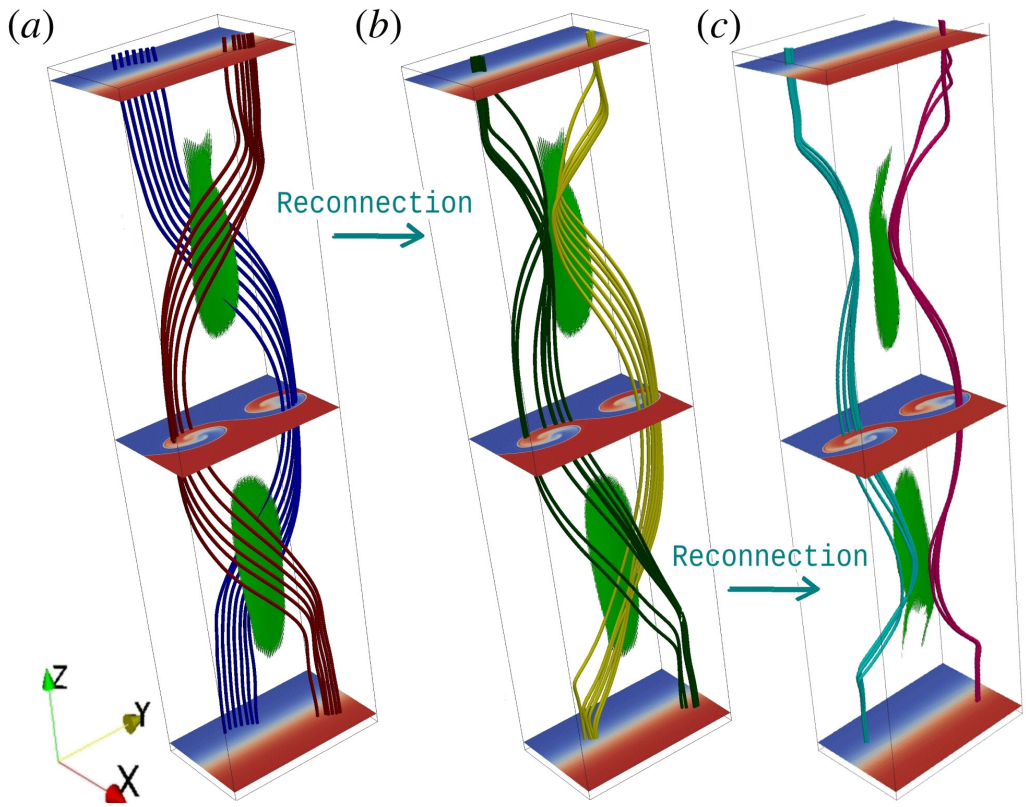

Figure 4.3: *Framed cartoon showing the doubled mid-latitude Induced magnetic reconnection [104], driven by the Kelvin Helmholtz instability (KHI). All the frames show the* $\{L_x, L_y, L_z\} = \{36, 60, \pm 180\} d_i$ *region intersecting the the magnetopause nearly at the left magnetospheric flank side (looking at the Sun). The magnetopause crosses each box along the y direction. Each frame shows three slices of the passive tracer (at* $L_z = [-180, 0, 180]$*): blue for the magnetospheric plasma and red for the magnetosheath plasma. The* $L_z = 0$ *slice (the central one in each panel) shows clearly an ongoing non-linear phase of the KHI, whereas the* $L_z = \pm 180 d_i$ *do not. The dimensions ratios of the simulated region are* $\{L_z/L_x, L_z/L_y\} = \{10, 6\}$ *and therefore it is very extended along the z direction in order to reach high-latitude regions. Credits: [94].*

mixed and difficult to be identified by observational studies. Albeit different, the situation can be compared to mixtures of non-miscible liquids: starting from an equilibrium state, if the fluids are partially mixed up, the separation surfaces are no longer parallel, liquids mix in unpredictable way and a probe (*i.e.* our spacecraft) crossing the mixture would not recognise the global structure.

4.3 The standard theory of discontinuities

If one considers the magnetopause boundary locally as a thin layer separating two quasi-homogeneous media, one would expect that this layer respects the standard theory of discontinuities. Here "thin" is used to stress the idea that the magnetopause represents the place where plasma quantities change in a small spatial interval with respect to the magnetosphere dimensions. Generally speaking, in isotropic media without heat flux on both sides, the number of conservation laws is equal to the number of variables characterising the downstream medium, so that this medium can be fully determined as a function of the upstream one, independently of the internal physics of the layer [96]. An integration of the fluid equations across the magnetopause returns the generalised Rankine-Hugoniot equations system[1] which are conservation laws for ϕ_m,ϕ_B,ϕ_i, ϕ_e

[1] $\mathbf{E}_t = 0$ in the null electric field frame known as the de Hoffmann-Teller frame [5, 53]

and ϕ_E defined as follow:

$$\begin{cases} \phi_m \equiv \rho u_n \\ \phi_i \equiv \rho u_n \mathbf{u} + \left(p + \frac{B^2}{2\mu_0}\right)\mathbf{n} - \frac{B_n \mathbf{B}}{\mu_0} \\ \phi_e \equiv \frac{1}{2}\rho u^2 u_n + \frac{5}{2} p u_n - \frac{1}{\mu_0}\left[B_n\left(\mathbf{B}\cdot\mathbf{u}\right) - B^2 u_n\right] \\ \phi_B \equiv B_n \\ \phi_E \equiv \mathbf{E}_t \end{cases} \tag{4.4}$$

where the indexes n and t indicate the normal and tangential directions to the magnetopause boundary. This system of equations links the upstream to the downstream quantities (bulk velocities $\mathbf{u}$, magnetic fields $\mathbf{B}$, densities ρ and pressures p) with respect to the discontinuity.

From this equations, indicating for instance with "1" the downstream quantities and with "2" the upstream quantities, it can be observed that:

1. if $B_n \neq 0$ then

   (a) $u_n^2 \neq B_n^2/\mu_0\rho$
   In this case, $\mathbf{B}_{t2} \propto \mathbf{B}_{t1}$, meaning that there is no rotation in the tangential plane of the magnetic field; furthermore their moduli as well as $u_{n,i}$ and ρ_i do change; it is a co-planar discontinuity, also known as a shock. In this case the discontinuity is called "compressional". And example of the behaviour of the tangential component of the magnetic field is shown in Figure (4.4.b).

   (b) $u_n^2 = B_n^2/\mu_0\rho$
   In this case, the solution is nothing but an Alfvén wave in which P, B^2 and ρ are conserved separately; it means that through this discontinuity the magnetic field vector is free to rotate tangentially without changing its modulus. In this case the discontinuity is called "rotational". And example of the behaviour of the tangential component of the magnetic field is shown in Figure (4.4.a) where the red and green colours aim at indicate respectively the upstream and the downstream tangential components of the magnetic field.

   (c) $u_{n2} = u_{n1} = 0$. This solution does exist from the theoretical point of view, and it is called "contact discontinuity". The only jumps are then those of density and temperature, keeping the product $P = nT$ constant. But this solution is not expected to be really observed in a plasma because it would be rapidly eroded by any diffusion mechanism.

2. if $B_n = 0$ then: In this case, the above general solution still exists (perpendicular fast shock), and the corresponding normal flow velocity is not null. But the two other solutions (slow shock and rotational discontinuity) are then degenerate and correspond to $u_{n1} = u_{n2} = 0$, meaning that there is no plasma flow across the boundary. This solution is called "tangential discontinuity".

At the magnetopause, the value of B_n is generally found to be non null but very small. This close vicinity of the tangential discontinuity is actually poorly described by the standard theory that we just described. Therefore, if B_n and u_n do not tend toward zero, the results above can easily be perturbed by any departure from the hypotheses that underlie this theory, in particular the 1D and stationary assumptions. Actually, experimentally it is very difficult to measure an exactly null value due to the experimental errors. Therefore, it is difficult to identify a tangential discontinuity with no doubt. An exception has been found in [103], where two distinct substructures (moving with respect to each other) have been found within the magnetopause : a rotational discontinuity and a slow shock.

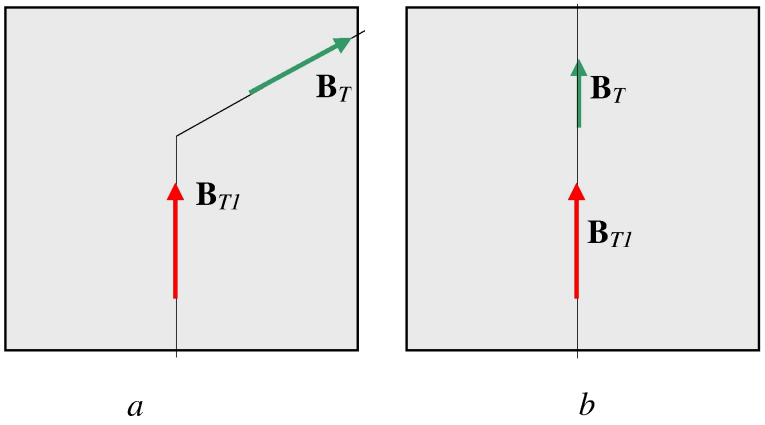

Figure 4.4: *Upstream (red) and downstream (green) tangential component of the magnetic field in case of rotational (panel a) and compressional (panel b) discontinuity cases. Gray squares represent the magnetopause. In case of rotational discontinuity, the tangential component of the magnetic field is free to rotate but its magnitude is fixed. In case of compressional discontinuity, the tangential component of the magnetic field changes its magnitude but its direction is fixed.*

Figure (4.5) shows for instance data recorded during a MMS magnetopause crossing happened on 16/10/2015, around 13:05:30+60s UT (hereafter called *Cr2*). The figure shows the normal (panel 4.5.a) and tangential components (panel 4.5.b) of magnetic field and the normal flow across the magnetopause (panel 4.5.c), respectively measured and computed thanks to methods introduced in section (8). "Normal" and "tangential" refers to the average magnetopause structure, assumed globally planar. The colour code used in panels 4.5.a and 4.5.b is an indication of $B_n/\max(|B_n|)$ (dark blue = 0, red = 1). Following the theoretical prediction of the generalised Rankine-Hugoniot equations (Equations (4.4)), the hodogram[2] would show either clear rotational (changes in the direction of $\overline{B}_t$ with constant $|\overline{B}_t|$) or clear compressional (changes in the modulus of $\overline{B}_t$ but no changes in its direction) features, everywhere $B_n \neq 0$. Panels (a) and (b) do not show such features. Furthermore, according to Equations (4.4) where $B_n \sim 0$ the normal flow should be zero if the discontinuity was a tangential discontinuity. Panels (a) and (c) does not agree either with this prediction. Note that the computations of the frame directions and of X_n have been validated in sections (7) and (8), respectively, and in Paper 1.

4.4 Determining the position of the spacecraft inside the magnetopause structure

The position of a spacecraft probing the magnetopause is known with respect to the Earth but unknown with respect to the magnetopause itself. Therefore the scientists observing the magnetopause with *in situ* measurements have to guess such a position from the data themselves. A sudden change in density and direction of the magnetic field is the indication of a magnetopause crossing. Anyway, this does not offer any guess about the relative motion of the spacecraft with respect to the magnetopause structure (note that usually the magnetopause moves much faster than the spacecraft itself). This information is actually very important for the analysis of the phenomena happening along the magnetopause: their dimensions are basic information for qualitative and quantitative characterisation of the plasma structures observed. This information is also important because it is needed to initialise the numerical simulations devoted to the

[2]Hodograms are 2D curves resulting from the projection in the plane tangential to the magnetopause of a 3D curve. The latter is obtained by the linking of the arrowheads of the series of magnetic field vectors probed, which are all applied to the origin of the axes. An example of such a curve is given in panel (*b*) of Figure (4.5).

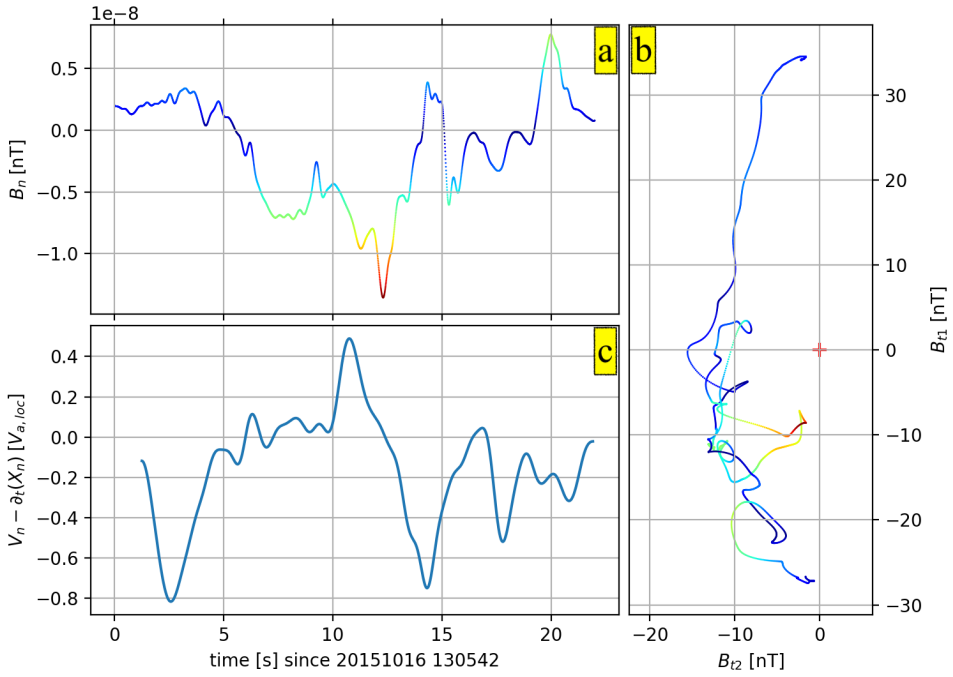

Figure 4.5: *Normal (panel (a)) and tangential (panel (b)) components of the magnetic field and normal ion flow across the magnetopause (panel (c). Normal and tangential refer to the magnetopause surface; such directions have been computed thanks to methods explained in sec. (7). The colour code used in panels (a) and (b) is proportional to $|B_n|/max(|B_n|)$ (dark blue = 0, red = 1). Panel (c) shows the computed normal ion flow crossing the magnetopause as measured in the magnetopause system of reference $V_{ni} - \partial_t X_n$ where X_n is the spacecraft position with respect to the magnetopause along its normal and computed as explained in sec. (8).*

analysis of their temporal and spatial evolution. Figure (4.6) shows for instance one of the first analyses of *Cr2* [112]. The crossing (that will be analysed in details in this thesis) has been deeply studied by the scientific community [112, 118, 115, 131] and [Paper 1, Paper 2], since MMS recorded a magnetic reconnection event. In the state-of-the-art studies, the spacecraft position is guessed *a posteriori* comparing the spacecraft data (expressed as a function of time) to the output of a numerical simulation. Such "known-how", even regarding to the attempts of automating [124], is a complicated procedure, and the results are uncertain as long as one is not able to initialise the simulation used for comparison with the data themselves. Many techniques have been forged to compute the spacecraft position with respect to the magnetopause structure from the data, but they generally assume the magnetopause structure to be stationary[3], mono-dimensional[4] and planar[5]. Actually, such assumptions are generally not justified [67, 77, 121, 131]. Therefore these techniques can be applied only on a restricted ensemble of case studies or they can produce biased results. This thesis aims at building new methods to overcome such limitations (*i.e.* relaxing some of these restricting assumptions) both in computing a spatial metric across the magnetopause where to locate data (sec. 8) and in computing the spacecraft path, directly from data (sec. 10).

[3] the time scale required for the magnetopause structure to deform is longer than the spacecraft crossing time duration

[4] the variations of physical quantities occur only along the direction normal to the magnetopause planar structure

[5] the orientation of the magnetopause surface is the same along its entire thickness

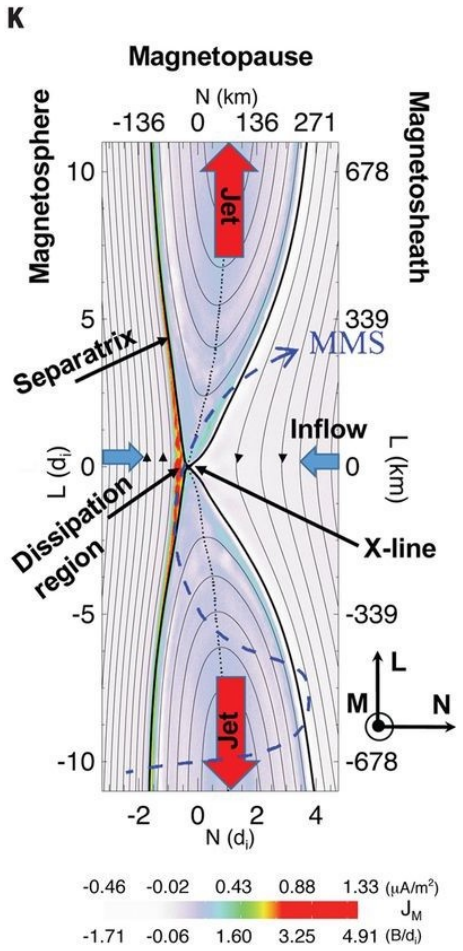

Figure 4.6: *Hand-drawn trajectory (blue curved and dashed arrow) guessed to be run by MMS during the Cr2 event. The trajectory has been drawn confronting temporal data to numerical simulation outputs. The colour code used in background indicates the current density; it shows a clear "X point" structure which is typical of magnetic reconnection events. Other details are shown such as the direction of the inflow plasma (blue horizontal arrows), the outgoing jets (red vertical arrows), the X line separatrix (black curved lines departing from the dissipation region at the centre of the figure), the magnetosheath region (at the right) and the magnetospheric region (at the left). Credits: [112].*

4.5 The observation of a multi-population plasma

Regarding the solar wind - Magnetosphere interaction, the thesis aims at proposing also a new analytical model for the modelling of the magnetopause structure. Since the populations coming from the two different sides of the magnetopause differ in density and temperature, modelling the magnetopause requires at least the use of a multi-population model. Figure (4.7) shows an example of the mixing region between magnetosphere and magnetosheath. Data have been recorded by MMS during the magnetopause crossing *Cr2*. In panel (4.7.a) the ion spectrogram has been plotted as a function of a spatial coordinate X_n (where the index "n" means "normal to the magnetopause surface"). The details explaining how the spatial coordinate is computed will be given in sec. 8). Roughly speaking, it derives from the temporal integration of the magnetopause magnetic structure velocity as seen by the spacecraft. The unit for X_n is the ion inertial length d_i of the magnetosheath which is equal to nearly $70km$. For the sake of completeness, below each particular $X_n(t^*)$ visualised along the x axis of panel (4.7.a), the associated time t^* is reported.

In the spectrogram, black points have been over-plotted to indicate its maxima. This allows to individuate more easily where the magnetosheath and the magnetospheric plasmas interact, as indicated by discontinuities in the curve joining the maxima. The mixing region, emphasised by the blue rectangle superposed to panel (4.7.a), stands at $X_n \sim 3d_i$. Panels (4.7.b), (4.7.d) and (4.7.c) show the ions Distribution Functions (hereafter "iDF"s) recorded by MMS respectively in the magnetosphere, in the magnetosheath and in the mixing region. The 2D iDFs[6] are plotted in the plane tangential to the magnetopause. In panel (4.7.c) (mixing region), one can observe that the iDF contains two peaks, which are emphasised by the over-plotted circles (blue and red dashed lines). These circles have a diameter equal to, respectively, the magnetosheath and magnetospheric thermal velocities (respectively equal to $\sim 300km/s$ and $\sim 800km/s$). The same circles are shown also in the magnetosheath and magnetospheric iDFs (panels (4.7.d) and (4.7.b)) where they emphasise the corresponding single peaks. Note that the iDF shown in panel (4.7.b) has actually been recorded a little earlier (~ 2 hours earlier), during a clear observation of the magnetosphere, in order to be sure not to observe magnetosheath particles when the spacecraft is too close to the magnetopause. This clearly shows that panel (4.7.c) and the region contained in the blue rectangle in panel (4.7.a) does contain a mixture of the magnetosheath and magnetospheric populations at the same time. Since the two peaks in panel (4.7.c) are close to each other and since the distributions of the two populations are partly superposed, it would be hazardous to find the hot/cold contributions, for a multi-population model to be built, by a direct fit of this region. Several multi-population models have been developed in the past, trying to model the magnetosheath/ magnetosphere interface [22, 93, 108, 121], for planetary studies [71, 75], solar chromospheric studies [110], or basic plasma physics studies [90]. Concerning the first ones, which are kinetic models, they are very complicated so that the authors are lead to make simplistic mathematical assumptions for choosing the iDFs (and so hopeless to get close to magnetopause data for the physical parameter profiles). They can involve many free parameters even in the simplest limit of a plane and tangential layer (*i.e.* without a normal magnetic field: $B_n = 0$). Some models moreover ignore the questions of accessibility and they can therefore not distinguish between particles of magnetospheric or magnetosheath origin. An alternative way how this task can be done will be therefore introduced in this thesis (sec. III).

[6] They result from an integration along the out-of-plane (normal) component of the velocity. Each plot is the average of 5 single iDFs recorded within a $\sim 0.75s$ long interval (equivalent to $0.5d_i$). The radius of the distribution functions is 10^3 km/s and the purple full circle drawn at its centre determines the bottom limits in energy of the FPI instrument (10 eV $\sim$ 53 km/s for ions). The direction of the local magnetic field is indicated by a white arrow.

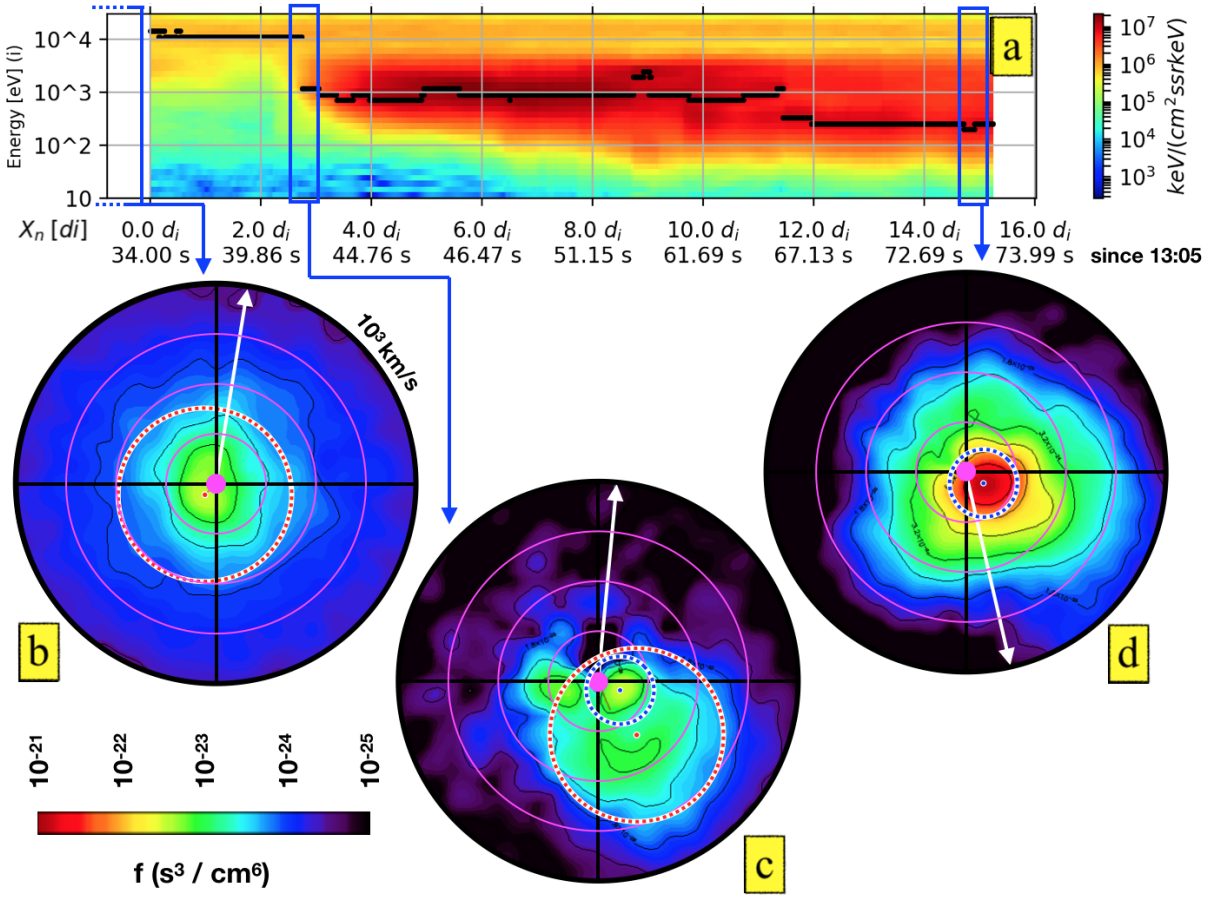

Figure 4.7: *MMS data recorded by the particle instruments [117] for the Cr2 event (October 16th 2015, 13:05:34 UT + 40s). Panel (a): ion spectrograms (roughly speaking it is the number of particles detected as a function of energy and time). Black points have been over-plotted to indicate its maxima. The first abscissa is the linear spatial coordinate normal to the magnetopause X_n expressed in units of $d_i(\simeq 70km)$ (see sec. (8) for details) and the second one is time (non linear scale). Panels (b), (d) and (c) are the ion distribution functions (iDFs) recorded respectively in the magnetosphere, in the magnetosheath and in the overlapping region. These iDFs are projected on the tangential plane by integration along the normal component of the velocity. Panels (b) and (d) show two dashed circles whose radii are equal to the magnetosheath and magnetospheric thermal velocities. The same circles have been drawn also in panel (c) in order to show the coexistence of the magnetospheric and the magnetosheath ion populations at the same place.*

Chapter

5 Thesis objectives: a more realistic model for the Magnetopause

The previous chapters aimed at demonstrating that the state of the art in studying the Earth's magnetopause is far from considering all the aspects actually happening on the real magnetopause. The simplifications (which are anyway previewed by the "successive improvements method" adopted by the Science) can no more be coherent with the high-quality data provided by the most recent spacecraft missions. This gap needs to be filled. Advances in this domain should allow breakthroughs for various domains of the magnetopause physics.
From the theoretical point of view, the models devoted to study the interaction between different plasmas are either oversimplified or exaggerated in the number of parameters taken into account so that data need to be somehow ignored. The thesis will introduce therefore a new multi-fluid analytical approach where two different ion populations are taken into account. The two ion populations aim at modelling the magnetosheath and the magnetospheric populations. The two fluids will be therefore characterised by different densities and temperatures, according to experimental data. Hereafter the multi-fluid approach will be called "3fluid" since a neutralising electron population (the same on both sides of the magnetopause for the moment) is taken into account too.
From the observational point of view, data are difficult to interpret since it is difficult to know where data have been probed with respect to the plasma structure under examination. Plasma structure dimensions are therefore hardly known. From the numerical point of view, this implies that simulations risk to be erroneously initialised since the initialisation procedures need for spatial profiles of quantities of interest to be known. The data analysis techniques required to compute the magnetopause local structure features (orientation and dimensions) will be introduced in section (7) and (8). The spacecraft paths (which is the direct byproduct of these techniques) will be discussed in section (10). The 3fluids model required to study the solar wind - magnetosphere interaction will be introduced in section (12) and tests of its numerical implementation will be shown in section (13). Finally section (IV) will show results of numerical simulations initialised with spatial profiles accurately reproducing the observed magnetopause structure.

Part II

Characterisation of mixing regions across the magnetopause

“ *... e dunque, affinché la costruzione sia solida, è necessario poter contare su buoni mattoni.*

.. so, in order the framework to be solid, good components are needed.

”

Giorgio Manzi, "L'evoluzione umana"

Chapter

6 From a global to a local analysis of the magnetopause

Chapter content

The previous section highlighted how the magnetopause is far from being an ideal planar and mono-dimensional current sheet. Actually, its non-stationarity brings other kinds of complications. The magnetopause current sheet is a boundary current subject to the perturbation of the two plasma systems interacting at its sides: the solar wind and the magnetosphere. Since the solar wind is a high dynamical system, the magnetopause passively inherits this temporal characteristic. Furthermore, the large inhomogeneities occurring across the magnetopause cause high dynamical MHD and kinetic plasma instabilities to occur. Since these phenomena can have time scales smaller than the magnetopause crossing time, it may be difficult to know where and how the spacecraft cross the magnetopause. Such incertitude translates into large uncertainties in the analyses of the length scales of the plasma structures crossed and in reproducing them by means of numerical simulations.

6.1 An overview on the history of spacecraft missions looking at the Earth's magnetopause

The very beginning of the solar wind - magnetosphere *in situ* investigations begun with the Pioneer 1 spacecraft, launched at the end of 1958. The analysis of the data acquired by the magnetometer on-board the Pioneer 1 spacecraft ([12, 14]), provided the first evidence of the "anomalous" behaviour of the magnetic field at $\sim 13R_E$ sun-ward from the Earth. The decrease in the magnitude of the magnetic field was interpreted in [14] as resulting from the sun-ward penetration of the magnetopause by the spacecraft. The concept of "magnetopause" as a current sheet sustaining the interaction between -and separating[1]- different plasma systems was known at that time since the various theoretical studies [1, 2, 4, 6, 7, 8] and the indirect observations [9] made in the preceding 20 years. Evidences of the presence of a complex current structure even in the night-ward side of the Earth come later with the NASA's Explorer missions 6 [13] and 10 [19, 16]. Finally, unambiguous evidences were shown by [17] using Explorer 12. All these

[1] A concept beautifully summarised by [91] using the image of a "*cellular structure*" for space (see the introductory quotation to part (I))

spacecraft missions where single spacecraft. This results in the impossibility to discriminate the temporal from the spatial dependencies of the measured quantities. For instance, if a change in orientation of the magnetic field is observed and if no other supplemental information is provided, it is impossible to say whether it is due to the penetration of the spacecraft in a different plasma system or to a change in the plasma state itself (or even both at once). More complete information has been provided at the end of the seventies from the use of multiple satellites at once. Using data from the two spacecraft ISEE 1 and 2 ([24]), whose inter-spacecraft distance was less than 1000 km, [25] succeeded in reducing the spatio-temporal ambiguity and they obtained a first estimation of the thickness and the kinematics of the magnetopause. These studies required strong assumptions about the magnetopause itself, mainly that the magnetopause current sheet structure is planar and stationary and that it is crossed with a constant velocity. Soon after, the multi-point measurements became the principal paradigm that steered the design of the next spacecraft missions devoted to study the solar wind - magnetosphere interaction.

ISEE has given the possibility, under some assumptions, to determine the spatial gradients in one single direction, defined by the two spacecraft separation. To be able to explore the three dimensions of space, the ESA Cluster mission [44] was the first spacecraft mission composed of 4 satellites orbiting around the Earth in a tetrahedron formation $\sim$ 1000 km apart. The multi-point measurements of Cluster mission, joint to the new data analysis techniques explicitly designed to exploit their information content [48], opened the possibility to determine the gradients of the plasma and field quantities under less strong hypotheses than that assumed for previous studies. The inter-spacecraft distance of the Cluster mission, which was of the order of the ion scales, was well suited for investigating the large scale characteristics of the magnetopause layer, as its thickness. Nevertheless, it turned out to be too large to investigate some aspects concerning the details of the magnetopause substructures. Such substructures, which can be at the electron scales ($\sim$ 10 km), can be due to some local plasma instabilities, and they are known to have an important role in particular when magnetic reconnection occurs. The need for multi-point measurements acquired only $\sim$ 10 km apart was finally satisfied by the Magnetospheric MultiScale mission (MMS) [113] (whose features have already been described in section (2.3)). Thanks also to the MMS on-board instruments that have unprecedentedly seen probing rates, the magnetopause structures can be resolved, both spatially and temporally. Nevertheless there is a last problem affecting the magnetopause studies. This problem is to determine the localisation of the spacecraft with respect to the magnetopause structure crossed (whose shape is *a priori* unknown), and their path during the crossing. In order to fully exploit the MMS data, this thesis aims at solving this difficulty, proposing new data analysis techniques that reduce the strength of yet necessary assumptions about the magnetopause structure (mainly its stationarity, see sections (8.2.3 and 8.2.4)).

6.2 A very global view of the magnetopause behaviour

The reason why data can not be easily located with respect to the magnetopause is that there is no link between the spacecraft and the magnetopause positions. While the spacecraft position is very precisely known since it is provided by specialised global positioning systems (*e.g.* the *Navigator/GPS* system adopted by NASA for MMS [85]) though stressed to their limits (MMS is indeed the farthest GPS-operated spacecraft cluster [126]), no equally precise way can be used to know where the magnetopause is in the same frame adopted to represent the spacecraft position. As a first approximation in determining the spacecraft position with respect to the magnetopause, one can adopt analytic models of the magnetopause shape. These models help to understand where the magnetopause is expected to be and how it is expected to behave.

Figure (6.1) shows for example the radial distance (orange curve) in the GSE frame at which the magnetopause is expected to be as a function of time during a 8 hour long data period observed by MMS on 16/10/15. The radial distance has been computed by means of the Shue

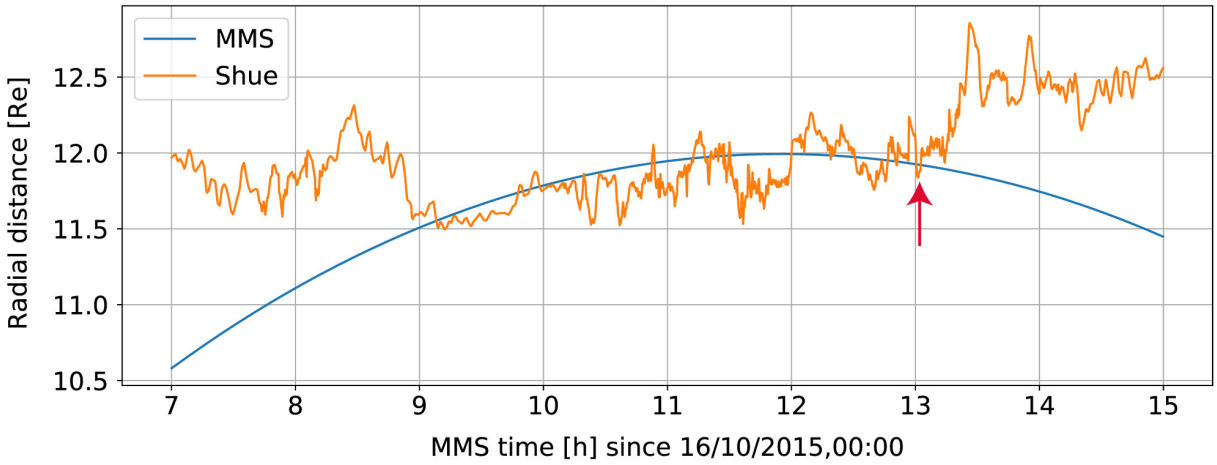

Figure 6.1: *Comparison between the magnetopause (orange curve) and the MMS (blue curve) radial distances in GSE within the 16/10/15,* $7.00 - 15.00$ *UT time interval. Data regarding the MMS position are retrieved from the GPS on-board the spacecraft. The magnetopause radial distance is computed by means of the Shue model [57]. The Cr2 crossing time location is highlighted by a red arrow. Credit: after [131]*

model [46] using solar wind data probed at the first Lagrangian point (L1) by the single spacecraft mission ACE [57] as input of the model. In particular, the solar wind pressure and magnetic field measured by ACE are used as a boundary condition for the Shue model with a propagation delay between ACE and MMS calculated using the solar wind velocity measured by ACE too. The comparison of this curve with the radial distance of MMS (blue curve) suggests the occurrence of multiple magnetopause crossings within the $9.00 - 13.00$ UT interval. The Interplanetary Magnetic Field (IMF) being directed southward during the whole interval, the prediction is confirmed comparing the modulus $|\mathbf{B}|$ and the B_z component of the magnetic field as recorded by MMS. In the magnetosphere, we expect to observe $B_z \sim |\mathbf{B}|$ where as in the magnetosheath we expect to observe $B_z \sim -|\mathbf{B}|$. Figure (6.2) confirms the expectations: when MMS is inside the magnetosphere (before 9.00 and after 14.00) the modulus of the magnetic field is mainly due to the B_z components which is positive. On the contrary B_z assume negative values when MMS is in the solar wind (between 9.00 and 14.00).

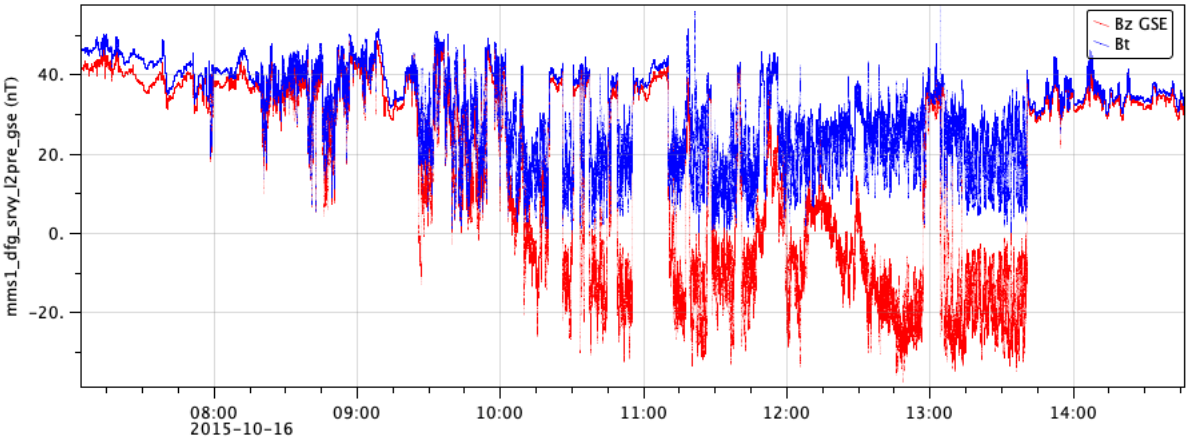

Figure 6.2: *Modulus* $|\mathbf{B}|$ *(blue curve) and* B_z *component in GSE (red curve) of the magnetic field measured by MMS-1 in survey mode (16S/s) on 16/10/15.*

The analytic models, such as the Shue model, grasp the magnetopause large scale kinematics and allow to predict where to expect signatures of magnetopause crossings in the large MMS

database. They represent the first step to correlate spacecraft and magnetopause positions. Unfortunately, comparisons similar to that of Figure (6.1) can predict neither individual crossings nor -therefore- their finest details. Further improvements are needed.

6.3 A step further (but not yet sufficient) toward the local analysis of the magnetopause

After the above very global view, the first step further consists in computing the magnetopause motion with respect to the probing spacecraft and the different magnetopause features, using the data acquired by the spacecraft itself. This task is similar to that of a blind pilot trying to know his position in the air having a measure of the flow passing across his aircraft as unique feedback coming from outside. Since the multi-spacecraft advent is a relatively recent "hardware" upgrade in the space plasma research, the majority of the data analysis techniques devoted to solve this task have been designed to take advantage of single spacecraft missions. In this case, when the data analysis needs computations that involve measurements other than punctual (in particular spatial gradients), strong assumptions have to be made about the plasma structure probed. In addition to the mono-dimensionality and planarity assumptions (already examined in section (4)), hypotheses about the magnetopause kinematics need to be assumed, in order that the data recorded by each spacecraft can be labelled by a specific position inside the magnetopause structure. The magnetopause has to be assumed to move with a given kinematics, generally a simple linear motion. Such assumption is far from being observed, as shown by the radial position of the magnetopause as modelled by the Shue model in Figure (6.1).

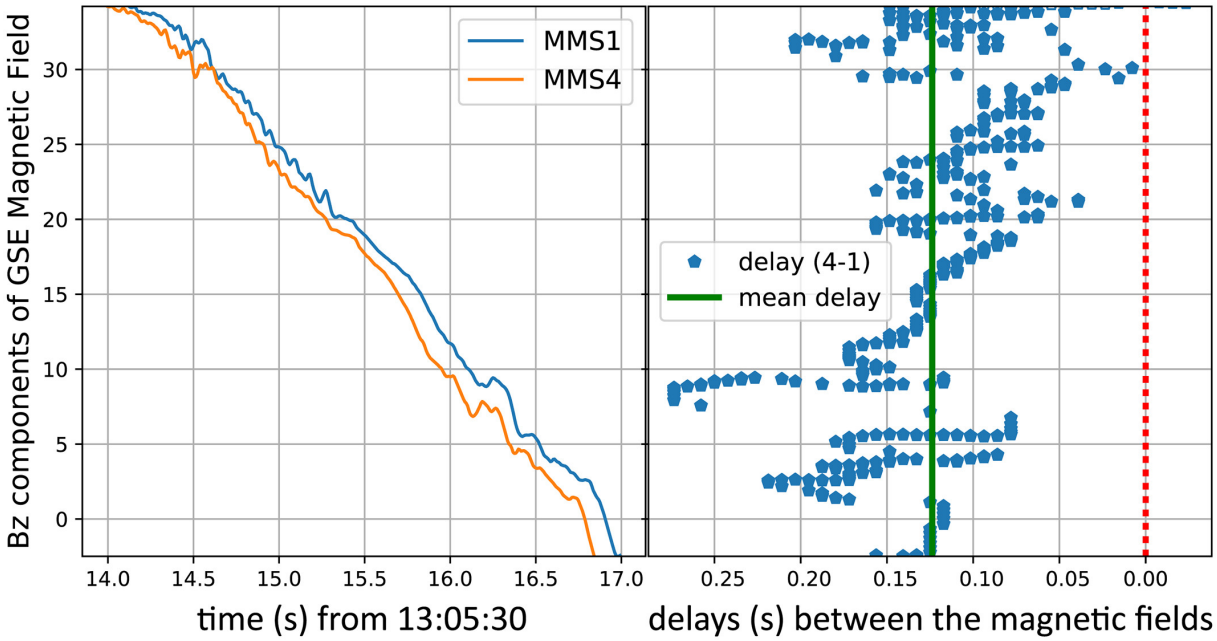

Figure 6.3: *Evaluation (by means of a simple difference) of the time delays (right panel) occurring between the measure of the same magnetic field (left panel) recorded by two different spacecraft belonging to the MMS spacecraft cluster and crossing the magnetopause. In this case the magnetic field component taken in consideration is the one showing the largest variation across the magnetopause. The interval analysed represents a small time windows recorded during the Cr2 crossing. It shows a mono-dimensional spatial dependence directed toward the normal to the magnetopause. Credit: after [131]*

The left panel of Figure (6.3) shows the most varying magnetic field component recorded by two of the four MMS spacecraft. The right panel shows the time delay between same-B_z-value records computed as a difference between time instants. The spatial dependence of the magne-

topause parameters, during the time interval examined, has been shown to be almost only 1D along the normal to the magnetopause. In these conditions, this delay should be constant for the different spacecraft if one assumes a magnetopause moving with a constant velocity, even if the spacecraft have different tangential positions. Anyway, the panel on the right clearly shows that the delay between same-B_z-value records is a function of time, with a secular variation superposed to a large fluctuating part. This result suggests that the magnetopause is slowing down, which will be confirmed by an independent analysis in section (8). It therefore invalidates the simplifying hypotheses often assumed about the magnetopause kinematics. It invalidates also the use of the multi-spacecraft techniques that base their analyses on the assumptions that the magnetopause is moving at constant velocity, such as the Constant Velocity Analysis (CVA) [82], which will be introduced in sections (7.1.2).

There are few studies considering less simplistic motions, comparable for instance to the motion shown in Figure (4.6) by [112]. These studies did not adopt hitherto an automatic way to compute the spacecraft motion in the magnetopause frame. The target is generally reached by: 1) studying data as a function of time, 2) choosing between them some with peculiar features, 3) individuating their probable location onto an idealised sketch of the phenomenon that is supposed to be observed and 4) joining these points (now localised in space) with splines. Figure (6.4) by [125] exemplifies this procedure. In this study some key points have been individuated on data and then placed onto the structure of an ideal X point (green circles). A green dashed line (which is assumed to represent the spacecraft trajectory) is so drawn to join these points. Such procedure is obviously subject to biases, mainly due to human interpretation.

Finally, since the inner part of the current sheet is generally not planar, one has to take care to distinguish between the global and local features. Using single spacecraft missions, one needs to span the entire magnetopause thickness in order to detect the spatial dependency of the layer. The quantities derived from these analyses are representative of the global magnetopause, but they must not be thought to be representative for the inner magnetopause substructures. As shown by the multi-spacecraft measurements, certain features, such as the gradients of the probed quantities or the orientation of the magnetopause current layer, are variable along the whole crossing.

Figure (6.5) demonstrates how the assumption of a strictly 1D layer can be far from being verified. The figure shows a 2D simulation [121] of a reconnection event pinching the magnetopause current sheet. The green straight line shows the trajectory along which a virtual satellite is crossing the magnetopause. Where the trajectory intersects the magnetopause, a multi-spacecraft technique (the Minimum Directional Derivative [70] which will be discussed after in this thesis) is applied in order to compute the normal to the magnetopause point-by-point. The normals, which clearly follow the magnetopause local curvature, keep distance from the vertical direction (which is the initial magnetopause normal), especially close to the reconnection point located at $x \sim 155$ (arbitrarily units). Since similar (and even larger) modifications of the magnetopause structure occur during all the phenomena interesting the magnetopause, the figure demonstrate how it could be erroneous to assume in this case a single normal to represent the magnetopause orientation.

6.4 The local analysis of the magnetopause structure

In the previous sections the motivations why the magnetopause needs to be analysed with more precision have been listed. It becomes clear that in order to analyse such a non stationary, non planar and accelerating plasma structure, a probe having dimensions smaller than the magnetopause finest sub-structures and adopting a relatively high - probing rate instruments able to follow the magnetopause movements is needed. The MMS spacecraft is the most recent multi-satellite mission probing the magnetopause. It is designed with an inter-spacecraft distance equal

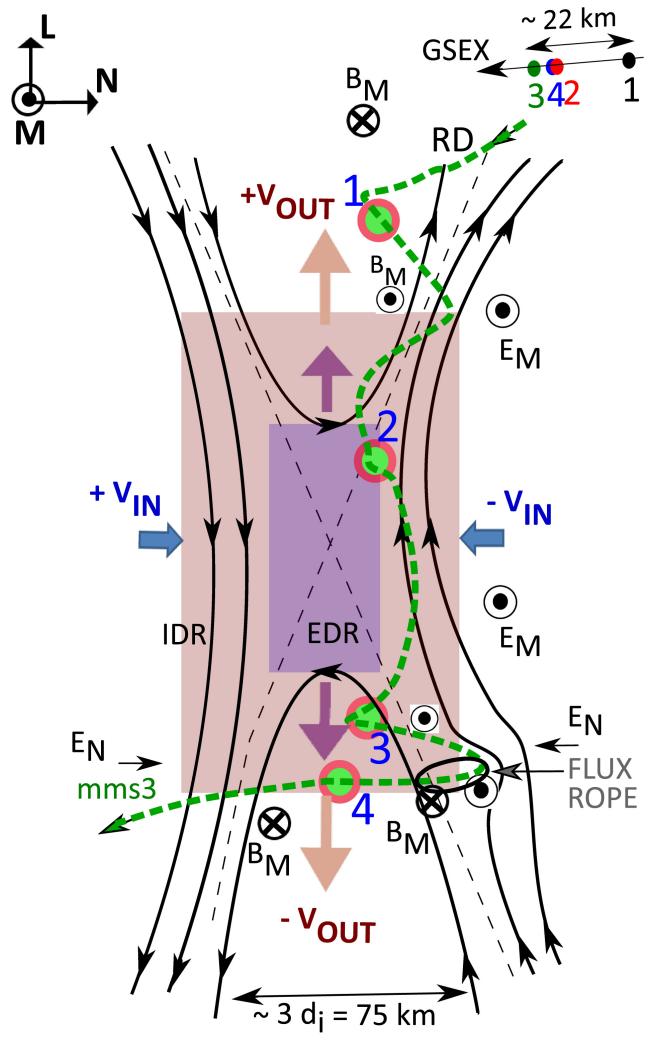

Figure 6.4: *Reconstruction of the spacecraft trajectory (green dashed line) for the MMS crossing happened on 30/11/2015, between 00:23:50 and 00:24:00 and studied by [125]. The spacecraft trajectory is superposed to the idealised structure of a reconnection X point. The location of peculiar points in temporal data are located with green spots onto the sketch and numbered in order of time. Other details are not significant here. Credit: after [125]*

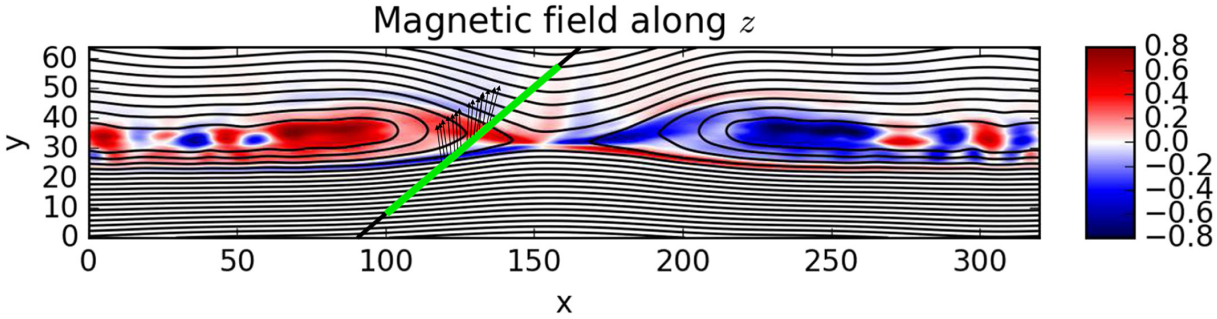

Figure 6.5: *Simulation snapshot of the magnetic field (the out of plane component in normalised units) behaviour during a magnetic reconnection event [121]. The green straight line outlines the trajectory of a virtual spacecraft passing close the reconnection point localised at the centre of the box. The black arrow spread along the spacecraft trajectory are computed by a multi-spacecraft method [70] allowing for local analysis of the magnetopause. Similar results will be found by a new single-spacecraft method [131] presented in section (7). Credit: after [131]*

to one hundredth of the inter-spacecraft distance kept by less recent multi-spacecraft missions (Cluster). MMS is therefore able to look at the interior of the magnetopause layer.

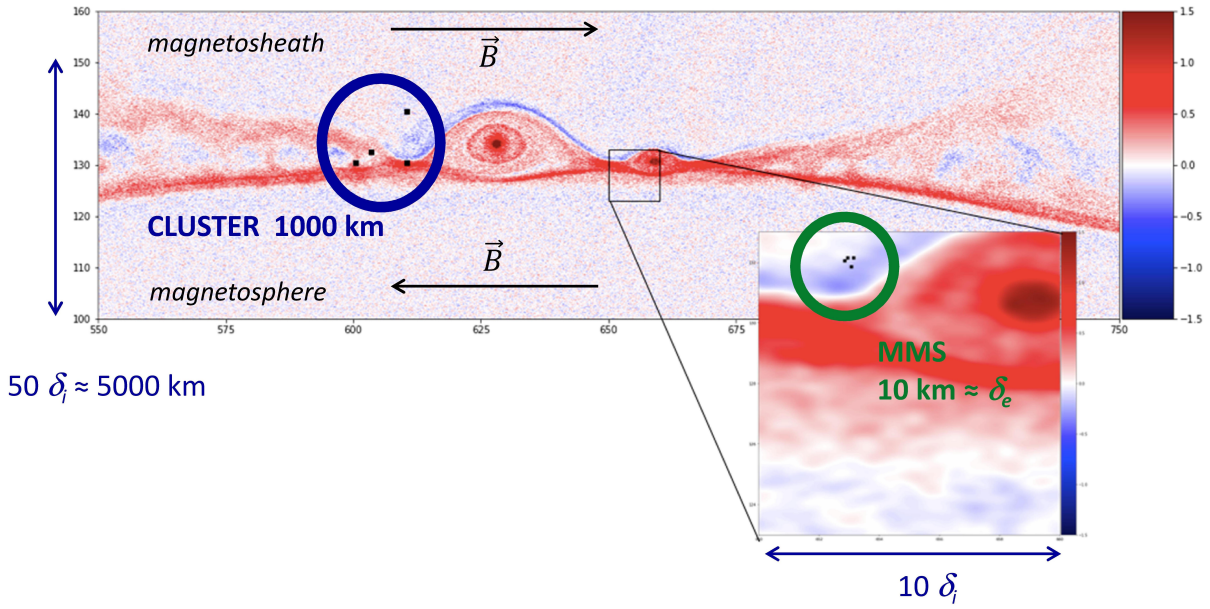

Figure 6.6: *Simulation snapshot of the magnetopause showing the aspect ratios between the magnetopause (outlined by the colour code indicating the current component perpendicular to the simulation box) and the inter-spacecraft distance for the Cluster and the MMS missions. The scales are in ion inertial lengths δ_i. A magnetic island is observed due to reconnection. Credit: after [121]*

Figure (6.6) shows for instance the superposition of the Cluster and the MMS spacecraft tetrahedron scales onto the cross section of the magnetopause retrieved from a numerical simulation introduced by [121]. The figure shows the difference in the inter-spacecraft distance for the two missions and how local the analysis of the magnetopause can be done using MMS data. The studies presented in this thesis take advantage from this feature and from the high probing rate of the MMS instruments.

In the next sub-sections (7, 8) new local single and multi-spacecraft analysis tools will be introduced in order to characterise the magnetopause, assuming less strong hypotheses about its structure and kinematics and taking care of the local variations of quantities of interests. Hereafter the term "*local*" will mean "at length scales less than the magnetopause layer thickness". In particular, regarding the multi-spacecraft methods, the length scales at which local variations can be discriminated are equal to the MMS inter-spacecraft distance (MMS has an inter-spacecraft distance of the order of the local electron inertial length which is $\sim$ 10 km at the magnetopause nose and $\sim$ 150 km in the magnetopause tail).

Section (7) will explain a new single spacecraft method called *Local Normal Analysis* [131] able to compute a normal for every data point collected by a single spacecraft. Potentially it broadens the possibility to analyse those events probed only by single spacecraft missions and to cross-check results between measurements performed by the single spacecraft belonging to the same multi-spacecraft cluster mission. Section (8) is devoted to introduce two new multi-spacecraft methods called *Single Variate Fit* and *Multi Variate Fit* methods [135] able to compute the magnetopause velocity point-by-point in the spacecraft frame. These methods do not assume the magnetopause structure to be time independent as other similar techniques do [72] and therefore allow to apply the computation even in non stationary conditions. These routines will be tested under artificial (and therefore known) conditions. The amelioration of an existing method (the *Spatio-Temporal Difference* method developed by [72]) will be proposed too in order to check the new methods

on a known case study (the *Cr2* event). All these routines will then be used in section (10) to characterise the *Cr2* crossing. This characterisation will be used for a realistic initialisation (section (IV)) of the numerical simulation model presented in section (III).

Chapter

7 A POINT-BY-POINT DETERMINATION OF THE MAGNETOPAUSE ORIENTATION

Chapter content

The first information needed to characterise the magnetopause current sheet is the orientation of its surface. To a first approximation it can be assumed to be planar. Nevertheless, since the magnetopause is affected by the many various phenomena presented in the previous sections, the possible departures from this assumption need to be investigated. The smaller the "probe" (no matter here whether one single spacecraft or a cluster of satellites), the more local departures from the planarity can be appreciated, even across plasma structures smaller than the magnetopause thickness. Yet, the state of the art methods (section (7.2)) provide partial information about the magnetopause orientation (sec. (7.4)). In this chapter a new single spacecraft method called "*Local Normal Analysis*" (LNA) [131] is introduced (sec. (7.3)) which occupies a niche where no other methods exist. An introduction on the most useful single and multi-spacecraft techniques to compute the magnetopause normal is written in the next section (7.1).

7.1 A survey on methods used to compute the magnetopause surface orientation

As one might expect reading about the history of space mission (section (6.1)), data analysis techniques passed through the same innovation steps as spacecraft missions did in order to exploit at best information provided by spacecraft. Mission after mission, data increased not only their quality (probing rates, accuracy, etc...) but their simultaneous observation capabilities too (thanks to the multi-spacecraft missions Cluster and MMS). Nowadays the data analysis techniques designed to compute the magnetopause orientation can be divided into four main domains, according to

1. their needs of data acquired by one spacecraft only or data acquired simultaneously at more than one point (4 at the present days) and

2. the length scales (compared to the magnetopause thickness) over which their results (the normal to the magnetopause in this case) characterise the observations.

Regarding the latter point it must be remembered that here, as well as in the rest of this thesis, the keywords "*global*" and "*local*" are attributes of magnetopause characteristics indicating the extension (compared to the magnetopause thickness) of the interval over which these features are valid. In particular a "*global*" magnetopause feature characterises the entire magnetopause thickness whereas a "*local*" feature characterises only a small interval of the magnetopause thickness. To make the reading easier in the following text, the global normal is going to be noted with a capital N, whereas the local normal will be noted with a small n. As will be evident in all the following sections, thanks to the inter-spacecraft distance and the magnetopause crossing velocity of MMS, throughout this thesis the term "*local*" indicates features valid for $\sim 1/100$ of the magnetopause thickness, *i.e.* $\sim 8 - 10km$. This distance is the MMS inter-spacecraft separation, meaning that the magnetopause orientation can be computed with a satisfying spatial resolution. In the following section a review of the principal methods used to compute the normal to the magnetopause is presented. A new single-spacecraft routine able to provide local information exploiting single-spacecraft data will be finally presented.

7.1.1 Single and global spacecraft methods

Independently of the principle at the base of their computations, all these methods (but a new method introduced by [131] and explained in section (7.3)) need to analyse the behaviour of one or more quantity along the spacecraft trajectory across the entire magnetopause crossing. The normal computed by these routines is therefore *global*, *i.e.* it is valid for the entire magnetopause layer.

Minimum Variance Analyses

One of the most used method to obtain a global normal characterising the entire magnetopause layer is the Minimum Variance Analysis technique [21]. This method is applied under the hypothesis that the magnetopause is a 1D stationary layer. The 1D hypothesis assures that the divergence-free Maxwell equation ($\nabla \cdot \mathbf{B} = 0$) for magnetic field reduces to $\partial B_{\mathbf{N}}/\partial \mathbf{N} = 0$ where $\mathbf{N}$ is the global normal to the magnetopause. This means that $B_{\mathbf{N}}$ is homogeneous across the magnetopause. The stationary conditions assures that the magnetopause structure does not change during the spacecraft crossing, *i.e.* that the global normal does not change during the spacecraft crossing. The method finds the vector $\mathbf{N}$ that minimises

$$\sum_i \|(\mathbf{B}_i - < \mathbf{B}_i >) \cdot \mathbf{N}\|^2 \tag{7.1}$$

where $< \mathbf{B} >$ is the mean of the series $\mathbf{B}_i$ acquired during the magnetopause crossing.

The computation, carried on with the Lagrangian multipliers method under the constraint $\|\mathbf{N}\|^2 = 1$, gives the estimation of the normal direction as the eigenvector $\mathbf{x}_n$ corresponding to the smallest eigenvalue λ_n obtained from the diagonalisation of the matrix

$$M_{\mu\nu} = \langle B_\mu B_\nu \rangle - \langle B_\mu \rangle \langle B_\nu \rangle \tag{7.2}$$

where $\mu, \nu = x, y, z$. The determination of the normal is properly done when the two smallest eigenvalues are well separated, as long as the noise (produced for instance by low frequency waves) can be neglected. Otherwise the uncertainty is large, preventing its utilisation, for instance, in a co-planar case as a shock. In this case other methods can be used [56].

Minimum Residue Analyses

The Minimum Residue Analysis technique is based on the homogeneity of some quantity occurring along the normal direction to the magnetopause once particular conditions occur. In particular, the first methods exploiting this observation were the Minimum Faraday-Residue (MFR) Analysis [42, 51] and the Minimum Mass-flux Residue (MMR) analysis [66]. MFR bases its computations on the homogeneity of the tangential (to the magnetopause) components of the electric field in the frame co-moving with a time-independent magnetopause. The MMR bases its computations on mass conservation across the magnetopause (*i.e.* homogeneity of the mass flux). The generalisation of MFR and MMR is the Generic Residue Analysis (GRA) technique provided by [73]. Basically, the GRA assumes that a one-dimensional magnetopause, having time independent structure and orientation ($\partial(...)/\partial t = 0$), moves past a spacecraft with constant speed u_N along the global normal $\mathbf{N}$. Under these assumptions, the generic conservation law (denoting q_{ij} the flux of η_i and adopting the Einstein summation convention)

$$\frac{\partial \eta_i}{\partial t} + \frac{\partial q_{ij}}{\partial x_j} = 0 \tag{7.3}$$

reduces to

$$-u_n \frac{d}{dx'}\eta_i + \frac{d}{dx'}\left(n_j q_{ij}\right) = 0 \tag{7.4}$$

where $x' \equiv x_j n_j - u_n t$ and $t' \equiv t$.
Once integrated, Equation (7.4) transforms into

$$-\eta_i u_n + n_j q_{ij} = C_i \tag{7.5}$$

The target of GRA is to find C_i, u_N and $\mathbf{n}$ that minimise the residue

$$R \equiv \frac{1}{M}\sum_{m=1}^{m=M} |-\eta_i^{(m)} u_N + n_j q_{ij}^{(m)} - C_i|^2 \tag{7.6}$$

where M is the total number of samples acquired during the entire magnetopause crossing. Since $|\mathbf{N}|^2 = 1$, this constraint is included in the minimisation process by means of the Lagrangian multipliers method. Depending on η and $\mathbf{q}$, various conservation laws can be used. Table (7.1) summarises several cases to which the Generic Residue Analysis can be applied. It is worth noticing that the specifications of the GRA method listed in Table (7.1) can be combined [73] to produce a normal potentially less affected by the particular errors biasing a particular quantity (errors due to not actually verified assumptions or instrumental errors).

Table 7.1: *Applications of the Generic Residue Analysis.*

principle	η	$\mathbf{q}$
Absence of magnetic mono-poles	0	$\mathbf{B}$
Conservation of charge	$q_i n$	$\mathbf{q_i n v}$
Conservation of magnetic flux	B_i	$\epsilon_{ijk} E_k$
Conservation of mass	mn	$mn\mathbf{v}$
Conservation of linear momentum	$mn\mathbf{v}$	$mn\mathbf{vv} + \mathbf{P} + \left(\lvert\mathbf{B}\rvert^2 - \mathbf{BB}\right)/\mu_0$
Conservation of total energy	$\left(P + nm\lvert\mathbf{v}\rvert^2 + \lvert\mathbf{B}\rvert^2/\mu_0\right)/2$	$\left(P + nm\lvert\mathbf{v}\rvert^2\right)\mathbf{v}/2 + \mathbf{v}\cdot\mathbf{P} + \mathbf{S}$
Conservation of entropy	$nm\ ln\left(P/\left(nm\right)^{5/3}\right)$	$nm\mathbf{v}\ ln\left(P/\left(nm\right)^{5/3}\right)$

It is worth noticing that GRA is the generalisation of MVA: GRA applied to $\mathbf{B}$ (the case "*Absence of magnetic mono-poles*" in Table (7.1) [73]) corresponds in fact to MVA.

The BV method

The uncertainty on MVA and on any GRA method is often large [73]. This happens especially when the jumps of data from magnetospheric to magnetosheath values (or vice versa) are comparable to the noise. In these case, since the GRA methods base on variances, their results are biased by the noise and not by the slopes in large scale profile. A way to improve the determination of the normal direction is to involve several data sets instead of only one (in MVA the magnetic field only for instance). This is the goal of the BV method, designed at LPP [102]. The name comes from the two physical quantities used: the magnetic field (**B**) and the bulk velocity (**V**). The BV method computes the normal **N** looking for the direction toward which the magnetic field behaves in a specified way (explained below). The reliability of the method has been tested comparing the results with other GRA methods [109]. It has been shown to be more robust than MVA for small intermediate variance, working also when the "intermediate variance" of the magnetopause crossing is not mainly due to the crossing itself but to various waves and turbulence superimposed thanks to a proper smoothing of data. The hypotheses taken into account in the BV method are:

1. the magnetopause is 1D
2. the velocity of the plasma normal to the magnetopause, in the reference frame of the magnetopause, is small compared to the normal velocity of the magnetopause boundary
3. the magnetic field is described by

$$\begin{cases} B_L = B_{0L} cos(\alpha) & \text{(7.7a)} \\ B_N = B_{0N} & \text{(7.7b)} \\ B_M = B_{0M} sin(\alpha) & \text{(7.7c)} \end{cases}$$

where **N** is the normal direction (**M** and **L** complete the global frame) and the angle α varies linearly along the normal coordinate X_n:

$$\alpha = \alpha_1 + (\alpha_2 - \alpha_1) \frac{X_n}{X_{n,max}} \tag{7.8}$$

where $X_{n,max}$ is the magnetopause thickness.

In the case of BV, the coordinate X_n spanning the N direction is computed by

$$y = \int_{crossing} \mathbf{V}_{BF}(t) \cdot \mathbf{N}\, dt \tag{7.9}$$

where $\mathbf{V}_{BF}(t) \cdot \mathbf{N}$ is the normal bulk flow velocity recorded by the spacecraft. The hypothesis (3) limits the applicability of the method to a particular ensemble of crossings where **B** field vectors draw an ellipsis ("C"-shaped like curves) on hodograms as that already observed in panel (*b*) of Figure (4.5)). The particular shape of the magnetic field evolution recognised by this method (due to the large number of degrees of freedom needed to characterise curves more complex than ellipsis) limits its applicability [107].

7.1.2 Multi spacecraft methods

Multi-spacecraft methods need for data acquired by different spacecraft in different places. Albeit some of the single-spacecraft methods (*e.g.* MVA) never fall thanks to their simplicity, a multi-point measurement allows the computation of spatial gradients without the need of

strong hypotheses about the magnetopause structure like those necessary to single-spacecraft methods. After CLUSTER and MMS, the multi-spacecraft techniques specialised in analysing data acquired at $N = 4$ different points (the vertex of a tetrahedron in the best case); anyway it is worth noticing that these techniques can be extended to any N (mainly previewed to study turbulence [136]). The following two sections explain the two basic principles onto which multi-spacecraft methods are based, *i.e.* time delay estimates in observing the same features by different spacecraft and the computation of spatial gradients.

Timing methods

Data acquired by different spacecraft belonging to the same cluster can show "similar" features. Being only 10 km apart, MMS satellites indeed observe very similar magnetopause features. Figure (7.1) shows the B_z GSE components of the magnetic field recorded by each satellite of the MMS cluster during the *Cr2* event. From the figure it can be observed how close the four profiles are in standard conditions (*i.e.* during all the period visualised by Figure (7.1) but in the interval underlined by the right box where a magnetic reconnection event occurs [112]).

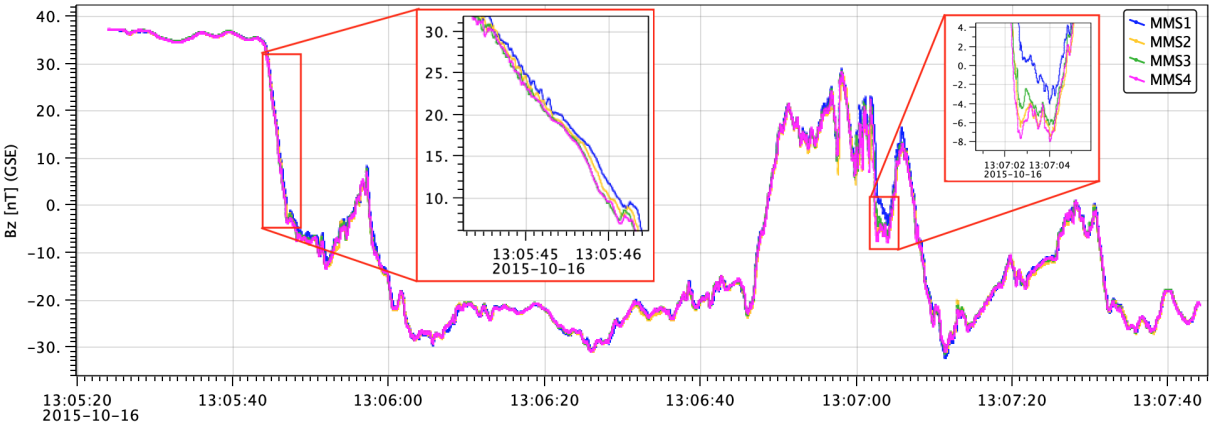

Figure 7.1: *Z component of the magnetic field probed by the four satellites of the MMS mission. The interval shown includes the Cr2 event. The two boxes inset shows the relatively small differences between the records of each spacecraft for two periods.*

Small differences occur. The box inset on the left to Figure (7.1) shows that the data profiles are delayed from each other. Since in this case no magnetopause structure modifications are supposed to happen, such a small difference is only due the fact that spacecraft do not cross the magnetopause at exactly the same time and location. Under some assumption (that will be explained below) the $(N-1)\,N/2$ time delays between the N satellites can be used to determine the direction of the movement of the magnetopause over-passing the spacecraft cluster. Since, in a first approximation, this direction coincides with the normal to the magnetopause then it can be a proxy to compute the magnetopause orientation. The delays between the spacecraft can be obtained from data in several ways. For instance, one method is to find the time shift τ for which two signals $S_\alpha(t)$ and $S_\beta(t)$ maximise their cross-correlation $\int S_\alpha(t)S_\beta(t+\tau)dt$. In presence of monotonic ramps in data, another way is to find the time delay between data points having the same (within the error bar) y coordinate. The latter method has been used to estimate the time delays shown in Figure (6.3). For these methods to work, the magnetopause velocity must be modelled by a simple expression such as

$$V(t) = A_0 + A_1 t + A_2 t^2 + A_3 t^3 \tag{7.10}$$

where A_0, A_1, A_2 and A_3 are constant to be determined from the timing data. In the spacecraft frame, the distance $\mathbf{R}_i$ ($i \in \{1,2,3,4\}$ for MMS) travelled by the magnetopause along

the normal direction $\mathbf{n}$ is

$$\mathbf{R}_i \cdot \mathbf{n} = \int_{t=t_{ref}}^{t=t_i} V(t)dt = A_0 t_i + A_1 \frac{t_i^2}{2} + A_2 \frac{t_i^3}{3} + A_3 \frac{t_i^4}{4} \tag{7.11}$$

where t_i is the time delay at which the spacecraft i crosses the magnetopause with respect to a reference time t_{ref}.

- **Constant Velocity Approach (CVA) [29]**
  This method assumes in Equation (7.10) $A_1 = A_2 = A_3 = 0$. Equation (7.11) then becomes

  $$\mathbf{R}_i \cdot \frac{\mathbf{n}}{A_0} = t_i \tag{7.12}$$

  where, since $|\mathbf{n}|^2 = 1$, the two components of $\mathbf{n}$ and A_0 can be determined knowing t_i for $i \in \{2, 3, 4\}$.

- **Constant Thickness Approach (CTA) [64]**
  The assumption of CVA can hardly be verified. [64] clearly exemplified the problem: in standard conditions ($P = 1$ nPa, $N = 15$ protons/cm^3, magnetopause thickness $d = 500$ km and $\gamma = 2$) a pressure imbalance of 10% produces a magnetopause acceleration of 8 km/s^2 and a thickness change $\sim 2.4\%$. In this case one has to use Equation (7.11) in its entire form considering the LHS to be fixed and equal for each spacecraft crossing (this is an assumption likely to be verified for MMS, remember figure (6.6)). It can be noted that for $N = 4$, there are 6 delays between the 4 spacecraft which are sufficient to solve the system Equations (7.11) joint with the condition $|\mathbf{n}|^2 = 1$.

Gradient based methods

Thanks to the multi-point measurements acquired by MMS, spatial gradients can be computed within a length scale relatively small with respect to the magnetopause thickness. This allows to perform local characterisations, a possibility not allowed by single-spacecraft measurements since, in this case the gradients can not be computed without assuming strong hypotheses, such as a strict stationary of the magnetopause structure and a constant direction of the gradients across the whole magnetopause layer thickness. Nevertheless the computation of a gradient by means of a multi-point measurement requires assumptions that must be kept in mind since the analyses performed in this thesis are mainly based on the computation of gradients. The technique used to compute gradients by means of multi-point measurements is the Curlometer technique [32]. The Curlometer technique assumes particular hypotheses concerning the respective positions where measurements are made and the characteristics of the measured field. The gradients are estimated by a linear estimator which is the gradient of the barycentric coordinates of the multi-spacecraft cluster (also known as reciprocal vector estimation) [39, 48]. Therefore, the accuracy of the results is better when the configuration of the spacecraft is reasonably regular [54] and when there is no important gradients at scales smaller than the inter-spacecraft distance. Figure (7.2) shows a schematic representation of the tetrahedron having at its vertex the spacecraft S_1, S_2, S_3, S_4. These spacecraft have positions $\mathbf{r}_1$, $\mathbf{r}_2$, $\mathbf{r}_3$, $\mathbf{r}_4$. According to the reciprocal vectors estimation technique, the gradient of some quantity $\mathbf{Q}$ is

$$\overline{\nabla}\mathbf{Q} = \sum_{i=1}^{4} k_i \mathbf{Q}_i \tag{7.13}$$

where, for instance,

$$k_4 = \frac{(\mathbf{r}_1 - \mathbf{r}_2) \times (\mathbf{r}_1 - \mathbf{r}_3)}{(\mathbf{r}_1 - \mathbf{r}_4) \times ((\mathbf{r}_1 - \mathbf{r}_2) \times (\mathbf{r}_1 - \mathbf{r}_3))} \tag{7.14}$$

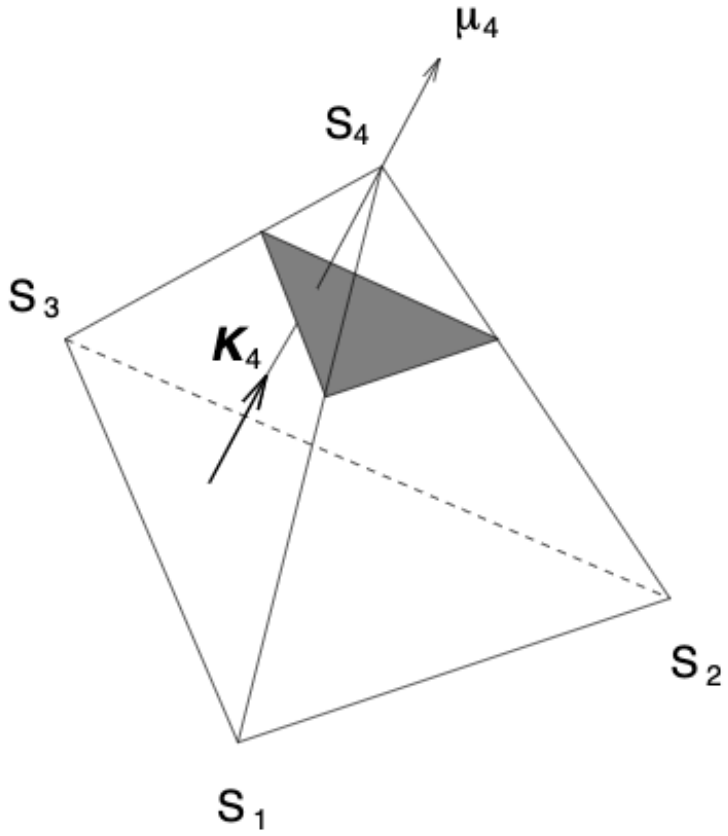

Figure 7.2: *Schematic representation of the tetrahedron geometry defined by the spacecraft S_1, S_2, S_3 and S_4 having positions $\mathbf{r}_1$, $\mathbf{r}_2$, $\mathbf{r}_3$ and $\mathbf{r}_4$. The reciprocal vector $\mathbf{k}_4$ (Equation (7.14)) points toward vertex S_4 and is the gradient of the barycentric coordinate μ_4 which is constant on any plane parallel to the surface containing S_1, S_2 and S_3. Credits: after [39].*

The estimation of gradients from multi-point measurements is at the hearth of very recent techniques able to compute locally the normal to the magnetopause. This allows to observe the spatial dependence of the normal direction and therefore allows to examine the sub-structure details of the magnetopause. These techniques are the Minimum Directional Derivative and the Local Normal Analysis techniques. These two techniques are described in the following sections.

7.2 The state of the art: the MDD technique

The Minimum Directional Derivative (MDD) is a multi-spacecraft technique forged by [70] to compute the dimensionality of a plasma structure and the directions of minimum, mean and maximum variation of a quantity $\mathbf{Q}$ across the magnetopause. For the sake of clarity, everywhere afterwards in the text $\mathbf{Q} = \mathbf{B}$ since the methods will be applied to the magnetic field data only. This methods remain valid if $\mathbf{B}$ is replaced by any other quantity (e.g.: $\mathbf{E}$, $\mathbf{V}_i$, $\mathbf{V}_e$, etc...). The method has been introduced using Cluster data. Since the MMS mission adopts inter-spacecraft separations smaller than those used by Cluster and smaller than the magnetopause cross section thickness (remember Figure (6.6)), the MDD technique is particularly adapted to local studies across the magnetopause. The dimensionality of plasma structures across the magnetopause and the directions of minimum, mean and maximum variation of a quantity $\mathbf{Q}$ are derived respectively as the eigenvalues (λ_n, λ_m, λ_l) and the associated eigenvectors ($\mathbf{n}$, $\mathbf{m}$, $\mathbf{l}$) resulting from the diagonalisation of the matrix

$$\mathbf{L} \equiv \mathbf{G} \cdot \mathbf{G}^{\mathbf{T}} \tag{7.15}$$

where $\mathbf{G}^T$ is the transpose of $\mathbf{G}$ and $\mathbf{G} \equiv \overline{\nabla}\mathbf{B}$. Let's order the $\mathbf{L}$ eigenvalues as $\lambda_n > \lambda_m > \lambda_l$. The plasma structure crossed by MMS is defined "quasi-1D" with respect to quantity $\mathbf{B}$ if $\lambda_n \gg \lambda_m \sim \lambda_l$. In this case $\mathbf{B}$ varies along only the direction $\mathbf{n}$ and therefore $\partial\mathbf{B}/\partial\mathbf{n} \gg \partial\mathbf{B}/\partial\mathbf{m} \sim \partial\mathbf{B}/\partial\mathbf{l}$. The structure is defined "quasi-2D" if $\lambda_n \sim \lambda_m \gg \lambda_l$. In this case $\mathbf{B}$ is invariant along the direction $\mathbf{l}$ and therefore $\partial\mathbf{B}/\partial\mathbf{l} \ll \partial\mathbf{B}/\partial\mathbf{n} \sim \partial\mathbf{B}/\partial\mathbf{m}$. Finally, if $\lambda_n \sim \lambda_m \sim \lambda_l$ the quantity $\mathbf{B}$ varies along all the $\mathbf{n}$, $\mathbf{m}$, $\mathbf{l}$ directions and the structure is said to be "3D" with respect to $\mathbf{B}$. The ratios between the three eigenvalues can be summarised in three a-dimensional parameters D_1, D_2 and D_3 proposed by [131]:

$$\begin{cases} D_1 \equiv \dfrac{\lambda_n - \lambda_m}{\lambda_n} & \text{(7.16a)} \\ D_2 \equiv \dfrac{\lambda_m - \lambda_l}{\lambda_n} & \text{(7.16b)} \\ D_3 \equiv \dfrac{\lambda_l}{\lambda_n} & \text{(7.16c)} \end{cases}$$

These three parameters have a total sum equal to 1 and vary in the $[0;1]$ interval allowing to understand at a glance if the crossed structure is $1D$ ($D_1 = 1, D_2 = D_3 = 0$), $2D$ ($D_2 = 1, D_1 = D_3 = 0$) or $3D$ ($D_3 = 1, D_1 = D_2 = 0$). Figure (7.3) shows for instance the three parameters introduced in Equations (7.16) for the $Cr2$ magnetopause crossing. Particular 1D intervals can be observed, such as within $[13.5;17]s$ and $[51.5;54]s$. Elsewhere it can be observed that when D_1 decreases D_2 increases whereas D_3 remains everywhere small but for a few very narrow intervals.

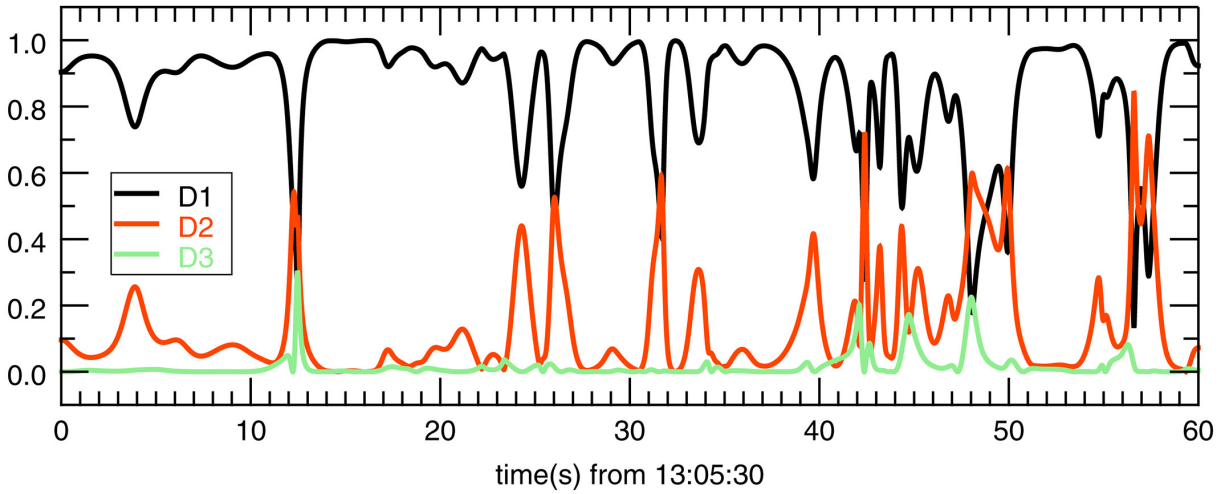

Figure 7.3: *The three parameters D_1, D_2 and D_3 as a function of time for the Cr2 case. Credit: after [131]*

Table (7.2) summarises the relations between the dimensionality of $\mathbf{B}$ across the magnetopause structure, the MDD eigenvalues, and the D_i parameters.

The MDD technique is based on the computation of $\mathbf{G} \equiv \overline{\nabla}\mathbf{B}$. This quantity is retrieved by means of the reciprocal vector method [48] that exploits the multi-point measurement of missions such as Cluster or MMS [112]. This means that the computation of $\overline{\nabla}\mathbf{B}$ is valid over regions an inter-spacecraft distance wide ($\sim 10km$ for MMS). As it will be explained in the next section, the LNA method is able to compute the magnetopause orientation at scales even smaller.

Table 7.2: *Summary of the relations between the eigenvalues ($\lambda_n > \lambda_m > \lambda_l$) and the eigenvectors (**n**,**m**,**l**) of* **L** *(Equation (7.15)) and the characteristics of the quantity* ***B*** *across the magnetopause (MP). The relation between the D_i parameters proposed by [131] and the dimensionality of* **B** *across the MP structure are shown in the right column. Note that* **B** *can be substituted with every else vector quantity.*

Eigenvalues ratios	variant directions for **B**	**B** across the MP	D_i [131]
$\lambda_m/\lambda_n \sim \lambda_l/\lambda_n \ll 1$	**n**	*quasi-1D*	$D_1 = 1, D_2 = D_3 = 0$
$\lambda_m/\lambda_n \sim 1 \ll \lambda_l/\lambda_n$	**n** and **m**	*quasi-2D*	$D_2 = 1, D_1 = D_3 = 0$
$\lambda_m/\lambda_n \sim \lambda_l/\lambda_n \sim 1$	**n**, **m** and **l**	*3D*	$D_3 = 1, D_1 = D_2 = 0$

7.3 The LNA technique

Table (7.3) presents a summary of the previously introduced methods used to determine the magnetopause orientation. From the table it can be observed that none of these methods allow to compute a local normal using single spacecraft data only. The Local Normal Analysis method introduced by [131] allows to do this.

Table 7.3: *Summary of data analysis techniques for the computation of the magnetopause current sheet orientation. Acronyms stand for: CVA → Constant Velocity Analysis, GRA → Generic Residue Analysis, MDD → Minimum Directional Derivative, LNA → Local Normal Analysis.*

	Multi s/c	Single s/c
Global	CVA [29],CTA [64]	GRA [73], BV [102]
Local	MDD [70]	LNA [131]

LNA computes the normal to the crossed plasma structure as

$$\mathbf{N} = \frac{\mathbf{J} \times \partial_t \mathbf{B}}{|\mathbf{J} \times \partial_t \mathbf{B}|} \tag{7.17}$$

where **B** and $\mathbf{J} \equiv n_i \mathbf{U}_i - n_e \mathbf{U}_e$ can be measured independently by a single spacecraft. The computation derives from the fact that when the spatial dependence of a plasma parameter **Q** is directed toward the same direction all along the magnetopause cross section, **Q** can be modelled by a scalar function $s \equiv (x, y, z)$. In this case the **N** direction toward which gradients occur is $\overline{\nabla} s / |\overline{\nabla} s|$. The following equivalence occurs: $\overline{\nabla} \times \mathbf{Q} = \overline{\nabla} s \times \partial \mathbf{Q}/\partial s = |\overline{\nabla} s| \mathbf{N} \times \partial \mathbf{Q}/\partial s$. If $\mathbf{U} = \mathbf{E}$, Equation (7.17) is demonstrated.

7.4 Comparison between the LNA and the MDD methods

[131] applied the MDD and the LNA methods to data acquired by the virtual satellite crossing the simulated magnetopause of Figure (6.5). Figure (7.4) shows in the bottom panel the angle between the y axis of Figure (6.5) and the MDD (blue curve) and the LNA (black curve) normals selected according to the values of D_1 (top panel). An additional selection criterion has been adopted: normal values are rejected if there are no significant magnetic field variations, quantitatively if $|\partial_t(\mathbf{B})|^2$ is less than one tenth of its maximum value. The figure shows that the LNA normal is closer than the MDD normal to the y direction - which is the real orientation of the magnetopause - for pure 1D intervals. Nevertheless, in pure 1D intervals **J** is perpendicular to **B**. The discrepancy between the MDD and the LNA results suggest therefore that the MDD (which uses the magnetic field data only, differently to LNA which uses the particle data too) should be generalised in order not to take into account only one field [131] whose features could differ from those of others quantities. LNA is anyway dependent by the computation of the D_i parameters to understand where to retain or discard results. MDD and LNA can be therefore

usefully combined. Furthermore, the tandem cooperation between MDD and LNA can overcome the information loss the two methods are afflicted by, which are, respectively, the plasma and fields variations happening at length scales smaller than the MMS inter-spacecraft distance and that part of the distribution function outside of the measurement windows of MMS instruments. Due to the local nature of the LNA and MDD investigations, the two methods are shown to agree with each other better than with other methods. Table (7.4) summarises the angular distances between the LNA, the MDD and the MVAB methods for six magnetopause crossings. Even if the distance between the LNA and the MDD normals are not smaller than the local variations of each determination, as estimated by the standard deviation of their direction with respect the global MVAB result, the LNA and the MDD normals both show to be often clearly different from the global MVAB determination.

Table 7.4: *Statistics (mean value and std) on the angles between the normals obtained by LNA, MDD and MVAB methods for MMS magnetopause cases identified by temporal coordinates (first column). Statistics are performed within the time interval shown in the second column. LNA and MDD normals selection criteria are* $D_1 > 0.99$ *and* $|\partial_t(\mathbf{B})|^2 > 0.5$ *of its maximum value. Credits: [131]*

Date	Interval [s]	LNA vs MVAB	MDD vs MVAB	LNA vs MDD
2015-10-16, 10:20:00 (+120s)	2.9	20 ± 3	17 ± 8	9± 6
2015-10-16, 10:29:30 (+120s)	4.2	56 ± 0.5	44 ± 3	12± 4
2015-10-16, 10:36:30 (+120s)	3.5	33 ± 0.8	21 ± 0.9	12± 0.4
2015-10-16, 10:55:00 (+60s)	3.3	12 ± 1	11 ± 4	3± 1
2015-10-16, 13:05:30 (+60s)	3.0	24 ± 2	20 ± 3	7± 3
2017-01-27, 12:05:23 (+70s)	3.5	35 ± 19	39 ± 14	9± 6

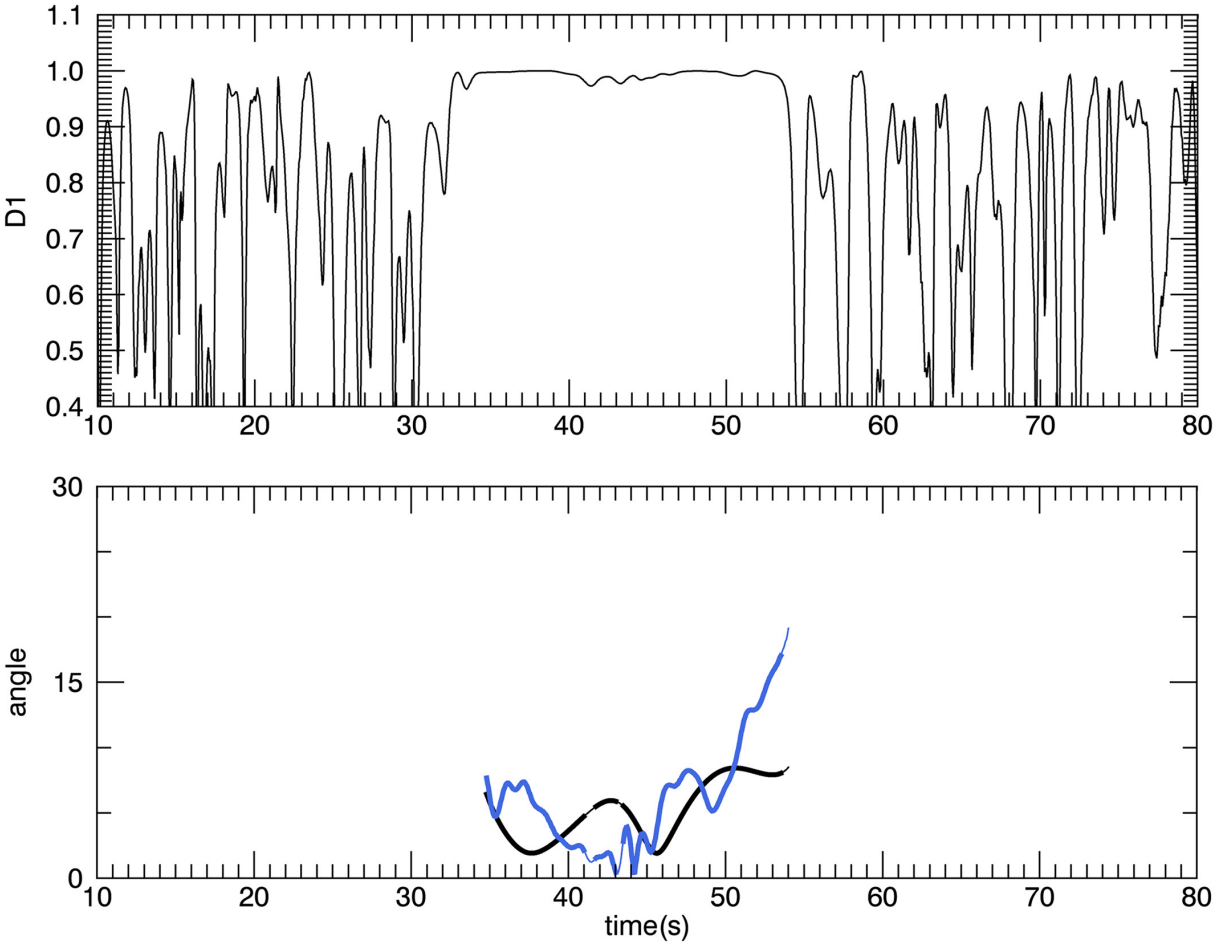

Figure 7.4: *D_1 parameter (top panel) and angular distance between the y axis of Figure (6.5) and the MDD (blue curve) and the LNA (black curve) normals (bottom panel). In the bottom panel the thin curves correspond to $D_1 > 0.9$ intervals whereas thick curves correspond to $D_1 > 0.98$ intervals. Credit: after [131]*

Chapter

8 A POINT-BY-POINT LOCALISATION OF DATA ACROSS THE MAGNETOPAUSE

Chapter content

When spacecraft missions probe the magnetopause the relative location of the spacecraft with respect to the magnetopause is unknown. This information is however needed to measure the geometrical features of the magnetopause (orientation, thickness and shape) and to understand the physical processes underlying its dynamics. Furthermore, the spatial distribution of data recorded as a function of time can be used also as a "boundary condition" for integrating the MHD Grad-Shafranov equations [10, 20] in order to reconstruct portions of the magnetopause out of the spacecraft trajectory. In Paper 1 we introduce new methods to compute the spacecraft trajectory across the magnetopause relaxing the strong assumption that are usually made about its structure. These assumptions allow to apply simple and useful data analysis methods to real case studies. Unfortunately, the hypotheses assumed by these methods are rarely observed. The less strong the assumptions of a method are, the greater is the ensemble of case studies that are potentially analysable by that method and the less the results are likely to be biased by the assumption themselves. Multi-spacecraft missions like Cluster and MMS help in extracting the information about the spacecraft path across the magnetopause. The multi-point measurements acquired by these missions help in recognising the variations caused by spatial dependencies from those caused by pure temporal dependencies. The temporal and the spatial variations are therefore partially disentangled and some of the strong assumptions can be released. Ultimately, they may allow to compute the geometrical shape of the magnetopause and to determine the spacecraft location in a broad ensemble of case studies.

8.1 Usual hypotheses used in tracing satellites

The temporal variations observed by a single spacecraft can be caused by a pure temporal variation of the magnetopause or by the magnetopause displacement as seen in the spacecraft frame. Due to this ambiguity, some assumptions about the magnetopause structure are required in order to trace the spacecraft trajectory across the magnetopause. These hypotheses concern the stationarity of the magnetopause, the characteristics of gradients of different data sets and the kinematics of the magnetopause:

1. **Stationarity of magnetopause**
   The first basic assumption that makes possible the conversion from temporal to spatial data consists in assuming the magnetopause to be stationary in its proper frame, even if this frame, relatively to the spacecraft, can undergo variable accelerations in all directions, directly driven by the incident solar wind or due to local surface waves. The fact that the proper frame of the structure can experience accelerations has been exemplified in section (6.2). Multiple and close crossings due to a back and forth motion of the magnetopause are observed on 16 October 2015 during the *Cr2* event (see [131] and Paper 1). In these cases, the spacecraft path is most generally guessed comparing the temporal data with an ideal sketch of the magnetopause structure that the spacecraft is likely to have crossed. Localising data this way has long been used by experimenters for drawing hand-made sketches to interpret data in the reconnection context [112, 125]. In real life, the observed magnetopause is not strictly stationary in its own frame. It can undergo modifications during the spacecraft crossing due, for instance, to MHD instabilities or turbulence. As will be shown in section (8.2.2), these departures from strict stationarity can lead to inaccuracies or even divergences in spacecraft trajectory when using methods that assumes strict stationarity.

2. **Gradients features shared between different data sets**
   The methods that use multiple field and particle data sets at once, may *a priori* help in determining the position of the spacecraft with respect to the magnetopause thickness. As explained in section (4.3), in stationary conditions the magnetopause consists in multiple, eventually superposed, discontinuities. Their signatures can be exploited to understand where the spacecraft is (7.1.1). But these methods can introduce serious inconsistencies since different data sets may show gradients that are shifted from each other (see Paper 1, Paper 2, and section (14) of this thesis).

3. **Simple spacecraft trajectories**
   The most known and simplistic method consists in assuming that the relative path of the s/c with respect to the structure is just a straight line, travelled with a constant velocity in a stationary structure. Obviously this is also the most dangerous assumption, since this event is rare. Recently, efforts have been made to consider different - but pre-determined - forms for this path [62, 65]. Other authors have taken into account possible intrinsic temporal evolution of the magnetopause structures [88, 87, 105]. However, in all these studies the spacecraft velocity, even locally, is assumed to be the deHoffmann-Teller velocity, which, in some cases, may be not determinable.

4. **Particular flows and/or spatial structures**
   In [77] the authors have introduced a different method that they called "empirical reconstruction". It is a multi-spacecraft method that allows determining a s/c path in the 1D hypothesis, and even in the 2D hypothesis, but under restrictive assumptions: no plasma flow across the magnetopause, the 2D shape is supposed known *a priori* (for instance it is a surface wave).

The target of methods introduced in the next section is to recover the velocity without any *a priori* assumption.

8.2 Drop assumptions for tracking spacecraft

Methods addressing the plasma structure as a whole (e.g.: the MVA method or the BV method both returning a *global frame*) adopt hypotheses that have to be checked only at local scales across the entire magnetopause (*e.g.* $B_n = 0$ for MVA and $V_n = 0$ for BV). The MDD and the LNA techniques allow to determine such local features. These methods allow one to fully account for the spatio-temporal modifications of the orientation of the crossed portion of magnetopause. The same can be done to compute the spacecraft trajectory. In the following, new methods are presented (see Paper 1) that relax the assumptions introduced in the previous section (8.1) and replace the full stationarity assumption by a more moderate "quasi-stationarity" assumption. The magnetopause can therefore be considered stationary on time scales that are smaller than the time needed for the spacecraft to cross the magnetopause. As shown in section (10), local features concern magnetopause portions of about 0.8% of its total width. This allows to investigate the magnetopause internal structure. In this sense the local features of the magnetopause can be discriminated from the global ones.

8.2.1 The Spatio-Temporal Difference technique

The working principle

The Spatio-Temporal Difference technique (STD, [72]) computes the velocity ($\partial_{t,0}\mathbf{X}$) of any field measured by spacecraft (in the spacecraft frame) that shows a gradient across the magnetopause (magnetic field, plasma flows and so on...). Assuming that the magnetopause is stationary, the method associates the temporal variations of observed field ($\partial_{t,sc}\mathbf{B}$, where *sc* means "spacecraft") to the pure spatial translation of the magnetopause ($\partial_{t,0}\mathbf{X} \cdot \overline{\nabla}\mathbf{B}$). Thanks to the multi-point measurement of the field taken into account, the STD computes the spatial gradient of the field ($\overline{\nabla}\mathbf{B}$) by means of the MDD method (section (7.2)). In contrast to the other methods, the STD method needs for the magnetopause full stationarity: no modifications of the magnetopause structure in its own frame is allowed. As done in Paper 1, if STD is applied to the magnetic field, it is able to recover the magnetopause magnetic structure velocity $\partial_{t,0}\mathbf{X}$ by means of inversion of $\partial_{t,0}\mathbf{X} = \partial_{t,0}\mathbf{X} \cdot \overline{\nabla}\mathbf{B}$ (Equation 1, Paper 1). Note that the method remains valid if $\mathbf{B}$ is replaced by any other vector quantity.

The limits

Although the method is one of the most advanced, it may fail in the following two cases:

1. when the velocity of the magnetic field structure in the frame of the spacecraft ($\partial_{t,sc}\mathbf{B}$) is due to both magnetic field gradient displacements ($\partial_{t,0}\mathbf{X} \cdot \overline{\nabla}\mathbf{B}$) and, even to a relatively low ratio, to the intrinsic temporal variations of the magnetic structure ($\partial_{t,0}\mathbf{B}$). When this happens, Equation 1 of Paper 1 shall be replaced by the following generalisation:

$$\partial_{t,sc}\mathbf{B} = \partial_{t,0}\mathbf{X} \cdot \overline{\nabla}\mathbf{B} + \partial_{t,0}\mathbf{B} \tag{8.1}$$

   In Equation (8.1) the subscripts 0 indicate the quasi-stationary frame where the intrinsic variation $\partial_{t,0}\mathbf{B}$ is minimum. The unknowns are the $\partial_{t,0}\mathbf{X}$ and the $\partial_{t,0}\mathbf{B}$ terms while the $\partial_{t,sc}\mathbf{B}$ and the $\overline{\nabla}\mathbf{B}$ terms are computed from data via a temporal derivative and the reciprocal vector method [48] that exploits the multi-point measurements provided by MMS.

2. when the magnetopause is not sufficiently three-dimensional the inversion of Equation 1 of Paper 1

$$\partial_{t,0}\mathbf{X} = \partial_{t,sc}\mathbf{B} \cdot \left[\overline{\nabla}\mathbf{B}\right]^{-1} = \frac{\partial_{t,sc}\mathbf{B} \cdot \left[\overline{\nabla}\mathbf{B}\right]^{A}}{\det\left[\overline{\nabla}\mathbf{B}\right]} \tag{8.2}$$

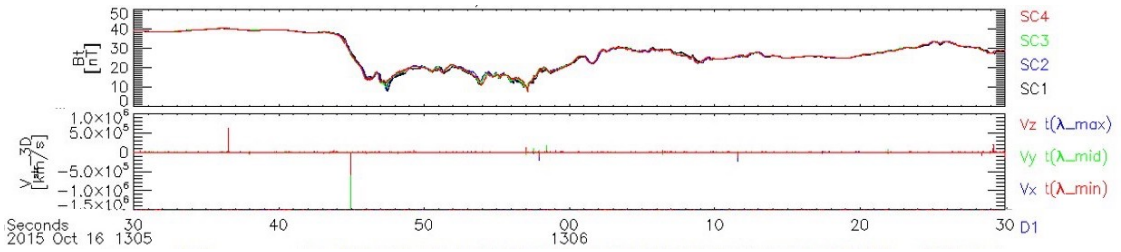

Figure 8.1: *Computation of the magnetopause magnetic field structure velocity (bottom panel) during the Cr2 crossing (magnetic field shown on the top panel). The computation has been done by means of SPEDAS routines.*

(Equation 3 of Paper 1) is particularly sensitive to the conditions for which the determinant of the gradient of the magnetic field $\det\left[\overline{\nabla}\mathbf{B}\right]$ becomes very small. In these cases, the numerator and denominator of Equation (8.2) both tend toward zero. Its value then strongly depends on any noise or to any departure from a strict stationarity that can make the numerator null at a place slightly different from the denominator. In order to prove such inconvenient, Figure (8.1) shows the peaks resulting in the computation (by means of SPEDAS routines) of the magnetopause magnetic field structure velocity (bottom panel) during the *Cr2* crossing. The magnetic field is shown in the top panel to facilitate the comparisons with other plots in this thesis. The velocity determined in this way for the plasma structure shows clearly large and nonphysical peaks.

8.2.2 STD revisited: suppression of singularities and stabilisation of eigenvectors

The suppression of singularities

According to [72] and [137], the problems arising using the STD method can be avoided using, respectively, the non singular part of $\overline{\nabla}\mathbf{B}$ in Equation (8.2) and adding a small amplitude noise to magnetic field data. Both solutions are of practical interest but have to be considered as compromises. The solution proposed in [72] is valid when the variations are approximately 1D, since the derivative of the most varying component of the magnetic field along the local normal is usually sufficient to determine the velocity of spacecraft along the normal direction and it is very rarely affected by the singularities. Nevertheless, this process may be an unnecessary loss of information. It is arbitrary since the 1D data intervals can not be determined but by empirically determined thresholds (see for instance [131]). It may be also dangerous, since the 2D or 3D local variations always exist and, even if weak, they may be relatively significant in the determination of the spacecraft trajectory (computed as integration of the spacecraft velocity, see section (8.3.1)). Disregarding the 2D or 3D local variations does not allow to determine 2D or 3D paths (even when it becomes possible, see section (8.3.1)).

In order to avoid the previous practical but dangerous solutions, the RHS of Equation (8.2) has to be taken into account using the full version of $\overline{\nabla}\mathbf{B}$. This practice is implemented in this thesis. In doing so, we had to face further problems regarding the poor determination of the tangential (to the magnetopause) reference frame. The solution to these problems will be discussed below, in section (8.3.1).

We do not agree with [137], where it is written that the problem related to the eventual remaining singularities can be solved by adding a small amplitude noise on the field used by STD. Following the above arguments, it seems clear that such artificial noise may introduce further artificially-induced singular points.

In order to suppress singularities, Paper 1 proposed a very local and surgical correction to force the numerator of Equation (8.2) to be zero at the times t^* when its denominator ($\det\left[\overline{\nabla}\mathbf{B}\right]$)

is zero. In order to do so, to each of the three components of $\partial_{t,sc}\mathbf{B} \cdot \left[\overline{\nabla}\mathbf{B}\right]^A$ is added a signal made by a linear combination of Gaussian curves each of which

1. is centred on times t^*,
2. has a amplitude equal to $-\partial_{t,sc}\mathbf{B}(t^*) \cdot \left[\overline{\nabla}\mathbf{B}(t^*)\right]^A$ and
3. is narrow enough not to modify the signal for a period larger than 1% of the global period analysed (*i.e.* $\simeq 10$ data points for the *Cr2* case) and not to overlap the adjacent corrections.

Figure (8.2) exemplifies the procedure for the suppression of singularities found in the x component of Equation (8.2). The interval shown includes the main magnetic field gradient observed during the *Cr2* event. The top panel shows the denominator of Equation (8.2). The zeros of this curve set the positions of the red, vertical and dashed lines drawn in all the other panels. The second panel shows the Gaussian peaks centred on the zeros previously individuated. The STD$^+$ method consists in subtracting these curves to the numerator of the RHS terms of Equation (8.2) (panels c, d and e). Panels c, d and e shows the numerators both corrected and not corrected. It can be observed that the non corrected curves have non-zero values corresponding to the null-point of the determinant of $\overline{\nabla}\mathbf{B}$ (panel a). This cause singularities to occur. This problem can be clearly observed comparing panels f and g, which show $\partial_{t,0}\mathbf{X}$ computed by STD$^+$ and STD, respectively. In the second case (STD), it can be observed that the velocity of the magnetic field structure is severely affected by non-physical peaks. Once the $\partial_{t,0}\mathbf{X}$ components are integrated in time in order to obtain the spacecraft trajectory across the magnetopause, the problem affecting STD causes the spacecraft trajectory to be badly determined (see panel i). The spacecraft trajectory obtained by the STD$^+$ method shows a more natural behaviour (see panel h). From the figure it can be observed also that each Gaussian peak deforms only very slightly the curves in panels c, d and e meaning that the final result is only slightly affected by using the STD$^+$ method. Furthermore, even where many Gaussian corrections are very close, no superposition between two of them occur, as expected.

This solution is actually more surgical than adding a small amplitude noise to the magnetic field as proposed by [137] and it allows using the three components of the result, without information loss.

For the sake of clarity, let's define the directions $\mathbf{l}$, $\mathbf{m}$ and $\mathbf{n}$ as the three linearly independent directions of the local frame coincident to the eigenvectors of $\mathbf{G} = \overline{\nabla}\mathbf{B} \cdot \overline{\nabla}\mathbf{B}^T$ associated, respectively, to the minimum, intermediate and maximum eigenvalues of $\mathbf{G}$. Note that the two frames, $\mathbf{lmn}$ and $\mathbf{LMN}$ (the latter coming from MVA, its axes corresponding respectively to the largest, intermediate and minimum variance directions) have the same "normal" directions ($\mathbf{n} = \mathbf{N}$) as soon as the local properties are identical to the global ones, but that their axes in the tangential plane are not the same.

In section 8.2 the LHS of Equation (8.2) with and without corrections was compared for a real case study. Anyway, the effects of these corrections can be clearly observed in panel f of Figure 6 of Paper 1, where the magnetopause structure velocities computed by means of the STD and the STD fixed by our methods are compared. The above method will be called STD$^+$ to differentiate it from the original STD method. It allows circumventing pragmatically the problem of singularities, but without tackling directly the original cause of this problem: the small non-stationarities that affect the data.

The stabilisation of G eigenvectors

When using the full version of $\overline{\nabla}\mathbf{B}$ with STD, a further correction is needed in order to fix the high frequency variations of the eigenvectors associated with the smallest eigenvalues of $\mathbf{G}$, *i.e.* the tangential directions of the local frame computed by the MDD method. Figure 1 of Paper 1 shows the high frequency irregular oscillations of the GSE components of the $\mathbf{m}$ and the $\mathbf{l}$

directions (panels c and d) in contrast to the more stable $\mathbf{n}$ direction (panel b) during the *Cr2* magnetopause crossing (the magnetic field is shown in panel a). This problem can be solved fixing the discontinuities in the evolution of the $\mathbf{m}$ and $\mathbf{l}$ directions and it can be circumvented retaining only the normal projection of $\partial_{t,0}\mathbf{B}$. Figure (8.3) shows the fixing of jumps observed on the GSE components of the MDD $\mathbf{n}$ normal. In this case, the sudden changes in the GSE components of the MDD normal (panel c) are automatically corrected (panel d). The same correction is applied to the m and l MDD directions. The projection of $\partial_{t,0}\mathbf{B}$ toward the normal direction $\mathbf{n}$ will be discussed in section (8.3.1). The following sub-section will explain how to manage Equation (8.1) to obtain $\partial_{t,0}\mathbf{X}$ in a general not-projected and non stationary case.

8.2.3 The Multi Variate Fit methods

In any but the local lmn frame, Equation (8.1) represents an intertwined relation between the temporal and spatial variations of the different components of $\mathbf{B}$ via the $\partial_{t,0}\mathbf{X} \cdot \overline{\nabla}\mathbf{B}$ term. The determination of the unknowns $\partial_{t,0}\mathbf{X}$ and $\partial_{t,0}\mathbf{B}$ can be done by means of a multi-variate fit procedure assuming the two unknowns are approximately constant over a short interval lasting a small number p of experimental points (typically, $p = 10$).

The fit minimises analytically the total squared difference between the observed temporal variations ($\partial_{t,sc}\mathbf{B}$) and the reconstructed ones ($\partial_{t,0}\mathbf{X} \cdot \overline{\nabla}\mathbf{B} + \partial_{t,0}\mathbf{B}$), normalised to the mean magnetic field temporal derivative:

$$D \equiv \frac{\sum_p \left\{ \sum_i \left[\partial_{t,sc} B_i - \left(\partial_{t,0} X_j \, \partial_j B_i + \partial_{t,0} B_i \right) \right]^2 \right\}_p}{\sum_p \left[\sum_i \left(\partial_{t,sc} B_i \right)^2 \right]_p} \tag{8.3}$$

where $i, j = \{x, y, z\}$. The analytical treatment of this problem is described in section (16). Once the $\partial_{t,0}\mathbf{X}$ and the $\partial_{t,0}\mathbf{B}$ terms are obtained, a selection procedure is made according to the comparison between the associated error (given by the Equation (8.3)) and a threshold $D_{lim,MVF}$: if $D > D_{lim,MVF}$ the results are discarded, otherwise the results are retained. In contrast to other methods, here the $D_{lim,MVF}$ threshold is chosen by an optimisation procedure that will be described in section (8.3.4). Since D is expected to be very small for a fit result to be retained, $D_{lim,MVF}$ is small as well, e.g.: 10^{-1} or 10^{-2}. Figures A.1 of Paper 1 and Figure (8.6) (both explained in next sections) confirm this expectation. The fits are performed on a number of data points p that can vary in accordance with a second optimisation procedure described in section 8.3.3 and that varies from a lower integer value p_{min} to a maximum integer value p_{max} based on the local curvature of the curve to be fitted. Here it is worth noticing that this method assumes the magnetopause to be stationary for, at least, an interval $p\nu_s^-1$ long, where p is usually not larger than 10 and $\nu_s = 128$ S/s. This interval is therefore $\sim$ one hundredth of the time interval required by a spacecraft to cross the magnetopause. The MVF method assumes therefore the magnetopause to be stationary over periods much smaller than those assumed by other methods. Finally, the $\partial_{t,0}\mathbf{X}$ and the $\partial_{t,0}\mathbf{B}$ terms which do not survive the selection procedure according to the comparison between D and $D_{lim,MVF}$ are replaced by means of interpolation.

8.2.4 The Single Variate Fit method

Since MVF aims at minimising the total error D, it is not able to discriminate which component of Equation (8.1) causes the fit to be rejected. The method can be improved by performing the fit procedure in the local lmn frame. In this frame, the $\overline{\nabla}\mathbf{B}$ matrix is diagonal so that the three components of Equation (8.1) do not share common unknowns; therefore the fit procedure can be performed independently for each component, disentangling the high quality fits of one component from the low quality fits of the others. Figure (8.4) shows an example of an interval where SVF fits the experimental points better than the MVF method. Nevertheless, it is worth

remembering that in some cases the *lmn* frame is far from being stable (remember section (8.2.2) and see Figure 1 of Paper 1). In these cases the SVF method can be applied anyway but it is clear that the local *lmn* frame has then no real physical significance. Only the directions corresponding to large derivatives are expected to be reliable and thus stable.

Here, as well as the MVF method, the results which do not survive the selection procedure according to the comparison between D and $D_{lim,MVF}$ are replaced by means of interpolation.

8.3 Optimisation procedures

8.3.1 Projection and integration of $\partial_{t,0}\mathbf{X}$

In this thesis, but for a particular case (section 10.2.2), the MVF and SVF final results are provided as 1D normal displacements $X_n(t)$ describing the position of the spacecraft with respect to the magnetopause along its normal as a function of time. The 1D projection of $\partial_{t,0}\mathbf{X}$ is obtained using Equation 6 of Paper 1. The term integrated by that equation results from a double projection. In particular the term $\partial_{t,0}\mathbf{X}$ is firstly projected along the local normal $(\partial_{t,0}\mathbf{X}(t)\cdot\mathbf{n}(t))$; secondly, the result is reduced by a factor originating from the local difference between the local normal and the global normal, where the latter is computed as the mean of the total ensemble of the former $(\mathbf{n}(t)\cdot\mathbf{N}_{glob})$. The reasons why this procedure is necessary are:

1. **Accuracy of tangential frame directions**
   Due to an intrinsic limitation of the methods which base their computations on the $\overline{\nabla}\mathbf{B}$ matrix, the **m** and **l** components of $\partial_{t,0}\mathbf{X}$ may be less accurate than the **n** component. The reason can be easily understood writing Equation 1 of Paper 1 in the **lmn** frame. This frame corresponds to the eigenvectors of $G \equiv \overline{\nabla}\mathbf{B}\cdot\overline{\nabla}\mathbf{B}^T$. In this frame $\partial_{t,0}X_i \propto 1/\lambda_i$ (with $i=\{l,m,n\}$), which goes to infinity when λ_i goes to zero.

2. **Accuracy of the normal joint with large tangential flows**
   The integration of the flow normal velocity (used also in [77] and BV [103] to determine the path along the normal) is very sensitive to inaccuracies in the determination of the normal direction as well. The large tangential flows that exist in the magnetosheath can indeed provide an apparent normal flow that is very inaccurate when projected on an approximate normal direction, even if the inaccuracy in the normal direction is small. Therefore the local differences between the local and the global normals must be taken into account.

Here it is worth noticing that the direct projections of $\partial_{t,0}\mathbf{X}$ toward the global normal would generate a loss of information due to the differences between the local and the global normals. This loss of information would cause the normal projection of the spacecraft trajectory to be underestimated.

In spite of the previous considerations, 2D maps of the spacecraft path can be obtained quite satisfactorily under favourable conditions (λ_m not much smaller than λ_n during the major part of the crossing). As explained in section (10), in Paper 1 both 1D and 2D reconstructions have been attempted on real data.

8.3.2 Selection of 1D intervals

The particular projection introduced by Equation 6 of Paper 1 is defined when local normals exist. It is therefore performed only when the magnetopause is quasi 1D, locally. Following [131], the 1D intervals are further selected depending whether the main magnetic field variations are related to the main current layer or not. These requirements can be checked for each data point selecting data according to the parameters $(\lambda_n-\lambda_m)/\lambda_n$ and dB/dt where, as usual, λ_n and λ_m

are the two largest eigenvalues of G and $B \equiv |\mathbf{B}|$ [131]. The selection is performed using two thresholds, K_{1D} and K_{d_tB} for which

$$(\lambda_n - \lambda_m)/\lambda_n > K_{1D} \tag{8.4}$$

and

$$dB/dt > K_{d_tB}\,[dB/dt]_{max} \tag{8.5}$$

The optimal values of both parameters are chosen accordingly to an optimisation procedure explained below (section (8.3.4)). Like for the MVF and SVF methods (sections 8.2.3 and 8.2.4), the data points that do not survive the selection procedure are replaced by means of interpolation.

8.3.3 The automatic choice of fit periods

This section concerns the choice of parameters p_{min} and p_{max} and how p is ultimately determined in the interval $[p_{min}, p_{max}]$.

The choice of p_{min} and p_{max}

The MMS magnetic field data used in this thesis are recorded in "burst mode" at $\nu_s = 128$Hz [119]. A filtering procedure (see section (15)) filters data in Fourier space to frequencies below ν_c in order to select the frequency windows to observe. p_{min} is chosen to be equal to int $\left(\frac{\nu_s}{4\nu_c}\right)$. As a matter of facts, the highest frequency component of a signal filtered using ν_c could still have large variations in a period $\nu_c^{-1}/4$ long. This period corresponds to $\nu_s/(4\nu_c)$ data points if the original signal is probed at ν_s. p_{max} is chosen to be equal to 13 so that a fit does not represent more than one hundredth of the total crossing duration. Since the magnetopause crossings examined in this study are no longer than 10s, the maximum time period corresponds to $128S/s * (10s/100) \simeq 13$ data points.

The choice of p within the interval $[p_{min}, p_{max}]$

The SVF and the MVF methods use linear fits performed over small data intervals composed by p data points. As it is discussed in the previous section, $p_{min} \leq p \leq p_{max}$. Here it is described the operative algorithm implemented to set dynamically the parameter p all along the examined interval in order to cut it into sub-intervals of unequal lengths where the linear fits are the best possible. The procedure will be exemplified step-by-step using Figure (8.5).

Figure (8.5) shows the positions of the boundaries of fits periods at iteration n and how the algorithm choose where to set a new fit boundary in passing from step n to step n+1. The figure shows the time interval of a full crossing in units of seconds on its y axis and the corresponding data points recorded by MMS on its x axis (in this case the probing rate was $128S/s$). The blue straight curve represents the total interval under consideration. The red "+" superposed to the blue straight curve mark the points where the algorithm introduced in this section already decided to fix the boundaries of fit intervals. It is clear that the sub-intervals between the red "+" are yet too large, each of them including $\sim 10^2$ points $\gg p_{max}$. In order to understand how the algorithm works, let's observe what happens next taking in consideration the orange sub-interval at the lower left corner of the figure. Let N be the number of data points in the orange interval to be examined. In this case $N = 210$ and the corresponding time interval is $\sim 1.7s$. For each possible value of i in the interval $[p_{min}, N - p_{min}]$ (*i.e.* $N - 2p_{min}$ possibilities):

1. the interval is divided into two sub-intervals with one point i in common,
2. two linear fits are performed, each over the two sub-intervals $[p_{min}, i]$ and $[i, N - p_{min}]$ and
3. the corresponding error D_i is recorded as a function of i.

The resulting curve $D = \{D_i, \text{ with } i \in [p_{min}, N - p_{min}]\}$ (shown inset to Figure (8.5)) has an absolute minimum for some i_{min0}, which is the value of i for which the error is minimised when fitting the orange interval by two straight lines. For the orange sub-interval shown in Figure (8.5), $i_{min0} = 150$. The point i_{min0} is therefore taken as a fixed boundary for the next iteration. The green "+" at $N = 150$ is promoted to be a fixed boundary and in a next iteration it will become a red "+". The next iteration applied to the orange interval works as the previous one but applied to each of the two intervals $[0, i_{min0}]$ and $(i_{min0}, N]$ (*e.g.* the intervals $[0, 150]$ and $(150, 210]$ for the case of figure (8.5)). The result is that the orange interval is so divided into four sub-intervals: $[0, i_{min1}]$, $(i_{min1}, i_{min0}]$, $(i_{min0}, i_{min2}]$, $(i_{min2}, N]$, where i_{min1} and i_{min2} are the new fixed boundaries for which the error in fitting the orange period $[0, N]$ by four straight lines is minimised. The procedure is so repeated until there are no more allowed divisions over the entire period since there are no more intervals longer than p_{max} points.

8.3.4 The Gradient Directed Monte Carlo approach

The methods described in the previous sections require values for a large number of thresholds. These thresholds are the minimum and the maximum number of fit points for the MVF and the SVF methods ($p_{min,SVF}$, $p_{min,MVF}$ and $p_{max,SVF}$, $p_{max,MVF}$), the thresholds that set a limit to the fit errors for a SVF or a MVF result to be retained or not ($D_{lim,SVF}$ and $D_{lim,MVF}$), and the thresholds for the selection procedures of 1D intervals associated with large currents (K_{1D} and K_{d_tB}). In the studies presented in this thesis, the parameters $p_{min,SVF}$, $p_{min,MVF}$, $p_{max,SVF}$ and $p_{max,MVF}$ are manually fixed for practical reasons (the automatic choice of these parameters would require a too large amount of time and computational power). These parameters are chosen in order to limit the fit procedures to periods between 0.04 s and 0.1 s. This choice allows to handle a sufficient number of data points per fit and fits per event.

The remaining parameters $D_{lim,SVF}$, $D_{lim,MVF}$, K_{1D} and K_{d_tB} can be thought as variables for $X_n(t)$. Collecting these parameters in a vector $C_r \equiv \{D_{lim,SVF}, D_{lim,MVF}, K_{1D}, K_{d_tB}\}$, it can be stated that $X_n(t)$ is an unknown non-linear function of C_r. $X_n(t)$ is therefore very sensitive to small variations of any of the C_r components. C_r is optimised by an iterative minimisation procedure based on a gradient descent algorithm known as Gradient-Directed Monte Carlo Approach (GDMC, [80]). The working principles of this algorithm are given exhaustively in Paper 1 (chapter 2.3 and appendix A.2) and will not be repeated here. Here it is worth noticing that this technique minimises the distance (ΔX_n) - and maximises the interval (Δt) shared by - the MVF and SVF $X_n(t)$ via the random sampling of the best candidates for C_r. The choice of these candidates is performed in regions of the C_r domain suggested by $-\overline{\nabla}_{C_r} F$, where F is a function that evaluates the distance between the results of MVF and SVF or between the results of MVF, SVF and a model (in case of artificial tests where $X_n(t)$ is known) and $-\overline{\nabla}_{C_r}(...)$ is the gradient computed in the C_r domain.

Figures (8.6) and (8.7) show the evolution of the converging process for the test case *Cr1* (presented in section 3.2.2 of Paper 1 and explained in this thesis in section (10)). In particular Figure (8.6) shows the evolution of both the mean value and the standard deviation (error bars) of the populations representing each components of C_r at each iteration. It can be observed that the algorithm finds quasi stable values for $D_{lim,SVF}$, $D_{lim,MVF}$, K_{1D} and K_{d_tB} after, respectively, the iteration number 10, 30, 10 and 5. Nevertheless the stability of the values found is confirmed by the lowering of the error bars which means that the populations test of each component of C_r is concentrating onto a mean and stable value. From the bottom panel of Figure (8.6) it can be observed that the minimisation of the population width of K_{d_tB} candidates is much slower with respect to the other parameters. This is probably due to the presence of large amplitude noise that make difficult the discrimination of the main magnetopause current from the noise itself by means of the criterion (8.5). Nevertheless for this test case both the ΔX_n and Δt evaluation parameters have been minimised and maximised, respectively. Furthermore, many

best-C_rs suggest the same values for their components $D_{lim,SVF}$, $D_{lim,MVF}$, K_{1D} and K_{d_tB}. This affirmation can be stated looking at Figure (8.7) that shows the evolution of ΔX_n and Δt for the first five best-C_rs. It can be observed that these C_rs are characterised by the same values of ΔX_n and Δt starting from, respectively, the iteration number 50 and 20. This behaviour is in agreement to what expected since the parameters K_{1D} and K_{d_tB} that control mainly Δt stabilise after the iteration number 15 whereas the parameters $D_{lim,SVF}$, $D_{lim,MVF}$ that control mainly ΔX_n stabilise only after the iteration number 50. It is worth observing that the final selected C_r agrees quite well with what expected: the GDMC algorithm suggests relatively low values for $D_{lim,SVF}$, $D_{lim,MVF}$ (close to 0), a relatively high value for K_{1D} (close to 1) and a mean K_{d_tB} (close to 0.5, similarly to what have been chosen in the statistical study of [131] and reported in Table (7.4)).

Figure A.1 of Paper 1 shows three steps (beginning, middle and final steps) of the GDMC when applied to data probed during the *Cr2* case study. The details are given section 2.3 and Appendix A.2 of Paper 1. The movie of this minimisation is uploaded at the following link.

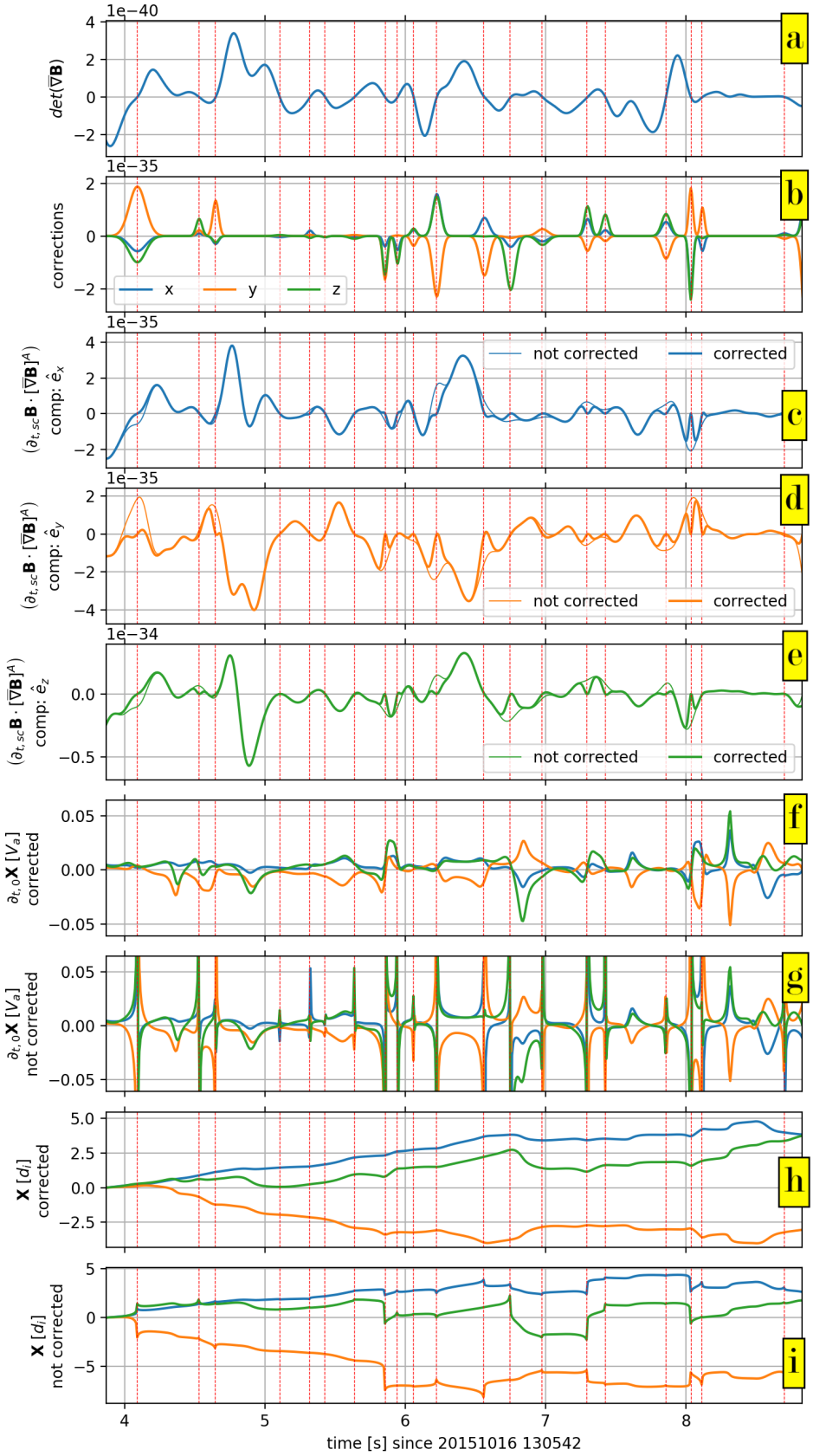

Figure 8.2: *Exemplification of the Gaussian correction introduced in section (8.2.2) for the suppression of singularities occurring to the STD method when applied to the Cr2 event. Panel a: determinant of* $\overline{\nabla}\mathbf{B}$*, i.e. the denominator of Equation (8.2); the red vertical and dashed lines are located onto the zero points of this curve. Panel b: Gaussian correction centred on the zeros of the curve shown in the top panel. Panels c, d and e: modified (thick curve) and not modified (thin curve)* x*,* y *and* z *GSE components of the numerator of Equation (8.2). Panel f: velocity of the magnetic field structure computed using the STD*$^+$ *method, i.e. the LHS of Equation (8.2) once singularities have been suppressed by means of the technique introduced in this section. Panel g: velocity of the magnetic field structure computed using the original STD method without the suppression of singularities. Panel h: temporal integration of curves shown in panel f. Panel i: temporal integration of curves shown in panel g.*

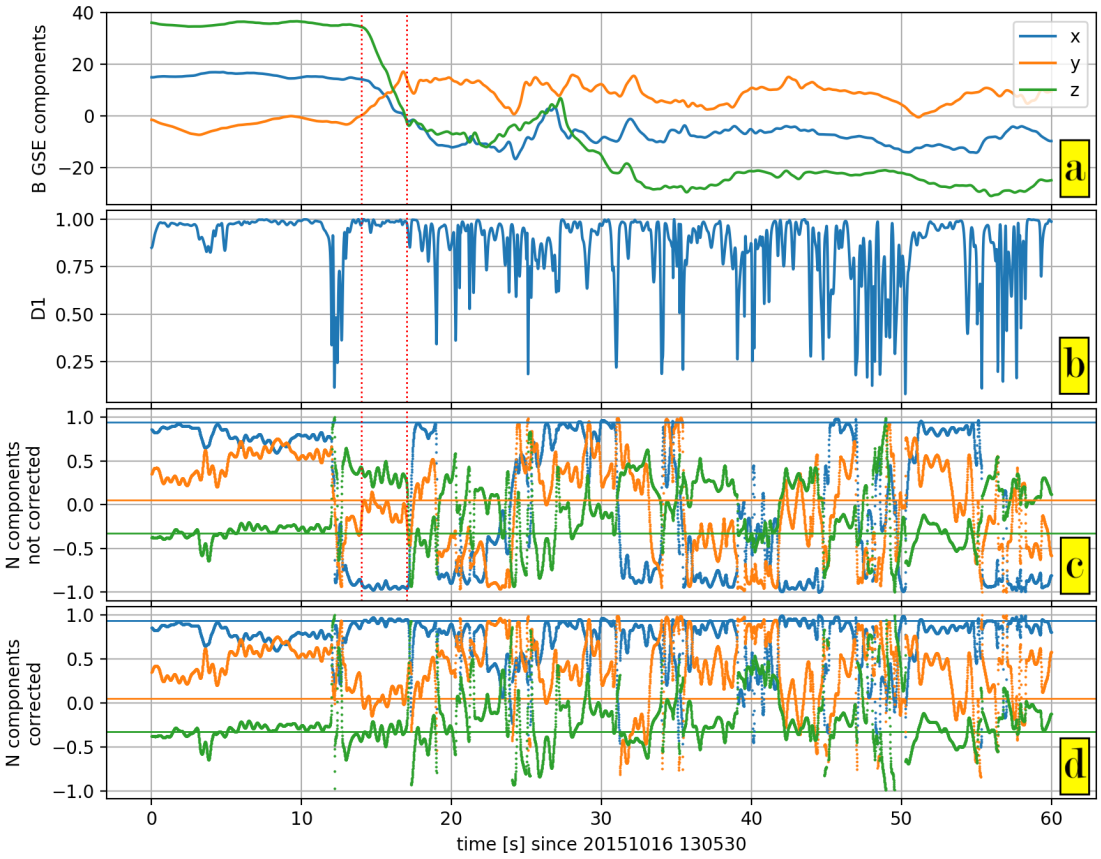

Figure 8.3: *Correction of the jumps observed on the GSE components of the MDD normal. Panel a: GSE component of the magnetic field as recorder by MMS during the Cr2 event. Panel b: D1 index showing where the magnetopause is 1D (see Equation 7.16a and [131]). Panel c: GSE components of the normal direction computed by the MDD technique [70]. Panel d: same as panel c but after the automatic correction of the jumps observed in the MDD normal components.*

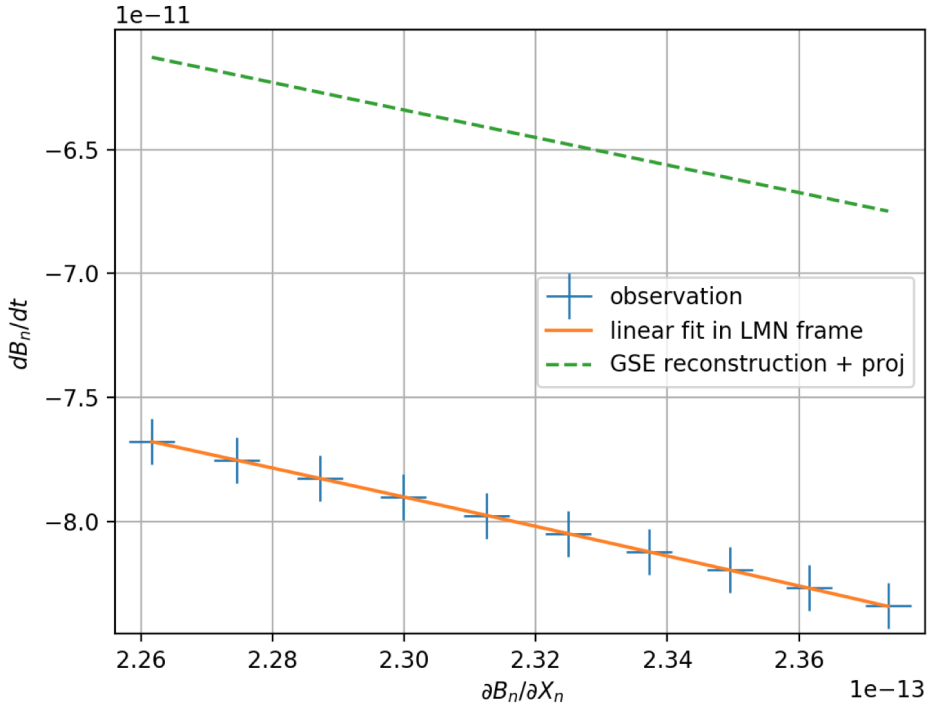

Figure 8.4: *Example of a SVF fit (orange line) performed over $p = 10$ experimental points (blue crosses) and compared to the MVF fit (green and dashed line) performed over the same period and projected toward the local normal.*

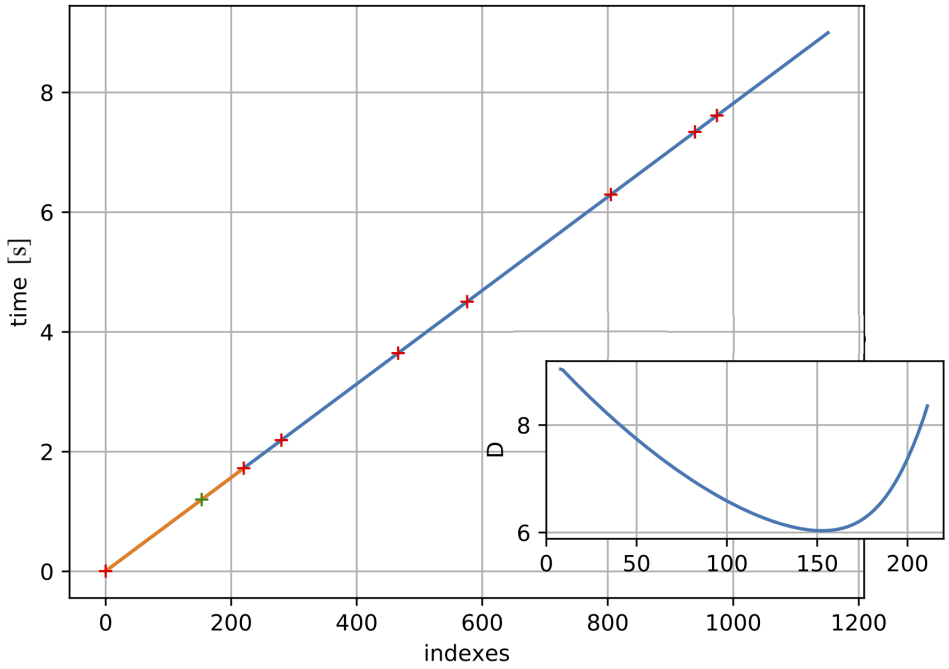

Figure 8.5: *Exemplification of the procedure for the automatic choice of the fit periods used in the SVF and MVF methods. Background plot: visualisation of a $\sim 9s$ long period ideally symbolised by the relation between the time (y axis) and the data sample numbers (x axis) recorded during that time period. Red "+" superposed to the blue straight line are fit boundaries already fixed. The orange interval at the bottom left corner shows the sub-interval under examination. The green "+" is a new fit boundary that has been individuated by the algorithm. Inset to the background figure there is a panel showing the error D as a function of the common point between the two linear fits with which the algorithm has fitted data in the orange sub-interval. The point of minimum for the curve $D(i)$ is the position of the green "+".*

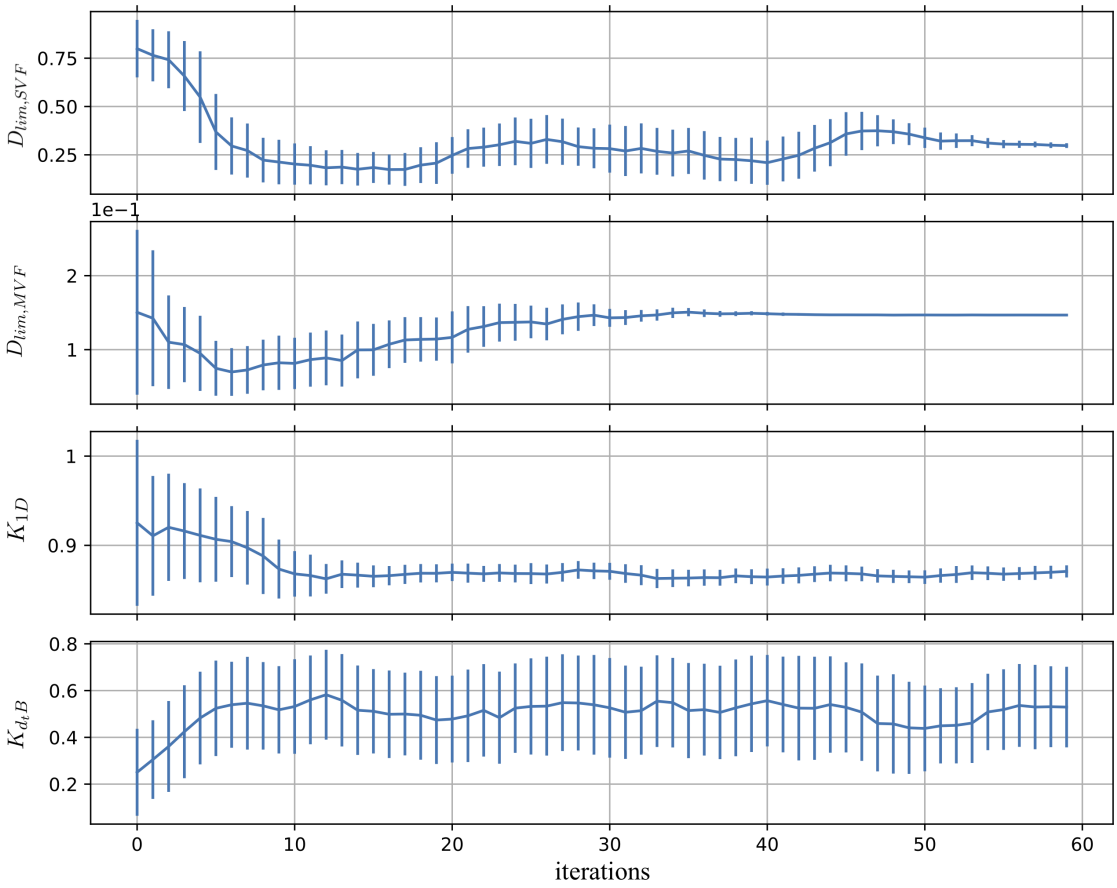

Figure 8.6: *Evolution of the mean value and the standard deviation (error bars) of the populations representing each components of C_r as a function of the iteration number of the GDMC algorithm.*

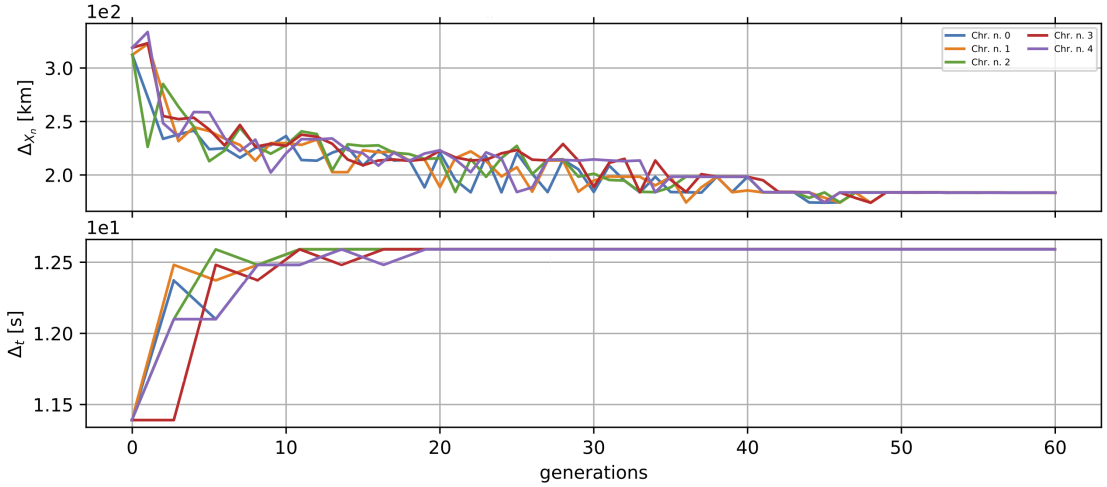

Figure 8.7: *Evolution of the distances ΔX_n and Δt between the SVF and MVF outputs for the first five best-C_rs as a function of the iteration number of the GDMC algorithm.*

Chapter

9 Application of the methods to artificial magnetic fields

Chapter content

The methods described in section (8.2) are tested on artificial signals modelling the Earth's Magnetopause. The following two sections will describe how the artificial signals have been modelled and the results of the tests. In Paper 1, the detailed description of these tests can be found in section 3.1.

9.1 The characteristics of artificial signals

9.1.1 The main magnetopause structure

Since we want the MVF and SVF methods to reproduce results given by similar routines (STD$^+$), the tests are designed to mimic spacecraft crossings during stationary southward IMF conditions. In these conditions the magnetic field (which is the best measured quantity provided by MMS and, therefore, the best candidate to be used with real data) is interested by a large jump ($\sim 40nT$) in passing from the magnetosheath to the magnetosphere. It means that a large amplitude current flows tangential to the magnetopause. These conditions allow the first term of the RHS of Equation (8.1), *i.e.* $\partial_{t,0}\mathbf{X} \cdot \overline{\nabla}\mathbf{B}$, to be larger than the second term, *i.e.* $\partial_{t,0}\mathbf{B}$.

The spatial dependence of the artificial magnetic field ($\mathbf{B}_{\text{model}}$) is modelled by $tanh(...)$ functions, properly modulated and shifted in order to fit at their best the MMS observations (see Equation 10 of Paper 1). The argument of the $tanh$ functions depends only on one direction (let's say x) in order the magnetopause orientation to be known. Then, it is normalised by a factor $1/L$ to mimic the magnetopause thickness. In this case the magnetopause thickness is equal to $\sim 6L$, if one define the thickness as twice the distance where each component of the current ($\partial_x(\mathbf{B}_{model})$) falls to 1% of its maximum value, *i.e.* twice the distance x^* where $L\partial_x(\tanh(x^*/L)) \simeq k^*$ with $k^* = 0.01$. By means of red and dashed vertical lines, Figure (9.1) shows the locations where the current (orange curve, derived as the derivative of the blue curve which represents the magnetic field) falls to 1% of its maximum value. In the same figure, the black and dashed vertical lines represent the location where the current falls to 10% of its maximum value; the reason for these lines will be explained soon.

The difference in the artificial magnetic field measured by different spacecraft is obtained allowing the four virtual satellites to encounter the artificial magnetopause 10 km apart from each other (remember that MMS is composed by four satellites orbiting around the Earth in

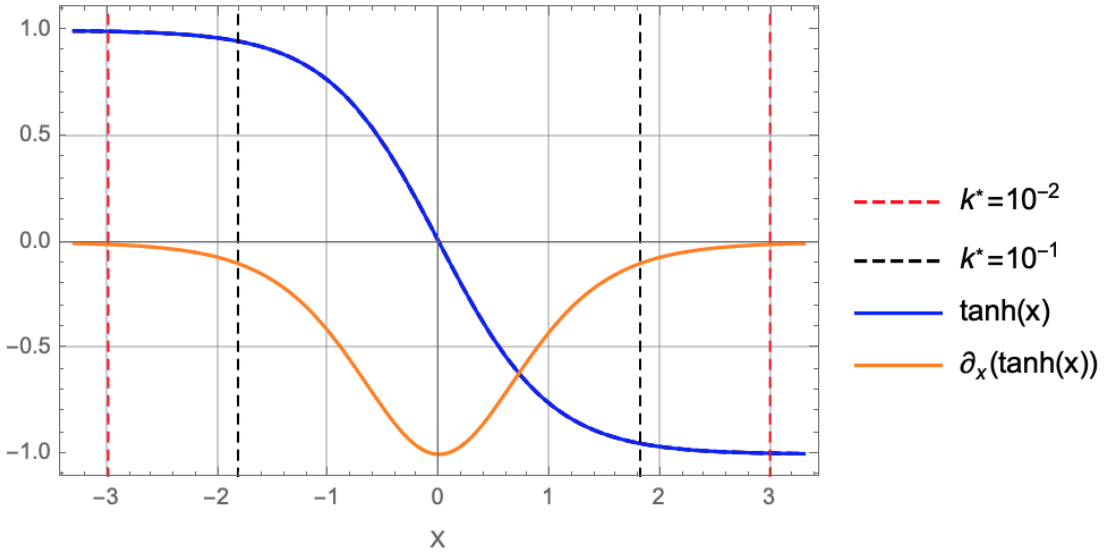

Figure 9.1: *Visual relation between the function tanh(x) (blue curve, used to model the magnetic field in tests), its derivative (orange curve) and the places where its derivative falls to* 1% *and* 10% *(added for future references) of its maximum value (pointed out by respectively the red and black vertical dashed lines).*

a tetrahedron formation, 10 km apart). Each virtual spacecraft measures therefore a slightly different magnetic field.

9.1.2 The artificial noise

The "noise" is designed to model all the waves and turbulence always present in magnetopause measurements, and which have typically amplitudes much larger than the instrumental errors [40]. This noise is superposed to the artificial magnetic field and, in real data, it is observed as a small scale fluctuations that remain after the filtering procedure (discussed in section 15). Its amplitude and spectrum have been chosen to mimic the observed one. Figure (9.2) shows an example of the subdivision between the large scale fields (also called "trend" in the legend), the high frequency noise filtered away by the filtering process and the remaining waves and turbulence fluctuations. In particular the figure shows in the top panel the GSE B_z component of the magnetic field recorded by MMS during the *Cr2* case study in green, orange and blue curve accordingly to the cut frequency ν_c that has been applied and in the bottom panel the associated spectra. The trend has been defined as the signal composed by the Fourier components associated to the $0Hz \leq \nu \leq 0.5Hz$ interval whereas the high frequency noise is defined as that part of the signal having frequency components above $\nu_c = 3Hz$. Accordingly, the $0.5Hz \leq \nu \leq 3Hz$ Fourier components define the remaining waves and turbulence fluctuations (red spectrum in the bottom panel of the figure). Once added to $\mathbf{B}_{\text{model}}$, the inverse Fourier transform of the artificial waves and turbulence fluctuations spectrum takes part in shaping an artificial signal (red curve in the top panel of figure (9.2)).

For the test signals in the two following examples (section (9.2)) the noise parameters (amplitudes and spectrum shapes) have been chosen differently. Nevertheless, in both cases the amplitudes remain compatible with the observations and the spectrum decays at frequencies above ν_c, the upper frequency limit above which the MMS data are filtered. In particular, the second example (section (9.2))) contains more large scale variations, mimicking the possible large scale evolution of the magnetopause.

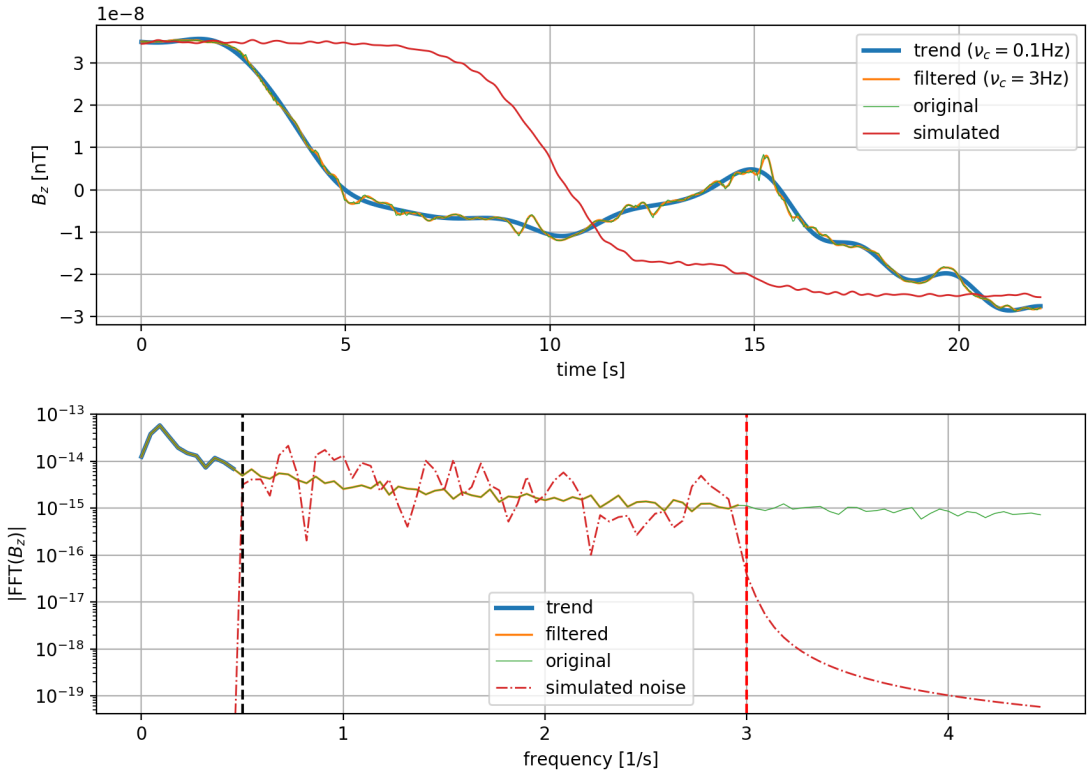

Figure 9.2: *Example of discrimination in signals (top panel) and respective spectra (bottom panel) between the large scale fields (blue curves), waves and turbulence fluctuations (orange curves) and high frequency noise (green curves). In this case the intervals defining these components are, respectively,* $0Hz \leq \nu \leq 0.5Hz$, $0.5Hz \leq \nu \leq 3Hz$ *and* $\nu \geq 3Hz$. *Red curves refers to the waves and turbulence fluctuations artificially created.*

9.2 Tests on artificial crossings

The following tests have been applied to STD*, SVF and MVF techniques:

- **Straight crossing**
  The first test simulated a straight crossing travelled at constant velocity. In this case the magnetopause planar surface is oriented toward the x direction and it is designed to have a thickness of $\sim 18d_i \sim 1500km$. The application of the MDD technique to this artificial current sheet confirms the orientation ($N_{MDD} \simeq \{0.99, -0.02, 0.02\}$) which differs only slightly from the expected $\{1, 0, 0\}$ due to the artificial noise. Figure 3 of Paper 1, panel c, shows the displacements $X_n(t)$ found by the three methods. Panel d shows the differences between each pair of $X_n(t)$. Since this crossing is artificial, this panel can show the differences between each $X_n(t)$ and the spacecraft trajectory model (this can not be done in real crossings). The figure shows also the artificial magnetic field (panel a) and the associated current (panel b). From that figure several observations can be made. Section 3.1.1 of Paper 1 explains in details these points. Here, it is worth noticing that the methods give the expected magnetopause thickness (see panel c) and that the errors between the different X_ns are lower than 1% of the magnetopause thickness in the spatial interval corresponding to the magnetopause current (the black and dashed horizontal line in panel d represents the inter-spacecraft distance which is $\sim 0.7\%$ of the magnetopause thickness). Out of this interval the methods stop working as expected, since $\overline{\nabla}\mathbf{B} \rightarrow 0$. There, the results should be ignored. Nevertheless, from panel c it can be observed that out of the magnetopause sheet, the SVF and the MVF agree quite well with each other and both regularly depart from the model whereas the STD* (which has no way to control $\partial_{t,sc}\mathbf{B}$ where $\overline{\nabla}\mathbf{B} \rightarrow 0$) shows large and irregular departures from the model.

- **Back and forth crossing**
  Figure 4 of Paper 1 shows the results from a test closer to the observations. In this tests the magnetopause thickness is reduced to $\sim 6d_i \sim 420$ km, the noise amplitude is enhanced and a back and forth motion of the magnetopause is simulated originating stagnation points. Such motion is close to those observed (remember the spacecraft trajectories of figures 4.6 and 6.4). Details are given in section 3.1.2 of Paper 1. In contrast to the previous claims, the enhancement of the noise makes the range of applicability of the three routines smaller than $6L$ and the total magnetopause thickness is underestimated. For this reason panel c of Figure 4 of Paper 1 shows a spacecraft trajectory ~ 0.6 times smaller than what expected. It is clear that this under-estimation is just due to the definition of the magnetopause thickness that has been used and which becomes incompatible with the relatively high noise used in this case. In particular, defining the magnetopause thickness as twice the distance at which the asymptotic current falls to 10% of its maximum value (remember the black dashed vertical lines in Figure (9.1)), the expected magnetopause thickness is $3.6L = 252$ km, which is equal to what is found. This must be kept in mind for future studies.

Chapter

10 Data as a function of space

Chapter content

As one may guess observing Figures (6.1) and (6.2), on 16/10/2015 MMS crossed many time the magnetopause. Between 10:36:55 and 10:37:50 UT, a crossing occurred that shows particular aspects worth considering in order to understand how the analysis of spacecraft data as a function of time can be misleading and therefore why the projection of data in space is fundamental. Between 13:05:30 and 13:05:60s UT, MMS recorded the *Cr2* event. Some of the details of this event have been already shown in the previous sections in order to justify the need for new methods relaxing some of the assumptions usually made in spacecraft data analyses. In GSE coordinates, the *Cr1* event occurred at $[9.3, 7.4, -0.6]R_E$ and the *Cr2* event occurred at $[8.3, 8.5, -0.7]R_E$. Figure (10.1) shows the locations of *Cr1* and *Cr2* in the Earth-magnetopause system. Both the crossings occurred when the IMF was southward so that there was a clear rotation of the magnetic field within the magnetopause (see for instance the hodogram in Figure (10.4)).

10.1 Case study $Cr1$: spatial profiles compared to time series

The analysis of this event is shown in Figure 9 of Paper 1. The figure shows two columns of plots showing the same data for each row. The difference is that the quantities on the left are plotted as a function of time, and the quantities on the right are plotted as a function of space. The crossing last ~ 20 s and the three $X_n(t)$ resulting from the SVF, MVF and STD$^+$ methods showed no particular differences. Therefore, during this crossing, the assumption of stationarity can be considered mostly valid. Figure (10.2) shows the $X_n(t)$ curve resulting from STD$^+$ and used as x coordinate to plot data in the right panel of Figure 8, Paper 1.

The reader interested to quantitative considerations is addressed to section 3.2.2 of Paper 1. Here it is worth considering the qualitative aspects. The first observation is that the spatial profiles of temperatures and ion bulk velocity (panels c, d and e of Figure 8, Paper 1) are more monotonic than the same profiles visualised as a function of time. No reasons are known why the profiles across the magnetopause should be not monotonic; the spatial visualisation of data is considered therefore the more natural and correct between the two visualisations. The spatial visualisation helps in better determining the spatial extension of the mixing layer since the spectrogram maxima (the black curves superposed to spectrograms) overlap in a well defined interval. Finally, comparing the bottom panels (electron bulk velocity) it becomes clear that MMS crossed multiple time a single electron beam (observable between $X_n = 200$km and

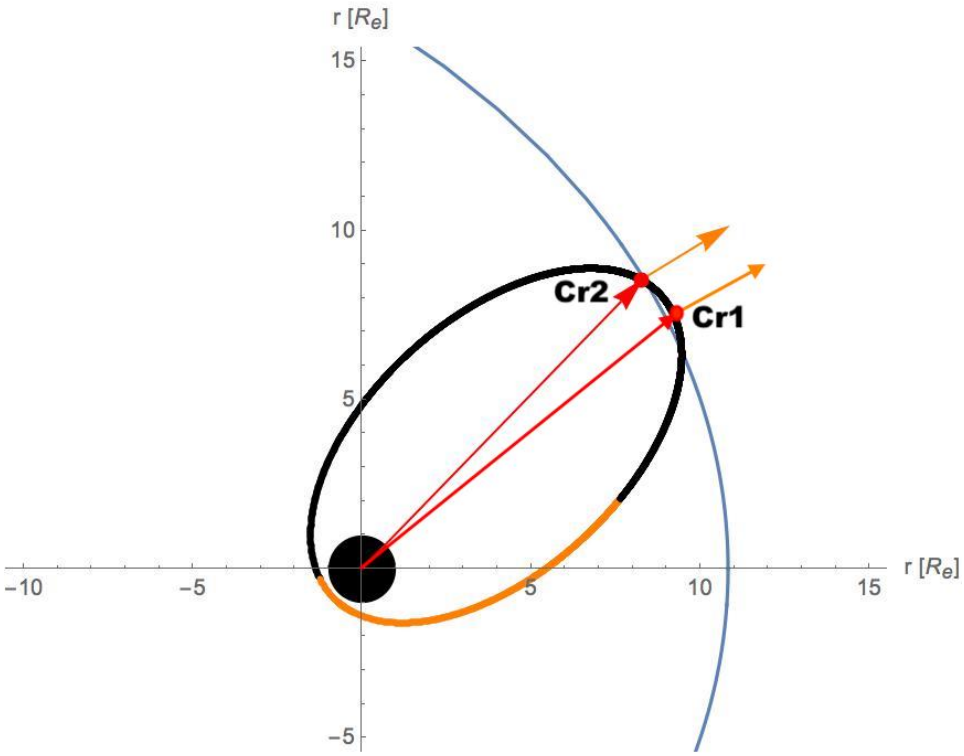

Figure 10.1: *Scheme of the Earth-magnetopause system showing the orbit of MMS during 16/10/15 in the GSE frame. Black (orange) points lie below (above) the equatorial plane. The blue curved line represents the position of the magnetopause computed with the Shue model [46]. The orange arrow is the normal to the Shue model at the Cr2 event (red point).*

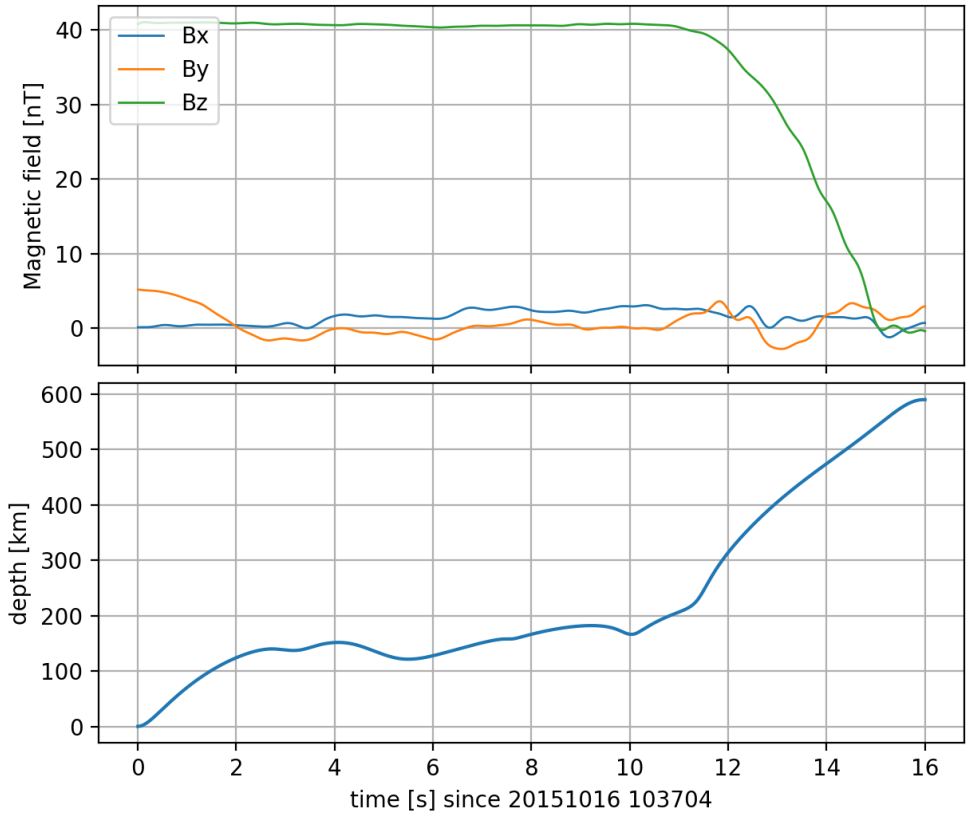

Figure 10.2: *Plot of the $X_n(t)$ coordinate resulting from STD^+ (bottom panel) temporally aligned with the magnetic field recorded during the Cr1 event.*

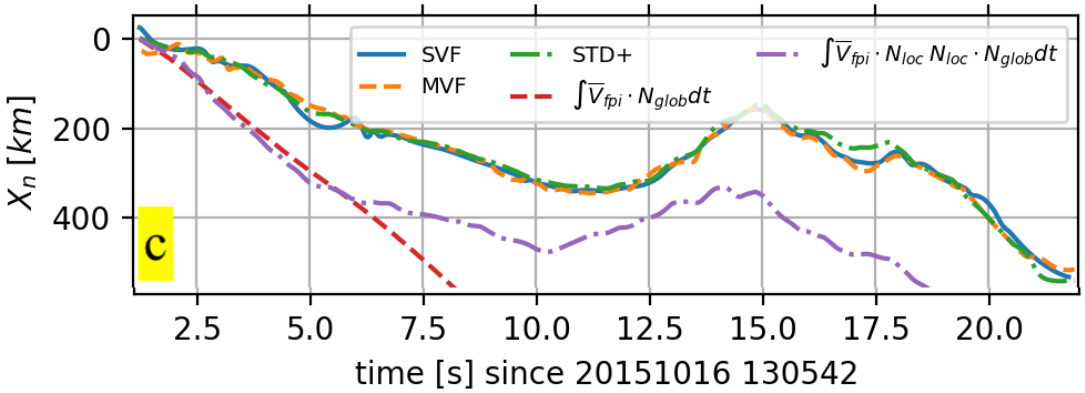

Figure 10.3: *Comparison between the $X_n(t)$ coordinates resulting from the application to the Cr2 event of SVF (blue curve), MVF (orange curve), STD$^+$ (green curve), and the direct integration of the normal component of the ions bulk velocity as projected toward the local normals (purple curve) and the global normal (red curve).*

300km) whereas, if observed in time, the electron beam signature appears to be caused by different multiple beams.

10.2 Case study $Cr2$: 1D and 2D projections of the MMS path

10.2.1 The 1D projection

The $Cr2$ crossing is very well known in the literature [112, 116, 118, 131] since it is a crossing interested by a close reconnection event which is very interesting to the magnetic reconnection community. The reconnection outflow velocity, reaching a maximum of ∼350 km/s near the *Cr2* event, prevents determination of the normal displacement $X_n(t)$ from integration of the normal component of the bulk velocity, since the inaccuracies in the determination of the normal direction (< 5 degrees) can cause the integration to yield an erroneous large normal flow. It is therefore a good test case to benchmark the new STD$^+$, SVF and MVF methods. Results are shown in Paper 1, section 3.2.1. Figure (10.3) shows a panel extracted from Figure 5 in Paper 1. In this panel the $X_n(t)$ resulting from five different methods are compared.

The displacements from the SVF and MVF methods ($X_{n,SVF}(t)$ and $X_{n,MVF}(t)$) agree within a few percent with that of the STD$^+$ method $X_{n,STD^+}(t)$ and their differences stay around the inter-spacecraft distance (see Paper 1, Figure 5, Panel d). Therefore, the magnetopause does not show any significant non-stationary behaviour. This can be observed also in Paper 1, Figure 6, where we observed that the $\partial_{t,0}\mathbf{B}$ term of Equation (8.1) - used only by SVF and MVF and not by the STD$^+$ method - is very small in comparison to the other terms of Equation (8.1). On the other hands the displacements found by integrating the normal component of the ions bulk velocity does not agree with the previous methods. This integration yields unusually large magnetopause thickness, which are not observed by other studies ([112]). By the way, it is worth noticing that the integration of the local projection of the bulk velocity (as introduced in section (8.3.1)) is closer to $X_{n,SVF}(t)$, $X_{n,MVF}(t)$ and $X_{n,STD^+}(t)$ with respect to the integration of the normal component of the ion bulk velocity resulting from a direct projection toward the global normal. This suggests that the deviations of the local details of the magnetopause from the global aspects may be fundamental. A further confirmation about the correctness of the $X_{n,SVF}(t)$, $X_{n,MVF}(t)$ and $X_{n,STD^+}(t)$ curves comes from the evaluation of the flow normal to the magnetopause. This evaluation is proposed in Paper 1, Figure 6, Panel e and it is reported in Figure (10.4) for a convenient comparison with the hodogram shown in Paper 1, Figure 4.

Since the *Cr2* crossing shows a non negligible B_n magnetic field component (see Paper 1,

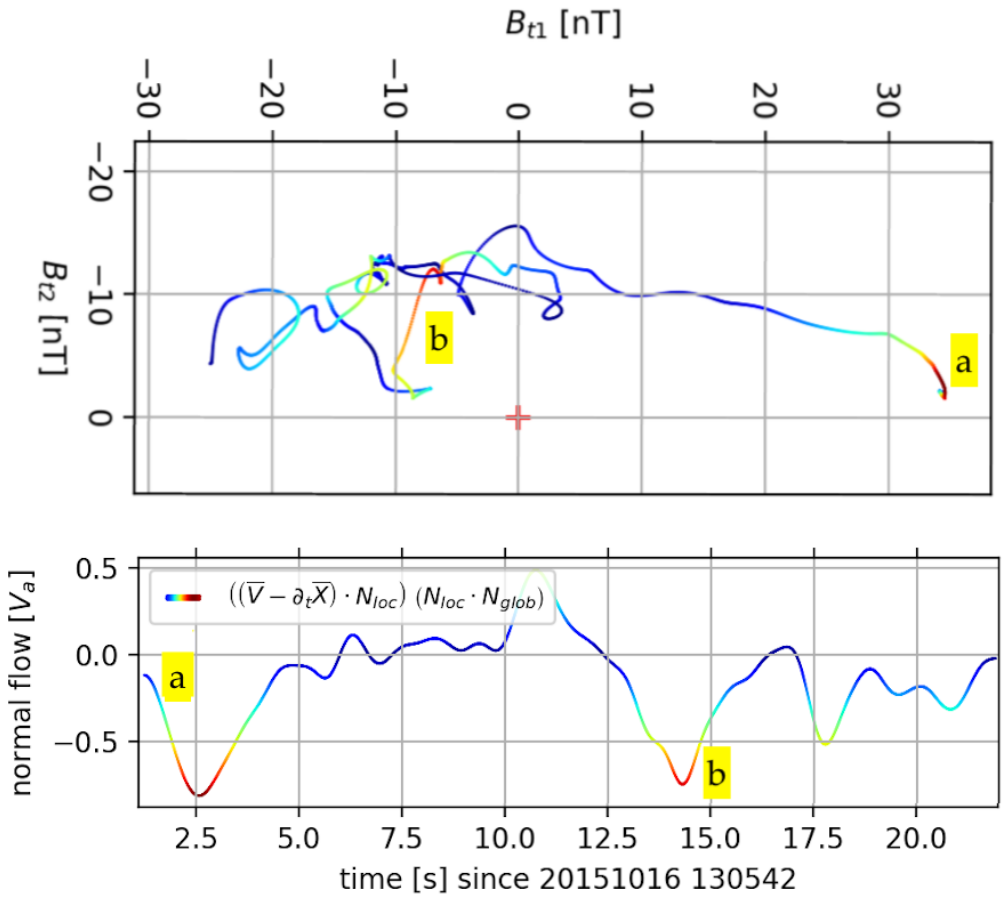

Figure 10.4: *Hodogram (top panel) and normal flow (bottom panel) computed for the Cr2 crossing. The color code in both figures refers to the magnitude of the normal flow crossing the magnetopause normalised to the local Alfvén velocity. The corresponding points in the two panels are labelled by equal letters.*

Figure 5, Panel a), the magnetopause is not a tangential layer and a non-negligible normal flow must be present (remember section (4.3)). The bottom panel of Figure (10.4) shows the normal flow across the magnetopause. It is computed as $[(\mathbf{V}_i - \partial_{t,0}\mathbf{X}) \cdot \mathbf{n}(t)]\,(\mathbf{n}(t) \cdot \mathbf{N}_{glob})$ and it is normalised point-by-point to the normal component of the local Alfvén speed $V_{a,n}$. The colour code of this curve indicates its magnitude. The hodogram in the top part of the same figure has been drawn with the same colour code. Comparing this panel with the superposed hodogram, it can be observed that the normal flow tends to reach $\pm V_{a,n}$ values (red intervals) everywhere the magnetopause sub-structures tend to be purely rotational (see the corresponding red intervals in the hodogram), which a quite satisfying result.

10.2.2 The 2D projection

For *Cr2*, the MDD eigenvalues ratios λ_m/λ_n and λ_l/λ_n (with $\lambda_n > \lambda_m > \lambda_l$) oscillate around, $1.2 \cdot 10^{-1}$ and $9.5 \cdot 10^{-3}$, respectively. The first and the second ratios are larger than 10^{-1} and 10^{-2} for, respectively, 37% and 19.5% of the selected time interval. These considerations suggest that the magnetopause shows a 2D structure for an interval large enough to a 2D reconstruction of the spacecraft path to be meaningful. The result of the computation has been shown in Paper 1, Figure 7. The figure shows on the right the 2D spacecraft trajectory obtained automatically by our MVF technique applied on a small interval of the *Cr2* event (within 13:05:42 UT - 13:06:04 UT). The trajectory is shown in comparison with the hand-made sketch inferred from the MMS observations in combination with a 2D PIC numerical simulation [112] (on the left) and a hand-made sketch suggested by the relative direction of the MDD normals with respect to the local magnetic field and the Shue model [46] (central sketch). The automatic reconstruction by MVF confirms the back and forth motion suggested by [112] and suggest a more complex motion of the spacecraft relative to the magnetopause than that suggested by the hand made sketch of [112]. Finally, both the automatic reconstruction and the central sketch show a opposite curvature in contrast to the expected global curvature of the magnetospheric boundary. This confirms that at small scales (tenths of km) the magnetopause characteristics can deviate from the global ones.

Part III

A 3fluid model for studies on mixing plasma systems

Chapter

11 The state of the art of the multi-population models

11.1 Introduction

The solar wind - magnetosphere boundary, called magnetopause, is a region where magnetic and velocity shears as well as jumps in density and temperature are observed. These inhomogeneities are the sources of many plasma instabilities developing on different space and time scales [34], in turn often triggering themselves secondary instabilities at smaller scales. As an example, secondary instabilities such as e.g., magnetic reconnection or Rayleigh-Taylor instability can efficiently develop on the shoulder of the primary Kelvin-Helmholtz instability at low latitude magnetosphere, see [81], [122] and references therein.

All of these phenomena can cause significant entering of magnetosheath plasma mass [45], momentum [15] and energy [26] into the magnetosphere. The study of the magnetopause is of particular interest since this system offers the unique opportunity to study a two-plasma large-scale interaction in conditions not achievable in laboratory. The magnetopause physics is also of basic importance in the studies addressing the Sun-Earth interaction, in particular concerning the impact of solar wind disturbances on the terrestrial environment and the attempts of space-weather forecasting (see for instance [111]). The question of modelling space plasmas using data provided by multi-spacecraft missions has been much developed during the Cluster era [47]. Concerning the magnetopause data, one of the key points concerns the mixing between magnetospheric and magnetosheath plasmas and the resulting non-Maxwellian shape of the distribution functions (hereafter d.f.) observed in these regions ([59], [61], [68], [69]). These d.f. are basic references for reconnection kinetic simulations ([58], [83], [89]). Some of the d.f. observed in simulations can be compared with simple analytic models as in the pioneering work by [36].

Since the populations belonging to the two different sides of the magnetopause differ in density and temperature, modeling the mixing requires at least the use of a multi-population model. In the perspective of investigating the dynamics of the magnetopause mixing layer by 3fluid numerical simulations, the main goal of this chapter is to build up a 3fluid analytical model (section (12.2))) and a 3fluid plasma equilibrium (section (12.3)) as realistic as possible for initializing the numerical simulation (whose results are shown in section (IV)).

Several multi-population models trying to simulate the plasma exchanges between magnetosheath and magnetosphere have been developed in the past.

1. The kinetic models assume a Vlasov equilibrium for ions and in some cases also for electrons. Such models are very complicated so that the authors are lead to make simplistic mathematical assumptions for choosing the initial Vlasov equilibrium, hopeless to get close to magnetopause data for the physical parameter profiles, as for instance the magnetic field or the ion first moments. Furthermore, these models involve many free parameters even in the simplest limit of a plane and tangential layer (*i.e.* without a normal magnetic field: $B_n = 0$). In particular there is no constraint for fixing the initial electric field profile of a tangential discontinuity in these approaches. Note also that all the equilibria built via d.f. that are functions of the particle invariants of motion only ([22]) can not really

be considered as "multi-population" models: they ignore the questions of accessibility and they can therefore not distinguish between particles of magnetospheric or magnetosheath origin. Some recent models (see [93] and [108] and references therein) allow to partly solve this problem. In these models, a few profiles can be fixed in a realistic way. However, all the other profiles still depend on simple mathematical assumptions, which are arbitrary, so that they are still far from being realistic.

2. For the PIC simulations, the lack of realistic equilibria in the literature makes difficult the initialization of the magnetopause studies. However, the multi-population character of the medium has been taken into account in a recent paper [121] addressing the influence of hot and cold magnetospheric ions on the development of magnetic reconnection. In this paper, the magnetospheric plasma included two populations with different temperatures in order to account for cold ions present in the magnetosphere close to the magnetopause.

3. Multi-fluid models have been developed in various domains, but not for magnetopause studies. In general, these studies address multi-species studies involving chemical processes and collisions. They have been used to study planetary atmospheres ([71], [75]), the solar chromosphere [110], basic plasma physics problems (drift turbulence in [90] for instance), etc.

In the present thesis a new technique is presented to build up a 3fluid equilibrium that derives directly from satellite observations. The model assumes uni-dimensional gradients in the normal direction and a tangential boundary ($B_n = 0$) at the magnetopause. The magnetic and velocity shears are both taken into account in a realistic way. The profiles are chosen to fit at best data from the Magnetospheric MultiScale mission (MMS) [112] for which the time-to-space conversion has been performed by means of recent techniques presented in Paper 1. As it will be shown in section (IV), the method provides a cold and a hot contribution in qualitative and quantitative agreement with observations, even if the model uses, as inputs, only the global ion macroscopic moments.

11.2 The fluid codes

As explained in section (3), plasma phenomena are processes involving several order of magnitudes wide spatial and temporal scales intervals. Due to the technical limits in the computational power available, numerical simulations of plasma dynamics are limited to particular regimes intervals in temporal and spatial scales. These limited intervals do not account for the full dynamics, from fluid to the ion and electron kinetic scales. The phenomena characterized by spatial and temporal scales large with respect to those of kinetic processes (first of all, the ion cyclotron particle movement) can be described assuming a fluid regime. In this regime the pressure is assumed isotropic and velocities are assumed non relativistic. A kinetic approach is required when plasma dynamics go beyond these restricted regimes. Although the mixing processes between the solar wind and the magnetosphere involve scales down to the electron kinetic scale, a fluid approach including electron inertia and/or resistivity to allow magnetic reconnection to occur is, as a first step, sufficient to study the mixing process. Furthermore the relatively low computational cost in terms of CPU hours and memory requirements of fluid codes allows to simulate large portion of the magnetopause ("large" with respect to the magnetopause paraboloid dimensions). In this thesis the plasma dynamics across the magnetopause is therefore investigated by means of a fluid numerical code. This code is an upgrade of an existing Hall-MHD code which will be described in the next section (section (11.3)).

11.3 The original 2fluid code

The 3fluid code is based on the same structure as a previously developed 2fluid code that has been developed in Pisa. This previous code has been widely used to study the role of fluid instabilities such as the magnetopause Kelvin-Helmholtz instability and its induced non-linear dynamics (see for instance [122, 127] and references therein). It belongs to the family of the "Hall-MHD" codes: it assumes quasi-neutrality, which allows to reduce the role of electrons to determine the electric field via an Ohm's law (including the electron inertia). It is based on a set of equations which describes the dynamics of the plasma, assuming isotropic pressures and polytropic closures for the two populations, coupled with the electromagnetic fields. These equations are obtained from Equations (3.7) by means of the same procedures by which the MHD Equations (3.16) are derived. Unlike the MHD assumptions, the terms $O(m_e/m_i)$ are not neglected. Under these conditions and remembering Equations (3.13) and the definition of the current $\mathbf{J} \equiv en(\mathbf{V}_i - \mathbf{V}_e)$, the equations adopted by this code are:

$$\begin{cases} \partial_t(n) + \nabla \cdot (n\mathbf{U}) = 0 & \text{(11.1a)} \\ \partial_t(nm_i\mathbf{U}) + \nabla \cdot \left(\dfrac{n}{m_i + m_e}(m_i\mathbf{V}_i\mathbf{V}_i + m_e\mathbf{V}_e\mathbf{V}_e) + \dfrac{1}{m_i}P\right) = \dfrac{1}{m_i}\mathbf{J} \times \mathbf{B} & \text{(11.1b)} \\ \partial_t(nS_\beta) + \nabla \cdot (nS_\beta\mathbf{U}_\beta) = 0 & \text{(11.1c)} \\ \mathbf{E} + \mathbf{V}_e \times \mathbf{B} = -\dfrac{1}{n}\overline{\nabla} P_e & \text{(11.1d)} \end{cases}$$

where $\beta = i, e$ and where $\mathbf{V}_e$ and $\mathbf{V}_i$ are obtained from $\mathbf{U}$ and $\mathbf{J}$ as

$$\begin{cases} \mathbf{V}_e = \mathbf{U} - \dfrac{m_i}{m_e + m_i}\dfrac{\mathbf{J}}{ne} & \text{(11.2a)} \\ \mathbf{V}_i = \mathbf{U} + \dfrac{m_i}{m_e + m_i}\dfrac{m_e}{m_i}\dfrac{\mathbf{J}}{ne} & \text{(11.2b)} \end{cases}$$

System (11.1) is completed by the Maxwell's Equations where the displacement current is neglected. The algorithm of the 2fluid code is presented in [84]. It advances in time with a standard third-order Runge-Kutta algorithm [33]. It uses sixth order explicit finite differences along the two periodic y and z direction and a sixth-order compact finite difference scheme with spectral like resolution for spatial derivative along the remaining in-homogeneous x direction. The numerical stability is guaranteed by means of a spectral filter along the periodic y and z directions and a spectral-like filtering scheme along the in-homogeneous x direction. The code is parallelised along the periodic y and z directions [38]. The x direction has transparent boundary conditions (open boundary conditions).

Chapter

12 The 3fluid model

Chapter content

As observed in section (4.5), the MMS data show clear signatures of mixing between the solar wind and the Earth's magnetopause. In order to study the specific role that each plasma species plays in the mixing process, we have to set up a numerical code able to follow the different ion and electron populations at play in the system. The first idea was to develop a 4fluid code to take into account the variety of behaviours of ions and electrons on both sides of the magnetopause. A preliminary version of the 4fluid algorithm has been written, but it shows technical problems difficult to solve (see Annex (20)). Therefore we decided to develop first a 3fluid code.

Here we introduce the 3fluid model at the base of the corresponding numerical code. It includes two ion populations, one cold and one hot, and one electron population.

12.1 The basic equations

The continuity and ion momentum equations are derived from the first two moments of the Vlasov equation. No viscosity or resistivity is used in the model. We assume charge neutrality and we neglect the displacement current. We assume an isotropic pressures and a polytropic closure for all populations. These equations are coupled to the electromagnetic fields via the Faraday's equation. An Ohm's law taking into account the electron pressure gradient but neglecting electron inertial effects is used. The 3fluid set of equations is normalised by using the following quantities:

- B_{ref} = mean magnetic field in the magnetosheath, out of the magnetopause layer
- n_{ref} = mean ion density in the magnetosheath, out of the magnetopause layer
- $t_{ref} = \Omega_{c,ref}^{-1}$ (gyro-frequency in the magnetosheath, out of the magnetopause layer)
- $l_{ref} = d_{i,ref}$ (ion inertial length in the magnetosheath, out of the magnetopause layer)

- $V_{ref} = l_{ref}/t_{ref}$
- $E_{ref} = V_{ref}B_{ref}$
- $T_{ref} = m_i V_{ref}^2$

Using index α when all plasma populations are concerned and β when only the ion populations are concerned, the non dimensional 3fluid system of equations reads:

$$\begin{cases} \sum_\alpha sign(q_\alpha) n_\alpha = 0 & \text{(12.1a)} \\ \sum_\alpha sign(q_\alpha) n_\alpha \mathbf{U}_\alpha = \overline{\nabla} \times \mathbf{B} & \text{(12.1b)} \\ \frac{\partial n_\beta}{\partial t} + \overline{\nabla} \cdot (n_\beta \mathbf{U}_\beta) = 0 & \text{(12.1c)} \\ \frac{\partial (n_\beta \mathbf{U}_\beta)}{\partial t} + \overline{\nabla} \cdot (n_\beta \mathbf{U}_\beta \mathbf{U}_\beta) + \overline{\nabla} (n_\beta T_\beta) = n_\beta (\mathbf{E} + \mathbf{U}_\beta \times \mathbf{B}) & \text{(12.1d)} \\ \frac{\partial (n_\alpha S_\alpha)}{\partial t} + \overline{\nabla} \cdot [\mathbf{U}_\alpha (n_\alpha S_\alpha)] = 0 \text{ with } S_\alpha = T_\alpha n_\alpha^{1-\gamma} & \text{(12.1e)} \\ \frac{\partial \mathbf{B}}{\partial t} = -\overline{\nabla} \times \mathbf{E} & \text{(12.1f)} \\ \mathbf{E} = -(\mathbf{U}_e \times \mathbf{B} + \frac{1}{n_e} \overline{\nabla} (n_e T_e)) & \text{(12.1g)} \end{cases}$$

These equations are the same shown in Paper 2 and are reported here for simplicity.

12.2 The numerical implementation

12.2.1 The temporal advancing scheme for the 3fluid equations

This section aims at explaining how the equations presented in sec. (12.1) have been implemented in the numerical code. The order with which the Equations (12.1) are advanced at a specific time step t is important since some of these equations need in inputs the non-updated quantities (*i.e.* the numerical values of quantities at step $t-1$) and others need for the updated quantities (*i.e.* the numerical values of quantities at step t). Furthermore, the memory requirements needed by the code to store each quantity imposes to limit the use of temporary variables, even when running the simulation on HPC servers. In the following, the LHS term of each equation is the quantity to be updated (marked by an asterisk). The RHS terms of the equations are composed by updated and not-yet updated quantities. The RHS of the equations of state (*e.g.* Equations (12.1a), (12.1b) and (12.1g)) are solved using in their RHS terms some of the quantities just updated (and therefore marked by an asterisk). The scheme used for the temporal advancement is a third order Runge-Kutta scheme.

1. ions and electrons entropy densities:

$$n_\alpha^* S_\alpha^* = n_\alpha S_\alpha - \Delta t \, \overline{\nabla} \cdot [\mathbf{U}_\alpha (n_\alpha S_\alpha)] \tag{12.2}$$

   with

$$S_\alpha \equiv T_\alpha n_\alpha^{1-\gamma} \tag{12.3}$$

2. ion densities:

$$n_\beta^* = n_\beta - \Delta t \, \overline{\nabla} \cdot (n_\beta \mathbf{U}_\beta) \tag{12.4}$$

3. electron density:

$$n_e^* = \sum_\beta n_\beta^* \tag{12.5}$$

4. ion momenta:

$$(n_\beta \mathbf{U}_\beta)^* = n_\beta \mathbf{U}_\beta - \Delta t \left\{ \overline{\nabla}(n_\beta T_\beta) - \overline{\nabla} \cdot (n_\beta \mathbf{U}_\beta \mathbf{U}_\beta) + n_\beta \left(\mathbf{E} + \mathbf{U}_\beta \times \mathbf{B} \right) \right\} \tag{12.6}$$

5. ions and electron temperatures:

$$T_\alpha^* = [n_\alpha S_\alpha]^* \left(n_\alpha^*\right)^{\gamma - 2} \tag{12.7}$$

6. ions velocities:

$$\mathbf{U}_\beta^* = (n_\beta \mathbf{U}_\beta)^* / n_\beta^* \tag{12.8}$$

7. magnetic field

$$\mathbf{B}^* = \mathbf{B} - \Delta t \, \overline{\nabla} \times \mathbf{E} \tag{12.9}$$

8. the electron velocities:

$$\mathbf{U}_e^* = \left[\sum_\beta \left(n_\beta^* \mathbf{U}_\beta^* \right) + \overline{\nabla} \times \mathbf{B}^* \right] / n_e^* \tag{12.10}$$

9. the electric field:

$$\mathbf{E}^* = -\mathbf{U}_e^* \times \mathbf{B}^* + \frac{1}{n_e^*} \overline{\nabla} (n_e^* T_e^*) \tag{12.11}$$

12.2.2 The simulation box

Section (11.2) explained the reasons why a fluid regime has been chosen to simulate the solar wind - magnetosphere interaction across the magnetopause. We must now fix the parameters of the simulation box, *i.e.* its dimensions and the number of grid points by which it is discretized. As a first step the numerical investigation in this thesis is limited to a 2D domain perpendicular to the magnetopause surface. The box is oriented in order the magnetopause to be parallel to one of the box boundaries (let call this direction y). The curvature of the magnetopause is neglected along the other direction x and the box dimension along y (let's call it L_y) is chosen to be the maximum for this assumption to be verified ($L_y \sim 70 d_i$, see section (17) for the calculation of this value). The boundary conditions in the y direction are periodic. On the other hand the perpendicular direction (identified hereafter with the x direction) needs special care due to the open boundary conditions. The 3fluid code can not allow for the transparent boundary conditions of the original MHD code because of the different set of equations (section (11.3)). For this reason, in all simulations discussed in sections (13)) and IV, we have implemented the so-called "free" boundary conditions. In this case no constraints are imposed onto the derivatives of fluid quantities at the boundaries. This is achieved by calculating the derivatives with internal points. We take the L_x dimension as $\sim 6 - 7$ times the magnetopause current sheet width apart from the magnetopause, both sides. This allows to minimise the effects of the boundary conditions onto the plasma dynamics.

12.3 The equilibrium

Our aim is to initialise a numerical simulation with conditions as realistic as possible with respect to the *Cr2* case. In order to do so, the following considerations occur. With respect to the time scales of plasma instabilities that the magnetopause hosts, the Earth's magnetopause can be assumed as a stationary system. It is therefore necessary to initialise any numerical simulation by means of a stationary condition, *i.e.* an equilibrium. This equilibrium is discussed in section 3.2 of Paper 2; there we show how to obtain an equilibrium condition for the 3fluid representing as close as possible the observed magnetopause. The analytical approach is described in the following sub-section. The comparison between data and the 3fluid model output is presented in section (IV).

12.3.1 A general analytical approach

Assuming $\partial/\partial t = 0$, the calculation is done in three steps:

1. **fits of high quality data:**
   the magnetic field $\mathbf{B}$, the density n_i, temperature T_i and velocity $\mathbf{U}_i$ profiles are fit by analytical functions without distinguishing the cold and hot populations. Data are fitted using a combination of hyperbolic tangents. These quantities have been chosen according to their high quality (fast probing rates and small instrumental errors).

2. **derivation of low quality data:**

   - the electron density n_e and velocity $\mathbf{U}_e$ are deduced by using the equilibrium equations (12.1a) and (12.1b).
   - The temperature T_e is obtained from

   $$P_e = P_{tot} - (P_B + n_i T_i) \tag{12.12}$$

     where the total pressure, P_{tot}, is assumed to be a constant in order to fulfil the equilibrium conditions.
   - The electric field $\mathbf{E}$ is obtained from the Ohm's Law, Equation (12.1g).

3. **split of total ions in cold and hot populations:**
   The cold ion population models the ions of magnetosheath origin and disappears more and more on the magnetospheric side. Conversely, the hot population models the ions of magnetosphere origin and disappears on the magnetosheath side.

Regarding P_e (computed at point (2)), it is worth noticing that it is much smaller than $P_i + P_B$ (see Figure 2 of Paper 2 and Figure (12.1)). Furthermore, it will be demonstrated that the electron are not well measured in the magnetospheric region (see section (14.1)). Therefore, P_{tot} in Equation 12.12 is taken as the maximum of $P_i + P_B$ in order to prevent P_e to acquire negative values.

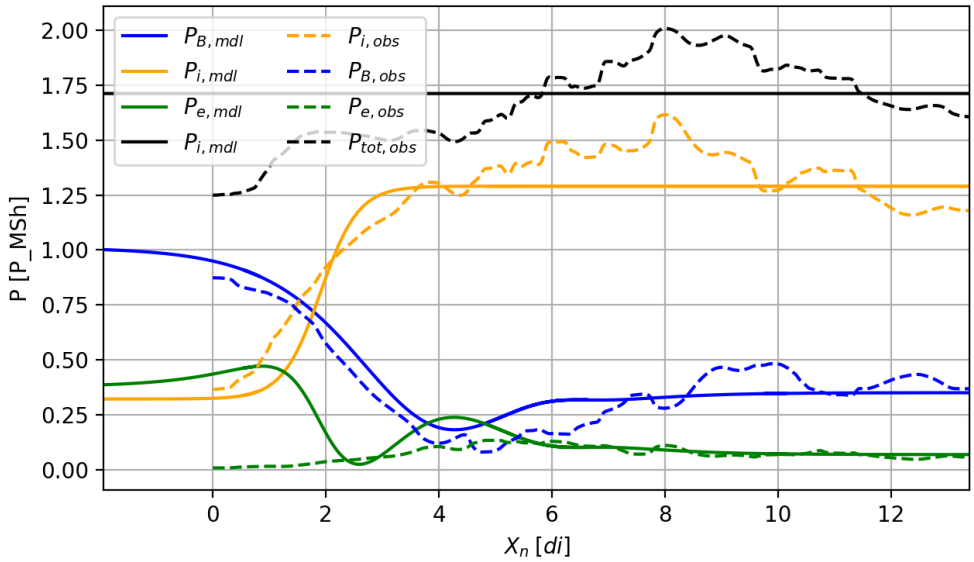

Figure 12.1: *Comparison between data (dashed curves) and the 3fluid analytical profiles (continue curves) for pressures as a function of space for the Cr2 case.*

Regarding the ion splitting into cold and hot components, we start by considering that cold and hot ion densities, currents and pressures add giving the total ion population:

- ...density:
$$n_i = n_{ic} + n_{ih} \tag{12.13}$$
- ...pressure:
$$n_i T_i = n_{ic} T_{ic} + n_{ih} T_{ih} \tag{12.14}$$
- ...current:
$$n_i \mathbf{U}_i = n_{ic} \mathbf{U}_{ic} + n_{ih} \mathbf{U}_{ih} \tag{12.15}$$

The splitting procedure is based on the following considerations:

- The temperatures of the cold and hot ion populations, T_{ic} and T_{ih}, are assumed to be constant and set to $T_{ih} = \lim_{x \to MSph} T_i$ and $T_{ic} = \lim_{x \to MSh} T_i$.
- from the homogeneity of cold and hot ion population temperatures and from the linear combination of pressures (Equation (12.14)) it can be shown (see appendix (18)) that, defining $\Gamma \equiv n_{ic}/n_i$ and $\Upsilon \equiv T_{ih}/T_{ic}$,
$$n_{ic} = n_i \frac{\Upsilon - \frac{T_i}{T_{ic}}}{\Upsilon - 1} \tag{12.16}$$
and
$$P_{ic} = P_i \left(1 + \frac{1-\Gamma}{\Gamma}\Upsilon\right)^{-1} \tag{12.17}$$
- The perpendicular currents, and by consequence the corresponding velocities, are fully determined by Equations (12.1d).

Regarding the parallel currents, they can not be determined by any equations. These are set by a reasonable choice of the ratio of the cold parallel ion current to the total parallel ion current, as seen in the electrons frame (see Equation 6 of Paper 2). In this frame the current is only due to ions and its partition can be done more easily. In general, the asymptotic values of the cold and hot ion currents are chosen in agreement with the asymptotic values of n_{ic} and n_{ih}, in order that all the corresponding values of the velocities U_{ic} and U_{ih} have reasonable values, although one of the two densities n_{ic} or n_{ih} tends to nearly zero on each side.

12.3.2 Particular considerations for the numerical implementations

The 3fluid code used here can not deal, because of computational reasons, with a population having a zero density somewhere in the domain. To avoid this technical problem, two parameters $\epsilon^{(c)} \ll 1$ and $\epsilon^{(h)} \ll 1$ are introduced in order to modify the large scale profiles in order not to reach too low values. Nevertheless, these parameters are kept small enough in order not to make the distance between model and data too large. In particular, the initialisation makes the cold and hot densities tend to $\epsilon^{(h)} n_i$ and $\left(1 - \epsilon^{(h)}\right) n_i$ on the magnetospheric side, and vice versa to $\left(1 - \epsilon^{(c)}\right) n_i$ and $\epsilon^{(c)} n_i$ on the magnetosheath side.

As a consequence of the modification of densities, the temperatures are changed accordingly (see appendix (19) for details). Indicating by T_{ic} and T_{ih} the observed values for magnetosheath and magnetospheric temperatures and by T_i^{MSph} and T_i^{MSh} the temperatures corresponding to

the magnetospheric and magnetosheath values of T_i according to the analytical 3fluid model, the temperatures are given by

$$T_{ic} = \frac{\epsilon^{(c)} T_i^{MSph} - \left(1 - \epsilon^{(h)}\right) T_i^{MSh}}{\epsilon^{(c)} + \epsilon^{(h)} - 1} \tag{12.18a}$$

$$T_{ih} = \frac{\epsilon^{(h)} T_i^{MSh} - \left(1 - \epsilon^{(c)}\right) T_i^{MSph}}{\epsilon^{(c)} + \epsilon^{(h)} - 1} \tag{12.18b}$$

Figure (12.2) shows how the $\epsilon^{(c)}$ and $\epsilon^{(h)}$ parameters affect density and temperature profiles. The panels on the left show density (top panel) and temperature (bottom panel) in the limit $\epsilon^{(h)} = \epsilon^{(c)} = 0$. It can be observed that the densities lower without bottom bounds. In this limit, a finite amplitude large scale currents would cause $\mathbf{U} = \mathbf{J}/n$ to diverge. Temperatures are not different from the values manually set ($T_{ic} = 1.0$ and $T_{ih} = 3.0$). The panels on the right show the same profiles but corrected using $\epsilon^{(h)} = 0.35$ and $\epsilon^{(c)} = 0.05$. We see that cold and hot densities reach an asymptotic limit within a few d_i from the central gradient. Temperatures are slightly modified according to Equations (12.18).

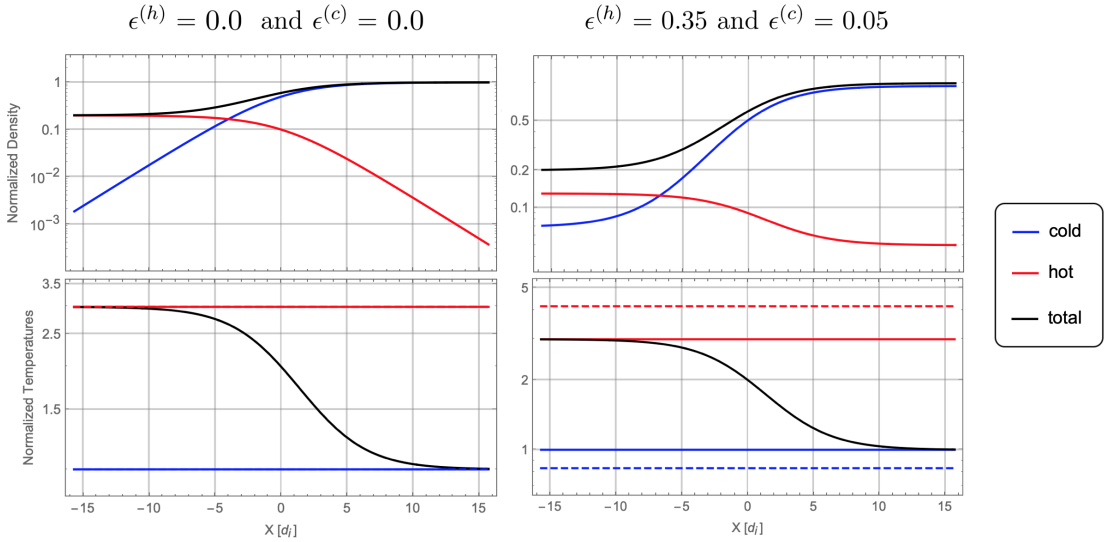

Figure 12.2: *Comparison between density (top panels) and temperature (bottom panels) profiles in case* $\epsilon^{(h)} = \epsilon^{(c)} = 0$ *(left panels) and in case* $\epsilon^{(h)} = 0.35$, $\epsilon^{(c)} = 0.05$ *(right panels).*

Finally, a similar correction is made for the ion velocities.

12.4 Resolution of numerical problems

12.4.1 The filtering

The 3fluid code filters the fields for numerical stability at high wave numbers using a sixth-order compact finite difference scheme with spectral like resolution [38]. Nevertheless, the "realistic" modelling of the magnetopause leads to a technical numerical problem on the 3fluid numerical implementation. If large inhomogeneities along the in-homogeneous x direction are presents, a finite-amplitude discrepancy between the filtered quantities and their analytical counterparts generates. Let's call "residual" these small discrepancies. Figure (12.3) shows the amplitude of the residuals for the electric field as a function of the number of points used to discretise the in-homogeneous direction $N_{pnt,x}$. Each point corresponds to a simulation having a particular value of $N_{pnt,x}$.

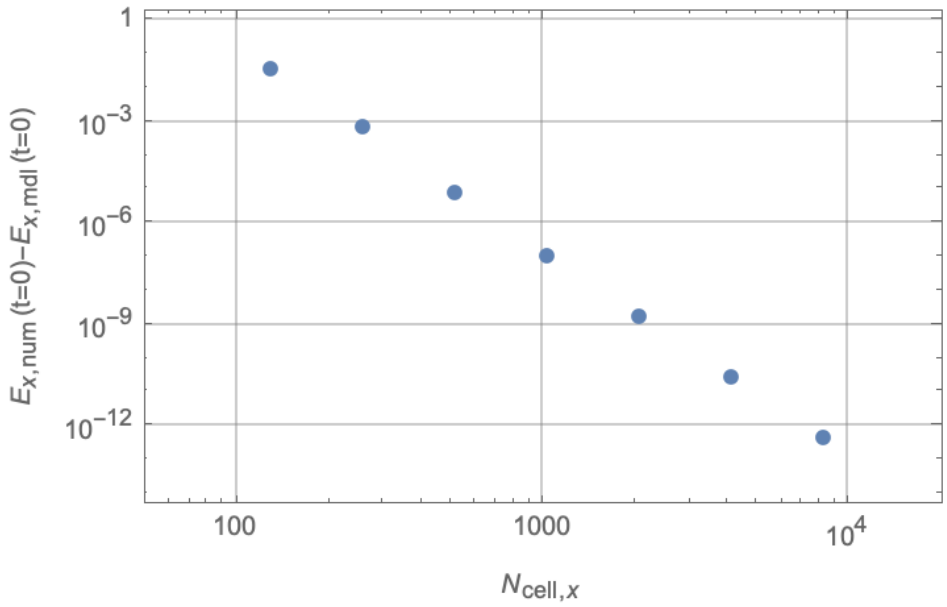

Figure 12.3: *Differences between the electric field computed by the numerical modules used by the 3fluid fortran code $E_{x,num}$ and the analytical model $E_{x,mdl}$ (Equation (12.1g)) at $t = 0$ as a function of the number of points used to discretise the in-homogeneous direction $N_{pnt,x}$.*

From the figure we see that there is a clear linear dependency (in log-log scale) of residuals by $N_{pnt,x}$. The negative slope of this curve is -6 and it is coherent with the order of the compact finite difference scheme adopted in the code.

Even if very small, this residual term is constant in time since it originates from the inhomogeneities of the equilibrium state which have, by definition, a fixed position. For this reason it accumulates in time and so it grows in amplitude. Eventually this growing artificial forcing causes numerical instabilities to appear. Figure (12.4) shows for instance the profiles for the electron, the hot and the cold ion densities (left column) recorded at three different times (the three rows) during a simulation specifically designed to verify the long standing behaviour of a 3fluid equilibrium state. The figure also shows the density perturbations (right column).

From the figure one observes that the equilibrium is modified by a growing sinusoidal perturbation localised at the equilibrium gradient. In order to avoid this artefacts one would be tempted to increase $N_{pnt,x}$ in order to decrease by order of magnitudes the residuals (see figure (12.3)). Anyway, this solution is not well suited since the increase of $N_{pnt,x}$ would impose a stronger and stronger constraint on Δt and would increase the computational cost of the simulation. In particular, for 3D simulations this solution would not be well suited. The 3fluid code presented in this thesis adopts therefore another strategy. We filter away only the perturbations by removing the mean quantities. In this way at zero order (the large-scale in-homogeneous equilibrium) the error is exactly zero. In particular, each time the filtering procedure is called, the perturbation $\Delta Q(t)$ ($Q(t)$ being a general quantity) can be obtained by subtracting to $Q(t)$ either its initial state $Q(t = 0)$ or its mean profile $< Q(t) >_\perp$. Here the mean operation $< ... >_\perp$ is the mean value along the (periodic) directions perpendicular to the in-homogeneous one. Though this solves the problem presented in Figure (12.4), it is a compromise since, regardless the method to compute $\Delta Q(t)$, this quantity does not include the large scale inhomogeneities generated non linearly (see for instance section 14.2).

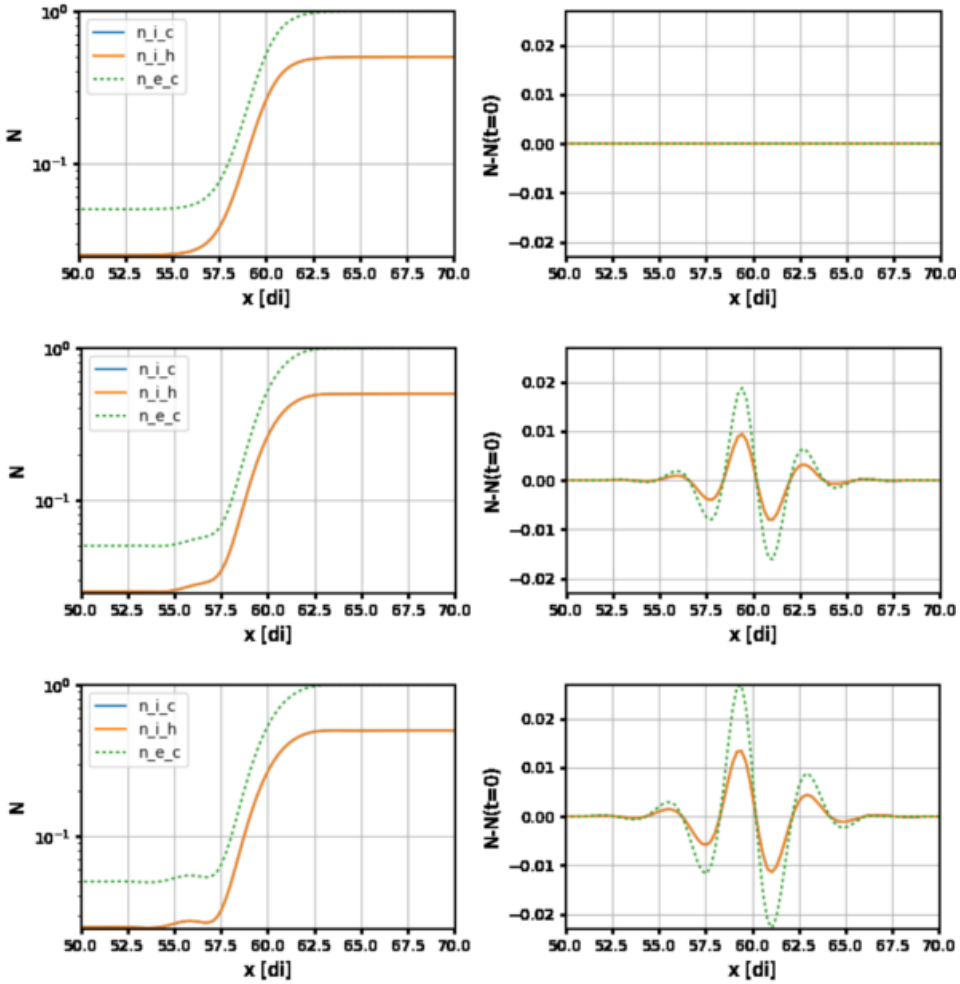

Figure 12.4: *Evolution (from top to bottom) of the electron, hot and cold ion density profiles (left column) and respective perturbations (right column) as a function of the in-homogeneous direction for a 3fluid simulation filtering both the perturbations and the equilibrium fields. The y axis is in normalised units; the x axis is in ions Debye length $d_i \simeq 70km$. All the pictures show only a small interval centred on the simulated magnetopause.*

12.4.2 Wave accumulation at boundaries

Figure (12.5) shows the contour plot of $B_x(x, y)$ at a given time for a 2D 3fluid simulation initialised by observed data and developing a reconnection mode instability. The snapshot is taken at $T_{max} = 1370\Omega_{ic}^{-1}$ when the instability growth has saturated ($T_{max} \simeq 5.5$ times the observed magnetic reconnection time growth). The simulation has been initialised with an equilibrium based on spacecraft data (see section 14) and the magnetic reconnection instability has been triggered with small amplitude magnetic field perturbations with random phase. The figure shows the shaded iso-contours of the x component of the magnetic field. The bottom and the left plot represent the curves $B_x(x, y^*)$ and $B_x(x^*, y)$ for $x^* = 120d_i$ and $y^* = 26d_i$, respectively. We observe that B_x forms a standing wave nearby the right boundary of the simulation box. This numerical effect is caused by the boundary conditions scheme to calculate the derivatives since we can not use open transparent boundaries as for the original Hall-MHD code (sec. (11.3)). The comparison between the $B_x(x^*, y)$ and the $B_x(x, y^*)$ maximum amplitudes shows that the standing wave reaches amplitudes comparable to that of the reconnection mode eigenfunction at saturation. This boundary standing wave is clearly a numerical artefact due to the accumulation of numerical noise at the boundary. This problem has been solved by introducing a localised

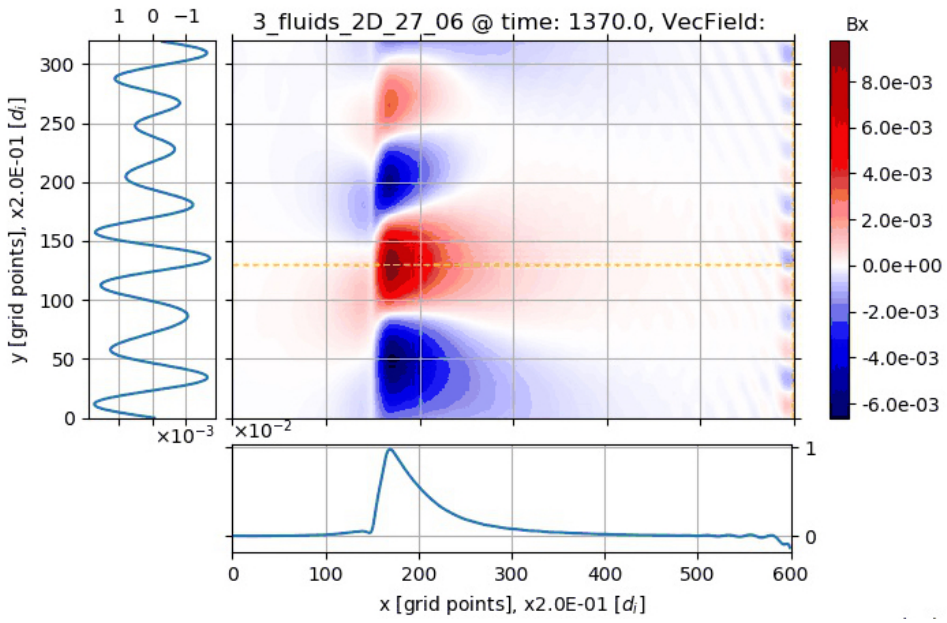

Figure 12.5: *Contour and cut plots of $B_x(x, y)$ recorded at $T = 1370\Omega_{ic}^{-1}$ during the linear growth phase of a reconnection mode instability in a 2D 3fluid simulation. The cuts (bottom and left blue curves) are $B_x(x, y^*)$ and $B_x(x^*, y)$ with $y^* = 26d_i$ and $x^* = 120d_i$. At the right extreme of the contour plot it can be observed a boundary wave. No viscous effects have been used here to show the wave accumulation at the boundaries.*

viscous term in the momentum equation (see section 12.1, Equation (12.1d)) in order to dissipate any growing wave at the boundaries. Adding this artificial viscosity, the equations for the momentum become [50, chapt.4]:

$$\frac{\partial\left(n_\alpha \mathbf{U}_\alpha\right)}{\partial t} + \frac{1}{m_\alpha}\overline{\nabla} P_\alpha + \overline{\nabla}\cdot\left(n_\alpha \mathbf{U}_\alpha \mathbf{U}_\alpha\right) - \frac{q_\alpha n_\alpha}{m_\alpha}\left(\mathbf{E} + \mathbf{U}_\alpha \times \mathbf{B}\right) = n_\alpha \nu \nabla^2 \mathbf{U}_\alpha \tag{12.19}$$

where $n_\alpha \nu \nabla^2 U_\alpha$ is the viscous term (cf. Eq. (12.1d)). In order to dissipate the fluctuations only at the simulation boundaries, the viscosity coefficient ν varies along the x direction being negligible everywhere except at the boundaries:

$$\frac{\nu(x)}{\nu_0} = 1 - \frac{1}{2} tanh\left(\frac{x - \frac{1}{2}\lambda}{\lambda/12}\right) - \frac{1}{2} tanh\left(\frac{L_x - (x - \frac{1}{2}\lambda)}{\lambda/12}\right) \tag{12.20}$$

Figure (12.6) shows the profile of the normalised viscosity (Equation (12.20)). This spatial dependence for the viscosity allows for a viscousless dynamics everywhere in the box except close to the box boundaries. In Equation (12.20) the parameter λ defines the characteristic width of the viscous regions close to the boundaries. In the case of Figure (12.6), λ is set to 15 d_i. Figure (12.7) shows $B_x(x, y^*)$ for several values of ν_0 (listed in the legend at the top left corner). From the zoom into the main figure we see that the value of ν_0 able to dissipate the boundary wave lies in between 0.05 and 0.1. Finally, it is worth observing that the reconnection mode is not affected by the viscous effect since the transverse dimension of the simulation box has been chosen large enough for the reconnection mode to vanish at the box boundaries. The viscous effect modifies therefore only the numerical artefact causing a growing standing wave at the boundaries.

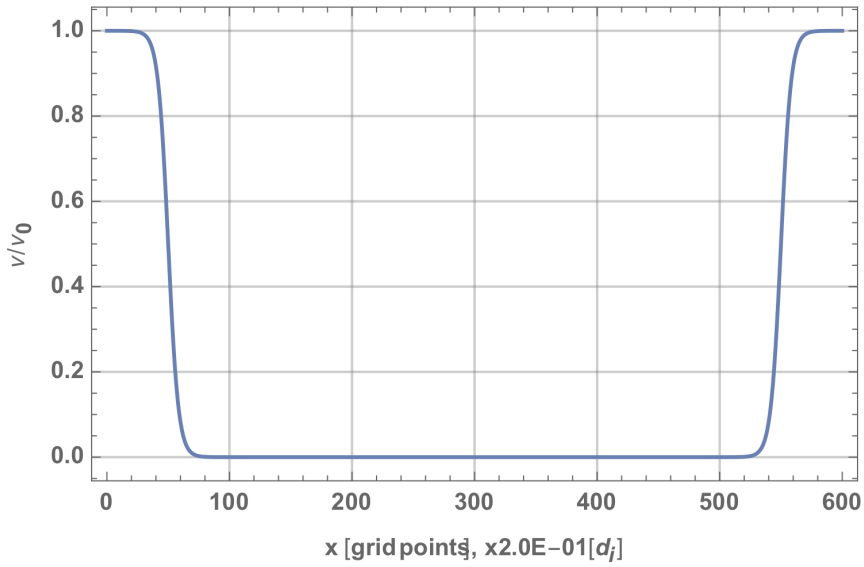

Figure 12.6: *Visualisation of the spatial profile normalised non-homogeneous viscosity adopted in the 3fluid simulations to solve the boundary wave problem described in section 12.4.2.*

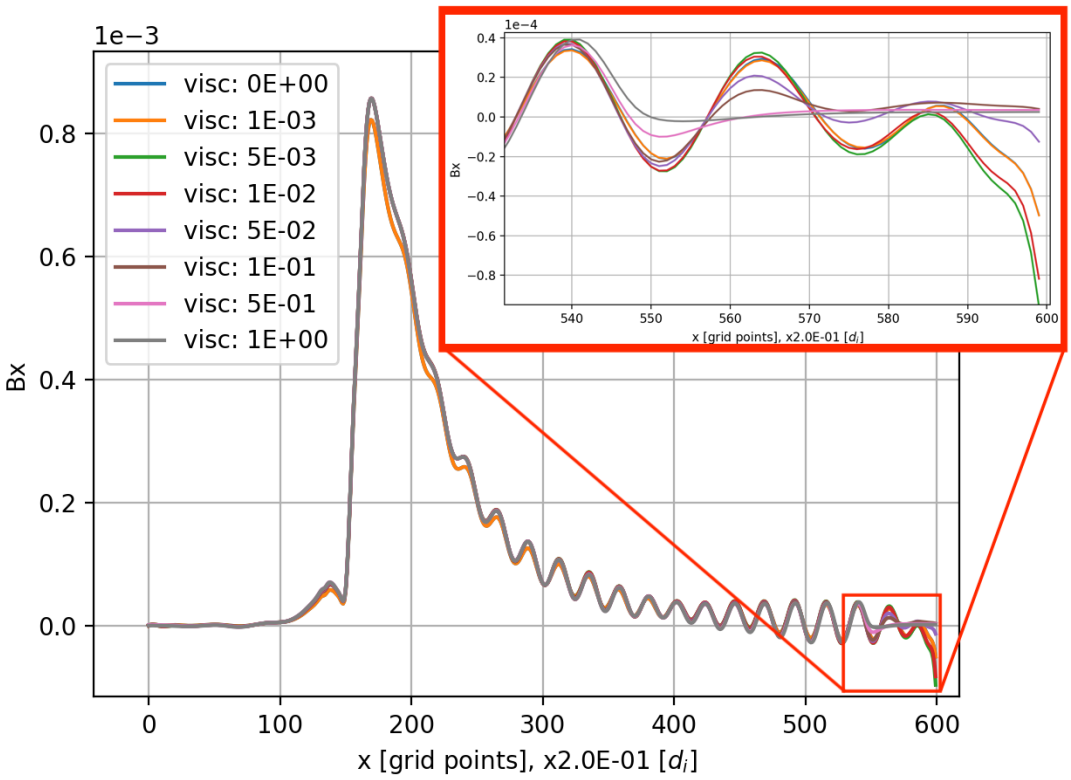

Figure 12.7: *Cuts for $B_x(x, y^*)$ with $y^* = 26d_i$ for 8 simulations adopting different values of ν_0 (Equation (12.20)). Inset to the main figure there is a zoom that helps to evaluate better the dissipation at the right boundary.*

Chapter

13 Validation tests of the 3fluid model

Chapter content

The code is tested on its ability in maintaining a time-independent equilibrium state, in simulating the propagation of simple waves and in simulating the evolution of a magnetic reconnection instability starting from a simple set up.

13.1 The time-independent equilibrium state

The zero - order test to verify the correctness of the implementation of analytical models into our numerical code corresponds to check that stable equilibrium states remain unchanged after the simulation has run for times much longer than the time scale τ over which any instability could develop. Regarding unstable equilibria, the numerical noise is expected to trigger some instability, even if the time scales over which this happen is expected to be much longer than τ. These tests have been applied to all the equilibria used in this thesis. In the case of stable equilibria, their stability has been checked perturbing the initial state by a small amplitude - random phase perturbation. The 3fluid code dissipates the initial perturbation in a few Ω_{ic}^{-1} and remains stable for thousands of Ω_{ic}^{-1}. In the case of unstable equilibria, since the 3fluid code is very accurate, the numerical noise has shown very small growth rates with respect to those typical of fluid instabilities ($1/\tau$) and the code remains stable for thousands of Ω_{ic}^{-1}.

13.2 A General Plasma Dispersion Relation Solver (GPDRS)

In this chapter a tool computing analytically the dispersion relation for the system (12.1) is presented. This tool will be used in the following to validate the 3fluid numerical code by means of wave propagation tests. System (12.1) is a set of 24 equations and 24 unknowns that reduce to 21 since $S_\alpha = S_\alpha(n_\alpha, T_\alpha)$. The large amount of equations to handle in order to obtain the dispersion relation for the 3fluid system is not an easy task. The dispersion relation can be computed by solving the linearised system (12.1) using the equilibrium quantities $\mathbf{Q}_0$ and

considering all fluctuations of the form $\mathbf{Q}_1 e^{(i(\mathbf{k}\cdot\mathbf{r})-(i\omega_i+\omega_r)t)}$. The linearised equations can be expressed in non conservative forms such as

$$\partial_t \mathbf{Q} + \mathbf{\Phi}_\mathbf{Q} \partial_x \mathbf{Q} = \mathbf{S} \tag{13.1}$$

$\mathbf{\Phi}_\mathbf{Q}$ and $\mathbf{S}$ being the flow and the source of $\mathbf{Q}$. Assuming $\mathbf{Q} = \mathbf{Q}_0 + \mathbf{Q}_1 e^{-ikx-i\omega t}$ ans $\mathbf{S} = 0$, the linearised system reads:

$$\{i\omega I + ik\mathbf{\Phi}_\mathbf{Q}(\mathbf{Q}_0)\}\mathbf{Q}_1 = 0 \tag{13.2}$$

where $\mathbf{I}$ is the unit matrix. For non-trivial solutions, the determinant of the matrix in the curly brackets must vanish. This condition leads to the dispersion relation $\omega = \omega(k)$. Similar approaches have already been successfully used by [63, 79, 106]. It is worth noticing that this method is different from obtaining dispersion relations from the dielectric tensor (as done by WHAMP for instance [27, 28] or [74]) which is a method difficult to be generalised to any number of fluid species with good convergence and/or to fully solve [106]. The numerical implementation used here (implemented in Mathematica language) is able to manage analytical functions by splitting each equation of the system (12.1) into separate equations according to the order of each term. As an example, equation (12.1a) is linearised as follows:

$$\frac{dn_\alpha}{dt} + n_\alpha \overline{\nabla} \cdot \mathbf{U}_\alpha = 0 \rightarrow \begin{cases} 0^{th} & 0 = 0 \\ 1^{th} & n_{\alpha,0}\left(\mathbf{k}\cdot\mathbf{U}_{\alpha,1}\right) + n_{\alpha,1}(\mathbf{k}\cdot\mathbf{U}_{\alpha,0} + \omega_i - i\omega_r) = 0 \\ 2^{nd} & n_{\alpha,1}(\mathbf{k}\cdot\mathbf{U}_{\alpha,1}) = 0 \end{cases} \tag{13.3}$$

where $d(...)/dt \equiv \partial(...)/\partial t + \mathbf{U}_\alpha \cdot \overline{\nabla}(...)$. The 0^{th} order is satisfied since it concerns the equilibrium quantities which in this case have been taken homogeneous. We must nevertheless take into account equation (12.1a) whose 0^{th} order part ($n_{e,0} = n_{ic,0} + n_{ih,0}$) is used to simplify computations. It is worth noticing that the polytropic closure that we use to solve systems (12.1) include fractional exponents. The difficulties of the ordering process in such equations can be overcome by substituting the $S_{\alpha,0}$ and the $S_{\alpha,1}$ terms with $T_{\alpha,0} n_{\alpha,0}^{1-\gamma}$ and $\left(n_{\alpha,0} T_{\alpha,1} + (1-\gamma)\, T_{\alpha,0} n_{\alpha,1}\right) n_{\alpha,0}^{-\gamma}$, respectively, which are derived from the definition of entropy in the form $n_\alpha^{a-b} S_\alpha^b = T_\alpha^b$ where $a/b \equiv \gamma$ and using the binomial expansion formula $(A_0 + A_1)^n = \sum_{k=0}^{n} \left(\begin{array}{c} n \\ k \end{array} \right) A_0^{n-k} A_1^k$. Finally, the determinant of the matrix collecting all the 1^{st} order coefficients (*i.e.* the terms in the curly brackets of Equation (13.2)) is computed and the $\omega = \omega(k)$ relation is derived as the solution of the resulting characteristic polynomial.

13.3 The propagation of elementary waves in the two fluid approximation

Neglecting the hot ion population terms in Equations (12.1) the 3fluid numerical implementation is reduced to a 2fluid system (one ion population and one electron population). In the following this regime will be often called as a $3 \rightarrow 2$fluid approximation. The resulting system is perturbed by monochromatic waves parallel and perpendicular directions with respect to the equilibrium magnetic field. The following chapters summarise and analyse the results.

13.3.1 Parallel wave propagation

The magneto-sonic wave

One possible way to test the magneto-sonic wave propagation, is to add a cos-like perturbation having $\mathbf{k} \parallel \mathbf{B}_0$ to the equilibrium cold ion pressure $\tilde{P}_{ic}$. The homogeneous equilibrium state is

defined by $n_{ic,0} = 0.5$, $P_{ic,0} = P_{e,0} = 0.5$, where $n_{ic,0}$, $P_{ic,0}$ and $P_{e,0}$ are the zero-order ion density and ions and electrons pressures, respectively. The polytropic index is set to $\gamma = 5/3$.

The temporal evolution of $\tilde{P}_{ic}$ is probed at a fixed point; the result is visualised in Fig. (13.1).

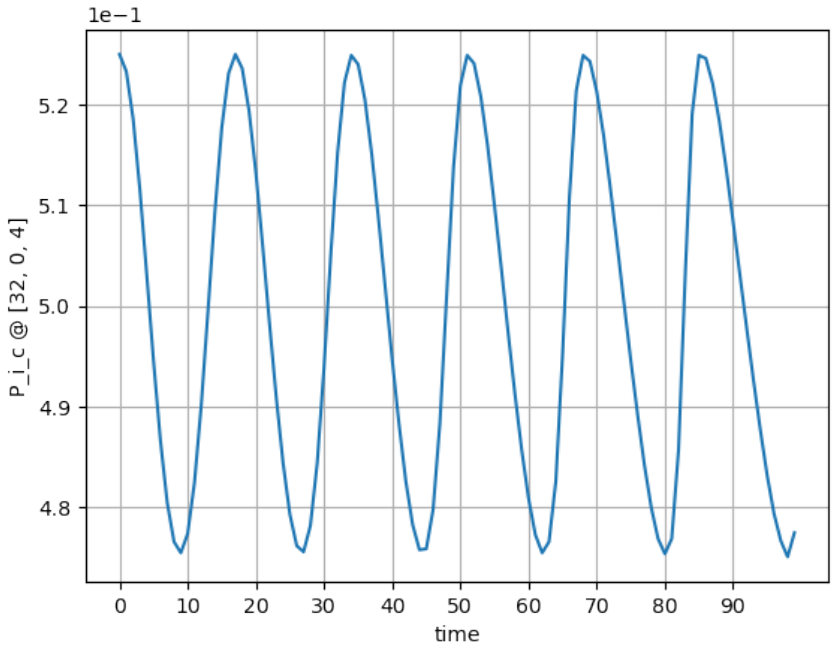

Figure 13.1: *Temporal evolution of $P_{ic} = P_{ic,0} + \tilde{P}_{ic}$ with $P_{ic,0} = 0.5$ in a $3 \rightarrow 2$fluid simulation, i.e. : where the ih population contribution has no feed back in Equations (12.1). Units of y axis: $\overline{n} m_i V_{a,i}^2$ with $\overline{n} = \frac{c^2 m_i \epsilon_0}{e^2 d_i^2}$. Units of x axis: $\Omega_{ic}^{-1} = \frac{B q_i}{m_i}$.*

From plots like (13.1), the wave period $\tau_{measured}$ is measured and associated to the wave number k_{pert}. The measure is performed for a certain number of wave-numbers k_{pert}. Table (13.1) summarises the results for $k_{pert} = \{1, 2, 3, 4\} d_i^{-1}$.

k_{pert} $[d_i^{-1}]$	λ $[d_i]$ $[\Omega_i^{-1}]$	$\tau_{measured}$ $[\Omega_i^{-1}]$	V_S $[d_i \Omega_i^{-1}]$
1/128	128	68,0	1,882
2/128	64,0	34,0	1,882
3/128	42,7	23,0	1,879
4/128	32,0	17,0	1,882

Table 13.1: *Summary of the phase velocities found in perturbing the P_{ic} pressure with $\mathbf{k} \parallel \mathbf{B_0}$ in a $3 \rightarrow 2$fluid simulation (sec. 13.3.1). 1^{st} column: wave number of the induced perturbations; 2^{nd} column: wave length of the induced perturbations; 3^{th} column: time periods measured; 4^{th} column: resulting ion magneto-sonic phase velocities.*

The phase velocity of the perturbation results to be $\sim 1.88 d_i \Omega_i^{-1}$ (see the right column of the table).

In a warm plasma with a constant and homogeneous equilibrium magnetic field $\mathbf{B}_0$, the pressure perturbations having wave number $\mathbf{k} \parallel \mathbf{B}_0$ behave like in an non-magnetised fluid under the assumption that $\omega < \Omega_p$, where ω is the wave frequency and $\Omega_p = \sqrt{n_i e^2/(\epsilon_0 m_i)}$ is the ions plasma frequency ([41]). The perturbation is a non dispersive wave with frequency ω proportional to the wave number k:

$$\omega = k C_s = k \sqrt{\gamma \frac{\sum_s K_B T_s}{m_i n_i}} \tag{13.4}$$

where C_s is the sound speed, K_B is the Boltzmann constant, T_s is the temperature of the population s, n_i is ions density and γ is the polytropic index.

$$V_S = \sqrt{\gamma \frac{P_{ic} + P_e}{m_i n_i}} \simeq 1,826 \tag{13.5}$$

in $d_i \Omega_i^{-1}$ units.

The comparison between the theoretical dispersion relation (equation (13.4)) and data presented in table (13.1) is shown in Figure (13.2).

The shear Alfvén waves

The propagation of the shear Alfvén waves is tested as well. The equilibrium magnetic field ($\mathbf{B}_0 = 1.0$) is perturbed with $\mathbf{B}_1 \perp \mathbf{B}_0$ and a parallel perturbation $\mathbf{k}$ (*i.e.* $\mathbf{k} \parallel \mathbf{B}_0$). The equilibrium density $n_{ic,0}$ is set to 1.0. In this case the perturbations are expected to oscillate at

$$\omega = kV_A = k \frac{|\mathbf{B}|}{\sqrt{\mu_0 n_i m_i}} \tag{13.6}$$

The frequencies with which the perturbation oscillates are listed in Table (13.2) as a function of the wave number $\mathbf{k}$.

k_{pert} $[d_i^{-1}]$	λ $[d_i]$	$\tau_{measured}$ $[\Omega_i^{-1}]$	V_S $[d_i \Omega_i^{-1}]$
1/128	128	126,6	1,01
2/128	64,0	63,3	1,01
3/128	42,7	41,5	1,03
4/128	32,0	30,0	1,07
5/128	25,6	25	1,02
6/128	21,3	20	1,07
7/128	18,3	18	1,02

Table 13.2: *Summary of the phase velocities found in perturbing* $\mathbf{B}_0$ *with* $\mathbf{k} \parallel \mathbf{B_0}$ *in a* $3 \rightarrow 2$*fluid simulation (sec. 13.3.1).* 1^{st} *column: wave number of the induced perturbations;* 2^{nd} *column: wave length of the induced perturbations;* 3^{th} *column: time period measured;* 4^{th} *column: resulting shear Alfvén wave phase velocity.*

The numerical Alfvén phase velocity V_A is $\sim 1 d_i \Omega_i^{-1}$, as expected:

$$V_A = \frac{|\mathbf{B}|}{\sqrt{\mu_0 n_i m_i}} = 1 \tag{13.7}$$

The comparison between the theoretical dispersion relation (equation (13.7)) and data presented in table (13.2) is shown in Figure (13.2).

13.3.2 Perpendicular wave propagation

We have tested the fast magneto-sonic waves propagation neglecting one of the ion population. In this case the perturbation $\mathbf{B}_1$ is modelled by a sin-like wave having wave-number $\mathbf{k} \perp \mathbf{B}_0$ and small amplitude as compared to $|\mathbf{B}_0|$ (*i.e.* $\mathbf{B}_1 << \mathbf{B}_0$). The equilibrium density $n_{ic,0}$ is set to 1.0, as well as $\mathbf{B}_0$; the polytropic index is set to 5/3 and the pressures of electrons and the cold ion component are set to 0.5. In this case the perturbation is expected to oscillate at the frequency: $\omega = kV_{ph} = k\sqrt{V_A^2 + V_S^2} \sim 1.633k$ (in $d_i \Omega_i^{-1}$ units). Table (13.3) shows the wave periods as a function of the wave number k of the induced perturbation.

Figure (13.3) shows the numerical points collected in table (13.3) in comparison with the theoretical dispersion relation computed by means of the GPDRS method introduced in section (13.2).

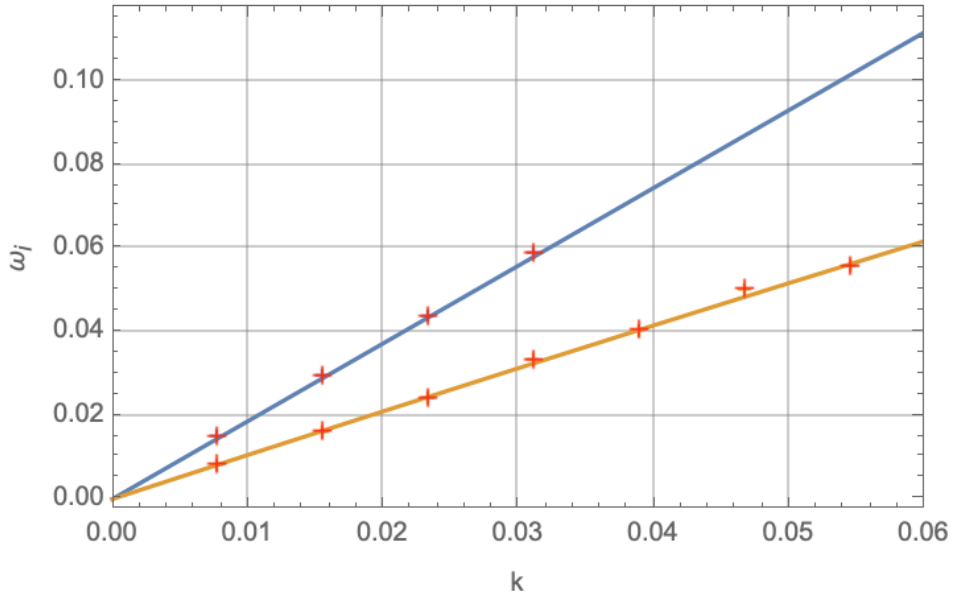

Figure 13.2: *Theoretical (continuous curves) and numerical ("+" points) sound (blue) and shear Alfvén (orange) branches of dispersion relations introduced in sections (13.3.1) and (13.3.1). Theoretical curves are computed by means of the GPDRS method introduced in section (13.2).*

k_{pert} $[d_i^{-1}]$	λ $[d_i]$	$\tau_{measured}$ $[\Omega_i^{-1}]$	V_S $[d_i\Omega_i^{-1}]$
1/128	128	76	1,68
2/128	64,0	38,5	1,66
3/128	42,7	25,7	1,66
4/128	32	19	1,68

Table 13.3: *Summary of the phase velocities found in perturbing* $\mathbf{B}_0$ *with* $\mathbf{k} \perp \mathbf{B_0}$ *in a* $3 \rightarrow 2$*fluid simulation (sec. 13.3.2). 1st column: wave number of the induced perturbations; 2nd column: wave lengths of the induced perturbations; 3th column: time period measured; 4th column: resulting magneto-sonic wave phase velocity.*

13.4 The propagation of perturbations in the full 3fluid regime

The full form of the 3fluid code (two ions population plus one neutralising electron population) is tested in propagating a ion magneto-sonic wave. The perturbation on the cold ion pressure is triggered with wave-number parallel to the equilibrium field (*i.e.* $\mathbf{k} \parallel \mathbf{B}_0$). With $n_{ic,0} = n_{ih,0} = 1/2$, $P_{ic,0} = P_{ih,0} = P_{e,0} = 1/3$ and the polytropic index set to 5/3, Equation (13.4) gives a phase speed equal to $1.29 d_i \Omega_i^{-1}$. Table (13.4) summarises the phase velocities recorded once the plasma is perturbed with pressure fluctuations using different k_{pert}.

Figure (13.4) compares the numerical points listed in table (13.4) and the ion magneto-sonic branch of the dispersion relation for the 3fluid plasma system as discussed in section (13.2).

13.5 The reconnection instability in the 3→2 fluid approximation

The $3 \rightarrow 2$ fluid configuration is tested against the reconnection instability. The test is performed in two dimensions and in symmetric conditions in order to fit the standard assumptions usually made in theoretical studies. In this case all the quantities are homogeneous while the magnetic field $\mathbf{B}_0$ is given by:

$$\mathbf{B}_0(x) = \{0, B_{0,y} tanh(x/a), 0\} \tag{13.8}$$

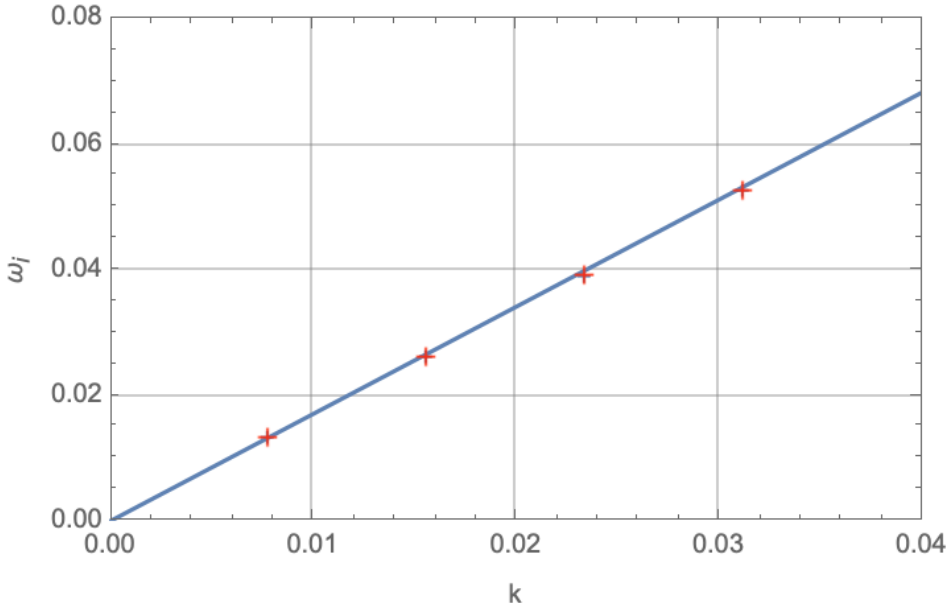

Figure 13.3: *Theoretical (blue continuous curve) and numerical ("+" points) fast magneto-sonic branch for the 3→2 approximation. Theoretical curve is computed by means of the GPDRS method introduced in section (13.2).*

k_{pert} $[d_i^{-1}]$	λ $[d_i]$	$\tau_{measured}$ $[\Omega_i^{-1}]$	V_S $[d_i\Omega_i^{-1}]$
1/128	128	99.2	1.29
2/128	64,0	49.4	1.30
3/128	42,7	33.2	1.28
4/128	32,0	24.71	1.30

Table 13.4: *Summary of the phase velocities found in perturbing the P_{ic} pressure with $\mathbf{k} \parallel \mathbf{B_0}$ in a 3 → 2fluid simulation (sec. 13.3.1). 1^{st} column: wave number of the perturbations; 2^{nd} column: wave length of the induced perturbations; 3^{th} column: time periods measured; 4^{th} column: resulting ion magneto-sonic phase velocities.*

with $B_{0,y} \sim 1$ and $a = 2.0$ in d_i units. In this case the configuration is expected to be able to release the "free" energy contained in the non-homogeneous magnetic field via a reconnection instability as, for instance, the tearing mode instability [18]. The equilibrium state is perturbed by small amplitude magnetic field fluctuations with random phases (see section (14.2)). After a period about two time longer than the Fastest Growing Mode (FGM) time-growth, the simulation is stopped and the final state is analysed. Figure (13.5) shows the profile of the eigen-mode B_x measured along the non-homogeneous direction x. This is the profile in the x direction of the modulus of the y-Fourier transform of B_x at a given time. The figure shows the typical shape of the tearing mode eigenfunction (see for instance the red rectangle inset to the figure where the normalised profile of the same quantity obtained by similar numerical studies [120, 18] is shown). In agreement with asymmetric cases that will be presented in sec. (IV), Figure (13.5) shows that the eigenfunction of B_x is symmetric with respect to the inversion point of B_x at $x^* = L_x/2$ where L_x is the extension of the simulation box in the non homogeneous direction x (in this case $L_x = 115d_i$). The reason for this symmetry is due to the symmetric equilibrium with respect to x^* chosen for the initialisation of this test.

Figure (13.6) shows the temporal evolution of the growth of the eigen-functions of B_x. The dispersion relation $\gamma(k)$ vs k for the B_x modes measured during the linear phase of the reconnection mode growth (bottom right panel) is obtained by linear fits of the growth rates curves of

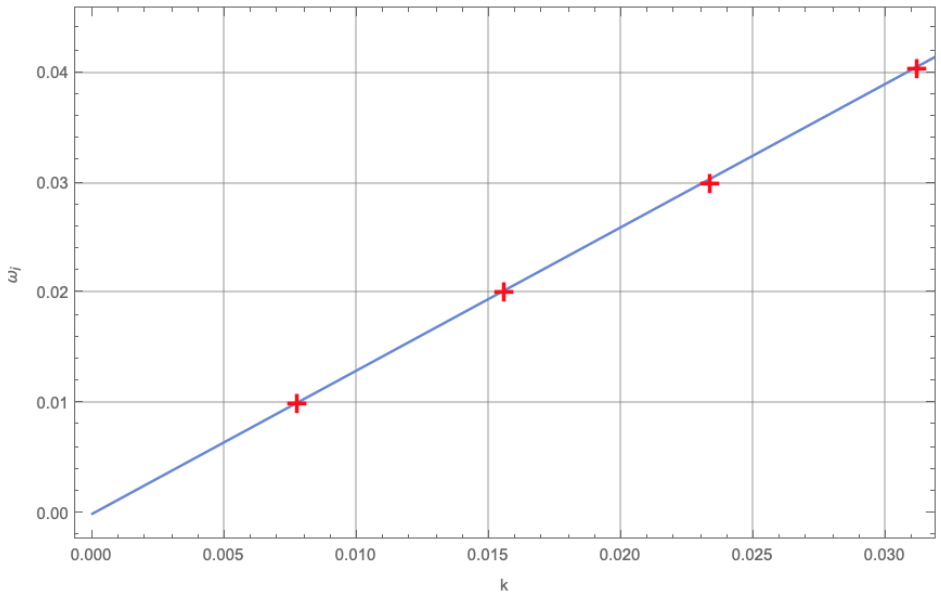

Figure 13.4: *Theoretical (continuous blue curve) and numerical (red "+") ion magneto-sonic branches of dispersion relation for the 3fluid plasma system. Theoretical curve is computed by means of the GPDRS method introduced in section (13.2). The experimental points are listed in table (13.4).*

each Fourier mode $m_y \equiv k_y L_y$ within the time interval indicated by the red vertical dashed lines in the left panel. The numerical values of the slopes of the linear fits (the γs) are listed in the table (top right panel). The FGM is characterised by $k_y a \simeq 0.1$. Yet, in the red rectangle inset to the figure we show similar curves obtained by published studies adopting similar numerical simulation models and initialisations ([120]).
Following [18], figure (13.7) shows the computation of Δ' as a function of $k_y a$ ($k_y \equiv m_y/L_y$). The formula has been derived from [18] for the "Harris sheet" equilibrium which adopt a tanh-like profile to model the equilibrium magnetic field similar to the profile used here (Equation (13.8)). The figure shows that a reconnection instability is expected to occur for $k_y a <= 0.25$, since for such wavelengths $\Delta' > 0$. Effectively, this is what is observed during the simulation, Figure (13.6) showing the unstable modes only.

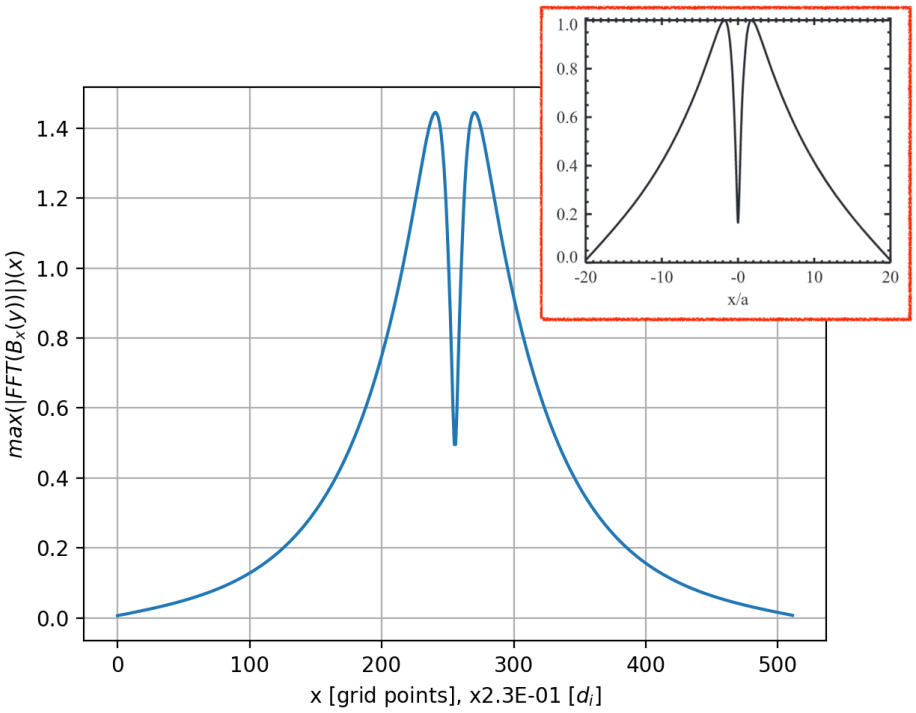

Figure 13.5: *Tearing mode magnetic field eigenfunction ($max(|FFT(B_x(y))|)(x)$) recorded at an evolved state in a $3 \rightarrow 2$fluid simulation. Inset to the figure it is shown the same profile obtained by numerical simulations adopting similar models and initialised with similar equilibria [120].*

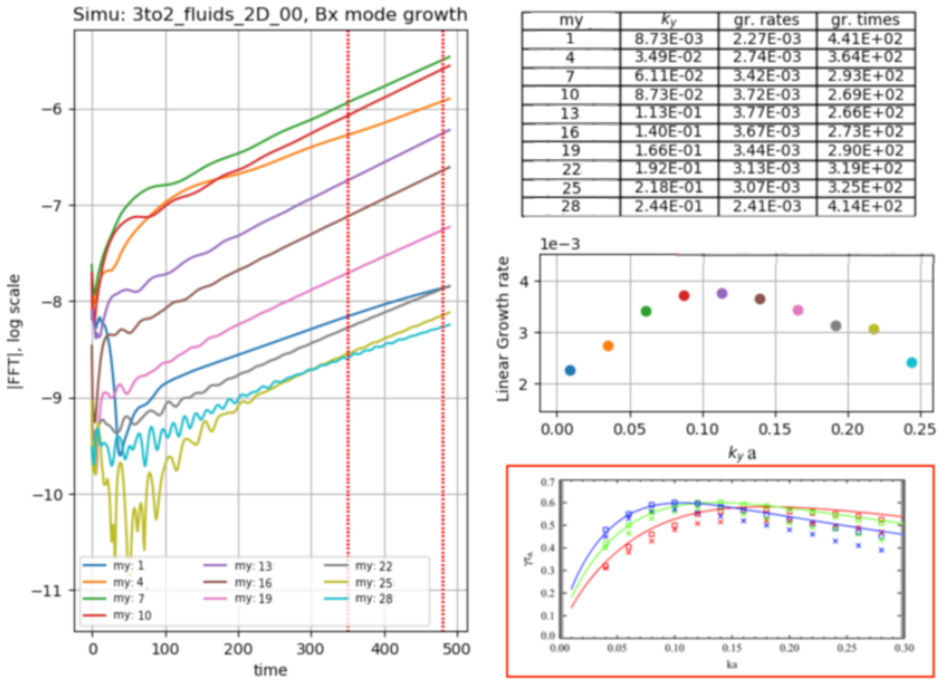

my	k_y	gr. rates	gr. times
1	8.73E-03	2.27E-03	4.41E+02
4	3.49E-02	2.74E-03	3.64E+02
7	6.11E-02	3.42E-03	2.93E+02
10	8.73E-02	3.72E-03	2.69E+02
13	1.13E-01	3.77E-03	2.66E+02
16	1.40E-01	3.67E-03	2.73E+02
19	1.66E-01	3.44E-03	2.90E+02
22	1.92E-01	3.13E-03	3.19E+02
25	2.18E-01	3.07E-03	3.25E+02
28	2.44E-01	2.41E-03	4.14E+02

Figure 13.6: *Diagnostics of the linear phase of the reconnection instability growing in a* $3 \rightarrow 2$*fluid simulation test, as described in section (13.5). Left panel: temporal behaviour of the first growing* $m_y (= L_y k_y)$ *components of the* $\|FFT\|$ *of* B_x*; the red dashed vertical lines mark the period where the curves are linearly fitted in order to compute the growth rates* γ*. Top right: table summarising the growth rates* γ *(*3^{rd} *column) as a function of the Fourier mode numbers* m_y *(*1^{st} *column) and the associated wave numbers* $k_y \equiv \frac{m_y}{L_y}$ *(*2^{nd} *column); the growth times* (γ^{-1}) *are make explicit in the* 4^{th} *column. Middle right panel: plot of* γ *as a function of the wave number* $k_y a$ *where* a *is the magnetopause current width. In the red rectangle at the bottom right corner of the figure similar curves published by [120] are shown for a qualitative comparison.*

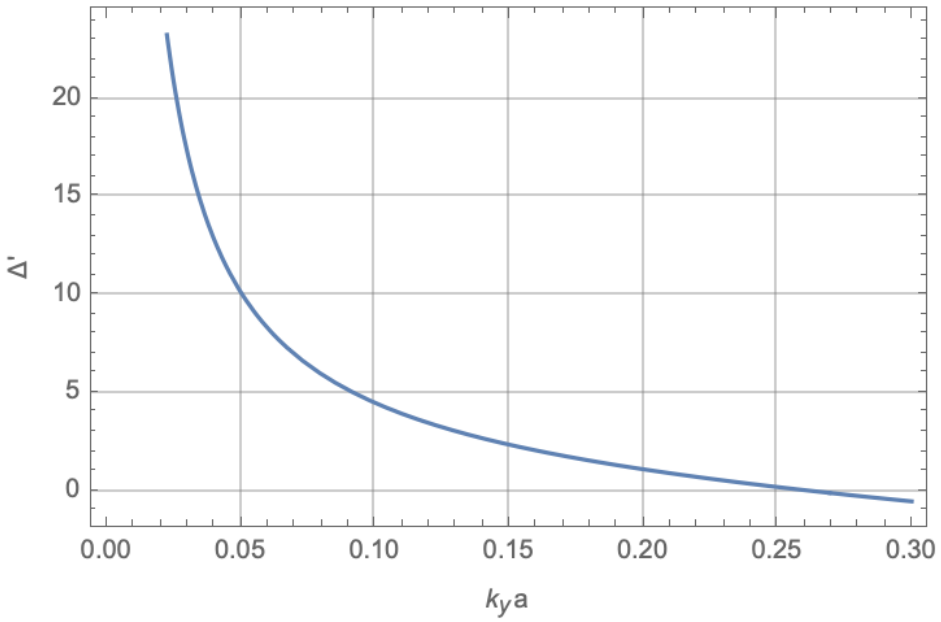

Figure 13.7: *Computation of* Δ' *(following [18]) for the tearing mode instability growing in the* $3 \rightarrow 2$*fluid simulation described in section (13.5).*

Part IV

Realistic initialisation of the 3fluid magnetopause simulations

Chapter

14 A SIMULATION OF A MAGNETIC RECONNECTION EVENT

Chapter content

14.1 Data vs analytical profiles: the 3fluid ability to mimic the real magnetopause

The procedures introduced in section (12) are applied to the case study *Cr2* (section (10.2)). The results have been included in Paper 2. As done previously, this section insists on the most important observations while the details can be found in the attached paper.

The magnetic field ($\mathbf{B}$), the ion temperature (T_i) and density (n_i) are obtained by a fit procedure using as fitting functions a linear superposition of *tanh* functions. The number of *tanh* components of each fitting function depends mainly by the slopes of the previous quantities but usually no more than three components are needed to reach the required accuracy. The analytic profiles passed as inputs to the 3fluid model are considered as good fits of the data if they correctly shape the large scale configuration, as well as the position and the length scale of the gradients within the magnetopause layer.

In Paper 2, Figure 3, the 3fluid inputs and outputs have been superposed to data in order to facilitate the comparison. The first observation about data is that the particle and fields gradients are characterised by different locations and length scales. In particular the densities and temperatures (panels *b* and *c*) show their gradients in a narrow interval ($\sim 1 - 2d_i$) which is shifted with respect to the magnetic and electric fields gradients (panels *a* and *d*). The latter show a more gentle gradient, nearly 4 times wider than the particle gradient length. This may indicate the presence of a boundary layer, possibly made of magnetosheath plasma observed on the magnetospheric side of the magnetopause [95]. This justifies the need of multiple *tanh* components for each fit function to correctly model the magnetopause during the *Cr2* event. Look for instance at the T_i curve (panel *b*, Figure 3, Paper 2): it shows clearly two gradients having different length scales and positions. A similar feature can be observed on densities (panel *c*): the cold ion density (computed by the 3fluid using the Γ parameter introduced in section (12.3.1)) falls rapidly to very low values in more or less $\sim 2\ d_i$ while the hot population density keeps nearly the same value over a longer interval (between 0 and 8 d_i). Here, the 3fluid model plays its role since it allows to reproduce a magnetopause feature that can not be reproduced in

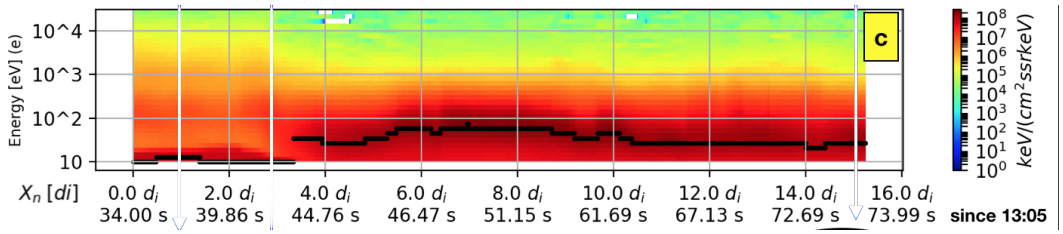

Figure 14.1: *Electron spectrograms measured by MMS during Cr2. The first abscissa is the spatial coordinate normal to the magnetopause X_n and the second one is time. $X_n(t)$ is the projection of the spacecraft path along the direction normal to the magnetopause as explained in section (8.3.1) (units of $d_{i,MSh}$ with $d_{i,MSh} \simeq 70km$). $X_n(t)$ is obtained from the temporal integration of the magnetopause magnetic structure velocity by means of a combination of the three distinct methods, STD+, SVF and MVF, optimised with the GDMC approach (section (8)). On the bottom left corner of the panel it can be observed that the electron magnetospheric population falls below the bottom limit of the instrument. Artefacts are due to extraction from Figure 1 of Paper 2.*

the framework of a MHD equilibrium model.

The 3fluid model can help in determining features poorly measured by spacecraft. This is the case of the electron density and velocity profiles. These quantities are not plotted in the respective panels of Figure 3 in Paper 2 since their experimental counterparts are likely to be biased in the magnetosphere by the cold electron population which is partially below the bottom threshold in energy of the FPI instrument. The proof of such inconvenient is provided in Paper 2, Figure 1, panel *c* and it is reported here in Figure (14.1). A comparison between data and 3fluid outputs would be meaningless. Nevertheless, the electric field (derived from Equation (12.1g) as a function of the electron density and velocity) agrees quite well with the one measured by the instrument independently of the electron measurements (see Paper 2, Figure 3, Panel *d*).

The 3fluid model tries to reproduce the finest magnetopause details but unfortunately a limitation prevent it to follow locally a local magnetopause feature. Looking at Paper 2, Figure 3, Panel *b*, in the $\sim 1.0d_i \leq X_n \leq \sim 2.5d_i$ interval the real total ion temperature becomes actually larger than its magnetospheric asymptotic limit. This feature can not be reproduced by the present 3fluid model since the constancy of hot and cold temperatures and the $\Gamma \geq 0$ constraint forces the T_i profile to be everywhere lower than T_{ih} (see Appendix (18) for an analytical treatment of this limitation).

Finally, the 3fluid model needs for further manipulations. In particular, whereas the perpendicular components of the cold and hot ion currents are set by equations (12.1d), the parallel components of the cold and hot ion currents can not computed by any of the 3fluid equation. In this case, the cold and hot contributions are set by a reasonable choice of the ratio $\phi \equiv (n_{ic}/n_i)(\mathbf{U}_{ic} - \mathbf{U}_e) \cdot \mathbf{b}/[(\mathbf{U}_i - \mathbf{U}_e) \cdot \mathbf{b}]$ which determines the ratio between the cold parallel ion current to the total parallel ion current as seen in the electrons frame. As for any of the other quantities, ϕ is defined by the asymptotic limits and the position(s) and length scale(s) of the gradient(s) within the magnetopause. In Paper 2, the choice has been to model ϕ by using only one *tanh* component. The length of the gradient of ϕ has been chosen of the same order of the density and temperature gradients length scales, *i.e.* $\sim 1 - 2d_i$. The position of the main gradient of ϕ is set in order to separate the magnetopause thickness in two parts, each of length proportional to the gyro-radii of the two populations (their ratio is $\simeq 2$). Finally, in the numerical implementation, the asymptotic values of ϕ differ from the $\lim_{x \to MSph} \phi = 0$; $\lim_{x \to MSh} \phi = 1$ limits by small amounts similarly to what have been done for temperatures (Eqs. (12.18)); as we already observed, this is a necessary compromise for implementing the model in the multi-population numerical simulation.

In spite of these corrections and these degrees of freedoms in the choice of the 3fluid parame-

ters, looking at Paper 2 Figure 3, one can observe that the total ion current is well fitted, as well as for all the other total ion quantities resulting from the sum of the cold and hot contributions (Equations (12.13), (12.14) and (12.15)).

14.2 The numerical simulation

14.2.1 Set up of the numerical simulation

The 3fluid model introduced in section (12) and in Paper 2 has been used to initialise a 2D 3fluid numerical simulation. The numerical code is the 3fluid code described in section (12) and validated in section (13). The numerical simulation is initialised with particle and field profiles mimicking the *Cr2* event, *i.e.* the profiles shown by Figure 3 of Paper 2 and summarised in the previous section. The simulation box dimensions have been decided according to criteria introduced in section (12.2.2). The box dimensions are given by $L_x = 160d_i$, $L_y = 20\pi d_i$ and the box is discretized using $n_x = 800$ and $n_y = 320$ grid points corresponding to $dx = dy = 0.2d_i$. The basic tests described in section (13) have been successfully passed.

14.2.2 The simulation results

The large scale equilibrium configuration used to initialise the simulation is unstable with respect to the reconnection mode. Results are presented in Paper 2, section 5. The equilibrium magnetic field is perturbed at $t = 0$ by means of a potential vector given by a sum of small amplitude, random phase magnetic potential modes localised onto the magnetopause. The simulation is run for about 1500 ion cyclotron times. Very rapidly (one tenth of the simulation duration) the initial perturbation triggers a magnetic reconnection instability the signatures of which are clearly visible on the B_x component of the magnetic field. Panel a of figure 5 in Paper 2 shows $|FFT(B_x(y)))|$ as a function of x at different times during the evolution of the magnetic reconnection instability. This quantity is often used as a proxy to examine if a magnetic structure is tearing mode unstable or not [18]. The growth of the reconnection mode can be easily traced computing, step by step, the $max(|FFT(B_x(y)))|)$ along the x direction, *i.e.* the maximum of the curves shown in panel a. The resulting curves can be observed in Paper 2, Figure 5, Panel b. From the figure it can be observed that only the first five modes are not stable. Following the classical reconnection theory [18], but ignoring the density in-homogeneity, the 3fluid equilibrium used for this simulation can be tested according to its being prone to develop magnetic reconnection instabilities. It can be checked that the equilibrium used is Δ' unstable just for the first five eigenmodes (see Figure 4 of Paper 2 that shows $\Delta' > 0$ only for these modes). The results shown in Paper 2 show that after an initial transient needed to set up the normal mode shape, the reconnection instability develops around the region where the magnetic field reverts. Since the equilibrium is asymmetric, the B_y eigenmodes are not symmetric with respect to the point where the magnetic field inverts. Finally, the cold and hot densities show "complementary" behaviour in the sense that, in the very beginning of the non linear phase of the magnetic reconnection instability, where one population shows a bump, the other ion population shows a hole (cf. figures 6 and 7 of Paper 2 where we plot the contour of the two ion populations density perturbations as a function of the spatial position over the simulation box).

Part V

Conclusions

The aim of this thesis is to present a method able to obtain a "realistic" multi-fluid analysis of the solar wind - magnetosphere interaction across the Earth's magnetopause. The goal has been achieved in three main steps: the analysis of spacecraft data acquired across the magnetopause, the set up of an analytical multi-fluid equilibrium model consistent with observations and the development of a multi-fluid code able to simulate the temporal evolution of this equilibrium.

Regarding the analysis of spacecraft data acquired across the magnetopause, the main objective was to determine the spatial characteristics of the particles and fields profiles across magnetopause in order to understand where and how the solar wind and the Earth's magnetosphere interact. For that purpose, we developed new methods that require hypotheses about the observed plasma structure weaker than those assumed by the previous methods. In particular, the Single Variate Fit (SVF) and the Multi Variate Fit (MVF) methods presented in this thesis and in Paper 1 are able to determine the spacecraft velocity in the magnetopause frame from any vector quantity varying across the magnetopause. The spacecraft path is then computed by temporal integration of the magnetopause velocity and the data can be localised where they were acquired along the spacecraft trajectory, contributing to reach the original goal. Thanks to the high quality data provided by the Magnetospheric MultiScale (MMS) mission (high probing rates joint with a small inter-spacecraft distance), these techniques allow to characterise the magnetopause characteristics down to local scales, where "local" means less than 1% of the magnetopause thickness. The shrinking of the length scales where the SVF and MVF results are valid has been necessarily accompanied by the relaxation of the assumption of strict stationarity of the magnetopause structure. The mathematical kernel of the SVF and MVF methods allows to distinguish the two kinds of contributions in the variations of spacecraft observations: the advection - in the spacecraft frame - of the magnetopause structure and its pure temporal variations. The SVF and MVF methods, joint with recent methods to determine locally the magnetopause orientation (the Minimum Directional Derivative and the Local Normal Analysis techniques) allowed to determine 1D - and in one case, 2D - spacecraft trajectories retaining the local informations about the magnetopause sub-structures. The methods were first tested on artificial data mimicking spacecraft crossing of a stationary 1D and artificial magnetopause. Both constant velocity and back-and-forth magnetopause motions have been considered. Since the artificial magnetopause was perfectly stationary (time independent), the results of both the new methods agreed with those of a modified version of the Spatio-Temporal Difference (STD) method [72]. We had to introduce an improved version of this method, that we called STD$^+$ since, as we showed, when the original method is applied to real data, all departures from strict stationarity lead to nonphysical signatures (singularities). All these new methods were then applied to two real magnetopause crossings observed by MMS on 16 October 2015: the 10:36:55+55s UT (*Cr1*) and the 13:05:30+60s UT (*Cr2*) events. From *Cr1* we have determined the position and the width of the layer where the magnetosheath and the magnetospheric plasmas mix. Visualising data as a function of space, these methods also helped in correctly identify the single structure that caused multiple signatures (and so misunderstandings) in data shown as a function of time. Analysing *Cr2*, we had determined the magnetopause dynamics by comparison of SVF, MVF and STD$^+$ results and confirmed what was expected by previous studies [131], in which the magnetopause motion was computed with less accuracy. Thanks to particular conditions during *Cr2*, we managed to reconstruct a 2D spacecraft path that gives a more detailed picture than that given by hand-made reconstructions [112]. Such remarkable results have been obtained also thanks to optimisation techniques that allowed to take objective decisions about the input parameters (thresholds) needed to analyse data and to merge the SVF and the MVF results.

The new techniques presented in this thesis will be useful to determine the validity of assumptions for more demanding approaches. For instance, the computation of the flow normal to the magnetopause can establish whether the BV technique could be applied or not. The stationary assumption, tested by comparison of the two RHS terms in Equation (8.1) (as done in Paper 1), could also be used fruitfully in turbulence studies for testing the Taylor's Hypothesis [3].

SVF and MVF can be used also as inputs in the reconstruction techniques, such as the Grad-Shafranov reconstruction method. Finally, as shown in this thesis and in Paper 2, the SVF and MVF output can be used as inputs for numerical simulations by providing more realistic initial conditions. In the literature, the simulations are initialised with relatively simple configurations (Harris sheets, or modified Harris sheets with little relationship with the real magnetopause). These new techniques should help in modelling more precisely the observed magnetopause.

The SVF and MVF outputs have been used to provide informations about the spatial profiles of data to a new 3fluid analytical model (two ion and one electron populations). The need for a 3fluid model concerns mainly the ability to model the magnetospheric and the magnetosheath ion populations which are now allowed to vanish in the magnetosheath and in the magnetospheric regions, respectively. The model also takes into account the main magnetopause features emerging from observations, such as the asymmetry in temperature and density between the magnetosphere and magnetosheath plasmas, the velocity shear that arises at the boundary and the different locations and scale lengths of particles and fields gradients. It is very important to initialise a simulation with a configuration as much as realistic as possible since the non linear dynamics - in particular the mixing properties - may strongly depend on the choice of the initial equilibrium. Although, to a first approximation, these characteristics can be ignored (*i.e.* the magnetopause modelisation can be over-simplified), they can not be ignored in case one investigates how do the positions and the scale of the different gradients influence the magnetopause stability and what is the instability feedback on gradients features. These are fundamental questions one should answer to understand the solar wind - magnetosphere interaction and the mixing processes that occur between these two plasmas. Furthermore, the 3fluid model allows to determine quantitatively the contributions of the magnetospheric and magnetosheath ion populations to the total ion population once the total ion population profiles (asymptotic values and length scales and positions of its gradients) have been provided by data. This thesis demonstrated that the 3fluid model is able to correctly represent the magnetospheric to magnetosheath ion ratio even when this information can not easily be obtained directly from kinetic data (for instance where many populations overlap in phase space). The derivation of the model is based on a fit of the most reliable experimental data and it is completed by the solution of the equilibrium fluid equations for the less reliable observations. The 3fluid model output is therefore an equilibrium state.

Investigating the magnetopause stability and trying to understand, in particular, when and where plasma instabilities can be triggered and how the plasmas of both sides can get mixed, is still nowadays a challenging issue for numerical simulations. Nevertheless, preliminary studies (see Paper 2) show that the 3fluid model can be successfully implemented in a 3fluid numerical code, validating the correctness of the equilibrium solution of our 3fluid model. This numerical code has been forged by us on the skeleton of a stable two-fluid numerical code. Nevertheless the features of the input profiles (*e.g.* the large gradients across the magnetopause and the vanishing of the magnetospheric and magnetosheath population in the magnetosheath and in the magnetosphere, respectively) forced us to face stability problems impeding the correct evolution of the simulated plasmas. A solution has be found to this problem, which led us to slightly depart from the above theoretical equilibrium. The resulting numerical simulations, initialised on the basis of the *Cr2* event, develop magnetic reconnection instability in agreement with what is observed by spacecraft during magnetopause crossing close to the *Cr2* event.

My work at the Laboratoire de Physique des Plasmas (LPP) and at the Physics Departement of Università di Pisa laid the bases for future studies to be free from many kind of constraints. Concerning the physics, we managed to relax some of the strongest assumptions biasing the data analyses and we managed to thaw the two-fluid constraint affecting the models and numerical simulations based on real data. Concerning the numerical methods, I developed new freeware tools, free from any proprietary frameworks and open to be analysed, used and modified for future works by anyone who is interested in. Although time consuming, this work was quite necessary.

It allowed us to forge a new and complete 3fluid framework (data analysis → analytical model → numerical simulation → comparison between data and simulations) that is now ready to be applied to other experimental cases in future studies.

The results obtained during this Thesis have been the subject of two papers, Paper 1: "*Crossing of Plasma Structures by spacecraft: a path calculator*" and Paper 2: "*A multi-fluid model of the magnetopause*" [134], which are under review at Journal of Geophysical Research (Space Physics) and at Annales Geophysicae, respectively. I participated as co-author also of a third paper [131] and I have been mentioned in a fourth [130]. Four posters have been presented in three international conferences: the American Geophysical Union (AGU) Fall Meetings 2017 [123], the AGU 2018 (both standard [129] and e-lighting posters) and the European Geoscience Union 2018 (standard poster). All these documents (but [130]) are attached to this thesis (see sections (23)). I run the numerical simulations using two High Performance Computing (HPC) centres, at LPP and at CINECA, thanks to two HPC grants (IscraC and IscraB projects) for which I hold the role of Principal Investigator. The thesis project has been awarded by the grant VINCI 2017 provided by the *Université Franco Italienne*.

Last but not least, this thesis has been supervised by three invaluable persons, whose expertise, kindness, patience and wisdom are, in my opinion, beyond any comparison: Laurence Rezeau, Francesco Califano and Gerard Belmont. To these mentors, my most sincere gratitude and friendship.

Part VI

Appendixes

Chapter

15 Procedure for filtering spacecraft data

Chapter content

The following sections deal with the filtering procedure applied to spacecraft data in order to get rid of the small scale fluctuations and waves that are present at the magnetopause interface.

15.1 The problem

A filtering of data is necessary to get rid of the small scale fluctuations and waves that are present at the magnetopause and that have an intensity much higher than the instrument noise [40]. The procedure cannot be done by applying a low-pass filter, because the reversal of the magnetic field, which is the signature of the crossing contains relatively high frequencies. These frequency components would be cut off by a low-pass filter while we want to keep the full information about this large scale variation that is called "*trend*" in signal processing.

15.2 The solution

The filtering procedure of a signal $S(t)$ divides in the following steps:

1. **de-trending of the signal** $S(t)$
   (a) $S(t)$ is fitted by means of the function
   $$Tr = a + bcos(t\omega/2) + csin(t\omega/2) \tag{15.1}$$
   where T is the temporal length or S and $\omega = 1/T$. Ref. to code: (1), lines 2-12.
   (b) The trend Tr is subtracted from $S(t)$, obtaining $S_{Tr} = S - Tr$. Ref. to code: (1), lines 13.
2. **Mirroring and windowing** S_{Tr}
   (a) In order to avoid the problems in the de-windowing procedure (point (4a)) due to divisions by zero, S_{Tr} is mirrored four times obtaining a longer lasting signal $S_{Tr,m}$ within which the original S_{Tr} is placed at the 2^{nd} and 4^{th} fourths. Graphically, if $S_{Tr} \equiv |- >$ then $S_{Tr,m} \equiv <-||- >< -||- >$. Ref. to code: (1), lines 14-17.

(b) $S_{Tr,m}$ is modulated by an windowing function $4T$ long (here defined as *Belmont's windowing function*, described in section (15.3) and visualised in Figure (15.1) for different choices of the input parameters) obtaining $S_{Tr,m,B}$. Ref. to code: (1), lines 18-19.

3. **Filtering** $S_{Tr,m,B}$

   (a) A Fast Fourier Transform (FFT) is applied to $S_{Tr,m,B}$ obtaining the spectrum $\hat{S}_{Tr,m,B}$. Ref. to code: (1), lines 21-22.

   (b) All the Fourier components of $\hat{S}_{Tr,m,B}$ corresponding to frequencies above a certain cut frequency ν_c (with $0 < \nu_c < \nu_{sf}/2$ where ν_{sf} is the sampling frequency) are forced to be zero, obtaining a spectrum $\hat{S}_{Tr,m,B,fr}$ filtered by the high frequencies. Ref. to code: (1), lines 23.

   (c) $\hat{S}_{Tr,m,B,fr}$ is transformed back to the time domain recovering $S_{Tr,m,B,fr}$. Ref. to code: (1), lines 25.

4. **De-windowing, de-mirroring and adding the trend** Tr **to** $S_{Tr,m,B,fr}$

   (a) $S_{Tr,m,B,fr}$ is modulated by the inverse of the *Belmont's windowing function* obtaining $S_{Tr,m,fr}$. Ref. to code: (1), lines 25. Here problems may arise due to the divisions by zeros. A suggestion to solve this point is proposed in section (15.4), point (1).

   (b) Being interested in the second fourth of the yet-mirrored signal $S_{Tr,m,fr}$, *i.e.* that part of $S_{Tr,m,fr}$ far away from divisions by zero performed at the previous point (4a), a slice of $S_{Tr,m,fr}$ is performed to keep the $T \leq t \leq 2T$. The resulting output is defined $S_{Tr,fr}$. Ref. to code: (1), lines 25.

   (c) The trend Tr is added to $S_{Tr,fr}$ obtaining S_{fr} which is similar to the original signal S but for its spectrum which decays at frequencies higher than ν_c. Ref. to code: (1), lines 26.

15.3 The Belmont's windowing function

In data analysis, the Fourier analysis of signals S defined in the interval T is often subordinated to a point-by-point modulation of S by a function having domain the interval T and co-domain the interval $[-1, 1]$ and lowering to zero at the extremes of T. This procedure aims at suppressing the spectral leakage of S produced by the discrete Fourier Transform of a finite-length waveform. On the other hands, the windowing results in the smoothing of the Fourier Transform of S (convolutional theorem of Fourier Transform properties). Therefore, care must be paid in the right choice of the windowing function (see for instance [23] for a review on the subject).

Figure (15.1) shows the Belmont's windowing function as a function of time (a standard interval for MMS magnetopause crossings) for several values of the input parameter N_{apod}. Its bandwidth is shown in Figure (15.2) in comparison with other standard windowing functions.

The data analyses shown in this thesis have been carried on with Belmont's windowing functions with $N_{apod} = 1$, this function having a slightly larger band-pass window in Fourier space.

15.4 Suggested improvements of the data analysis methods

The following improvements are suggested for future optimisations of the code.

1. de-windowing of $S_{Tr,m,B,fr}$ and selection of the 2^{nd} part of $S_{Tr,m,fr}$ (code (1), lines 25.) can be inverted in order to avoid divisions by zero located at the extremes of the de-windowing

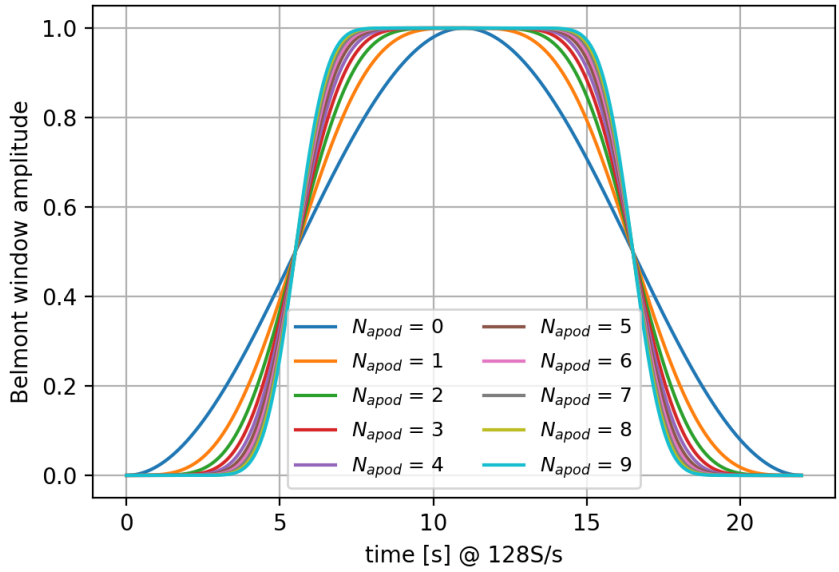

Figure 15.1: *Belmont's windowing function as a function of a normalised time interval for several values of the input parameter* N_{apod}.

windows. In particular, the 2^{nd} part of $S_{Tr,m,fr}$ can be de-windowed by the inverse of the windowing function computed at point (2b) and inverted only in the interval $T \leq t \leq 2T$.

15.5 Codes

Here the programs coded in Python:

1. Main module for filtering signals.
   (a) Inputs:
      i. *time*: array containing the times coordinate at which the signal S is recorded; units: seconds.
      ii. S: array containing the numerical value of the signal S to be filtered; units: it depends by the quantity S.
      iii. *frq_ cut*: frequency ν_c above which the spectrum of S is zeroed.
      iv. *Napod*: parameter setting for the windowing function (see section (15.3)).
   (b) Outputs:
      i. S: array similar to the input S but filtered by the frequencies above ν_c (*i.e. frq_ cut*)

   (a) Inputs:
      i. *time*: array containing the times coordinate at which the signal S is recorded; units: seconds.
      ii. *Napod*: integer number denoting the order of the Belmont's windowing function
   (b) Outputs: array of length equal to *time* and containing the Belmont's windowing function profile.
      i. *apodgb*:

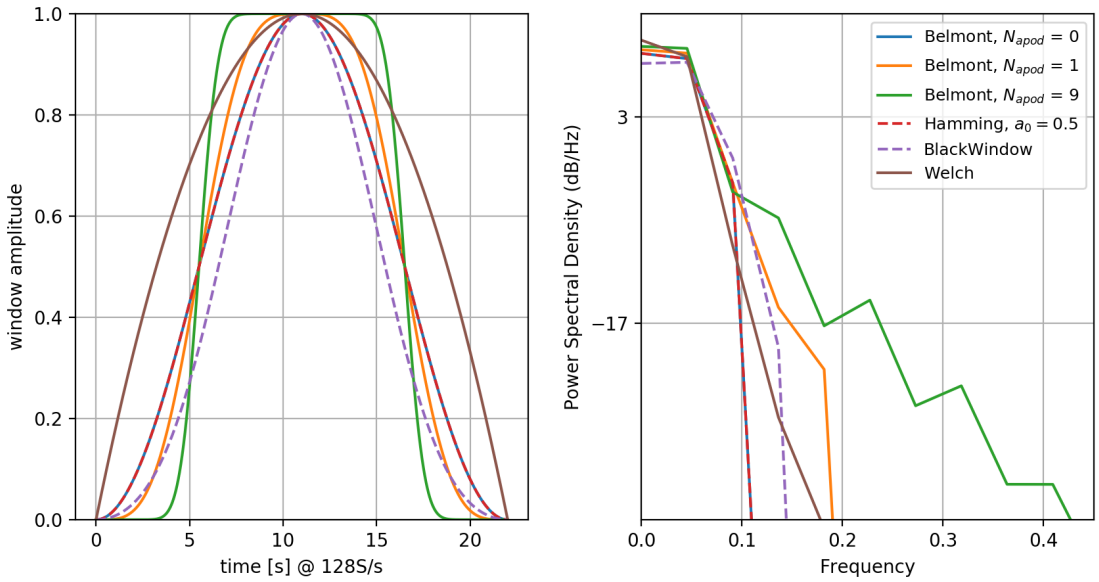

Figure 15.2: *Comparison between the Belmont's windowing functions with $N_apod = \{0, 1, 9\}$ to other standard windowing functions (see legend in the right panel).*

```
def Filter_S(time, S, frq_cut, Napod):
    def func(x, a, b, c):
        return a + b * np.cos(omega/2 * x) + c * np.sin(omega/2 * x)
    #_subtraction of the trend
    omega = 2 * np.pi / (time[-1]-time[0])
    semi_amp, cst = abs(max(S)-min(S))/2, abs(np.mean(S))
    bound1 = [cst - semi_amp, -semi_amp, -semi_amp]
    bound2 = [cst + semi_amp, semi_amp, semi_amp]
    if bound1 == bound2:
        popt, pcov = curve_fit(func, time, S)
    else:
        popt, pcov = curve_fit(func, time, S, bounds=(bound1, bound2))
    S = S - func(time, *popt)
    #_mirroring and windowing
    te, tlen = (time[-1]-time[0])/(len(time)), len(time)
    S = np.concatenate((S[::-1], S, S[::-1],S), axis=0)
    new_time = np.linspace(time[0],time[-1],4*tlen)
    window = Belmont_window(new_time,Napod)
    S = apo_R(S,window)
    #_FFT and filtering
    spectrum, freq = fftpack.fft(S), fftpack.fftfreq(4*tlen,te)
    ind_cut = np.argmin(abs(freq-frq_cut))
    spectrum[ind_cut:4*tlen-ind_cut] = 0
    #_demirroring and adding the trend
    S = deapo_R(ifft(spectrum).real,window)[tlen:2*tlen]
    S = S + func(time, *popt)
    return(S)
```

2. Belmont's function for windowing

```
def Belmont_window(time,Napod):
    apodgb=np.zeros_like(time)
    p=2*Napod+1
    binome=np.zeros(Napod+1)
    puis=np.zeros(Napod+1)
    coeffgb=np.zeros(Napod+1)
    valeur1=0.0
    valeur0=0.0
```

```
    for i in range(0,Napod+1):
        binome[i]= factorial(Napod)/(factorial(i)*factorial(Napod-i))
        puis[i]=2.*i+1.0
        coeffgb[i]=((-1)**i)/(2.0*i+1.0)
        valeur1=valeur1+binome[i]*coeffgb[i]*(-1.0)**puis[i]
        valeur0=valeur0+binome[i]*coeffgb[i]
    k=1.0/(valeur1-valeur0)
    c=valeur1/(valeur1-valeur0)
    apodgb=apodgb+c
    t0=(time.min()+time.max()+time[1]-time[0])/2.0
    for i in range(0,Napod+1):
        apodgb=apodgb-k*(binome[i]*coeffgb[i]* (np.cos(2*np.pi*(time-t0)/(
    time.max()-time.min()+time[1]-time[0])))**(puis[i]))
    return apodgb
```

Chapter

16 The analytical procedure for the minimisation of D

Chapter content

The following sections deal with the analytical procedure adopted to implement the Multi Variate Fit method (section (8.2.3)).

16.1 The problem

The target it to minimise the distance between the LHS and the RHS terms of Equation (8.1), *i.e.* find the unknowns $\partial_{t,0}\mathbf{X}$ and $\partial_{t,0}\mathbf{B}$ that minimise the error (derived from Equation (8.3))

$$D \propto \sum_{p}^{N} \left\{ \sum_{i} \left[\frac{\partial B_i}{\partial t_{sc}} - \left(\frac{\partial X_j}{\partial t_0} \frac{\partial B_i}{\partial X_j} + \frac{\partial B_i}{\partial t_0} \right) \right]^2 \right\}_p \tag{16.1}$$

where $i, j = \{x, y, z\}$, $\partial(...)/\partial t_0 \equiv \partial_{t,0}$ and $\partial(...)/\partial t_{sc} \equiv \partial_{t,sc}$ are the temporal derivatives in, respectively, the magnetopause and the spacecraft frame and N is the number of data points defining the period under exam. Note that both $\partial_{t,0}\mathbf{X}$ and $\partial_{t,0}\mathbf{B}$ are assumed to be constant during this period. Thanks to the high probing rate measurements provided by MMS ($128S/s$, [119]), this requirements reduce approximately to periods $\sim 0.08s$ long, N being chosen in the $[10; 15]$ interval (see section 8.2.3 for a exhaustive explanation). In Equation (16.1) the $\partial_{t,sc}\mathbf{B}$ and the $\overline{\nabla}\mathbf{B}$ terms are known, the latter being computed from data via a temporal derivative and the reciprocal vector method [48] thanks to the multi-point measurements provided by MMS.

16.2 The solution

16.2.1 Procedure

The unknowns $\partial_{t,0}\mathbf{X}$ and $\partial_{t,0}\mathbf{B}$ can be found minimising Equation (16.1) with respect to them. Such a minimisation is done in two steps:

1. $\partial_{t,0}B_i$ with $i = \{x, y, z\}$ are found from $\frac{\partial D}{\partial(\partial_{t,0}B_i)} = 0$
2. $\partial_{t,0}X_i$ with $i = \{x, y, z\}$ are found from $\frac{\partial D}{\partial(\partial_{t,0}X_i)} = 0$ with $\partial_{t,0}B_i$ known from the previous point.

16.2.2 Analytical solutions

1. from $\frac{\partial D}{\partial(\partial_{t,0} B_i)} = 0$ the following solutions are derived:

$$\begin{cases} \dfrac{\partial B_x}{\partial t_0} = \dfrac{1}{N}\left[d_1 - a_1\,\partial_{t,0}X_x - b_1\,\partial_{t,0}X_y - c_1\,\partial_{t,0}X_z\right] & \text{(16.2a)} \\ \dfrac{\partial B_y}{\partial t_0} = \dfrac{1}{N}\left[d_2 - a_2\,\partial_{t,0}X_x - b_2\,\partial_{t,0}X_y - c_2\,\partial_{t,0}X_z\right] & \text{(16.2b)} \\ \dfrac{\partial B_z}{\partial t_0} = \dfrac{1}{N}\left[d_3 - a_3\,\partial_{t,0}X_x - b_3\,\partial_{t,0}X_y - c_3\,\partial_{t,0}X_z\right] & \text{(16.2c)} \end{cases}$$

where

$$\begin{array}{llll} a_1 = \sum_p^N \left(\frac{\partial B_x}{\partial X_x}\right)_p; & b_1 = \sum_p^N \left(\frac{\partial B_x}{\partial X_y}\right)_p; & c_1 = \sum_p^N \left(\frac{\partial B_x}{\partial X_z}\right)_p; & d_1 = \sum_p^N \left(\frac{\partial B_x}{\partial t_{sc}}\right)_p \\ a_2 = \sum_p^N \left(\frac{\partial B_y}{\partial X_x}\right)_p; & b_2 = \sum_p^N \left(\frac{\partial B_y}{\partial X_y}\right)_p; & c_2 = \sum_p^N \left(\frac{\partial B_y}{\partial X_z}\right)_p; & d_2 = \sum_p^N \left(\frac{\partial B_y}{\partial t_{sc}}\right)_p \\ a_3 = \sum_p^N \left(\frac{\partial B_z}{\partial X_x}\right)_p; & b_3 = \sum_p^N \left(\frac{\partial B_z}{\partial X_y}\right)_p; & c_3 = \sum_p^N \left(\frac{\partial B_z}{\partial X_z}\right)_p; & d_3 = \sum_p^N \left(\frac{\partial B_z}{\partial t_{sc}}\right)_p \end{array} \quad \text{(16.3)}$$

2. insert Equations (16.2) with (16.3) in Equations (16.1) and compute $\frac{\partial D}{\partial(\partial_{t,0} X_i)} = 0$. $\frac{\partial D}{\partial(\partial_{t,0} X_x)} = 0$ can be re-organized as (similar procedures are involved for $\frac{\partial D}{\partial(\partial_{t,0} X_y)} = 0$ and $\frac{\partial D}{\partial(\partial_{t,0} X_z)} = 0$ and will not be shown here):

$$e_1\,\partial_{t,0}X_x + e_2\,\partial_{t,0}X_y + e_3\,\partial_{t,0}X_z + e_4 - e_5 = 0 \quad \text{(16.4)}$$

where

$$\begin{array}{l} e_1 = \sum_p^N \left[\left(\frac{\partial B_x}{\partial X_x}\right)_p \left(\frac{\partial B_x}{\partial X_x}\right)_p + \left(\frac{\partial B_y}{\partial X_x}\right)_p \left(\frac{\partial B_y}{\partial X_x}\right)_p + \left(\frac{\partial B_z}{\partial X_x}\right)_p \left(\frac{\partial B_z}{\partial X_x}\right)_p\right] \\ e_2 = \sum_p^N \left[\left(\frac{\partial B_x}{\partial X_y}\right)_p \left(\frac{\partial B_x}{\partial X_x}\right)_p + \left(\frac{\partial B_y}{\partial X_y}\right)_p \left(\frac{\partial B_y}{\partial X_x}\right)_p + \left(\frac{\partial B_z}{\partial X_y}\right)_p \left(\frac{\partial B_z}{\partial X_x}\right)_p\right] \\ e_3 = \sum_p^N \left[\left(\frac{\partial B_x}{\partial X_z}\right)_p \left(\frac{\partial B_x}{\partial X_x}\right)_p + \left(\frac{\partial B_y}{\partial X_z}\right)_p \left(\frac{\partial B_y}{\partial X_x}\right)_p + \left(\frac{\partial B_z}{\partial X_z}\right)_p \left(\frac{\partial B_z}{\partial X_x}\right)_p\right] \\ e_4 = \frac{\partial B_x}{\partial t_0} \sum_p^N \left[\left(\frac{\partial B_x}{\partial X_x}\right)_p\right] + \frac{\partial B_y}{\partial t_0} \sum_p^N \left[\left(\frac{\partial B_y}{\partial X_x}\right)_p\right] + \frac{\partial B_z}{\partial t_0} \sum_p^N \left[\left(\frac{\partial B_z}{\partial X_x}\right)_p\right] \\ e_5 = \sum_p^N \left[\left(\frac{\partial B_x}{\partial t_{sc}}\right)_p \left(\frac{\partial B_x}{\partial X_x}\right)_p + \left(\frac{\partial B_y}{\partial t_{sc}}\right)_p \left(\frac{\partial B_y}{\partial X_x}\right)_p + \left(\frac{\partial B_z}{\partial t_{sc}}\right)_p \left(\frac{\partial B_z}{\partial X_x}\right)_p\right] \end{array} \quad \text{(16.5)}$$

As can be observed, there is a latent dependency on $\partial_{t,0}X_x$, $\partial_{t,0}X_y$ and $\partial_{t,0}X_z$ due to the presence of the LHS terms of Equations (16.2) inside e_4. Using Equations (16.2) in the definition of e_4 (Eq. (16.5)) and reordering Equation (16.4) with respect to the terms $\partial_{t,0}X_x$, $\partial_{t,0}X_y$ and $\partial_{t,0}X_z$, we get

$$A_1\,\partial_{t,0}X_x + B_1\,\partial_{t,0}X_y + C_1\,\partial_{t,0}X_z = D_1 \quad \text{(16.6)}$$

where

$$\begin{cases} A_1 = A_{11} + A_{12} + A_{13} & \text{(16.7a)} \\ B_1 = B_{11} + B_{12} + B_{13} & \text{(16.7b)} \\ C_1 = C_{11} + C_{12} + C_{13} & \text{(16.7c)} \\ D_1 = D_{11} + D_{12} + D_{13} & \text{(16.7d)} \end{cases}$$

and (using definitions (16.3))

$$\begin{cases} A_{11} = \sum_p^N \left[\left(\frac{\partial B_x}{\partial X_x} \right)_p \left(\frac{\partial B_x}{\partial X_x} \right)_p \right] - \frac{a_1 a_1}{N} & \text{(16.8a)} \\ A_{12} = \sum_p^N \left[\left(\frac{\partial B_y}{\partial X_x} \right)_p \left(\frac{\partial B_y}{\partial X_x} \right)_p \right] - \frac{a_2 a_2}{N} & \text{(16.8b)} \\ A_{13} = \sum_p^N \left[\left(\frac{\partial B_z}{\partial X_x} \right)_p \left(\frac{\partial B_z}{\partial X_x} \right)_p \right] - \frac{a_3 a_3}{N} & \text{(16.8c)} \\ B_{11} = \sum_p^N \left[\left(\frac{\partial B_x}{\partial X_y} \right)_p \left(\frac{\partial B_x}{\partial X_x} \right)_p \right] - \frac{b_1 a_1}{N} & \text{(16.8d)} \\ B_{12} = \sum_p^N \left[\left(\frac{\partial B_y}{\partial X_y} \right)_p \left(\frac{\partial B_y}{\partial X_x} \right)_p \right] - \frac{b_2 a_2}{N} & \text{(16.8e)} \\ B_{13} = \sum_p^N \left[\left(\frac{\partial B_z}{\partial X_y} \right)_p \left(\frac{\partial B_z}{\partial X_x} \right)_p \right] - \frac{b_3 a_3}{N} & \text{(16.8f)} \\ C_{11} = \sum_p^N \left[\left(\frac{\partial B_x}{\partial X_z} \right)_p \left(\frac{\partial B_x}{\partial X_x} \right)_p \right] - \frac{c_1 a_1}{N} & \text{(16.8g)} \\ C_{12} = \sum_p^N \left[\left(\frac{\partial B_y}{\partial X_z} \right)_p \left(\frac{\partial B_y}{\partial X_x} \right)_p \right] - \frac{c_2 a_2}{N} & \text{(16.8h)} \\ C_{13} = \sum_p^N \left[\left(\frac{\partial B_z}{\partial X_z} \right)_p \left(\frac{\partial B_z}{\partial X_x} \right)_p \right] - \frac{c_3 a_3}{N} & \text{(16.8i)} \\ D_{11} = \sum_p^N \left[\left(\frac{\partial B_x}{\partial t_{sc}} \right) \left(\frac{\partial B_x}{\partial X_x} \right)_p \right] - \frac{a_1}{N} \sum_p^N \left(\frac{\partial B_x}{\partial t_{sc}} \right) & \text{(16.8j)} \\ D_{12} = \sum_p^N \left[\left(\frac{\partial B_y}{\partial t_{sc}} \right) \left(\frac{\partial B_y}{\partial X_x} \right)_p \right] - \frac{a_2}{N} \sum_p^N \left(\frac{\partial B_y}{\partial t_{sc}} \right) & \text{(16.8k)} \\ D_{13} = \sum_p^N \left[\left(\frac{\partial B_z}{\partial t_{sc}} \right) \left(\frac{\partial B_z}{\partial X_x} \right)_p \right] - \frac{a_3}{N} \sum_p^N \left(\frac{\partial B_z}{\partial t_{sc}} \right) & \text{(16.8l)} \end{cases}$$

Chapter

17 Determination of L_y

Chapter content

17.1 The problem

Here we compute the maximum dimensions L_y of the simulation box (hereafter "box") that allows not to take into account the curvature of the magnetopause. For the sake of simplicity, we suppose the box to be 2D, we being interested in simulating a 2D region across the magnetopause.

17.2 The solution

In the case of the spacecraft crossings analysed in this thesis (*Cr2* for instance), the crossing happened close to the equatorial plane. Therefore we can solve the problem in a 2D perspective as done in Figure (17.1), where a quasi-northward view of the profile of the magnetopause is shown. This profile is obtained as the intersection between the magnetosphere and the plane containing the centre of the Earth and the spacecraft position during the magnetopause crossing. Let's define some quantities:

- θ the angular position of the box;
- $\mathbf{N}$: the direction normal to the magnetopause at angular position θ;
- R_θ: the curvature of the magnetopause profile at angular position θ,
- s: the thickness of the magnetopause (*i.e.* the thickness of the purple line)
- $L_x = \nu s$: the thickness of the box in the direction N. ν depends by considerations introduced in section (12.2.2) and will be set to $\sim 12 - 15$;
- L_y the length of the box in the tangential direction to the magnetopause;
- c: the distance between the centre of one of the smallest sides of the box and the point of intersection between this side and the magnetopause.

Assuming that L_y is small enough in order R_θ to be constant within the box, the aim is to compute L_y in order $c \ll L_x/2$. Otherwise, the deformation of the magnetopause near the edges of the box should be taken into account in modelling the magnetopause by numerical simulations.

Since $c = R_\theta(1 - cos(\theta))$ and $\frac{L_y}{2} = R_\theta sin(\theta)$, the criterion $c \ll L_x/2$ can be written as $1 \mp \sqrt{1 - (L_y/(2R_\theta))^2} \ll L_x/(2R_\theta)$. The change of variables $\alpha = L_y/(2R_\theta)$ and $\beta = L_x/(2R_\theta)$ allows to simplify the problem. From the last change it can be seen that $L_y \ll \sqrt{2L_xR_\theta}$.

For the *Cr2* case, $\theta \sim 45°$. Figure (17.2) shows the values of R_θ as a function of θ and ϕ (ϕ being the angular coordinate that describes the positions out of plane the plane of Figure (17.1)). In case $L_x = 120d_i$ and $R_\theta \sim 18R_E$ where $R_E = 6378$ km and $d_i = 78$ km, L_y should be $\ll 7.26R_E$. The boxes adopted for the numerical simulations presented in this thesis do not exceed $0.73R_E$ in L_y.

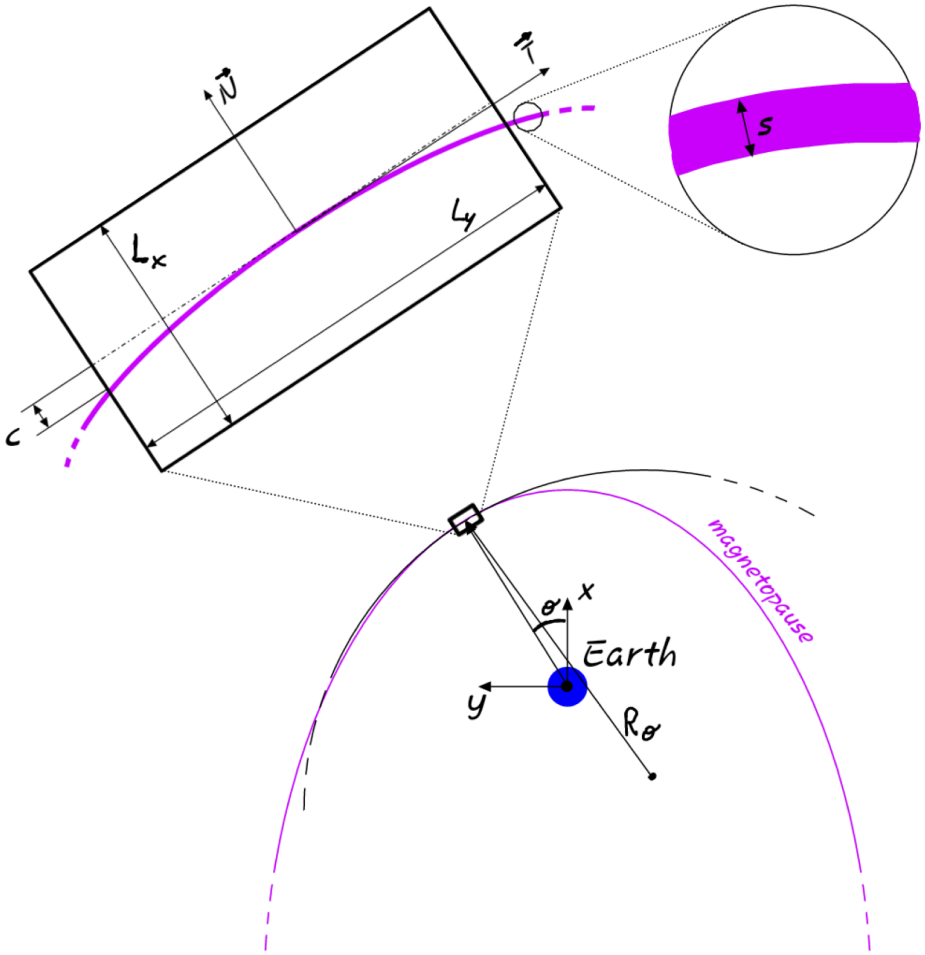

Figure 17.1: *Position of the region simulated by the numerical simulations presented in this thesis (bottom sketch) and zoom onto the simulation box (top sketch). The magnetopause is drawn in purple. The Earth is the blue circle. Superposed to the magnetopause, the sketch shows the circle of radius R_θ that locally approximates the magnetopause shape at spherical position θ. The bottom sketch adopts GSE coordinates; the sketch of the simulation box shows the normal (**N**) and tangential (**T**) directions frame. A further zoom in the top right corner of the figure shows the thickness of the magnetopause. The sketch is not to scale.*

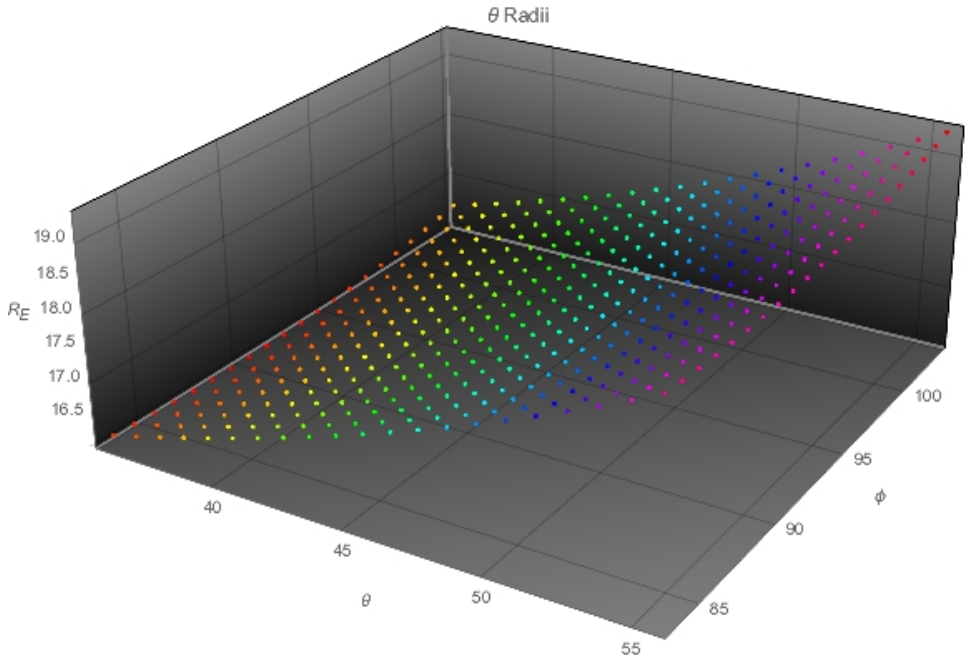

Figure 17.2: *Curvature radius of the Shue surface [46] as a function of the spherical coordinates θ and the ϕ. The interval shown is centred on the angular position of the Cr2 event ($\{\theta, \phi\} \approx \{45, 93\}^\circ$).*

Chapter

18 Determination of Γ, Π and discussion on temperature limits

Chapter content

This section aims at showing the procedure to obtain Equations (12.16) and (12.17). As a direct application, it is discussed why the 3fluid model can not reproduce a total ion temperature T_i higher than the hot ion population temperature T_{ih}, as observed in section (14.1) and Paper 2.

18.1 Γ and ϒ

Let's define $\Gamma \equiv n_{ic}/n_i$ and $\Upsilon \equiv T_{ih}/T_{ic}$ (section (12.3.1)). From Equation (12.14), the following steps occur:

$$\begin{aligned} n_i T_i &= n_{ic}T_{ic} + n_{ih}T_{ih} \\ &\overset{\Gamma}{\Downarrow} \\ &= n_i\Gamma T_{ic} + n_i\left(1-\Gamma\right)T_{ih} \\ &= n_i T_{ic}\left[\Gamma + \left(1-\Gamma\right)\frac{T_{ih}}{T_{ic}}\right] \\ &\overset{\Upsilon}{\Downarrow} \\ &= n_i T_{ic}\left[\Gamma + \left(1-\Gamma\right)\Upsilon\right] \end{aligned} \tag{18.1}$$

Equation (18.1) can be easily solved for Γ. The solution is Equation (12.16).
In the same way, Equation (18.1) can be exploited to obtain the definition (12.17).

18.2 $T_{ih} > T_i$

From Equation (12.13) it is clear that $0 \leq \Gamma \leq 1$. Using the Equation (12.16), the previous limitation for Γ becomes

$$0 \leq \frac{\Upsilon - \frac{T_i}{T_{ic}}}{\Upsilon - 1} \leq 1 \tag{18.2}$$

where $\Upsilon \equiv T_{ih}/T_{ic}$. The conditions (18.2), joint with the assumption $T_{ic} < T_{ih}$, become

$$T_{ic} \leq T_i \leq T_{ih} \tag{18.3}$$

The condition of homogeneity for T_{ic} and T_{ih} makes equations (18.3) valid also locally.

Chapter

19 Modification of temperatures for numerical implementation

Chapter content

19.1 The problem

According to the analytical implementation of the 3fluid equilibrium, the magnetosheath and the magnetospheric densities disappear respectively in the magnetosphere and in the magnetosheath (section (12.3.1)). Nevertheless, the numerical implementation need for bulk flows $\mathbf{U}$ that are computed from currents $\mathbf{J}$ and densities n as $\mathbf{U} = \mathbf{J}/n$. Null values of densities may cause singularities and therefore they are not allowed.

19.2 The solution

To avoid the problem of singularities caused by potentially null densities, two parameters $\epsilon^{(c)} \ll 1$ and $\epsilon^{(h)} \ll 1$ are introduced in order to modify the large scale profiles of densities. In particular we have:

$$n_{ic}^{(h)} = \epsilon^{(h)} n_i^{(h)} \tag{19.1}$$

and

$$n_{ih}^{(c)} = \epsilon^{(c)} n_i^{(c)} \tag{19.2}$$

with $n_i^{(h)}$ being the density of the total ion population in the magnetospheric region and $n_i^{(c)}$ the density of the total ion population in the magnetosheath region. From the definitions of $n_i^{(h)}$ and $n_i^{(c)}$ and from Equation (12.13), the density of the ion hot population in the magnetosheath region $n_{ih}^{(c)}$ and the density of the ion cold population in the magnetosheath region $n_{ic}^{(c)}$ are, respectively,

$$n_{ih}^{(h)} = n_i^{(h)} - n_{ic}^{(h)} = n_i^{(h)} - \epsilon^{(h)} n_i^{(h)} = \left(1 - \epsilon^{(h)}\right) n_i^{(h)} \tag{19.3}$$

and

$$n_{ic}^{(c)} = n_i^{(c)} - n_{ih}^{(c)} = n_i^{(c)} - \epsilon^{(c)} n_i^{(c)} = \left(1 - \epsilon^{(c)}\right) n_i^{(c)} \tag{19.4}$$

In the magnetospheric region, $n_i^{(h)}T_i^{(h)}$ is:

$$\begin{array}{rcl} n_i^{(h)}T_i^{(h)} & = & n_{ic}^{(h)}T_{ic}^{(h)} + n_{ih}^{(h)}T_{ih}^{(h)} \\ & \underset{Eq.(19.1)}{\Downarrow} & \\ & = & \epsilon^{(h)}n_i^{(h)}T_{ic}^{(h)} + n_{ih}^{(h)}T_{ih}^{(h)} \\ & \underset{Eq.(19.3)}{\Downarrow} & \\ & = & \epsilon^{(h)}n_i^{(h)}T_{ic}^{(h)} + \left(1-\epsilon^{(h)}\right)n_i^{(h)}T_{ih}^{(h)} \\ & = & \epsilon^{(h)}n_i^{(h)}\left(T_{ic}^{(h)} - T_{ih}^{(h)}\right) + n_i^{(h)}T_{ih}^{(h)} \end{array} \tag{19.5}$$

whereas in the magnetosheath region $n_i^{(c)}T_i^{(c)}$ is:

$$\begin{array}{rcl} n_i^{(c)}T_i^{(c)} & = & n_{ic}^{(c)}T_{ic}^{(c)} + n_{ih}^{(c)}T_{ih}^{(c)} \\ & \underset{Eq.(19.4)}{\Downarrow} & \\ & = & \left(1-\epsilon^{(c)}\right)n_i^{(c)}T_{ic}^{(c)} + n_{ih}^{(c)}T_{ih}^{(c)} \\ & \underset{Eq.(19.2)}{\Downarrow} & \\ & = & \left(1-\epsilon^{(c)}\right)n_i^{(c)}T_{ic}^{(c)} + \epsilon^{(c)}n_i^{(c)}T_{ih}^{(c)} \\ & = & n_i^{(c)}T_{ic}^{(c)} + \epsilon^{(c)}n_i^{(c)}\left(T_{ih}^{(c)} - T_{ic}^{(c)}\right) \end{array} \tag{19.6}$$

Summarising, the following system is found:

$$\begin{cases} T_i^{(h)} = T_{ih}^{(h)} - \epsilon^{(h)}\left(T_{ih}^{(h)} - T_{ic}^{(h)}\right) \\ T_i^{(c)} = T_{ic}^{(c)} + \epsilon^{(c)}\left(T_{ih}^{(c)} - T_{ic}^{(c)}\right) \end{cases} \tag{19.7}$$

From system (19.7) the relations $T_{ic} = T_{ic}\left(T_i^{(h)}, T_i^{(c)}\right)$ and $T_{ih} = T_{ih}\left(T_i^{(h)}, T_i^{(c)}\right)$ can be easily found remembering that the cold and hot temperatures are considered homogeneous: $T_{ic}^{(h)} = T_{ic}^{(c)} \equiv T_{ic}$ and $T_{ih}^{(h)} = T_{ih}^{(c)} \equiv T_{ih}$.

System (19.7) can be solved for T_{ic} and T_{ih}. Let's write system (19.7) as

$$\overline{\overline{M}} \cdot \begin{pmatrix} T_{ic} & T_{ih} \end{pmatrix}^T = \begin{pmatrix} T_i^{(h)} & T_i^{(c)} \end{pmatrix}^T \tag{19.8}$$

with

$$\overline{\overline{M}} \equiv \begin{pmatrix} \epsilon^{(h)} & 1-\epsilon^{(h)} \\ 1-\epsilon^{(c)} & \epsilon^{(c)} \end{pmatrix} \tag{19.9}$$

The determinant of $\overline{\overline{M}}$ is

$$\begin{array}{rcl} det\,(M) & = & \left|\begin{pmatrix} \epsilon^{(h)} & 1-\epsilon^{(h)} \\ 1-\epsilon^{(c)} & \epsilon^{(c)} \end{pmatrix}\right| \\ & = & \epsilon^{(h)}\epsilon^{(c)} - \left(1-\epsilon^{(h)}\right)\left(1-\epsilon^{(c)}\right) \\ & = & \epsilon^{(c)} + \epsilon^{(h)} - 1 \end{array} \tag{19.10}$$

This means that $\epsilon^{(c)} + \epsilon^{(h)} \neq 1$. Ultimately, the expressions for T_{ic} and T_{ih} are:

$$T_{ic} = \frac{\epsilon^{(c)}T_i^{(h)} - \left(1-\epsilon^{(h)}\right)T_i^{(c)}}{\epsilon^{(c)} + \epsilon^{(h)} - 1} \tag{19.11}$$

and

$$T_{ih} = \frac{\epsilon^{(h)}T_i^{(c)} - \left(1-\epsilon^{(c)}\right)T_i^{(h)}}{\epsilon^{(c)} + \epsilon^{(h)} - 1} \tag{19.12}$$

Chapter

20 A sketch for a 4fluid algorithm

Chapter content

This appendix show a possible - but problematic - scheme to advance in time the set of fluid equations describing a 4fluid plasma. Differently by the 3fluid equation set, in this case the plasma is composed by two ions and two electrons populations. Section (20.1) suggests the order with which the equations shall be called to optimise the scheme, both from a observational and a computational point of view. The problems arising from this scheme are analysed in section (20.2).

20.1 A temporal advancing scheme for the 4fluid equations

The scheme used here is similar to that used for the 3fluid scheme (section (12.2.1)). For the sake of simplicity, here we only suggest the equations to be used without explicit expansions. Where needed, the quantities to be updated are marked by an asterisk. Equations are presented in a a-dimensional form using the normalisation factors introduced in section (12.1). The index β means that the equation concerns both the hot (ih) and the cold (ic) populations. We suppose the ion and electron densities, temperatures and bulk velocities to be known from data at $t = 0$. The electric and magnetic fields have to be known as well. d_e^2 is equivalent to m_e/m_i.

1. ion densities:
$$\frac{\partial n_{i,\beta}}{\partial t} + \overline{\nabla}_x \cdot (n_{i,\beta}\mathbf{U}_{i,\beta}) = 0 \tag{20.1}$$

2. ion momenta:
$$\frac{\partial (n_{i,\beta}\mathbf{U}_{i,\beta})}{\partial t} + \overline{\nabla}_x \cdot (n_{i,\beta}T_{i,\beta}\mathbf{I} + n_{i,\beta}\mathbf{U}_{i,\beta}\mathbf{U}_{i,\beta}) - n_{i,\beta}\,(\mathbf{E} + \mathbf{U}_{i,\beta} \times \mathbf{B}) = 0 \tag{20.2}$$

3. ion temperatures ($T_{i,\beta} = S_{i,\beta}(n_{i,\beta})^{\gamma-2}$):
$$\frac{\partial S_{i,\beta}}{\partial t} + \mathbf{U}_{i,\beta} \cdot \overline{\nabla}_x S_{i,\beta} = 0 \tag{20.3}$$

4. magnetic field:
$$\frac{\partial \mathbf{B}}{\partial t} + \overline{\nabla}_x \times \mathbf{E} = 0 \tag{20.4}$$

5. electron densities:

(a) define $n^*_{e,+} = n^*_{i,h} + n^*_{i,c}$ and $n_{e,-} = n_{e,h} - n_{e,c}$

(b) compute $n^*_{e,-}$ ($\equiv n^*_{e,h} - n^*_{e,c}$) from

$$\frac{\partial n_{e,-}}{\partial t} + \overline{\nabla}_x \cdot (n_{e,h}\mathbf{U}_{e,h} - n_{e,c}\mathbf{U}_{e,c}) = 0 \tag{20.5}$$

(c) obtain $n^*_{e,h} = \frac{n^*_{e,+}+n^*_{e,-}}{2}$ and $n^*_{e,c} = \frac{n^*_{e,+}-n^*_{e,-}}{2}$

6. electron temperatures ($T_{e,\beta} = S_{e,\beta}(n_{e,\beta})^{\gamma-2}$):

$$\frac{\partial S_{e,\beta}}{\partial t} + \mathbf{U}_{e,\beta} \cdot \overline{\nabla}_x S_{e,\beta} = 0 \tag{20.6}$$

7. electron momenta:

(a) define $(n^*_e\mathbf{U}^*_e)_+ = n^*_{i,h}\mathbf{U}^*_{i,h} + n^*_{i,c}\mathbf{U}^*_{i,c}$ and $(n_e\mathbf{U}_e)_- = n_{e,h}\mathbf{U}_{e,h} - n_{e,c}\mathbf{U}_{e,c}$

(b) compute $(n^*_e\mathbf{U}^*_e)_-$ ($\equiv n^*_{e,h}\mathbf{U}^*_{e,h} - n^*_{e,c}\mathbf{U}^*_{e,c}$) from

$$\begin{aligned}\frac{\partial (n_e\mathbf{U}_e)_-}{\partial t} + \overline{\nabla}_x \cdot [(n_{e,h}\mathbf{U}_{e,h}\mathbf{U}_{e,h} - n_{e,c}\mathbf{U}_{e,c}\mathbf{U}_{e,c})] + \\ + \frac{1}{d_e^2}\left\{\overline{\nabla}_x \cdot [(n_{e,h}T_{e,h} - n_{e,c}T_{e,c})\,\mathbf{I}]\right\} + \\ + \frac{1}{d_e^2}\left\{[(n_{e,h} - n_{e,c})\,\mathbf{E} + (n_{e,h}\mathbf{U}_{e,h} - n_{e,c}\mathbf{U}_{e,c}) \times \mathbf{B}]\right\} = 0\end{aligned} \tag{20.7}$$

(c) obtain $n^*_{e,h}\mathbf{U}^*_{e,h} = \left[(n^*_e\mathbf{U}^*_e)_+ + (n^*_e\mathbf{U}^*_e)_-\right]/2$ and $n^*_{e,c}\mathbf{U}^*_{e,c} = \left[(n^*_e\mathbf{U}^*_e)_+ - (n^*_e\mathbf{U}^*_e)_-\right]/2$

8. compute the electric field from:

$$\begin{aligned}d_e^2\frac{\partial (n^*_e\mathbf{U}^*{}_e)_+}{\partial t} + d_e^2\overline{\nabla}_x \cdot \left[\left(n^*_{e,h}\mathbf{U}^*_{e,h}\mathbf{U}^*_{e,h} + n^*_{e,c}\mathbf{U}^*{}_{e,c}\mathbf{U}^*{}_{e,c}\right)\right] + \\ + \left\{\overline{\nabla}_x \cdot \left[\left(n^*_{e,h}T^*_{e,h} + n^*_{e,c}T^*_{e,c}\right)\mathbf{I}\right]\right\} + \\ + \left(n^*_{e,h} + n^*_{e,c}\right)\mathbf{E}^* + \left(n^*_{e,h}\mathbf{U}^*{}_{e,h} + n^*_{e,c}\mathbf{U}^*{}_{e,c}\right) \times \mathbf{B}^* = 0\end{aligned} \tag{20.8}$$

where $\frac{\partial (n^*_e\mathbf{U}^*{}_e)_+}{\partial t}$ can be guessed using $n_{e,c}\mathbf{U}_{e,c}$, $n_{e,h}\mathbf{U}_{e,h}$, $n^*_{e,c}\mathbf{U}^*_{e,c}$ and $n^*_{e,h}\mathbf{U}^*_{e,c}$.

20.2 Analysis of the problems

The scheme introduced in the previous section (20.1) suffers from the following problems:

1. in the beginning of the advancing scheme, $\mathbf{E}$ is assumed to be known from data. Anyway it is a function of $n_{e,\beta}$, $T_{e,\beta}$, $\mathbf{U}_{e,\beta}$ and $\mathbf{B}$ trough Equation (20.8) simplified by the equilibrium condition ($\partial(...)/\partial t = 0$). If data do not match, the quality of data should be evaluated in order to chose for $\mathbf{E}$ between its measurement or its computation.

2. d_e^2 can not be zero since it would lead to singularities in Equation (20.7).

3. in Equation (20.8) it is safer to compute $\mathbf{E}$ as a function of $(n_e\mathbf{U}_e)_+$ instead of $(n_e\mathbf{U}_e)_-$ because otherwise the denominator would be $n_{e,h} - n_{e,c}$ which implies singularities.

4. the term $\frac{\partial (n^*_e\mathbf{U}^*{}_e)_+}{\partial t}$ may suffer from inaccuracies that could lead to numerical instabilities.

Part VII

Lists

Bibliography

[1] S. Chapman and V. C. A. Ferraro. "A new theory of magnetic storms". In: *Terrestrial Magnetism and Atmospheric Electricity* 36.2 (Jan. 1931), pp. 77–97. ISSN: 0096-8013. DOI: 10.1029/TE036i002p00077.

[2] S. Chapman and V. C. A. Ferraro. "A new theory of magnetic storms". In: *Terrestrial Magnetism and Atmospheric Electricity* 38.2 (1933), pp. 79–96. DOI: 10.1029/TE038i002p00079.

[3] G. I. Taylor. "The Spectrum of Turbulence". In: *Proceedings of the Royal Society of London Series A* 164.919 (1938), pp. 476–490. DOI: 10.1098/rspa.1938.0032.

[4] S. Chapman and V. C. A. Ferraro. "The theory of the first phase of a geomagnetic storm". In: *Terrestrial Magnetism and Atmospheric Electricity* 45.3 (Sept. 1940), pp. 245–268. ISSN: 0096-8013. DOI: 10.1029/TE045i003p00245.

[5] F. De Hoffmann and E. Teller. "Magneto-Hydrodynamic Shocks". In: *Phys. Rev.* 80 (4 1950), pp. 692–703. DOI: 10.1103/PhysRev.80.692.

[6] V. C. A. Ferraro. "On the theory of the first phase of a geomagnetic storm: A new illustrative calculation based on an idealised (plane not cylindrical) model field distribution". In: *Journal of Geophysical Research* 57.1 (Mar. 1952), pp. 15–49. ISSN: 0148-0227. DOI: 10.1029/JZ057i001p00015.

[7] J. W. Dungey. "Electrodynamics of the Outer Atmosphere". In: *Physics of the Ionosphere*. 1955, p. 229.

[8] E. N. Parker. "On the geomagnetic storm effect". In: *Journal of Geophysical Research* 61.4 (Dec. 1956), pp. 625–637. ISSN: 0148-0227. DOI: 10.1029/JZ061i004p00625.

[9] L. Biermann. "Solar corpuscular radiation and the interplanetary gas". In: *The Observatory* 77 (1957), pp. 109–110.

[10] Harold Grad and Hanan Rubin. "Hydromagnetic equilibria and force-free fields". In: *Journal of Nuclear Energy (1954)* 7.3-4 (1958), pp. 284–285.

[11] E N. Parker. "Dynamics of the Interplanetary Gas and Magnetic Fields". In: *The Astrophysical Journal* 128 (Oct. 1958), p. 664. DOI: 10.1086/146579.

[12] C. P. Sonett, D. L. Judge, and J. M. Kelso. "Evidence concerning instabilities of the distant geomagnetic field: Pioneer I". In: *Journal of Geophysical Research (1896-1977)* 64.8 (1959), pp. 941–943. DOI: 10.1029/JZ064i008p00941.

[13] E. J. Smith et al. "Characteristics of the extraterrestrial current system: Explorer VI and Pioneer V". In: *Journal of Geophysical Research (1896-1977)* 65.6 (1960), pp. 1858–1861. DOI: 10.1029/JZ065i006p01858.

[14] C. P. Sonett et al. "A radial rocket survey of the distant geomagnetic field". In: *Journal of Geophysical Research (1896-1977)* 65.1 (1960), pp. 55–68. DOI: 10.1029/JZ065i001p00055.

[15] J. W. Dungey. "Interplanetary Magnetic Field and the Auroral Zones". In: *Phys. Rev. Lett.* 6 (2 1961), pp. 47–48. DOI: 10.1103/PhysRevLett.6.47.

[16] Edward J. Smith. "A comparison of Explorer VI and Explorer X magnetometer data". In: *Journal of Geophysical Research (1896-1977)* 67.5 (1962), pp. 2045–2049. DOI: 10.1029/JZ067i005p02045.

[17] L. J. Cahill and P. G. Amazeen. "The boundary of the geomagnetic field". In: *Journal of Geophysical Research (1896-1977)* 68.7 (1963), pp. 1835–1843. DOI: 10.1029/JZ068i007p01835.

[18] H. P. Furth, J. Killeen, and M. N. Rosenbluth. "Finite-Resistivity Instabilities of a Sheet Pinch". In: *Physics of Fluids* 6 (1963), pp. 459–484. DOI: 10.1063/1.1706761.

[19] J. P. Heppner et al. "Explorer 10 magnetic field measurements". In: *Journal of Geophysical Research* 68.1 (Jan. 1963), pp. 1–46. ISSN: 0148-0227. DOI: 10.1029/JZ068i001p00001.

[20] VD Shafranov. "Plasma equilibrium in a magnetic field". In: *Reviews of plasma physics* 2 (1966), p. 103.

[21] B. U. Ö. Sonnerup and L. J. Cahill. "Magnetopause structure and attitude from Explorer 12 observations". In: *Journal of Geophysical Research: Space Physics* 72.1 (1967), pp. 171–183. ISSN: 2156-2202. DOI: 10.1029/JZ072i001p00171.

[22] Paul J. Channell. "Exact Vlasov-Maxwell equilibria with sheared magnetic fields". In: *The Physics of Fluids* 19.10 (1976), pp. 1541–1545. DOI: 10.1063/1.861357.

[23] F. J. Harris. "On the use of windows for harmonic analysis with the discrete Fourier transform". In: *Proceedings of the IEEE* 66.1 (1978), pp. 51–83. ISSN: 0018-9219. DOI: 10.1109/PROC.1978.10837.

[24] C. T. Russell and R. C. Elphic. "Initial ISEE magnetometer results: magnetopause observations". In: *Space Science Reviews* 22.6 (1978), pp. 681–715. ISSN: 1572-9672. DOI: 10.1007/BF00212619.

[25] Jean Berchem and C. T. Russell. "The thickness of the magnetopause current layer: ISEE 1 and 2 observations". In: *Journal of Geophysical Research: Space Physics* 87.A4 (1982), pp. 2108–2114. DOI: 10.1029/JA087iA04p02108.

[26] L. C. Lee and J. G. Roederer. "Solar wind energy transfer through the magnetopause of an open magnetosphere". In: *Journal of Geophysical Research: Space Physics* 87.A3 (1982), pp. 1439–1444. DOI: 10.1029/JA087iA03p01439.

[27] K. Rönnmark. *KGI Report No. 179*. 1982.

[28] K. Rönnmark. "Computation of the dielectric tensor of a Maxwellian plasma". In: *Plasma Physics* 25.6 (1983), pp. 699–701. DOI: 10.1088/0032-1028/25/6/007.

[29] C. T. Russell et al. "Multiple spacecraft observations of interplanetary shocks: Four spacecraft determination of shock normals". In: *Journal of Geophysical Research: Space Physics* 88.A6 (1983), pp. 4739–4748. DOI: 10.1029/JA088iA06p04739.

[30] Margaret Galland Kivelson and Pu Zu-Yin. "The Kelvin-Helmholtz instability on the magnetopause". In: *Planetary and Space Science* 32.11 (1984), pp. 1335–1341. ISSN: 0032-0633. DOI: https://doi.org/10.1016/0032-0633(84)90077-1.

[31] Dennis V Kent and Felix M Gradstein. "A Jurassic to recent chronology". In: (1986).

[32] "Analysis of multipoint magnetometer data". In: *Advances in Space Research* 8.9 (1988), pp. 273–277. ISSN: 0273-1177. DOI: https://doi.org/10.1016/0273-1177(88)90141-X.

[33] C. Canuto. *Spectral methods in fluid dynamics*. Springer series in computational physics. Springer-Verlag, 1988. ISBN: 9783540522058. URL: https://books.google.it/books?id=2TbvAAAAMAAJ.

[34] J. Labelle and R. A. Treumann. "Plasma waves at the dayside magnetopause". In: *Space Science Reviews* 47 (1988), pp. 175–202. DOI: 10.1007/BF00223240.

[35] Gérard Belmont and Gérard Chanteur. "Advances in magnetopause Kelvin-Helmholtz instability studies". In: *Physica Scripta* 40.1 (1989), pp. 124–128. DOI: 10.1088/0031-8949/40/1/018.

[36] S. W. H. Cowley and C. J. Owen. "A simple illustrative model of open flux tube motion over the dayside magnetopause". In: *Planetary and Space Science* 37 (1989), pp. 1461–1475. DOI: 10.1016/0032-0633(89)90116-5.

[37] N.A. Tsyganenko. "A solution of the Chapman-Ferraro problem for an ellipsoidal magnetopause". In: *Planetary and Space Science* 37.9 (1989), pp. 1037–1046. ISSN: 0032-0633. DOI: https://doi.org/10.1016/0032-0633(89)90076-7.

[38] Sanjiva K. Lele. "Compact finite difference schemes with spectral-like resolution". In: *Journal of Computational Physics* 103.1 (1992), pp. 16–42. ISSN: 0021-9991. DOI: https://doi.org/10.1016/0021-9991(92)90324-R.

[39] G Chanteur and F Mottez. "Geometrical tools for Cluster data analysis". In: *Spatio-temporal analysis for resolving plasma turbulence (START), ESA WWP* 47 (1993), pp. 341–344.

[40] L. Rezeau, A. Roux, and C. T. Russell. "Characterization of small-scale structures at the magnetopause from ISEE measurements". In: *Journal of Geophysical Research: Space Physics* 98.A1 (1993), pp. 179–186. DOI: 10.1029/92JA01668.

[41] R.J. Goldston and P.H. Rutherford. *Introduction to Plasma Physics*. CRC Press, 1995. ISBN: 9781439822074. URL: https://books.google.fr/books?id=7kM7yEFUGnAC.

[42] "On the determination of a moving MHD structure: Minimization of the residue of integrated Faraday's equation". English. In: *Earth, Planets and Space* 48.5-6 (Jan. 1996), pp. 603–614. ISSN: 1343-8832.

[43] Q. Chen, A. Otto, and L. C. Lee. "Tearing instability, Kelvin-Helmholtz instability, and magnetic reconnection". In: *Journal of Geophysical Research: Space Physics* 102.A1 (1997), pp. 151–161. DOI: 10.1029/96JA03144.

[44] C.P. Escoubet, R. Schmidt, and M.L. Goldstein. "Cluster - Science and mission overview". In: *Space Science Reviews* 79.1 (1997), pp. 11–32. DOI: 10.1023/A:1004923124586.

[45] Götz Paschmann. "Observational Evidence for Transfer of Plasma Across the Magnetopause". In: *Space Science Reviews* 80.1 (1997), pp. 217–234. ISSN: 1572-9672. DOI: 10.1023/A:1004926004806.

[46] J.-H. Shue et al. "A new functional form to study the solar wind control of the magnetopause size and shape". In: *Journal of Geophysical Research: Space Physics* 102.A5 (1997), pp. 9497–9511. DOI: 10.1029/97JA00196.

[47] J. Büchner, J.-P. Kuska, and H. Wiechen. "Numerical Modelling and Simulation for Multi-Spacecraft Data Analysis: Approaches and Examples". In: *ISSI Scientific Reports Series* 1 (1998), pp. 449–478.

[48] G. Chanteur. "Spatial Interpolation for Four Spacecraft: Theory". In: *ISSI Scientific Reports Series* 1 (1998), pp. 349–370.

[49] C. J. Farrugia et al. "Charts of joint Kelvin-Helmholtz and Rayleigh-Taylor instabilites at the dayside magnetopause for strongly northward interplanetary magnetic field". In: *Journal of Geophysical Research: Space Physics* 103.A4 (1998), pp. 6703–6727. DOI: 10.1029/97JA03248.

[50] Tamás I Gombosi. *Physics of the space environment*. English. Includes bibliographical references (p. 331-332) and index. Cambridge ; New York : Cambridge University Press, 1998. ISBN: 052159264X. URL: http://site.ebrary.com/id/10451971.

[51] Alexander V. Khrabrov and Bengt U. Ö. Sonnerup. "Orientation and motion of current layers: minimization of the Faraday residue". In: *Geophysical Research Letters* 25.13 (1998), pp. 2373–2376. DOI: 10.1029/98GL51784.

[52] D.J. McComas et al. "Solar Wind Electron Proton Alpha Monitor (SWEPAM) for the Advanced Composition Explorer". In: *Space Science Reviews* 86.1 (1998), pp. 563–612. ISSN: 1572-9672. DOI: 10.1023/A:1005040232597.

[53] G. Paschmann and P. W. Daly. "Analysis Methods for Multi-Spacecraft Data. ISSI Scientific Reports Series SR-001, ESA/ISSI, Vol. 1. ISBN 1608-280X, 1998". In: *ISSI Scientific Reports Series* 1 (1998).

[54] P. Robert et al. "Tetrahedron Geometric Factors". In: *ISSI Scientific Reports Series* 1 (1998), pp. 323–348.

[55] C.W. Smith et al. "The ACE Magnetic Fields Experiment". In: *Space Science Reviews* 86.1 (1998), pp. 613–632. ISSN: 1572-9672. DOI: 10.1023/A:1005092216668.

[56] Bengt U.O. Sonnerup and Maureen Scheible. "Minimum and maximum variance analysis". In: *Analysis methods for multi-spacecraft data* (1998), pp. 185–220.

[57] E.C. Stone et al. "The Advanced Composition Explorer". In: *Space Science Reviews* 86.1 (1998), pp. 1–22. ISSN: 1572-9672. DOI: 10.1023/A:1005082526237.

[58] Masao Nakamura and Manfred Scholer. "Structure of the magnetopause reconnection layer and of flux transfer events: Ion kinetic effects". In: *Journal of Geophysical Research: Space Physics* 105.A10 (2000), pp. 23179–23191. DOI: 10.1029/2000JA900101.

[59] J. M. Bosqued et al. "Cluster observations of the high-latitude magnetopause and cusp: initial results from the CIS ion instruments". In: *Annales Geophysicae* 19.10 (2001), pp. 1545–1566. DOI: 10.5194/angeo-19-1545-2001.

[60] Johan De Keyser and M Roth. "Structural analysis of periodic surface waves on the magnetospheric boundary". In: *Planetary and Space Science* 51 (Oct. 2003), pp. 757–768. DOI: 10.1016/S0032-0633(03)00112-0.

[61] H. U. Frey et al. "Continuous magnetic reconnection at Earth's magnetopause". In: *Nature* 426.6966 (2003), pp. 533–537. DOI: 10.1038/nature02084.

[62] Qiang Hu and Bengt U. Ö. Sonnerup. "Reconstruction of two-dimensional structures in the magnetopause: Method improvements". In: *Journal of Geophysical Research: Space Physics* 108.A1 (2003). DOI: 10.1029/2002JA009323.

[63] JP Hans Goedbloed, JP Goedbloed, and Stefaan Poedts. *Principles of magnetohydrodynamics: with applications to laboratory and astrophysical plasmas*. Cambridge university press, 2004.

[64] S. E. Haaland et al. "Four-spacecraft determination of magnetopause orientation, motion and thickness: comparison with results from single-spacecraft methods". In: *Annales Geophysicae* 22.4 (2004), pp. 1347–1365. URL: https://hal.archives-ouvertes.fr/hal-00329308.

[65] H. Hasegawa et al. "Reconstruction of two-dimensional magnetopause structures from Cluster observations: verification of method". In: *Annales Geophysicae* 22.4 (2004), pp. 1251–1266. DOI: 10.5194/angeo-22-1251-2004.

[66] B. U. Ö. Sonnerup et al. "Orientation and motion of a discontinuity from single-spacecraft measurements of plasma velocity and density: Minimum mass flux residue". In: *Journal of Geophysical Research: Space Physics* 109.A3 (2004). DOI: 10.1029/2003JA010230.

[67] H. Hasegawa et al. "Optimal reconstruction of magnetopause structures from Cluster data". In: *Annales Geophysicae* 23.3 (Mar. 2005), pp. 973–982. ISSN: 0992-7689. DOI: 10.5194/angeo-23-973-2005.

[68] T. D. Phan et al. "Magnetopause Processes". In: *Space Science Reviews* 118.1 (2005), pp. 367–424. ISSN: 1572-9672. DOI: 10.1007/s11214-005-3836-z.

[69] Alessandro Retinò et al. "Cluster multispacecraft observations at the high-latitude dusk-side magnetopause: Implications for continuous and component magnetic reconnection". In: *Annales Geophysicae* 23 (Feb. 2005). DOI: 10.5194/angeo-23-461-2005.

[70] Q. Q. Shi et al. "Dimensional analysis of observed structures using multipoint magnetic field measurements: Application to Cluster". In: *Geophysical Research Letters* 32.12 (2005). DOI: 10.1029/2005GL022454.

[71] Ronan Modolo et al. "Simulated solar wind plasma interaction with the Martian exosphere: influence of the solar EUV flux on the bow shock and the magnetic pile-up boundary". In: *Annales Geophysicae* 24.12 (2006), pp. 3403–3410. URL: https://hal.archives-ouvertes.fr/hal-00330103.

[72] Q. Q. Shi et al. "Motion of observed structures calculated from multi-point magnetic field measurements: Application to Cluster". In: *Geophys. Res. Lett.* 33.8 (2006). L08109, n/a–n/a. ISSN: 1944-8007. DOI: 10.1029/2005GL025073.

[73] B. U. Ö. Sonnerup et al. "Orientation and motion of a plasma discontinuity from single-spacecraft measurements: Generic residue analysis of Cluster data". In: *Journal of Geophysical Research: Space Physics* 111.A5 (2006). DOI: 10.1029/2005JA011538.

[74] A. Bret. "Beam-plasma dielectric tensor with Mathematica". In: *Computer Physics Communications* 176.5 (2007), pp. 362–366. ISSN: 0010-4655. DOI: https://doi.org/10.1016/j.cpc.2006.11.006.

[75] Y.-J. Ma et al. "3D global multi-species Hall-MHD simulation of the Cassini T9 flyby". In: *Geophysical Research Letters* 34, L24S10 (2007), L24S10. DOI: 10.1029/2007GL031627.

[76] A. Retinò et al. "In situ evidence of magnetic reconnection in turbulent plasma". In: *Nature Physics* 3 (Mar. 2007). URL: https://doi.org/10.1038/nphys574.

[77] J. De Keyser. "Empirical Reconstruction". In: *ISSI Scientific Reports Series* 8 (2008), pp. 91–98.

[78] M. Faganello, F. Califano, and F. Pegoraro. "Competing Mechanisms of Plasma Transport in Inhomogeneous Configurations with Velocity Shear: The Solar-Wind Interaction with Earth's Magnetosphere". In: *Phys. Rev. Lett.* 100 (1 2008), p. 015001. DOI: 10.1103/PhysRevLett.100.015001.

[79] Ammar H. Hakim. "Extended MHD Modelling with the Ten-Moment Equations". In: *Journal of Fusion Energy* 27.1 (2008), pp. 36–43. ISSN: 1572-9591. DOI: 10.1007/s10894-007-9116-z.

[80] Xiangqian Hu, David N. Beratan, and Weitao Yang. "A gradient-directed Monte Carlo approach to molecular design". In: *The Journal of Chemical Physics* 129.6 (2008), p. 064102. DOI: 10.1063/1.2958255.

[81] P. L. Pritchett. "Collisionless magnetic reconnection in an asymmetric current sheet". In: *Journal of Geophysical Research: Space Physics* 113.A6 (2008). DOI: 10.1029/2007JA012930.

[82] B. U. O. Sonnerup, S. E. Haaland, and G. Paschmann. "Discontinuity orientation, motion, and thickness". In: *Multi-Spacecraft Analysis Methods Revisited, edited by: Paschmann, G. and Daly, P* (2008), pp. 1–15.

[83] K. G. Tanaka et al. "Effects on magnetic reconnection of a density asymmetry across the current sheet". In: *Annales Geophysicae* 26.8 (2008), pp. 2471–2483. DOI: 10.5194/angeo-26-2471-2008.

[84] M Faganello, F Califano, and F Pegoraro. "Being on time in magnetic reconnection". In: *New Journal of Physics* 11.6 (2009), p. 063008. DOI: 10.1088/1367-2630/11/6/063008.

[85] Luke M. B. Winternitz, William A. Bamford, and Gregory W. Heckler. "A GPS Receiver for High-Altitude Satellite Navigation". In: *IEEE Journal of Selected Topics in Signal Processing* 3.4 (Jan. 2009), pp. 541–556. ISSN: 1932-4553. DOI: 10.1109/JSTSP.2009.2023352.

[86] A. V. Guglielmi, A. S. Potapov, and B. I. Klain. "Rayleigh-Taylor-Kelvin-Helmholtz combined instability at the magnetopause". In: *Geomagnetism and Aeronomy* 50.8 (Dec. 2010), pp. 958–962. ISSN: 0016-7932. DOI: 10.1134/S0016793210080050.

[87] Hiroshi Hasegawa, Bengt U. Ö. Sonnerup, and Takuma K. M. Nakamura. "Recovery of time evolution of Grad-Shafranov equilibria from single-spacecraft data: Benchmarking and application to a flux transfer event". In: *Journal of Geophysical Research: Space Physics* 115.A11 (2010). DOI: 10.1029/2010JA015679.

[88] Bengt U. Ö. Sonnerup and Hiroshi Hasegawa. "On slowly evolving Grad-Shafranov equilibria". In: *Journal of Geophysical Research: Space Physics* 115.A11 (2010). DOI: 10.1029/2010JA015678.

[89] N. Aunai, G. Belmont, and R. Smets. "Proton acceleration in antiparallel collisionless magnetic reconnection: Kinetic mechanisms behind the fluid dynamics". In: *Journal of Geophysical Research: Space Physics* 116.A9 (2011). DOI: 10.1029/2011JA016688.

[90] U. Shumlak et al. "Advanced physics calculations using a multi-fluid plasma model". In: *Computer Physics Communications* 182.9 (Sept. 2011), pp. 1767–1770. ISSN: 0010-4655. DOI: 10.1016/j.cpc.2010.12.048.

[91] H. Alfvèn. *Cosmic Plasma*. Astrophysics and Space Science Library. Springer Netherlands, 2012. ISBN: 9789400983748. URL: https://books.google.fr/books?id=gAnvCAAAQBAJ.

[92] W. Baumjohann and R. Treumann. *Basic Space Plasma Physics - Revised Edition*. Jan. 2012. DOI: 10.1142/P850.

[93] G. Belmont, N. Aunai, and R. Smets. "Kinetic equilibrium for an asymmetric tangential layer". In: *Physics of Plasmas* 19.2 (2012), p. 022108. DOI: 10.1063/1.3685707.

[94] M Faganello et al. "Magnetic reconnection and KelvinâHelmholtz instabilities at the Earth's magnetopause". In: *Plasma Physics and Controlled Fusion* 54.12 (Dec. 2012), p. 124037. ISSN: 0741-3335. DOI: 10.1088/0741-3335/54/12/124037.

[95] H. Hasegawa. "Structure and Dynamics of the Magnetopause and Its Boundary Layers". In: *Monographs on Environment, Earth and Planets* 1.2 (2012), pp. 71–119. DOI: 10.5047/meep.2012.00102.0071.

[96] G. Belmont et al. *Collisionless Plasmas in Astrophysics*. Wiley, 2013. ISBN: 9783527656240. URL: https://books.google.it/books?id=bYrHAAAAQBAJ.

[97] Paul S. Cannon. "Extreme Space Weather-A Report Published by the UK Royal Academy of Engineering". In: *Space Weather* 11.4 (2013), pp. 138–139. DOI: 10.1002/swe.20032.

[98] Y.L. Klimontovich and D. Haar. *The Statistical Theory of Non-Equilibrium Processes in a Plasma: International Series of Monographs in Natural Philosophy*. v. 9. Elsevier Science, 2013. ISBN: 9781483214627. URL: https://books.google.it/books?id=SbU3BQAAQBAJ.

[99] J. G. Luhmann and S. J. Bauer. "Solar Wind Effects on Atmosphere Evolution at Venus and Mars". In: *Venus and Mars: Atmospheres, Ionospheres, and Solar Wind Interactions*. American Geophysical Union (AGU), 2013, pp. 417–430. ISBN: 9781118663844. DOI: 10.1029/GM066p0417.

[100] Akira Miura. "Kelvin-Helmholtz Instability at the Magnetopause: Computer Simulations". In: *Physics of the Magnetopause*. American Geophysical Union (AGU), 2013, pp. 285–291. ISBN: 9781118663974. DOI: 10.1029/GM090p0285.

[101] Paul H Roberts and Eric M King. "On the genesis of the Earth's magnetism". In: *Reports on Progress in Physics* 76.9 (2013), p. 096801. DOI: 10.1088/0034-4885/76/9/096801.

[102] N. Dorville et al. "BV technique for investigating 1-D interfaces". In: *Journal of Geophysical Research: Space Physics* 119.3 (2014), pp. 1709–1720. ISSN: 2169-9402. DOI: 10.1002/2013JA018926.

[103] N. Dorville et al. "Rotational/compressional nature of the magnetopause: Application of the BV technique on a magnetopause case study". In: *Journal of Geophysical Research: Space Physics* 119.3 (2014), pp. 1898–1908. DOI: 10.1002/2013JA018927.

[104] M. Faganello et al. "Kelvin-Helmholtz vortices and double mid-latitude reconnection at the Earth's magnetopause: Comparison between observations and simulations". In: *EPL (Europhysics Letters)* 107.1 (2014), p. 19001. DOI: 10.1209/0295-5075/107/19001.

[105] Hiroshi Hasegawa et al. "Reconstruction of an evolving magnetic flux rope in the solar wind: Decomposing spatial and temporal variations from single-spacecraft data". In: *Journal of Geophysical Research: Space Physics* 119.1 (2014), pp. 97–114. DOI: 10.1002/2013JA019180.

[106] Hua-sheng Xie. "PDRF: A general dispersion relation solver for magnetized multi-fluid plasma". In: *Computer Physics Communications* 185.2 (2014), pp. 670–675. ISSN: 0010-4655. DOI: https://doi.org/10.1016/j.cpc.2013.10.012.

[107] Nicolas Dorville. "Boundary layers in plasmas : structure and stability of the Terrestrial magnetopause". Theses. Ecole Polytechnique, 2015. URL: https://pastel.archives-ouvertes.fr/tel-01181616.

[108] Nicolas Dorville et al. "Asymmetric kinetic equilibria: Generalization of the BAS model for rotating magnetic profile and non-zero electric field". In: *Physics of Plasmas* 22.9, 092904 (2015), p. 092904. DOI: 10.1063/1.4930210.

[109] Nicolas Dorville et al. "Magnetopause orientation: Comparison between generic residue analysis and BV method". In: *Journal of Geophysical Research: Space Physics* 120.5 (2015), pp. 3366–3379. DOI: 10.1002/2014JA020806.

[110] Alejandro Alvarez Laguna et al. "Multi-fluid modeling of the Earth's magnetosphere". In: *Comparative Heliophysics Program, Summer 2016 at NASA Ames Research Center*. July 2016.

[111] Daniel N. Baker and Louis J. Lanzerotti. "Resource Letter SW1: Space Weather". In: *American Journal of Physics* 84.3 (2016), pp. 166–180. DOI: 10.1119/1.4938403.

[112] J. L. Burch et al. "Electron-scale measurements of magnetic reconnection in space". In: *Science* 352.6290 (June 2016), aaf2939. ISSN: 0036-8075.

[113] J. L. Burch et al. "Magnetospheric Multiscale Overview and Science Objectives". In: *Space Science Reviews* 199.1 (2016), pp. 5–21. ISSN: 1572-9672. DOI: 10.1007/s11214-015-0164-9.

[114] P. A. Cassak. "Inside the Black Box: Magnetic Reconnection and the Magnetospheric Multiscale Mission". In: *Space Weather* 14.3 (2016), pp. 186–197. DOI: 10.1002/2015SW001313.

[115] O. Le Contel et al. "Whistler mode waves and Hall fields detected by MMS during a dayside magnetopause crossing". In: *Geophysical Research Letters* 43.12 (2016), pp. 5943–5952. DOI: 10.1002/2016GL068968.

[116] O. Le Contel et al. "Whistler mode waves and Hall fields detected by MMS during a dayside magnetopause crossing". In: *Geophys. Res. Lett.* 43.12 (2016). 2016GL068968, pp. 5943–5952. ISSN: 1944-8007. DOI: 10.1002/2016GL068968.

[117] C. Pollock et al. "Fast Plasma Investigation for Magnetospheric Multiscale". In: *Space Science Reviews* 199.1 (2016), pp. 331–406. ISSN: 1572-9672. DOI: 10.1007/s11214-016-0245-4.

[118] R. B. Torbert et al. "Estimates of terms in Ohm's law during an encounter with an electron diffusion region". In: *Geophysical Research Letters* 43.12 (June 2016), pp. 5918–5925. ISSN: 1944-8007. DOI: 10.1002/2016GL069553.

[119] R. B. Torbert et al. "The FIELDS Instrument Suite on MMS: Scientific Objectives, Measurements, and Data Products". In: *Space Science Reviews* 199.1 (2016), pp. 105–135. ISSN: 1572-9672. DOI: 10.1007/s11214-014-0109-8.

[120] L. Del Zanna et al. "The ideal tearing mode: theory and resistive MHD simulations". In: *Journal of Physics: Conference Series* 719 (2016), p. 012016. DOI: 10.1088/1742-6596/719/1/012016.

[121] J. Dargent et al. "Kinetic simulation of asymmetric magnetic reconnection with cold ions". In: *Journal of Geophysical Research: Space Physics* 122.5 (May 2017), pp. 5290–5306. ISSN: 2169-9402. DOI: 10.1002/2016JA023831. URL: https://doi.org/10.1002/2016JA023831.

[122] Matteo Faganello and Francesco Califano. "Magnetized Kelvin-Helmholtz instability: theory and simulations in the Earth's magnetosphere context". In: *Journal of Plasma Physics* 83.6 (2017), p. 535830601. DOI: 10.1017/S0022377817000770.

[123] R. Manuzzo, G. Belmont, and L. Rezeau. "Determining the Thickness and the Sub-Structure Details of the Magnetopause from MMS Data". In: *AGU Fall Meeting Abstracts* (Dec. 2017).

[124] J. R. Shuster et al. "Hodographic approach for determining spacecraft trajectories through magnetic reconnection diffusion regions". In: *Geophysical Research Letters* 44.4 (Feb. 2017), pp. 1625–1633. ISSN: 0094-8276. DOI: 10.1002/2017GL072570.

[125] Zoltan Vörös et al. "MMS Observation of Magnetic Reconnection in the Turbulent Magnetosheath". In: *Journal of Geophysical Research: Space Physics* 122 (Oct. 2017). DOI: 10.1002/2017ja024535.

[126] Luke B. Winternitz et al. "Global Positioning System Navigation Above 76,000 KM for NASA's Magnetospheric Multiscale Mission". In: *Navigation* 64.2 (Jan. 2017), pp. 289–300. ISSN: 2161-4296. DOI: 10.1002/navi.198.

[127] S. Fadanelli et al. "North-South Asymmetric Kelvin-Helmholtz Instability and Induced Reconnection at the Earth's Magnetospheric Flanks". In: *Journal of Geophysical Research: Space Physics* 123.11 (2018), pp. 9340–9356. DOI: 10.1029/2018JA025626.

[128] S Galtier. "Turbulence in space plasmas and beyond". In: *Journal of Physics A: Mathematical and Theoretical* 51.29 (2018), p. 293001. DOI: 10.1088/1751-8121/aac4c7.

[129] Roberto Manuzzo et al. "A new multi-fluid model for space plasma simulations". In: *Earth and Space Science Open Archive* (2018). URL: https://www.essoar.org/doi/abs/10.1002/essoar.10500082.1.

[130] Rezeau, Laurence and Belmont, Gérard. "Reconnexion magnétique entre le vent solaire et la magnétosphère terrestre : la mission MMS". In: *Reflets phys.* 59 (2018), pp. 20–25. DOI: 10.1051/refdp/201859020.

[131] L. Rezeau et al. "Analyzing the Magnetopause Internal Structure: New Possibilities Offered by MMS Tested in a Case Study". In: *Journal of Geophysical Research: Space Physics* (2018), pp. 227–241. ISSN: 2169-9380. DOI: 10.1002/2017JA024526.

[132] V. Angelopoulos et al. "The Space Physics Environment Data Analysis System (SPEDAS)". In: *Space Science Reviews* 215.1 (2019). DOI: 10.1007/s11214-018-0576-4.

[133] G. Belmont et al. *Introduction to Plasma Physics*. Elsevier Science, 2019. ISBN: 9780128189788. URL: https://books.google.it/books?id=Q8OJDwAAQBAJ.

[134] R. Manuzzo et al. "A multi-fluid model of the magnetopause". In: *Annales Geophysicae Discussions* 2019 (2019), pp. 1–19. DOI: 10.5194/angeo-2019-135.

[135] R. Manuzzo et al. "Crossing of Plasma Structures by spacecraft: a path calculator". In: *Journal of Geophysical Research: Space Physics* (2019).

[136] WH Matthaeus et al. "[Plasma 2020 Decadal] The essential role of multi-point measurements in turbulence investigations: the solar wind beyond single scale and beyond the Taylor Hypothesis". In: *arXiv preprint arXiv:1903.06890* (2019).

[137] Q. Q. Shi et al. "Dimensionality, Coordinate System and Reference Frame for Analysis of in situ Space Plasma and Field Data". In: *Space Science Reviews* 215.4 (2019), p. 35. ISSN: 1572-9672. DOI: 10.1007/s11214-019-0601-2.

[138] J.E.T. Channell and L. Vigliotti. "The role of geomagnetic field intensity in late Quaternary evolution of humans and large mammals". In: *Reviews of Geophysics* 0 (). DOI: 10.1029/2018RG000629.

Chapter

21 Figures

Chapter

22 Tables

Chapter

23 Papers and Posters

Chapter content

The following sections list the papers and posters this thesis refers to.

23.1 Paper 1: Crossing of Plasma Structures by spacecraft: a path calculator

manuscript submitted to *JGR-Space Physics*

Crossing of Plasma Structures by spacecraft: a path calculator

R. Manuzzo[1,2], G.Belmont[1], L.Rezeau[1], F.Califano[2], R.E.Denton[3]

[1]LPP, CNRS, Ecole Polytechnique, Sorbonne Université, Univ. Paris-Sud, Observatoire de Paris, Université Paris-Saclay, PSL Research University
[2]Department of Physics E. Fermi, Universitá di Pisa, Italia
[3]Department of Physics and Astronomy, Dartmouth College, Hanover, New Hampshire, USA

Key Points:

- The Spatio-Temporal-Difference method is extended to determine non mono-dimensional spacecraft trajectories.
- Two new methods are developed for this determination: the Single and the Multi Variate Fit methods. They are compared to previous ones.
- A Gradient-Directed Monte Carlo approach is applied to optimize the results. The spacecraft path and magnetopause thickness are so computed.

Corresponding author: Laurence Rezeau, laurence.rezeau@lpp.polytechnique.fr

This article has been accepted for publication and undergone full peer review but has not been through the copyediting, typesetting, pagination and proofreading process, which may lead to differences between this version and the Version of Record. Please cite this article as doi: 10.1029/2019JA026632

manuscript submitted to *JGR-Space Physics*

Abstract

When spacecraft (s/c) missions probe plasma structures (PS) the relative location of the s/c with respect to the PS is unknown. This information is however needed to measure the geometrical features of the PS (orientation and thickness) and to understand the physical processes underlying the PS dynamics. Methods to determine the s/c location exist but they need strong assumptions to be satisfied (stationarity and special spatial dependencies). The number of cases for which these assumptions are likely to be valid for the entire PS seems to be limited and even weak departures from these hypothesis may affect the results. For a quasi-1D geometry in particular, the determination of the velocity component along the two quasi-invariant directions is very inaccurate and the assumption of strict stationarity may lead these quantities to diverge. In this paper we present new methods to compute the s/c trajectory through a PS, without *a priori* assumption on its spatial geometry, and able to work even in the presence of weak non-stationarities. The methods are tested both on artificial and real data, the latter provided by the Magnetospheric MultiScale (MMS) mission probing the Earth's magnetopause (MP). 1D and 2D trajectories of the MMS are found that can be used as an initial step for future reconstruction studies. Advanced minimization procedures to optimize the results are discussed.

1 Introduction

When spacecraft (s/c) cross plasma structures (PSs), the different parameters characterizing these structures are measured only as time series along the s/c trajectories. The shape and the motion of the PSs being unknown, it is quite difficult to determine both only from such temporal data. Multi-spacecraft missions like Cluster (Escoubet, Schmidt, & Goldstein, 1997) and the Magnetospheric MultiScale (MMS) (Burch, Moore, Torbert, & Giles, 2016b) have enabled considerable progress to determine the shape and motion of PSs since they make measurements at multiple locations, which helps to separate spatial and temporal variations. Nevertheless, in the general case of a complex geometrical shape for a PS and of a complex relative path of the s/c with respect to it, getting a full determination of the shape and motion of PSs remains challenging. Such determinations cannot be done, in general, without strong assumptions. But information about the shape and location of PSs is necessary for understanding the physical processes being studied. Regarding the Earth's Magnetopause (MP) for instance, which is the field and particle boundary between the shocked solar wind and the Earth's magnetosphere, one has to know first whether this boundary can be approximated by a 1D plane structure, as the simplest models assume, or not. If so, one only has to determine what is the direction of its normal and what is its global thickness (and the thickness of its different sub-structures if any (Rezeau, Belmont, Manuzzo, Aunai, & Dargent, 2018)). Actually, such a plane-like equilibrium is easily perturbed and it is rarely observed. Perturbations generally involve 2D and 3D variations, either due to inhomogeneities in the incident solar wind or to surface instabilities such as, for instance, Kelvin-Helmholtz (KH) or tearing instabilities. One has then to determine what are the shape and the dimensions of the vortices in the KH case (Faganello & Califano, 2017), or, in the case of reconnection, one has to determine the invariance directions, the shapes and dimensions of the ion and electron demagnetized regions, the location of the separatrices, the exhaust flow, etc. (Burch et al., 2016c), which is a very difficult task.

The first basic assumption that makes possible the conversion from temporal to spatial data consists in assuming the PSs to be stationary in their proper frame, even if this frame, relatively to the s/c, can undergo variable accelerations in all directions, directly driven by the incident solar wind or due to local surface waves. The fact that the proper frame of the structure can experience accelerations can be exemplified, concerning the MP, by the existence of multiple and close crossings, such as those observed on 16 October 2015 (Rezeau et al., 2018), which are clearly due to a back and forth motion of the

manuscript submitted to *JGR-Space Physics*

MP. Under these conditions, it makes sense to draw a complex s/c path across a fixed structure, this relative motion being mainly due, in reality, to motions of the MP itself, rather than due to the s/c motion, which is quite slow. This assumption has long been used by experimenters for drawing hand-made sketches to interpret data in the reconnection context (see Figure (3) of Burch et al. (2016c), reproduced hereafter in the left part of Figure (8)).

The observed PSs are not always strictly stationary in their own frame. They can undergo modifications during the crossing due, for instance, to slowly growing MHD instabilities. We will show that these departures -even weak- from strict stationarity can lead to difficulties if the usual methods are used without caution for determining the relative motion between a structure and a s/c. For a quasi-1D structure for instance, the determination of the velocity components along the two quasi-invariant directions can be very inaccurate. This property, which is mentioned in the very recent review paper by Shi et al. (2019) will be demonstrated hereafter in this paper. We will show that any weak non-stationarity causes these components to diverge when using a method that assumes strict stationarity. The projection of the trajectory along the 1D direction is actually not much affected by this problem, but it is difficult to know *a priori* when the second and the third component can be reliably used or not. In the present paper we will therefore relax the assumption of strict PSs stationarity and replace it by a more moderate "quasi-stationarity" assumption. This means that we consider the PS to be stationary on time scales that are smaller than the time needed for the crossing of the entire PS (namely the MP crossing). In this sense we will discriminate the "global" from the "local" features of the PS characterizing, respectively, the entire PS and its sub parts. In the experimental example given below, the stationarity is assumed on ~ 10 data points only (~ 0.1 s) while the global crossing takes ~ 1200 points (~ 10 s). It therefore concerns a portion of about 0.8% of the total MP width. We will characterize as much as possible the local features of a PS, taking into account the possible slow modifications that can affect its structure during the crossing time. This will enable us to investigate its internal structure. Such information cannot be obtained by methods addressing the PS as a whole (e.g.: the MVA method Sonnerup and Cahill (1967) or the BV method Dorville, Belmont, Rezeau, Aunai, and Retinò (2014b) both returning a *global frame* known as LMN frame, where N is the direction of the normal and M and L are two other directions perpendicular to N and to each others). The methods that use multiple field and particle data sets may *a priori* be very beneficial for investigating PSs. But they can be difficult in practice because the different data sets often evidence gradients that are shifted from each other. This can be interpreted as the presence of different discontinuities. For instance, the MP is sometimes made of a slow shock (mainly seen on particles) and a rotational discontinuity (mainly seen on the magnetic field) (Dorville, Belmont, Rezeau, Grappin, & Retinò, 2014a).

Recently it has been possible to determine local PS normals thanks to methods providing a point-by-point reference frame (hereafter defined as a "*local frame*" in contrast to the "*global frame*" valid for the entire PS). These methods allow one to account for the spatio-temporal modifications of the orientation of the crossed PS (MDD (Denton et al., 2018; Shi et al., 2005) and LNA (Rezeau et al., 2018) techniques). When the local variations are quasi 1D in particular, these methods are efficient to obtain the corresponding varying normal (and the dimensionality, 1D or not, can be determined thanks to the MDD technique itself).

On the other hand, even if one can determine the dimensionality of the local variations as well as the local normal when it exists, the geometrical shape of the PS cannot be determined without strong hypotheses. When a s/c crosses a PS, the measurements provide data only along its trajectory. Beyond the determination of a local normal, one would like to determine the shape of the observed PS all around, in the vicinity of the trajectory. This problem is referred in the literature as a "reconstruction prob-

lem". The most known method consists in assuming the structure is stationary and that the relative path of the s/c with respect to the structure is just a straight line, traveled with a constant velocity. This knowledge is then used as a "boundary condition" for integrating the MHD Grad-Shafranov equations. This has been done under different assumptions: 2D or 3D structure, stationary or slowly evolving, with a computation based on MHD or electron-MHD equations (see for instance Sonnerup, Hasegawa, Teh, and Hau (2006), Hasegawa, Sonnerup, Eriksson, Nakamura, and Kawano (2015), among many other papers). It has also been applied to MMS observations of the electron diffusion region observed on 16 October 2015, 13:07 UT, nearly one minute later than the case we study Burch et al. (2016c); Hasegawa et al. (2017).

Our paper does not deal with such reconstructions, but with the determination of the path of the s/c relative to the PS. It can be understood as a necessary first step, prior to any reconstruction study. As this path can be, as it will be shown hereafter, quite different from a straight line traveled at a constant velocity, relaxing this assumption should allow to greatly improve the reliability of the reconstruction results. Obtaining the path information is the object of this paper. Beyond the straight line assumption, efforts have been made to improve the determination of the spacecraft path across the magnetopause, by considering different (but pre-determined) forms for this path Hasegawa et al. (2004); Q. Hu and Sonnerup (2003). Other authors have taken into account possible intrinsic temporal evolution of the structures Hasegawa, Sonnerup, Hu, and Nakamura (2014); Hasegawa, Sonnerup, and Nakamura (2010); Sonnerup and Hasegawa (2010). However, in all these studies the spacecraft velocity, even locally, is assumed to be the deHoffmann-Teller velocity, whereas the target of this paper is to recover the velocity without any *a priori* assumption.

(De Keyser, 2008) has introduced a different method that he called "empirical reconstruction". It is a multi-spacecraft method that allows determining a s/c path in the 1D hypothesis, and even in the 2D hypothesis, but under restrictive assumptions: no plasma flow across the PS, the 2D shape is supposed known a priori (for instance it is a surface wave).

Note that the integration of the flow normal velocity, used in (De Keyser, 2008) and also in BV (Dorville et al., 2014a) (which uses the magnetic field $\mathbf{B}$ and the ion velocity $\mathbf{V}$) to determine the path along the normal, is very sensitive to inaccuracies in the determination of the normal direction. The large tangential flows that exist in the magnetosheath can indeed, when projected on an approximate normal direction, provide an apparent normal flow that is very inaccurate, even if the inaccuracy in the normal direction is small.

Finally, the Spatio-Temporal Difference technique (STD, (Shi et al., 2006)) deserves a separate discussion since, in contrast to the other methods, it is not affected by any of the strong assumptions previously discussed, except for the stationarity of the PS. With respect to a fixed frame, the STD method is able to recover the PS velocity ($\partial_{t,0}\mathbf{X}$, where $\mathbf{X}$ is the PS position) by means of inversion of the equation

$$\partial_{t,sc}\mathbf{B} = \partial_{t,0}\mathbf{X} \cdot \overline{\nabla}\mathbf{B} \tag{1}$$

The left hand side (LHS) term represents the temporal derivative of the magnetic field in the s/c frame and the right hand side (RHS) term involves the spatial derivative. These are computed by means of the reciprocal vector method (Chanteur, 1998) that exploits the multi-point measurement of missions such as CLUSTER or MMS (Burch et al., 2016c)). For the sake of clarity, we have specified here and everywhere afterwards in the text that the methods are applied to the magnetic field data. These methods remain valid, however, if $\mathbf{B}$ is replaced by any other quantity (e.g.: $\mathbf{E}$, $\mathbf{V}_i$, $\mathbf{V}_e$, etc...). The assumption of stationarity causes the method to fail when the term $\partial_{t,0}\mathbf{X}\cdot\overline{\nabla}\mathbf{B}$ becomes comparable to or smaller than the intrinsic temporal variations of the PS magnetic struc-

manuscript submitted to *JGR-Space Physics*

ture: ($\partial_{t,0}\mathbf{B}$), *i.e.* when the PS can no longer be considered as strictly stationary in its own reference frame. When the intrinsic temporal variation of the PS is not negligible, we will have to replace Equation (1) by Equation (2), which is its generalization:

$$\partial_{t,sc}\mathbf{B} = \partial_{t,0}\mathbf{X} \cdot \overline{\nabla}\mathbf{B} + \partial_{t,0}\mathbf{B} \tag{2}$$

The subscripts 0 indicate the particular frame used: supposing that a quasi-stationary frame does exist, in which the intrinsic variation $\partial_{t,0}\mathbf{B}$ is minimum, the term $\partial_{t,0}\mathbf{X}$ represents the s/c velocity in this frame.

This paper will present new methods to perform this generalization (sections 2.1.2 and 2.1.3). These new methods are tested on artificial magnetic fields mimicking linear (section 3.1.1) and back and forth motions (section 3.1.2) of the MP. The results are compared to those from a modified version of the STD method able to suppress singularities occurring to STD in analyzing nearly 1D PSs (section 2.1.1). We will present 1D and 2D reconstructions of the MMS s/c path during two real MP crossings (section 3.2). Finally, a summary of our results and a discussion of future perspects for these methods is presented in section 4.

2 Methods

In the following sections, we explain the methods used to compute the s/c path with respect to the observed PS. In sub-section (2.1) we discuss the problems that occur when using the STD method for that purpose and how we solve them. This is done in two different ways: via the suppression of the singularities that occur in STD when the PS is not sufficiently three-dimensional (sub-section 2.1.1) and via new methods that extend the computation beyond the strict stationarity assumption (sub-sections 2.1.2 and 2.1.3). In sub-section (2.2) we show how to integrate the s/c velocity to obtain the s/c path. Finally, in sub-section (2.3), we present the optimization procedure we adopt to determine the optimal values for the different threshold parameters that are used in the methods.

2.1 The computation of $\partial_{t,0}X$

2.1.1 From STD to STD$^+$: the suppression of singularities

As previously discussed, the STD method of (Shi et al., 2006) computes point-by-point values of $\partial_{t,0}\mathbf{X}$ by inverting Equation (1):

$$\partial_{t,0}\mathbf{X} = \partial_{t,sc}\mathbf{B} \cdot \left[\overline{\nabla}\mathbf{B}\right]^{-1} = \frac{\partial_{t,sc}\mathbf{B} \cdot \left[\overline{\nabla}\mathbf{B}\right]^{A}}{\det\left[\overline{\nabla}\mathbf{B}\right]} \tag{3}$$

In this expression, the superscript A indicates the adjoint matrix. Combined with the MDD method (Shi et al., 2005), the STD allows computation of both the dimensionality (1D, 2D or 3D) of the space variations and the orientation of the PS. It also allows one to calculate the thickness of the crossed PS (via the cumulative sum of $\partial_{t,0}\mathbf{X}$) under the strong assumption that $\partial_{t,0}\mathbf{B} \ll \partial_{t,sc}\mathbf{B}$ and $\partial_{t,0}\mathbf{B} \ll \partial_{t,0}\mathbf{X} \cdot \overline{\nabla}\mathbf{B}$. As we observe from Equation (3), the method is particularly sensitive to the conditions for which the determinant $\det\left[\overline{\nabla}\mathbf{B}\right]$ becomes very small. This determinant tends to zero everywhere the variations are not sufficiently three-dimensional, *i.e.* everywhere there is locally one or two nearly invariant directions. Under these conditions, the numerator and denominator of Equation (3) both tend toward zero and the result becomes undetermined: its value then strongly depends on any noise or to any departure from a strict stationarity that can make the numerator null at a place slightly different from the denominator.

Following (Shi et al., 2006), this problem can be in practice circumvented by reducing the matrix $\overline{\nabla}\mathbf{B}$ used in Equation (3) to its non singular part, *i.e.* by retaining only the largest partial derivatives, the number of which depends on the dimensionality of the *PS*. For instance, when the variations are approximately 1D (with a threshold empirically determined for the eigenvalues), one can keep only the derivative along the local normal and determine only this normal trajectory, so giving up for the determination of a 2D or 3D path. However, one may foresee that this reduction process would cause an unnecessary loss of information. Actually, the 2D or 3D local variations that always exist may be significant enough, even if weak, to be used for determining the 2D or 3D paths. (Shi et al., 2006) also evoked the possibility of adding some artificial noise (called "random errors") to ensure that, even in the strictly 1D case, the determinant is non-null almost everywhere. This artificial noise actually would come in addition to the "natural noise" as defined in the present paper (see section 3.1). The velocity component along the maximum gradient direction would *a priori* not be much affected by this noise addition. On the contrary, the two other components, which would only be due to the noise when the physics is really 1D, should then be rejected, even out of the singular points. This method would therefore not allow one to reach the goal proposed in the present paper, which is to draw as much information as possible from the small variations that can be extracted out of the noise.

For the sake of clarity, let's define the directions **l**, **m** and **n** as the three linearly independent directions of the local frame coincident to the eigenvectors of $\mathbf{G} = \overline{\nabla}\mathbf{B} \cdot \overline{\nabla}\mathbf{B}^T$ associated, respectively, to the minimum, intermediate and maximum eigenvalues of **G**. Note that the two frames, **lmn** and **LMN** (the latter coming from MVA, its axes corresponding respectively to the largest, intermediate and minimum variance directions) have the same "normal" directions ($\mathbf{n} = \mathbf{N}$) as soon as the local properties are identical to the global ones, but that their axes in the tangential plane are not the same. The eigenvectors associated with the smallest eigenvalues of **G** are often significantly affected by high frequency variations, which may lead one to prefer, for some applications, projecting the motion onto a more stable global frame. In Figure (1), the time interval chosen in this paper for discussing the methods is presented. It shows the high frequency irregular oscillations of the GSE components of the **m** and the **l** directions (panels 1.*c* and 1.*d*) in contrast to the more stable **n** direction (panel 1.*b*) during the 16 October 2015, 13:05:30+60s UT (*i.e.*, 13:05:30–13:06:30 UT) *MP* crossing (the magnetic field is shown in panel 1.*a*).

The method that we propose consists in taking into account as much as possible any small departure from the 1D geometry in order to determine 2D or 3D paths across the magnetic structure. When the structure is approximately mono-dimensional, the local determinant has a very small value, fluctuating in time and changing its sign. It is the product of one large eigenvalue, with little inaccuracy, and two small eigenvalues with possibly fluctuating signs. Each of the zero crossings of the small eigenvalues leads to a singularity for the velocity component in the direction of the corresponding eigenvector. This effect is evidenced in Fig. (2), as well as the effect of the corrections made.

In this figure, the results are shown in GSE frame, so that all components are to be corrected in the same way. It is clear that in the local (**l**, **m**, **n**) frame, only the components **l** and **m** can be concerned by the singularity problem since the eigenvalue corresponding to the largest spatial derivative is never zero as long as the signal is not strictly constant. Nevertheless, this local frame is varying inside the magnetopause crossing, so that even the global **N** direction (as obtained via a global MVA or by average on the local **n** directions) is not exempted from the singularity problem: even a 1 degree variation in the direction of **n** has significant consequences in the global normal direction if the singularity leads to values larger than 100 times the neighbouring values. This is important since we need to know the velocity in a fixed frame to be able to calculate the path by integration.

As we do not know *a priori* at which threshold the structure is to be considered as 1D or not, we propose here to consider by default that it is 3D and derive the three components of the velocity. We do not add any artificial noise and we expect that the "natural one" will not change much the results as soon as we get rid of the singularities in the calculated velocity, which would lead to non physical jumps in the calculated path. Doing so, the choice of keeping the 1D, 2D or 3D projections of the path can be done *a posteriori*.

In order to avoid the reduction process (determining only one projection of the path), we use here the entire $\overline{\nabla}\mathbf{B}$ matrix with a procedure for suppressing automatically the singularities affecting some components of the velocity of the structure when using the original STD method without caution. For this purpose, we introduce a "very local" correction to force the numerator of Equation (3) to be zero at the times t^* when the denominator ($\det\left[\overline{\nabla}\mathbf{B}\right]$) is zero. In order to do so, we add to each of the three components of $\partial_{t,sc}\mathbf{B}\cdot\left[\overline{\nabla}\mathbf{B}\right]^A$ a signal made by a linear combination of gaussian curves each of which 1) is centered at times t^*, 2) has a amplitude equal to $-\partial_{t,sc}\mathbf{B}(t^*)\cdot\left[\overline{\nabla}\mathbf{B}(t^*)\right]^A$ and 3) is narrow enough not to modify the signal for a period larger than 1% of the global period analyzed (*i.e.* $\simeq 10$ data points for the cases studied in this paper) and not to overlap the nearby corrections. In section 3.2.1 the LHS of Equation (3) with and without corrections will be compared for a real case study.

Hereafter, we dub the above method STD$^+$. It aims at circumventing pragmatically the problem of singularities but without tackling directly the main cause of the problem: the small non-stationarities affecting the data. As previously mentioned, the STD method assumes strict stationarity. Unfortunately, the presence of weak non stationarities can cause infinite values for some components of the velocity determined by this method. Even if the non-stationarity $\partial_{t,0}\mathbf{B}$ is weak, it cannot be ignored wherever it is non-negligible with respect to the convective term $\partial_{t,0}\mathbf{X}\cdot\overline{\nabla}\mathbf{B}$. This systematically occurs when the latter tends to zero, *i.e.* wherever the s/c is approximately at rest with respect to the *PS*. In this case, $\partial_{t,sc}\mathbf{B}$ must be replaced by $\partial_{t,sc}\mathbf{B}-\partial_{t,0}\mathbf{B}$ in the numerator of Equation 3. It is then clear from this equation that the effect of this change on the determination of $\mathbf{X}$ is all the larger as the determinant of $\det\left[\overline{\nabla}\mathbf{B}\right]$ is smaller, *i.e.* when the spatial variations are not sufficiently three-dimensional (we know that $\det\left[\overline{\nabla}\mathbf{B}\right]\rightarrow 0$ whenever one or two eigenvalues tend to zero) . Note that, at the limit $\det\left[\overline{\nabla}\mathbf{B}\right]=0$, the STD method leads to divergences whatever the velocity $\partial_{t,0}\mathbf{X}$ is. Therefore, in order to generalize the computation of the s/c velocity ($\partial_{t,0}\mathbf{X}$) to non stationary *PS* cases, we need to distinguish the sources of the time variations $\partial_{t,sc}\mathbf{B}$ of the magnetic field seen by the s/c: convective ($\partial_{t,0}\mathbf{X}\cdot\overline{\nabla}\mathbf{B}$) and pure temporal variation of the *PS* itself ($\partial_{t,0}\mathbf{B}$). We will therefore have to retrieve the $\partial_{t,0}\mathbf{X}$ term from Equation (2) instead of Equation (1), *i.e.* without neglecting the intrinsic variation $\partial_{t,0}\mathbf{B}$.

In the following two sub-sections, we explain how we manage to obtain $\partial_{t,0}\mathbf{X}$ from Equation (2).

2.1.2 The Multi-Variate fit method (MVF)

In Equation (2), the unknowns are the $\partial_{t,0}\mathbf{X}$ and the $\partial_{t,0}\mathbf{B}$ terms while the $\partial_{t,sc}\mathbf{B}$ and the $\overline{\nabla}\mathbf{B}$ terms are computed from data via a temporal derivative and the reciprocal vector method (Chanteur, 1998) thanks to the multi-point measurements provided by MMS. In any but the local lmn frame, this equation represents an intertwined relation between the temporal and spatial variations of the different components of $\mathbf{B}$ via the $\mathbf{X}\cdot\overline{\nabla}\mathbf{B}$ term. The determination of $\partial_{t,0}\mathbf{X}$ and $\partial_{t,0}\mathbf{B}$ can be done by means of a multivariate fit procedure assuming the two unknowns are approximately constant over a short interval lasting p experimental points. A fit is performed that minimizes analytically the total squared difference between the observed temporal variations ($\partial_{t,sc}\mathbf{B}$) and the reconstructed ones ($\partial_{t,0}\mathbf{X}\cdot\overline{\nabla}\mathbf{B}+\partial_{t,0}\mathbf{B}$), normalized to the mean magnetic field tempo-

ral derivative:

$$D \equiv \frac{\sum_p \left\{ \sum_i \left[\partial_{t,sc} B_i - \left(\partial_{t,0} X_j \, \partial_j B_i + \partial_{t,0} B_i \right) \right]^2 \right\}_p}{\sum_p \left[\sum_i \left(\partial_{t,sc} B_i \right)^2 \right]_p} \tag{4}$$

where $i, j = \{x, y, z\}$. Once the $\partial_{t,0}\mathbf{X}$ and the $\partial_{t,0}\mathbf{B}$ terms are obtained, a selection procedure is made according to the comparison between the associated error (given by the Equation (4)) and a threshold $D_{lim,MVF}$: if $D > D_{lim,MVF}$ the results are discarded, otherwise the results are retained. Since D is expected to be very small for a fit result to be retained, $D_{lim,MVF}$ is chosen to be very small too, e.g.: 10^{-1} or 10^{-2}. The fits are performed on a number of data points that can vary (in accordance with the optimization procedure described in appendix A.1) from a lower integer value p_{min} to a maximum integer value p_{max} based on the local curvature of the curve to be fitted. We use MMS magnetic field data recorded in "burst mode" at $\nu_s = 128$Hz (Torbert et al., 2016) and preliminarily filter data in Fourier space to frequencies below ν_c in order to select the frequency windows to observe. This filtering is necessary to get rid of the small scale fluctuations and waves that are present at the MP and that have an intensity much higher than the instrument noise (Rezeau, Roux, & Russell, 1993). Then we set

$$\{p_{min}, p_{max}\} = \{\text{int}\left(\frac{\nu_s}{4\nu_c}\right), 13\}. \tag{5}$$

As a matter of facts, the highest frequency component of a signal filtered using ν_c could still have large variations in a period $\nu_c^{-1}/4$ long. This period corresponds to $\nu_s/(4\nu_c)$ data points if the original signal is probed at ν_s. On the other hand, we do not want a fit to represent more than one hundredth of the total crossing duration. Since the MP crossing examined in this study are no longer than 10s and thanks to the high magnetic field probing rate of MMS, the maximum time period corresponds to 13 data points. The $\partial_{t,0}\mathbf{X}$ and the $\partial_{t,0}\mathbf{B}$ terms which do not survive the selection procedure are replaced by means of interpolation. This method assumes the PSs to be stationary for, at least, an interval $p\nu_s^-1$ long, *i.e.* much smaller than the periods during which other methods assume the PSs to be stationary.

2.1.3 The Single-Variate fit method (SVF)

The working principle for MVF is the minimization of the total error D which is the squared modulus of the vectorial normalized error when fitting the temporal derivative of $\mathbf{B}$ (Equation (4)). For this reason, the MVF method is not able to discriminate which component of Equation (2) causes the fit to be rejected: a large error in the l component leads to rejection of the entire velocity while the n component might well be determined. The method can be improved by performing the fit procedure in the local lmn frame. In this frame, the $\overline{\nabla}\mathbf{B}$ matrix is diagonal so that the three components of Equation (2) do not share common unknowns; therefore the fit procedure can be performed independently for each component, disentangling the high quality fits of one component from the low quality fits of the others. Nevertheless, it is worth remembering that in some cases the lmn frame is far from being stable (remember Figure (1)): the SVF method can be applied anyway in these cases but it is clear that the local lmn frame has then no real physical significance. Only the directions corresponding to large derivatives are expected to be reliable and thus stable.

2.2 The projection and the integration of $\partial_{t,0}\mathbf{X}$

STD$^+$, MVF and (in some cases) SVF, generally compute a 3D $\partial_{t,0}\mathbf{X}$; the goal of this section is to explain how we obtain a 3D path $\mathbf{X}(t)$ from $\partial_{t,0}\mathbf{X}$. Actually, due to an intrinsic limitation of the methods which base their computations on the $\overline{\nabla}\mathbf{B}$ matrix, we will first focus on the projection of $\partial_{t,0}\mathbf{X}$ on the eigenvector that corresponds to the largest eigenvalue (here called $\mathbf{n}$), which is *a priori* the best determined component. The

manuscript submitted to *JGR-Space Physics*

final result will be therefore a 1D displacement $X_N(t)$ describing the position of the s/c with respect to the PS along its normal as a function of time. The reason why the $\mathbf{m}$ and $\mathbf{l}$ components of $\partial_{t,0}\mathbf{X}$ may be less accurate than the $\mathbf{n}$ component can be easily understood. Writing Equation (1) in the $\mathbf{lmn}$ frame, which corresponds to the eigenvectors of $G \equiv \overline{\nabla}\mathbf{B} \cdot \overline{\nabla}\mathbf{B}^T$, $\partial_{t,0} X_i \propto 1/\lambda_i$ (with $i = \{l, m, n\}$) , which clearly goes to infinity when λ_i goes to zero. We come here across the same difficulty that was causing the singularities in STD. In the rest of this section, we will concentrate only on the best determined normal projection of the s/c path. We will however show in section 3.2 that 2D maps of the s/c path can be obtained quite satisfactorily under favorable conditions (λ_m not much smaller than λ_n during the major part of the crossing).

Due to the previous considerations and since we ultimately need a global direction along which to plot the s/c path, the 1D map $X_N(t)$ is computed in the following way:

$$X_N = \int (\partial_{t,0}\mathbf{X}(t) \cdot \mathbf{n}(t)) (\mathbf{n}(t) \cdot \mathbf{N}_{glob})\, dt \tag{6}$$

where $\mathbf{N}_{glob}$ is defined as the mean of the $\mathbf{n}(t)$ directions computed over the main magnetic field gradient interval (between the two vertical dotted red lines in Figure (1)). This double projection ensures that we use the best determined $\mathbf{n}$ component of the $\partial_{t,0}\mathbf{X}$ velocity, but projected on the global direction $\mathbf{N}_{glob}$. The projection involved in Equation (6) is performed only when the PS is quasi 1D and the magnetic field variations are related to the main current layer. Following (Rezeau et al., 2018), these requirements can be checked for each data point by using the parameters K_{1D} and K_{d_tB}. We require that

$$(\lambda_n - \lambda_m)/\lambda_n > K_{1D} \tag{7}$$

with $K_{1D} \ll 1$ and

$$dB/dt > K_{d_tB} [dB/dt]_{max} \tag{8}$$

with $K_{d_tB} \ll 1$, $B \equiv |\mathbf{B}|$ and, as usual, λ_n and λ_m are the two largest eigenvalues of G.

The time derivatives dB/dt are those measured in the s/c frame. As before (section 2.1.2), the data points that do not survive the selection procedure are replaced by means of interpolation.

2.3 A Gradient-Directed Monte Carlo approach for thresholds decision

The methods described in the previous sections require values for a large number of thresholds. These thresholds are the minimum and the maximum number of fit points for the MVF and the SVF methods ($p_{min,SVF}$, $p_{min,MVF}$ and $p_{max,SVF}$, $p_{max,MVF}$), the thresholds that set a limit to the fit errors for a SVF or a MVF result to be retained or not ($D_{lim,SVF}$ and $D_{lim,MVF}$), and the thresholds for the selection procedures of 1D PSs associated with large currents (K_{1D} and K_{d_tB}). In the present study we fix manually the parameters $p_{min,SVF}$, $p_{min,MVF}$, $p_{max,SVF}$ and $p_{max,MVF}$ as discussed in section 2.1.2 in order to limit the fit procedures to periods between 0.04 and 0.1s; this allows to handle a sufficient number of data points per fit and fits per event. We collect all the remaining parameters in a vector

$$C_r \equiv \{D_{lim,SVF}, D_{lim,MVF}, K_{1D}, K_{d_tB}\} \tag{9}$$

that points to a general state in a 4D phase space $\mathcal{F}_{C_r}$. The spacecraft displacement $X_N(t)$ is an unknown nonlinear function of the C_r components. As it is very sensitive to small variations of $C_r \in \mathcal{F}_{C_r}$, it is reasonable to let it automatically evolve toward values that

make the SVF and MVF outcomes to be as close as possible to each other wherever they can both be determined and make this common interval of validity as long as possible. Such a problem is efficiently solvable by means of an iterative minimization procedure based on a gradient descent algorithm known as Gradient-Directed Monte Carlo Approach (GDMC, (X. Hu, Beratan, & Yang, 2008)). The GDMC technique is a stochastic approach for optimization procedures. It was conceived to find the best C_r^* that optimizes some result $R(C_r)$ via the random sampling of the best candidates for C_r^* in regions of $\mathcal{F}_{C_r}$ as suggested by $-\overline{\nabla}F$, where F is a function that evaluates the distance between $R(C_r)$ and the expected result. In our case, we use the GDMC to select the optimal C_r^* that minimizes (maximizes) the distance (the shared period) between the two $X_N(t)$ resulting from the application of the SVF and MVF methods to the same data set. The GDMC approach has been conceived in molecular design to study the proteins folding properties (X. Hu et al., 2008) and, since it is necessary to obtain the optimal solution in our problem, we describe in detail how we adapt it for our purposes in Appendix (A.2).

3 Results

In the following sections we apply the methods that we have described to artificial and real magnetic fields representing -and probed across- the Earth's Magnetopause (MP). During southward IMF conditions, the MP is characterized by a jump in magnetic field from positive values (within the magnetosphere) to negative values (within the magnetosheath). With this magnetic configuration we use the magnetic field in Equations (3) and (2) to recover, for each case, three different s/c displacements $X_N(t)$ across the MP and, therefore, the magnetic field profile across this physical discontinuity. The MP has gradients also in other quantities ($\mathbf{E}$, $\mathbf{V_i}$, $\mathbf{V_e}$, etc...). The profiles of these quantities can be investigated in the same way, but we will not do this in the present paper.

3.1 Tests on artificial magnetic fields

The artificial magnetic fields we use to test the routines are created by a linear combination of a 1D model ($\mathbf{B}_{\text{model}}$) and a random noise ($\mathbf{B}_{\text{random}}$). The $\mathbf{B}_{\text{model}}$ term is

$$\mathbf{B}_{\text{model}}(x) = \{0, B_{y0} + B_{y1}\tanh(\frac{x}{L}), B_{z0} + B_{z1}\tanh(\frac{x}{L})\} \tag{10}$$

so that the MP normal is oriented toward the X direction and has a thickness equal to $\sim 6L$, if one define the thickness as twice the distance where each component of the current ($\partial_x(\mathbf{B}_{model})$) falls to 1% of its maximum value, *i.e.* twice the distance x^* where:

$$L\partial_x(\tanh(x^*/L)) \simeq k^* \tag{11}$$

with $k^* = 0.01$. Each virtual s/c measures a slightly different $\mathbf{B}_{\text{model}}$ since their trajectories are modeled to be ~ 10 km apart, similar to the smallest MMS separation.

Finally, the "noise" is designed to model all the waves and turbulence always present in these regions, and which have typically amplitudes much larger than the instrumental errors Rezeau et al. (1993). This noise, superposed to the large scale fields could have an impact and may therefore alter the results. Such a "natural noise" is observed on the small scale fluctuations that remain after the filtering procedure discussed in section (2.1.2). Its amplitude and spectrum have been chosen differently for the test signals in the two following examples. In both cases, the amplitudes remain compatible with the observations and the spectrum decays at frequencies above ν_c, the upper frequency limit above which the MMS data are filtered. The second example contains more large scale variations, mimicking the possible large scale evolution of the magnetopause PS.

3.1.1 A straight crossing

Figure (3) shows results for the first test case in which the virtual spacecraft cross an artificial MP along a straight path traveled at constant velocity. The modeled mag-

manuscript submitted to *JGR-Space Physics*

netic field $\mathbf{B}_{\text{model}}$ is defined by Equation (10) with $\{B_{y0}, B_{y1}, B_{z0}, B_{z1}\} = \{12, 0, 10, 30\}$ nT and $L = 250$ km. The mean MDD normal found from the virtual s/c data along their paths is $\mathbf{N}_{MDD} \simeq \{0.99, -0.02, 0.02\}$, which is slightly different from the true normal $\{1, 0, 0\}$ due to the noise $\mathbf{B}_{\text{random}}$. The displacements X_N found from the three methods are plotted in panel 3.*c* in comparison with the model (the result obtained with STD is the same as the one obtained with STD$^+$ and therefore is not shown). Also plotted in panel 3.*a* and 3.*b* are the magnetic fields and the currents found from the curlometer technique; the panel 3.*d* shows the differences between each pair of X_N (call it $\Delta X_{N,ij}$ with i, j equal to a 2-permutation choice between STD$^+$, SVF and MVF). From panel 3.*d* we observe that

1. During the time for which the current is large, the $\Delta X_{N,ij}$ are comparable to - and often lower than- 10 km, marked by the horizontal black dashed line. This is roughly equal to the mean electron inertial length δ_e and the MMS inter-spacecraft distance adopted by the mission to probe the MP at the magnetospheric nose (Burch & Torbert, 2016a);
2. The width of the main current layer defines the limits of the MP so that the total MP thickness can be estimated by the difference of the two displacements X_N at the upper and lower limits of this interval. In this case, these limits are at about $t \sim 6$s and $t \sim 15$s so that the MP thickness is $\sim 1.4 \times 10^3$ km thick, *i.e.* $\sim$ six times the parameter L used in Equation (10) for this case, as expected;
3. Outside the $[6, 15]s$ interval, the differences $\Delta X_{N,ij}$ become larger at the left and the right sides. In these regions the results should be ignored since the displacements are no longer associated with the main MP current.

From these X_N values we can determine the relative error of the s/c location within the $[6, 15]s$ interval, which, for this case, can be estimated to $\sim \Delta X_{N,ij}/(6L) \simeq 7 \cdot 10^{-3}$.

3.1.2 A back and forth crossing

Figure (4) shows a test case that is more similar to observations than the test performed in the previous section, both in regards to the MP thickness and the kinematics. The artificial MP is defined using Equation (10) with $\{B_{y0}, B_{y1}, B_{z0}, B_{z1}\} = \{5, -15, 10, 30\}$ nT and L=70 km. The MP is now $6d_{i,MSh}$ wide (where $d_{i,MSh}$ is the ion inertial length measured within the magnetosheath). There is now a back and forth motion starting at about the middle of the crossing with two stagnation points at $t_1 = 3.75$s and at $t_2 = 4.3$s.

Moreover, we take $\mathbf{B}_{\text{random}}$ with a larger amplitude (by a factor of 3.5). The electric current is so made clearly "noisier" than that computed in section 3.1.1 (compare panel 3.*b* of Figure 3 with panel 4.*b* of Figure 4) and so closer to the observed one (panel 6.*b*, Figure 6). Let us recall that what we call "noise" in this paper is not the instrumental one, which is quite negligible, but the "plasma noise", just discussed above. Note that this "plasma noise" can also model any other non stationarity affecting the boundary, such as the large scale ones that affect the magnetopause in the vicinity of a reconnection X point.

Looking at panels 4.*c* and 4.*d* we observe that the STD$^+$, the MVF and the SVF methods yields quite similar displacements (as before, the STD results are not shown being equal to the STD$^+$ results); SVF gives the best results, which is closest to that of the model. The agreement between MVF and STD$^+$ is expected since no pure temporal variations are introduced in $\mathbf{B}_{\text{model}}$. The enhancement of the noise makes the range of applicability of the three routines smaller than $6L$ and prevents them to be safely applied outside the [2-5.5]s interval. For this reason our methods could not determine the total MP thickness which was about 6L = 420 km, about 1.5 times larger than what the methods detected. It is clear that this under-estimation is just due to the definition

of the MP thickness that has been used here and can easily be corrected. The MP thickness is defined as twice the distance x^* at which the asymptotic current falls to a fraction k^* of its maximum. Taking $k^* = 0.01$ in Equation 11 is clearly too small with respect to the value of the noise. Using $k^* = 0.1$ instead of $k^* = 0.01$ would make the expected MP thickness ($3.6L = 252$ km) equal to what is found. This must be kept in mind for future studies.

3.2 Applications to MMS data

3.2.1 Case study I: 1D and 2D projections of the MMS path

The 1D projection

We applied the STD$^+$, SVF and MVF methods to magnetic field data probed in burst mode (128 Hz) by MMS on 16 October 2015 during the 13:05:30+60s UT crossing. This crossing is very well known in the literature (Burch et al., 2016c; Le Contel et al., 2016; Rezeau et al., 2018; Torbert et al., 2016) and so it is a good test case to benchmark our methods. During this crossing, there was a reconnection outflow jet within the MP coming from a nearby northward magnetic reconnection event that was probed by MMS just a minute later (Figure 3 of (Burch et al., 2016c)); the reconnection outflow velocity, reaching a maximum of ∼350 km/s near the magnetosheath side, prevents determination of the normal displacement $X_N(t)$ from integration of the normal component of the bulk velocity, even though the outflow is mostly tangential to the MP. This is because even a small inaccuracy (say $\pm 5°$) in the determination of the normal direction can cause the integration to yield an erroneously large normal flow.

The crossing occurred at $[8.3, 8.5, -0.7]R_E$ in the GSE frame, when the IMF was southward so that there was a clear rotation of the magnetic field within the MP. This can be seen in Figure 5, where we plot the magnetic field hodogram. In this figure, the out-of-plane direction coincides with the mean MDD normal $\mathbf{N}_{glob}$, which is computed as the mean of the instantaneous MDD normals $\mathbf{n}$ satisfying our dimensionality and variation conditions (Equations. 7 and 8) with the parameters $K_{1D} = 0.73$, $K_{d_tB} = 0.11$ within the [13:05:43 - 13:05:49] interval. The $\mathbf{t}2$ direction is the direction along which the tangential magnetic field varies the least.

In this reference frame, the resulting magnetic field is shown in panel 6.a of Figure (6): the B_n and the B_{t2} components are quasi-constant whereas the B_{t1} component has an irregular tanh dependence, changing from magnetospheric values (∼ 30 nT at early times) to magnetosheath values (∼ −25 nT at late times). The local peak in B_{t1} at around $t = 15.0s$ has already been suspected to be caused by a back and forth motion of the MP (Rezeau et al., 2018). The panel 6.b shows the curlometer current; as expected the largest component is that directed toward the -$\bar{t}_2$ direction. The modulus of the current reduces on the left and on the right extremes of the interval signing the overall MP thickness. The panel 6.c shows the $X_N(t)$ resulting from five different methods. The STD$^+$, SVF and MVF displacements are quite close to each other (see panel 6.d to evaluate their mutual distances $\Delta X_{N,i,j}$), all confirming the back and forth motion, while the red and purple lines, which come from two different integrations of the ion velocity, are significantly different. The red curve results from the integration of the ion bulk velocity $\mathbf{V}_i$ projected on $\mathbf{N}_{glob}$, *i.e.* $\int \mathbf{V}_i \cdot \mathbf{N}_{glob} dt$. The purple curve also results from the integration of $\mathbf{V}_i$ but projected as shown in Equation (6), *i.e.* $\int (\mathbf{V}_i \cdot \mathbf{n}(t))\,(\mathbf{n}(t) \cdot \mathbf{N}_{glob})\, dt$. The red curve does not agree with those resulting from the other methods: it does not yield either the same MP thickness or the back-and-forth motion of the MP. The purple curve succeeds in finding the back-and-forth motion but fails to yield a thickness similar to those computed with the STD$^+$, SVF and MVF methods. Since a non negligible B_n component is present, the MP is not a tangential layer and the differences between the purple curve and the STD$^+$, SVF and MVF displacements are caused by the existence of a normal flow across the MP. The panel 6.e of Figure (6) shows the nor-

mal flow computed as $[(\mathbf{V}_i - \partial_{t,0}\mathbf{X}) \cdot \mathbf{n}(t)]\,(\mathbf{n}(t) \cdot \mathbf{N}_{glob})$ and normalized point-by-point to the normal component of the local Alfvén speed $V_{a,n}$. Comparing Figure (6) with Figure (5), where the color code indicates the magnitude of the normal flow, we observe that the normal flow tends to reach $\pm V_{a,n}$ values everywhere the MP sub-structures tend to be purely rotational, which a quite satisfying result.

Let us now compare the spacecraft velocities obtained using Equation (3) when the singularities explicated in section 2.1.1 are corrected (STD$^+$) and when they are not corrected (STD). Panel 6.f shows the modulus of the LHS terms of Equation (3), *i.e.* $|\partial_{t,0}(\mathbf{X}_{STD})|$ and $|\partial_{t,0}(\mathbf{X}_{STD^+})|$. The orange curve is obtained by using Equation (3) without correcting the singularities. We observe that it is affected by large and very narrow spikes, that would lead to nonphysical jumps in the calculation of the s/c path. The figure shows also that the gaussian corrections do not modify the overall behaviour except during the very small periods where the STD results become large, preserving in this way the information provided by the original STD. They so allow computing the s/c path across the magnetopause.

Finally this crossing does not show any significant non-stationary behavior since the displacements from the SVF and MVF methods agree within a few percent with that of the STD$^+$ method. This indicates that the $\partial_{t,0}\mathbf{B}$ term in Equation (2), used by SVF and MVF, does not lead to a significant correction to the displacements. The conclusion is verified through a direct comparison of the three terms of each component of Equation (2). Figure (7) shows such a comparison. Panels 7.b, 7.c and 7.d compare the three terms of Equation (2) for each of its components and show that the $\partial_{t,0}\mathbf{B}$ terms (green curves), though non negligible, are always smaller than the observed $\partial_{t,sc}\mathbf{B}$ terms (blue curves) and the computed $\partial_{t,0}\mathbf{X} \cdot \overline{\nabla}\mathbf{B}$ terms (orange curves). This can explain why, at some times, the SVF and MVF results are closer to each other in panel d than that of STD$^+$, (see for instance between $t = 15s$ and $t = 18s$).

The 2D projection

During the crossing the MDD eigenvalues ratios λ_m/λ_n and λ_l/λ_n (with $\lambda_n > \lambda_m > \lambda_l$) oscillate around, $1.2{\cdot}10^{-1}$ and $9.5{\cdot}10^{-3}$, respectively. The first and the second ratios are larger than 10^{-1} and 10^{-2} for, respectively, 37% and 19.5% of the selected time interval. Corrections due to the calibration errors (Denton et al., 2010) have been taken into account but results does not change significantly. These considerations suggest that, at least, a 2D reconstruction of the s/c path can be meaningful, since λ_m is not too much smaller than the λ_n for a relative long period of time.

Figure (8) shows the automatic calculation (AC) of the MMS path resulting from the application of the MVF technique to the 16/10/15, 13:05:42 UT - 13:06:04 UT period (multi-colored curve on the right) in comparison with that of two hand-made sketches of the s/c path on a larger scale (left and central sketches). The AC refers to the path included within the red squares drawn on both the hand made sketches. The left sketch is adapted from (Burch et al., 2016c) and was inferred from the MMS observations in combination with a 2D PIC numerical simulation. The sketch in the center is drawn using the instantaneous orientations of the MDD normal (purple arrows) with respect to the local magnetic field and the Shue magnetopause model (Shue et al., 1997). All the three drawings have the magnetosphere on the left, the magnetosheath on the right and the MP located approximately at their center. The color code of the AC indicates the GSE B_z component (positive/red within the magnetosphere and negative/blue within the magnetosheath) and the black and the purple arrows departing from the curve at regular intervals indicate the local directions of, respectively, the magnetic field and the MDD normals. We observe that

1. the mutual orientations of $\mathbf{B}$ and $\mathbf{n}$ from the AC are almost perpendicular everywhere as expected since the remoteness of the reconnection point (cf. the left and

the central sketches) suggests that B_n should be small (*i.e.* the MP should be close to a tangential discontinuity);

2. the AC and the MDD-normal-driven sketches
   (a) look very similar;
   (b) agree in describing the back and forth motion already shown in panel 6.*c* of Figure (6);
   (c) suggest a more complex motion of the s/c relative to the MP than that sketched in the hand made sketch of (Burch et al., 2016c) and
   (d) show a local MP curvature opposite to the global curvature of the magnetospheric boundary (this is at a much smaller scale: tenths of km instead of tens of thousands km).

3.2.2 Case study II: spatial profiles compared to time series

On the morning of the same day of case study I, between 10:36:55 and 10:37:50 UT, a crossing occurred that shows clearly that visualization of spacecraft data as a function of time can be misleading. Our analysis of this event is shown in Figure (9). There, the same data have been plotted twice: once as function of time (left column) and once as a function of space (right column). The different rows of panels show: the GSE magnetic field (panels 9.*a* and 9.a^*); the ion spectrograms where the local maxima with respect to energy have been marked at each time by black points (panels 9.*b* and 9.b^*); the ion temperatures (panels 9.*c* and 9.c^*); the electron temperatures (panels 9.*d* and 9.d^*); the bulk velocity for ions (panels 9.*e* and 9.e^*) and for electrons (panels 9.*f* and 9.f^*). We make the following observations:

1. quantitative measures:
   (a) The length scale of the magnetic field gradient is 500km$\simeq 6.5 d_{i,MSh}$ (see panel 9.a^*); this value agrees both with case study I and the typical magnetopause thickness based on statistical studies (Berchem & Russell, 1982);
   (b) The magnetic field gradient is significantly displaced to the right compared to the region of the largest variations in the particles (compare panel 9.a^* with respect to panel 9.b^*, 9.c^*, 9.d^*, 9.e^* and 9.f^*);
   (c) The low energy magnetosheath plasma and the high energy magnetospheric plasma mix in a $\sim 1 d_{i,MSh} \sim 100$ km thick sub layer (observe the black points in the panel 9.b^*).
2. qualitative considerations:
   (a) The spatial profiles of the ion and the electron temperatures appear approximately monotonic while the temporal ones do not (cf. panels 9.*c* and 9.*d* with respect to panels 9.c^* and 9.d^*)
   (b) The feature that looks like a multiple electron beam (panel panels 9.*f*, between $12s$ and $16.5s$) is actually one electron beam probed multiple times (panel panels 9.f^*, between $X_N = 200$km and 300km).

Here, as well as for the case study analysed in section (3.2.1), the $\partial_{t,0}\mathbf{B}$ term is negligible with respect to the observed $\partial_{t,sc}\mathbf{B}$ term and the computed $\partial_{t,0}\mathbf{X} \cdot \overline{\nabla}\mathbf{B}$ term.

4 Conclusions

In this paper we discuss methods to compute spacecraft (s/c) trajectories across weak-stationary plasma structures (PSs). We present two new methods (SVF, section 2.1.3 and MVF, section 2.1.2) conceived for the computation of the s/c velocity with respect to the PS and therefore useful to find a s/c path by temporal integration. These

methods allow us to observe the PS kinematics and the details of its internal structures avoiding the assumption of strict stationarity, *i.e.* when the PS itself can be subjected to weak modifications during the crossing. By using data provided by MMS crossing the Earth's MP, we have been able to determine features down to temporal and spatial scales $\sim 5\times10^{-3}$ times smaller than, respectively, the time period needed by MMS to cross the MP and the MP thickness.

The methods are first tested on artificial data mimicking an MMS crossing of a stationary 1D MP. Both constant velocity and back-and-forth motions of the s/c relative to the artificial MP are examined (sections 3.1.1 and 3.1.2). Since the artificial MP is precisely stationary (time independent), the results of both the new methods agree with those of an improved version of the STD method (Shi et al., 2006) (which we called STD$^+$) specifically modified to deal with problems of singularities affecting the original STD.

The SVF and MVF methods are then applied to two real MP crossings observed by MMS on 16 October 2015. The calculated s/c paths are first limited to 1D projections along the normal to the MP due to a common intrinsic inaccuracy of the three methods (SVF, MVF and STD$^+$) in computing the magnetic field structure velocity along the tangential directions. Nevertheless these results (section 3.2) lead to detailed informations about the kinematics and the thickness of the MP structure. Regarding the 13:05:30+60s crossing (case study I, section 3.2.1) the displacements $X_N(t)$ resulting from the SVF, MVF and STD$^+$ methods agree with each other in describing a back-and-forth motion of the MP, as indicated also by previous studies (Rezeau et al., 2018) but with less accuracy. The fundamental importance of the time-to-space translation of the s/c data is ultimately underlined by the analysis performed for the 10:36:55 + 55s crossing (case study II, section 3.2.2). The analysis of this crossing by means of our techniques allows us to determine 1) the position and the extension of the layer where the magnetosheath and the magnetospheric plasmas actually mix, 2) the spatial profiles of the different quantities that mark the MP boundary and 3) the exact attribution of multiple signatures to plasma structures that are probed multiple times because back-and-forth motions.

Finally, thanks to the particular conditions occurring during the 13:05:30+60s crossing (section 3.2.1), a 2D reconstruction of the s/c path gives a more detailed picture of the motion of the s/c relative to the MP than that of hand-made reconstructions (Burch et al., 2016c). The weak assumptions and the optimisation procedures used to set the parameters used by these methods (sections 2.3 and Appendixes) make the results of the SVF and MVF methods reproducible and unbiased by any strong assumptions about the PSs and/or by any non-objective decision about the input parameters needed to analyse data.

The SVF and the MVF methods open new possibilities to exploit the ability of multi-spacecraft missions to discriminate temporal from spatial dependencies of observed PSs. For any quantity $\mathbf{Q}$, they allow distinguishing the two kinds of contributions in its variations: 1) the advection of $\mathbf{Q}$ due to the bulk motion of the PS with respect to the s/c and 2) the purely temporal variations of $\mathbf{Q}$. The methods therefore allow independent computations of the spatial profiles of different quantities $\mathbf{Q}$ across the MP. Therefore, they can be used to better understand the real dispositions and thicknesses of the several kinds of sub-structures that may be the elements of the MP, without *a priori* assumptions, giving a better access to the phenomena at play. Used as inputs in the reconstruction techniques, these methods should help to improve their results. Used as inputs for numerical simulations, they should help in getting more realistic initial conditions. The SVF and MVF methods could also be fruitfully used in turbulence studies for testing the Taylor's Hypothesis (Taylor, 1938) with multi-s/c missions.

manuscript submitted to *JGR-Space Physics*

A Appendices

A.1 The optimization of fit periods

The SVF and the MVF methods use linear fits performed with small sequences of data points. As we discussed in the text (section 2.1.2), each fit uses p points where $p_{min} \leq p \leq p_{max}$, and p_{min} and p_{max} are found from Equation (5). In the following, we describe the operative algorithm we implemented to set dynamically the parameter p all along the examined interval in order to cut it into sub-intervals of unequal lengths where the linear fits are the best possible.

Let N be the total number of data points in the total interval to be examined. This interval is divided into two sub-intervals with one point i in common. This point belongs to the interval $[p_{min}, N - p_{min}]$ and there are therefore $N - 2p_{min}$ possibilities for i. For each possible value of i, the linear fits are performed over the two sub-intervals and the corresponding error D_i is recorded. The curve $D = \{D_i, \text{ with } i \in [p_{min}, N-p_{min}]\}$ has an absolute minimum for some i_{min0}, which is the value of i for which the error is minimized when fitting the entire interval by two straight lines. The point i_{min0} is therefore taken as a fixed boundary for the next iteration. The second iteration works as the previous one but applied to each of the two intervals $[0, i_{min0}]$ and $(i_{min0}, N]$. The result is that the whole interval is so divided into four sub-intervals: $[0, i_{min1}]$, $(i_{min1}, i_{min0}]$, $(i_{min0}, i_{min2}]$, $(i_{min2}, N]$, where i_{min1} and i_{min2} are the new fixed boundaries for which the error in fitting the entire period $[0, N]$ by four straight lines is minimized. The procedure is so repeated until there are no more divisions are allowed since there are no more intervals longer than p_{max} points.

A.2 The GDMC method

The STD$^+$, the SVF and the MVF methods depend on some thresholds that define the minimum quality of the fits to be retained ($D_{lim,SVF}$ and $D_{lim,MVF}$) and the minimum MP properties (K_{1D} and K_{d_tB}) for which the methods are valid. In order to set these parameters automatically, we use a gradient-directed Monte Carlo Approach (GDMC, see section (2.3)) to find the thresholds that make the displacements $X_N(t)$ for SVF and MVF as close as possible to each other for the longest time period. In section (2.3) we introduced the GDMC approach briefly. Here we explain how we implemented it for our purposes in more details.

We organize the ensemble of thresholds in a vector C_r (see Equation 9) that represents a general state in a 4D phase space $\mathcal{F}_{C_r}$. The goal is to find the particular C_r^* that minimizes the distance between the displacements $X_N(t)$ of the SVF and MVF methods for the maximum amount of time. The resulting K_{1D} and K_{d_tB} parameters are so used to evaluate the $X_N(t)$ displacement according to the STD$^+$ method too.

For a particular crossing, the optimization algorithm proceeds as follows:

1. We manually define a starting C_r^* usually having $K_{1D} \leq 1$ and $K_{d_tB} \simeq D_{lim,SVF} \simeq D_{lim,MVF} \ll 1$;
2. Then the following operations are iterated (iteration index: i):

   (a) A population Λ_i of C_rs is generated, each deviating from C_r^* by a relatively small variation ϵ of one (or more than one) of its components (note: Λ_i occupies a sub region $f^i \in \mathcal{F}_{C_r}$);

   (b) The SVF and MVF methods are applied to the same data set for every $C_r \in \Lambda_i$. All the C_r of this ensemble are sorted according to a fitness function $F(C_r)$ that evaluates the closeness of $X_N^{SVF}(t)$ and $X_N^{MVF}(t)$ (see later, Equation (A.1));

manuscript submitted to *JGR-Space Physics*

(c) A new sub-region $f^{i+1} \in \mathcal{F}_{C_r}$ is individuated by a procedure explained hereafter, allowing to extrapolate the trend of the best $C_r s \in \Lambda_i$ in the direction where the fitness function is surmised to be minimized;

(d) If $f^{i+1} \neq f^i$ a new population Λ_{i+1} is generated sampling randomly the subspace f^{i+1} and the previous instructions are repeated. Otherwise, the target is selected between the highest ranked $C_r s \in \Lambda_i \in f^i$.

The above algorithm therefore looks for a minimum of $F(C_r)$ in $\mathcal{F}_{C_r}$, by sampling new possible candidates, at each iteration, in the direction given by $-\overline{\nabla} F(C_r)$ (until $\overline{\nabla} F(C_r) \simeq 0$).

Now we explain 1) how we defined the fitness function $F(C_r)$ and 2) how a new population Λ_{i+1} is generated learning from the errors made by the population Λ_i:

1. The fitness function F judges each C_r according to the following criteria:
   (a) The closer the X_N displacements are for SVF and MVF, the better the C_r is and
   (b) The longer the time period for which X_N can be calculated for both SVF and MVF is, the better the C_r is.

   Therefore we define the fitness function as a linear combination of the ranks $r_{\Delta X_N}$ and $r_{\Delta t}$ with which a particular $C_r^* \in \Lambda_i$ is classified in comparison with the others $C_r \in \Lambda_i$ according to, respectively, the total distance between the displacements X_N and the extension of the time period during which both the displacements can be computed:

$$F(C_r) \equiv k_{\Delta X_N} r_{\Delta X_N}(C_r) + k_{\Delta t} r_{\Delta t}(C_r) \tag{A.1}$$

   Both $r_{\Delta X_N}$ and $r_{\Delta t}$ are integer values $\in [1, card(\Lambda_i)]$ with 1 for the best result and $card(\Lambda_i)$ for the worst. Here both the weights $k_{\Delta X_N}$ and $k_{\Delta t}$ are set to 1, the two ranking criteria being of equal importance.
2. The procedure for generating a new population Λ_{i+1} is governed by the gradient of $F(C_r)$, where $C_r \in \Lambda_i$. A sub-set of C_r is first determined, gathering the best ranked vectors. Then, for each component m of C_r in this sub-set, a linear fit is performed and this trend is extrapolated in the direction that minimizes F. The m^{th} component of the new set f^{i+1} is then chosen around this extrapolated trend. The new population Λ_{i+1} is finally randomly chosen in the new sub-region f^{i+1}. The number of the best-ranked C_rs to be fitted, the extension of the extrapolation and the random generation of the new elements around the extrapolated trend are details to be set according to a preliminary analysis. Anyway, they do not influence the shape of the displacements X_N but only the speed of convergence of the optimization process. This procedure, likewise the cross-over procedure adopted by the genetic algorithms (GA, (Holland, 1992)), allows one to modify ongoing the sub-regions $f \in \mathcal{F}_{C_r}$ but, in contrast to GAs, it allows one to take into account a smaller initial population $\Lambda_{i=0}$ (good for reducing computational cost) since, at the generation $i > 0$, it allows to generate C_rs that are not already produced by some crossing-over combination of the $C_r \in \Lambda_0$. In some sense, the GDMC approach can be seen as a GA with two main differences: it is applied to an optimization problem where the parameters to be found are continuous variables and its mutation rate (Holland, 1992) has been pushed to its maximum (which is otherwise very low in GAs).
   Figure (A.1) illustrates the optimization procedure. It concerns the 1^{st} component of C_r (*i.e.* $D_{lim,SVF}$) in the case of the real crossing studied in section 3.2.1. Each of the three panels represents one iteration ($i = \{0, 20, 40\}$). Panel A.1.*a* represents the starting step: a population Λ_0 of 250 C_rs is randomly generated and all the 1^{st} components (blue "+") are sorted by means of the fitness function

F (Equation A.1). We observe that the points having the best rank show a clear trend (see the green line which is the fit of the first 70 best ranked elements). The red dashed line extrapolates this trend to a region where the elements are expected to get better ranks if they were taken into account. Therefore, a new population Λ_1 of possible $D_{lim,SVF}$ are randomly generated around the red dashed line and ranked according to Equation (A.1) (orange "x"). The generation procedure maintains the number of C_r constant and all new components are chosen with positive ordinates since negative values of $D_{lim,SVF}$ are meaningless. After 20 generations (panel A.1.*b*), both the spread of the points and the slope of their fit have decreased: the algorithm is converging. As a matter of fact, at generation 40 (panel A.1.*c*), all the $D_{lim,SVF}$ values $\in \Lambda_{40}$ are located in a small region near ~ 1.7 and the next -randomly generated- values of $D_{lim,SVF} \in \Lambda_{41}$ shares the same region: the algorithm has so converged.

Acknowledgments

The authors thank Laurent Mirioni for his help in dealing with the MMS data and for fruitful discussions. The French involvement on MMS is supported by CNES and CNRS. Work at Dartmouth College was supported by NASA grant 80NSSC19K0254. All the data used are available on the MMS data server: https://lasp.colorado.edu/mms/sdc/public/about/browse-wrapper/.

References

Berchem, J., & Russell, C. T. (1982). The thickness of the magnetopause current layer: Isee 1 and 2 observations. *Journal of Geophysical Research: Space Physics*, *87*(A4), 2108-2114. doi: 10.1029/JA087iA04p02108

Burch, J. L., Moore, T. E., Torbert, R. B., & Giles, B. L. (2016b). Magnetospheric multiscale overview and science objectives. *Space Science Reviews*, *199*(1), 5–21. doi: 10.1007/s11214-015-0164-9

Burch, J. L., & Torbert, R. B. (2016a). Preface. *Space Science Reviews*, *199*(1-4), 1–3. Retrieved from `https://doi.org/10.1007/s11214-015-0153-z` doi: 10.1007/s11214-015-0153-z

Burch, J. L., Torbert, R. B., Phan, T. D., Chen, L.-J., Moore, T. E., Ergun, R. E., ... Chandler, M. (2016c). Electron-scale measurements of magnetic reconnection in space. *Science*, *352*, aaf2939. doi: 10.1126/science.aaf2939

Chanteur, G. (1998). Spatial Interpolation for Four Spacecraft: Theory. *ISSI Scientific Reports Series*, *1*, 349-370.

De Keyser, J. (2008). Empirical Reconstruction. *ISSI Scientific Reports Series*, *8*, 91-98.

Denton, R. E., Sonnerup, B. U. Ö., Birn, J., Teh, W.-L., Drake, J. F., Swisdak, M., ... Baumjohann, W. (2010). Test of methods to infer the magnetic reconnection geometry from spacecraft data. *Journal of Geophysical Research*, *115*(10). doi: 10.1029/2010JA015420

Denton, R. E., Sonnerup, B. U. Ö., Russell, C. T., Hasegawa, H., Phan, T.-D., Strangeway, R. J., ... Vines, S. K. (2018). Determining L-M-N current sheet coordinates at the magnetopause From Magnetospheric Multiscale Data. *Journal of Geophysical Research: Space Physics*, *123*(3), 2274-2295. doi: 10.1002/2017JA024619

Dorville, N., Belmont, G., Rezeau, L., Aunai, N., & Retinò, A. (2014b). BV technique for investigating 1-D interfaces. *Journal of Geophysical Research: Space Physics*, *119*(3), 1709–1720. doi: 10.1002/2013JA018926

Dorville, N., Belmont, G., Rezeau, L., Grappin, R., & Retinò, A. (2014a). Rotational/compressional nature of the magnetopause: Application of the BV

technique on a magnetopause case study. *Journal of Geophysical Research: Space Physics*, *119*(3), 1898–1908. doi: 10.1002/2013JA018927

Escoubet, C., Schmidt, R., & Goldstein, M. (1997). Cluster – science and mission overview. *Space Science Reviews*, *79*(1), 11–32. doi: 10.1023/A:1004923124586

Faganello, M., & Califano, F. (2017). Magnetized Kelvin-Helmholtz instability: theory and simulations in the Earth's magnetosphere context. *Journal of Plasma Physics*, *83*(6). doi: 10.1017/S0022377817000770

Hasegawa, H., Sonnerup, B. U. ., Denton, R. E., Phan, T.-D., Nakamura, T. K. M., Giles, B. L., ... Saito, Y. (2017). Reconstruction of the electron diffusion region observed by the Magnetospheric Multiscale spacecraft: First results. *Geophysical Research Letters*, *44*(10), 4566-4574. doi: 10.1002/2017GL073163

Hasegawa, H., Sonnerup, B. U. O., Dunlop, M. W., Balogh, A., Haaland, S. E., Klecker, B., ... Rème, H. (2004). Reconstruction of two-dimensional magnetopause structures from Cluster observations: verification of method. *Annales Geophysicae*, *22*(4), 1251–1266. doi: 10.5194/angeo-22-1251-2004

Hasegawa, H., Sonnerup, B. U. O., Eriksson, S., Nakamura, T. K. M., & Kawano, H. (2015). Dual-spacecraft reconstruction of a three-dimensional magnetic flux rope at the Earth's magnetopause. *Annales Geophysicae*, *33*(2), 169–184. doi: 10.5194/angeo-33-169-2015

Hasegawa, H., Sonnerup, B. U. Ö., Hu, Q., & Nakamura, T. (2014). Reconstruction of an evolving magnetic flux rope in the solar wind: Decomposing spatial and temporal variations from single-spacecraft data. *Journal of Geophysical Research: Space Physics*, *119*(1), 97-114. doi: 10.1002/2013JA019180

Hasegawa, H., Sonnerup, B. U. Ö., & Nakamura, T. K. M. (2010). Recovery of time evolution of Grad-Shafranov equilibria from single-spacecraft data: Benchmarking and application to a flux transfer event. *Journal of Geophysical Research: Space Physics*, *115*(A11). doi: 10.1029/2010JA015679

Holland, J. (1992). Genetic Algorithms. *Scientific American*, *267*(1). doi: 10.1038/scientificamerican0792-66

Hu, Q., & Sonnerup, B. U. Ö. (2003). Reconstruction of two-dimensional structures in the magnetopause: Method improvements. *Journal of Geophysical Research: Space Physics*, *108*(A1), SMP 9-1-SMP 9-9. doi: 10.1029/2002JA009323

Hu, X., Beratan, D. N., & Yang, W. (2008). A gradient-directed Monte Carlo approach to molecular design. *The Journal of Chemical Physics*, *129*(6), 064102. doi: 10.1063/1.2958255

Le Contel, O., Retinò, A., Breuillard, H., Mirioni, L., Robert, P., Chasapis, A., ... Saito, Y. (2016). Whistler mode waves and hall fields detected by mms during a dayside magnetopause crossing. *Geophys. Res. Lett.*, *43*(12), 5943–5952. (2016GL068968) doi: 10.1002/2016GL068968

Rezeau, L., Belmont, G., Manuzzo, R., Aunai, N., & Dargent, J. (2018). Analyzing the Magnetopause Internal Structure: New Possibilities Offered by MMS Tested in a Case Study. *Journal of Geophysical Research: Space Physics*, 227–241. doi: 10.1002/2017JA024526

Rezeau, L., Roux, A., & Russell, C. T. (1993). Characterization of small-scale structures at the magnetopause from ISEE measurements. *Journal of Geophysical Research: Space Physics*, *98*(A1), 179-186. doi: 10.1029/92JA01668

Shi, Q. Q., Shen, C., Dunlop, M. W., Pu, Z. Y., Zong, Q.-G., Liu, Z. X., ... Balogh, A. (2006). Motion of observed structures calculated from multi-point magnetic field measurements: Application to Cluster. *Geophys. Res. Lett.*, *33*(8), n/a–n/a. (L08109) doi: 10.1029/2005GL025073

Shi, Q. Q., Shen, C., Pu, Z. Y., Dunlop, M. W., Zong, Q.-G., Zhang, H., ... Balogh, A. (2005). Dimensional analysis of observed structures using multipoint magnetic field measurements: Application to Cluster. *Geophys. Res. Lett.*, *32*, L12105. doi: 10.1029/2005GL022454

Shi, Q. Q., Tian, A. M., Bai, S. C., Hasegawa, H., Degeling, A. W., Pu, Z. Y., ... Liu, Z. Q. (2019, May 28). Dimensionality, coordinate system and reference frame for analysis of in-situ space plasma and field data. *Space Science Reviews*, *215*(4), 35. doi: 10.1007/s11214-019-0601-2

Shue, J.-H., Chao, J. K., Fu, H. C., Russell, C. T., Song, P., Khurana, K. K., & Singer, H. J. (1997). A new functional form to study the solar wind control of the magnetopause size and shape. *Journal of Geophysical Research: Space Physics*, *102*(A5), 9497–9511. doi: 10.1029/97JA00196

Sonnerup, B. U. Ö., & Cahill, L. J. (1967). Magnetopause structure and attitude from Explorer 12 observations. *Journal of Geophysical Research: Space Physics*, *72*(1), 171–183. doi: 10.1029/JZ072i001p00171

Sonnerup, B. U. Ö., & Hasegawa, H. (2010). On slowly evolving grad-shafranov equilibria. *Journal of Geophysical Research: Space Physics*, *115*(A11). doi: 10.1029/2010JA015678

Sonnerup, B. U. Ö., Hasegawa, H., Teh, W., & Hau, L. (2006). GradShafranov reconstruction: An overview. *Journal of Geophysical Research: Space Physics (1978–2012)*, *111*. doi: 10.1029/2006ja011717

Taylor, G. I. (1938). The spectrum of turbulence. *Proceedings of the Royal Society of London. Series A, Mathematical and Physical Sciences*, *164*(919), 476–490.

Torbert, R. B., Burch, J. L., Giles, B. L., Gershman, D., Pollock, C. J., Dorelli, J., ... Bounds, S. (2016). Estimates of terms in Ohm's law during an encounter with an electron diffusion region. *Geophys. Res. Lett.*, *43*(12), 5918–5925. doi: 10.1002/2016GL069553

manuscript submitted to *JGR-Space Physics*

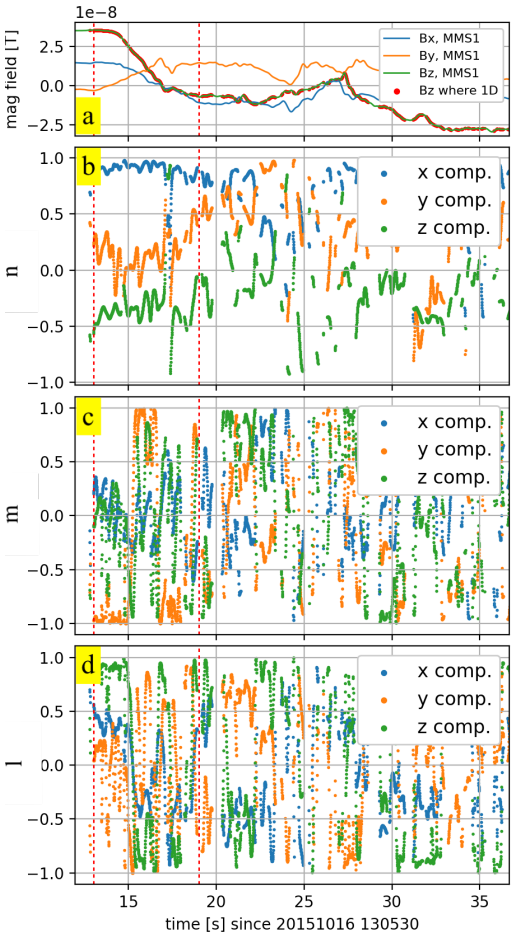

Figure 1. GSE components of magnetic field observed by MMS 1 (panel *a*, the sections in red are the times when the structure is 1D), the l, m, and n components of the MP frame (panels *b*, *c* and *d*) computed by means of the MDD method (Shi et al., 2005) for 16 October 2015, 13:05:30+60s, using burst mode data (128S/s). Note that the m and l directions oscillate rapidly even during times where n is stable.

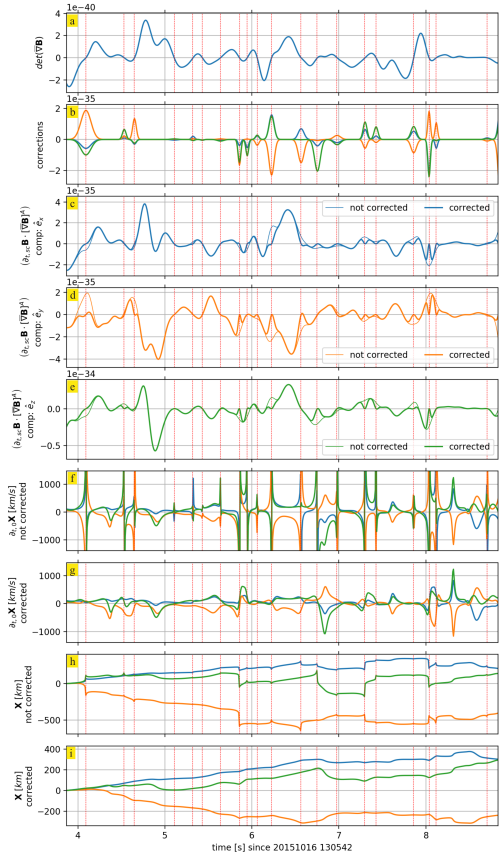

Figure 2. Five second zoom for evidencing the origin of the singularities and the way they are corrected. Each component of the calculated velocity is the ratio between a numerator (panels *c*, *d*, and *e* and a denominator (panel *a*), which is the determinant. The denominator cancels at several places which are slightly different from the places where the different numerators cancel (here in GSE frame). This results in singularities, even in the normal coordinate V_X (panel *f*). If local corrections are applied (panel *b*), these singularities are suppressed (panel *g*) as well as the corresponding jumps in the normal position obtained by integration (panels *h* and *i*).

manuscript submitted to *JGR-Space Physics*

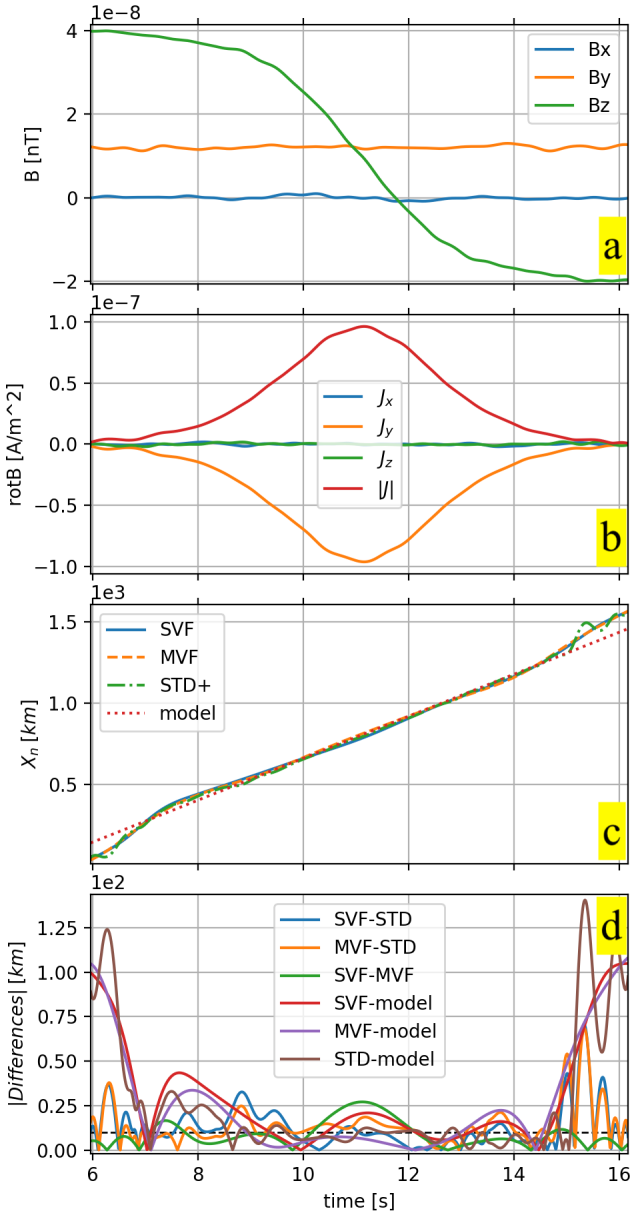

Figure 3. Test case I: artificial crossing with constant velocity. Comparison between the STD$^+$, SVF and MVF displacements with the exact model (panel *c*). The magnetic field, the associated curlometer currents and the differences between the displacements are plotted, respectively, in panel *a*, *b* and *d*.

manuscript submitted to *JGR-Space Physics*

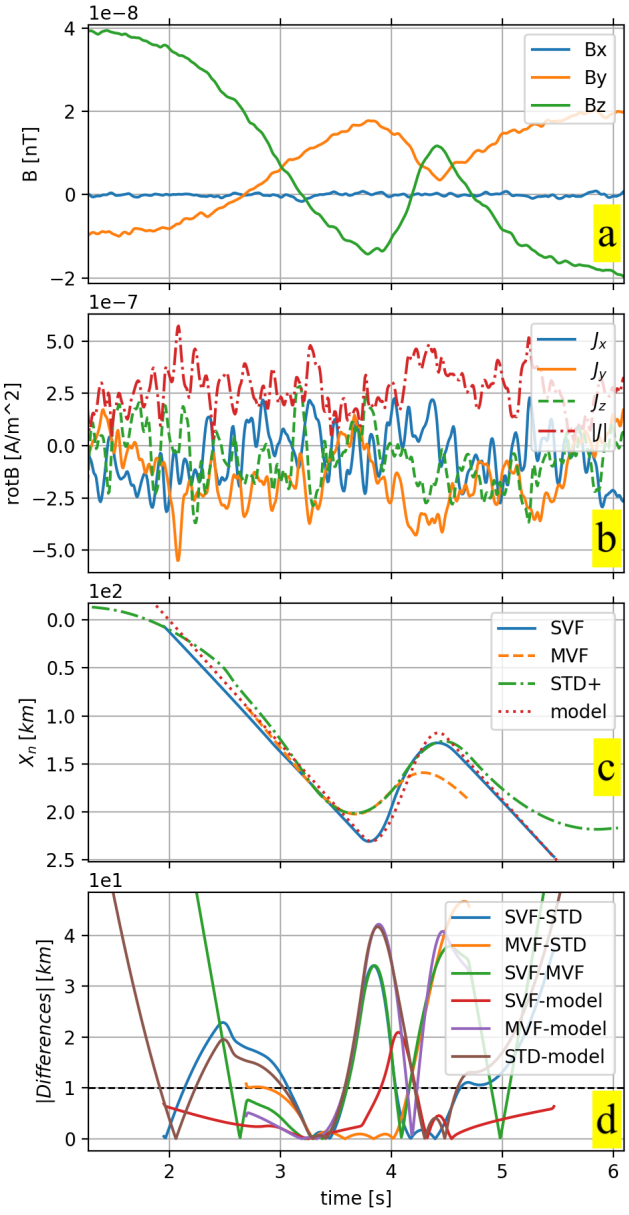

Figure 4. Test case II: back and forth crossing. Displacements found using the STD$^+$, SVF and MVF methods along with the exact model displacement (panel *c*). The artificial magnetic field, the associated curlometer currents and the differences between the displacements are plotted, respectively, in panel *a*, *b* and *d*.

manuscript submitted to *JGR-Space Physics*

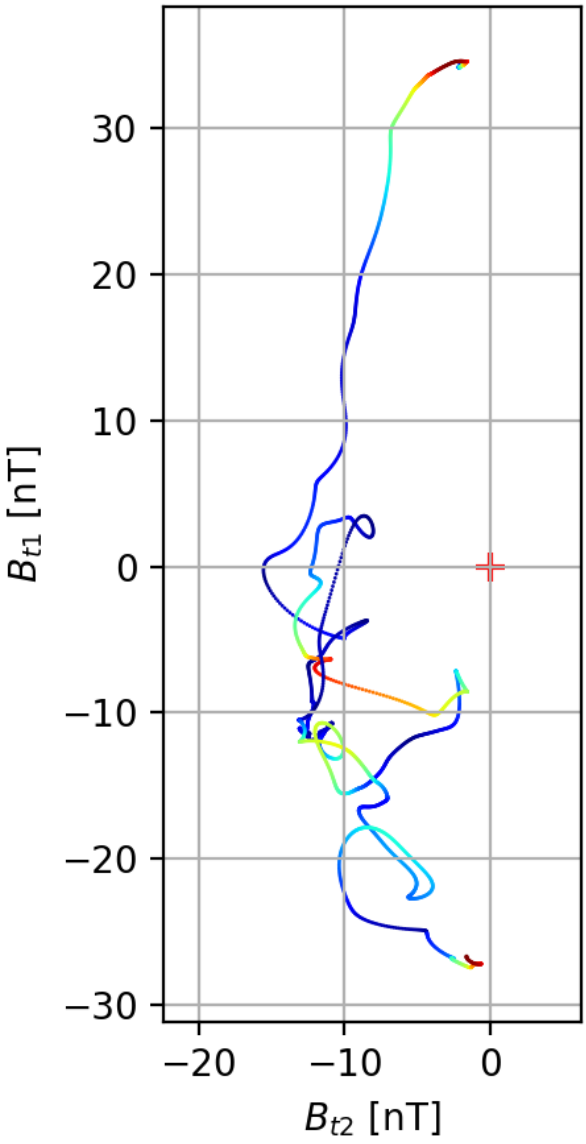

Figure 5. Hodogram of the tangential magnetic field measured by MMS during the 16 October 2015, 13:05:42+22s crossing. The indexes t1 and t2 refers to the tangential directions used to project data (see the text for more details). The color code refers to the magnitude of the normal flow crossing the MP plotted in panel 6.*e* of Figure (6).

manuscript submitted to *JGR-Space Physics*

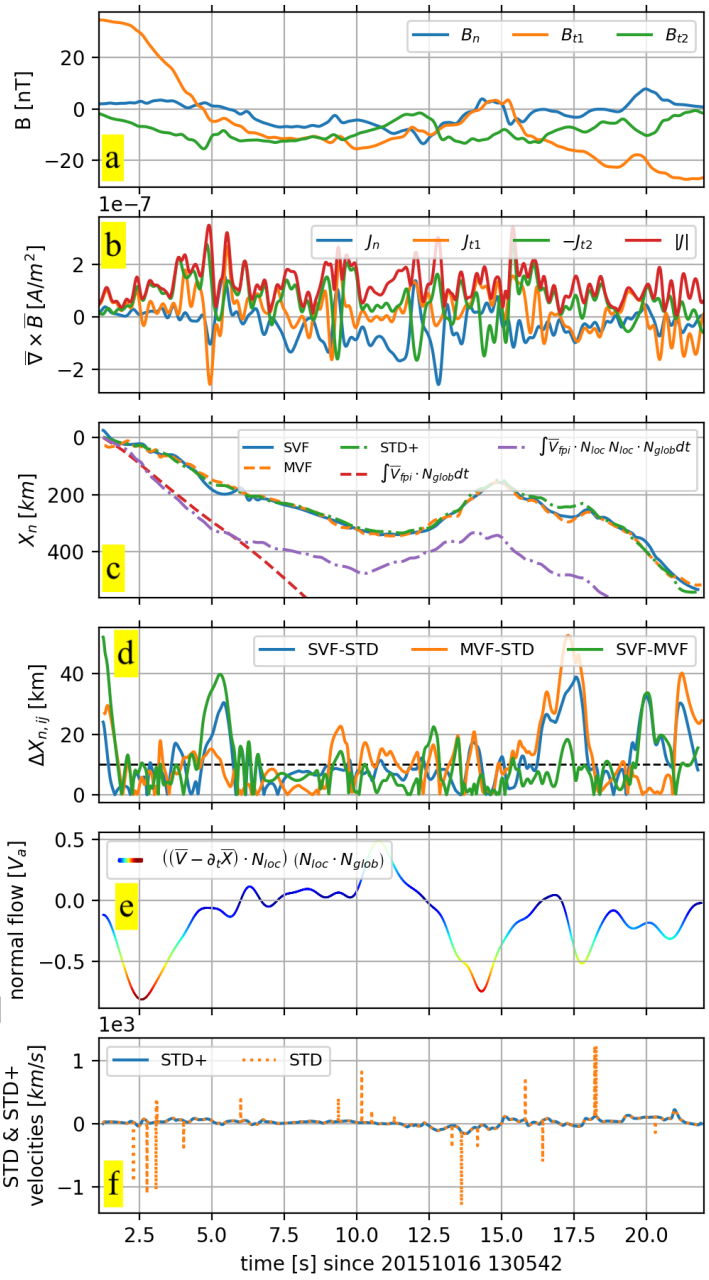

Figure 6. Magnetic field (panel *a*), curlometer current (panel *b*), $X_N(t)$ coordinates (panel *c*), $\Delta X_{N,ij}$ differences (panel *d*), residual normal flow (panel *e*) and comparison between $|\partial_{t,0}(\mathbf{X}_{STD})|$ and $|\partial_{t,0}(\mathbf{X}_{STD+})|$ recorded or computed during the 16 October 2015, 13:05:30+60s crossing (here reduced to the 13:05:42+22s window).

manuscript submitted to *JGR-Space Physics*

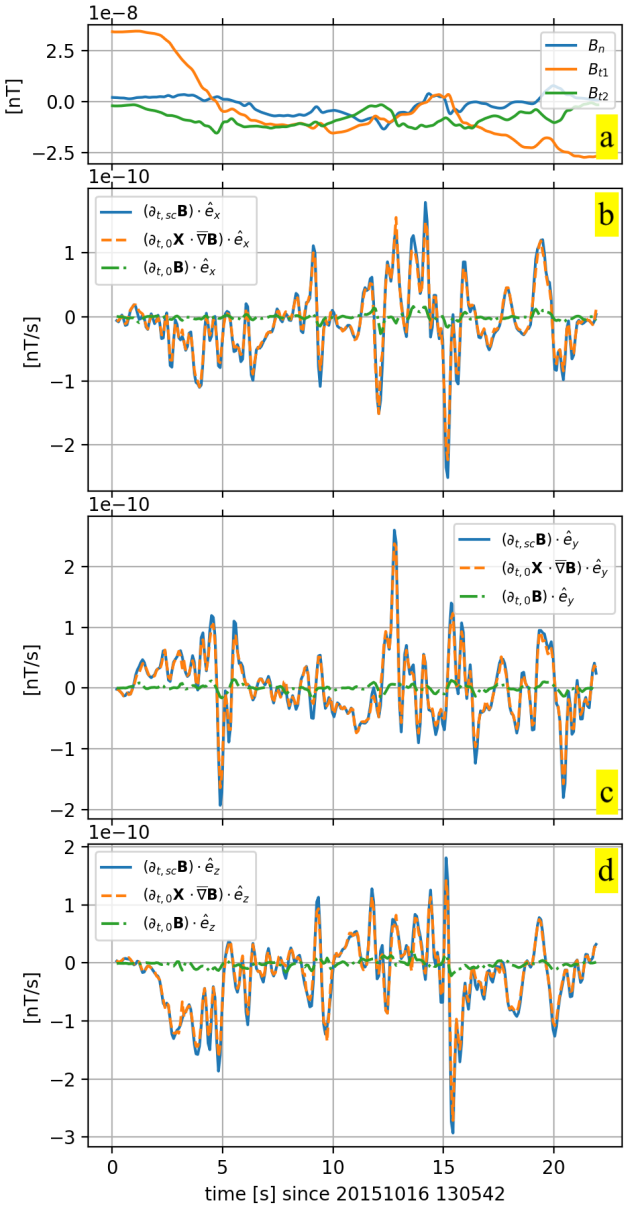

Figure 7. Comparison between the terms of Equation (2) (blue = $\partial_{t,sc}\mathbf{B}$, orange = $\partial_{t,0}\mathbf{X}\cdot\overline{\nabla}\mathbf{B}$ and green = $\partial_{t,0}\mathbf{B}$ curves) for each of its GSE components (panels *b*, *c* and *d*).

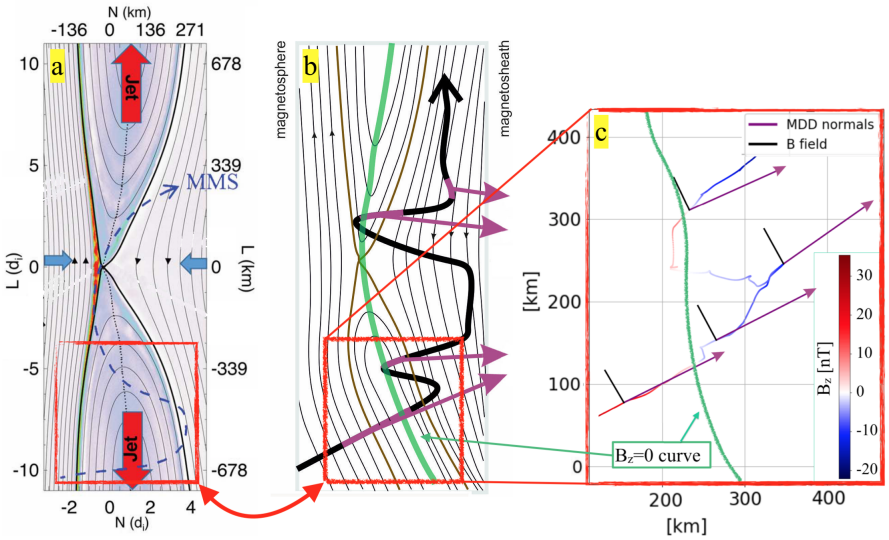

Figure 8. Comparison between the hand-made sketch made by (Burch et al., 2016c) (on the left), a hand-made sketch suggested by the relative direction of the MDD normals with respect to the local magnetic field and the Shue model (Shue et al., 1997) (central sketch) and the path obtained automatically by our MVF technique applied on the 16/10/15, 13:05:42 UT - 13:06:04 UT period (on the right). The automatic result concerns the portion of the path enclosed in the red squares drawn on the hand made sketches. In both panels *b* and *c* the green curved lines joining the $B_z = 0$ points are drawn by hand.

manuscript submitted to *JGR-Space Physics*

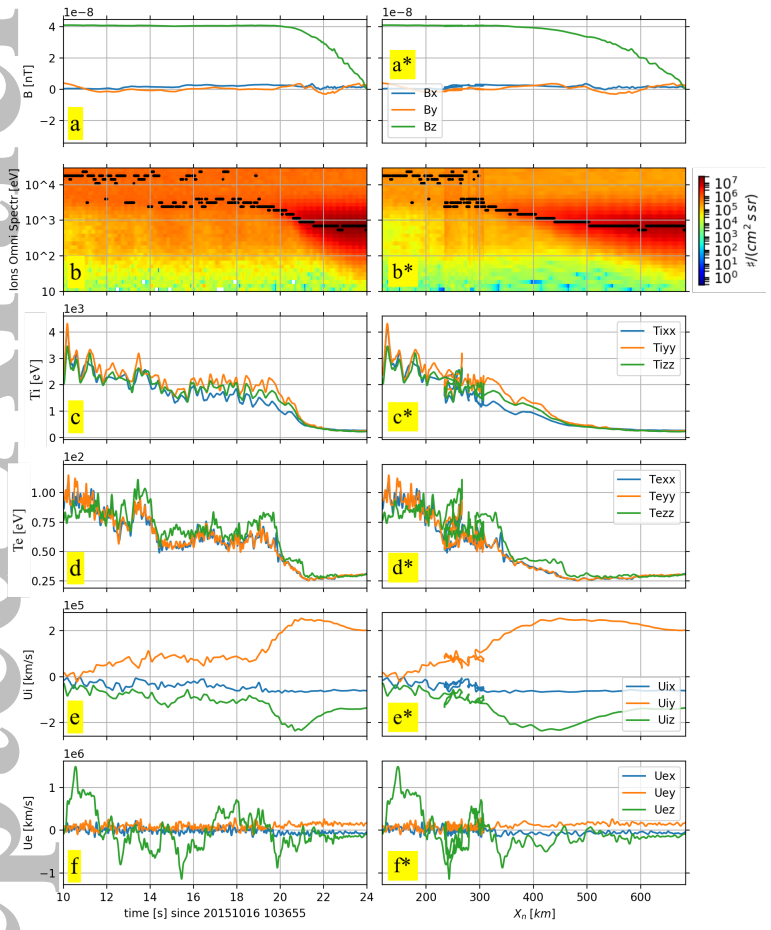

Figure 9. Time vs space visualization of some quantities of interest for the case 16/10/2015, 10:36:55 + 55s. The quantities are visualised twice: as a function of time on the left and as a function of space on the right. The figure shows the GSE components of the magnetic field (panels a and a^*), the ions spectrograms and their maxima (panels b and b^*), the ions and electrons temperatures (panels c, c^* and d, d^*), the ions and electrons bulk velocities (panels e, e^* and f, f^*).

manuscript submitted to *JGR-Space Physics*

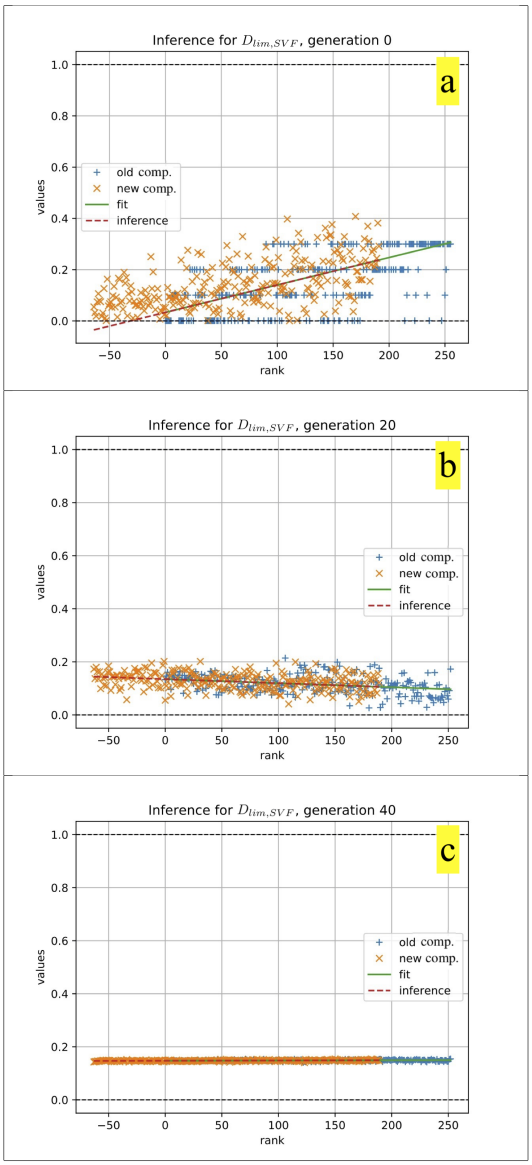

Figure A.1. Illustration of the GDMC optimization procedure for determining the threshold $D_{lim,SVF}$. Panels *a*, *b* and *c* show three different moments of the convergence process: the begin (panel *a*), the end (panel *c*) and a step in between (panel *b*). Each panel shows the first components of C_r ($D_{lim,SVF}$) already sorted by means of the fitness function (blue "+"), the fit of the best-classified 70 elements (green line), the extrapolated trend (red dashed line) and the new values randomly generated around the extrapolated trend (orange "X"). Note that the orange points, which are derived from a purely mathematical extrapolation, can go without problem to the negative range of x, even if negative ranks have no meaning in themselves. On the contrary, the blue points, which are obtained by ranking, always correspond to positive values of x.

23.2 Paper2: Multi-fluid model of the magnetopause

A multi-fluid model of the magnetopause

Roberto Manuzzo[1,2], Francesco Califano[2], Gerard Belmont[1], and Laurence Rezeau[1]

[1]LPP, CNRS, Ecole Polytechnique, Sorbonne Université, Univ. Paris-Sud, Observatoire de Paris, Université Paris-Saclay, PSL Research University

[2]Department of Physics E. Fermi, Universitá di Pisa, Italia

Correspondence: F. Califano (francesco.califano@unipi.it)

Abstract. Observation of the solar wind - magnetosphere boundary provides a unique opportunity to investigate the physics underlying the interaction between two collisionless magnetized plasmas with different temperature, density and magnetic field topology. Their mixing across the interface as well as the boundary dynamics are affected by the development of fluid (and kinetic) instabilities driven by large scale inhomogeneities in particle and electromagnetic fields. Building up a realistic initial equilibrium state of the magnetopause according to observations is still a challenge nowadays. In this paper we address the modeling of the particles and electromagnetic fields configuration across the Earth's magnetopause by means of a three-fluid analytic model. The model relies on one hot and one cold ion population and on a neutralizing electron population. The goal is to build up an analytic model able to reproduce as closely as possible the observations. Some parameters of the model are set by using a fit procedure aiming at minimizing their difference with respect to experimental data provided by the Magnetospheric MultiScale mission. All the other profiles, concerning the electron pressure and the relative densities of the cold and hot ion populations, are calculated in order to satisfy the fluid equilibrium equations. Finally, by means of a new tri-fluid code, we have checked the stability of the large-scale equilibrium model for a given experimental case and given the proof that the system is unstable to reconnection. This model could be of interest for the interpretation of satellite results and for the study of the dynamics at the boundary between the Magnetosphere and the solar wind.

1 Introduction

The solar wind - magnetosphere boundary, known as the magnetopause, is characterized by the presence of magnetic and velocity shears as well as jumps in magnetic and velocity magnitudes, in density and temperature. These inhomogeneities are the sources of many plasma instabilities at different spatio-temporal scales (Labelle and Treumann, 1988), in turn often triggering themselves secondary instabilities at smaller scales. As an example, secondary instabilities such as magnetic reconnection, Kelvin-Helmholtz and/or Rayleigh-Taylor instability can efficiently develop on the shoulder of the primary instability as for instance the Kelvin-Helmholtz at the low latitude magnetopause (see Faganello and Califano (2017) and references therein).

All of these phenomena can cause significant entering of magnetosheath plasma mass (Paschmann, 1997), momentum (Dungey, 1961) and energy (Lee and Roederer, 1982) into the magnetosphere. The study of the magnetopause is of particular interest since this system offers the unique opportunity to study a two-plasma large-scale interaction in conditions not achievable in laboratory. The magnetopause physics is also of basic importance in the studies addressing the Sun-Earth interaction, in particular concerning the impact of solar wind disturbances on the terrestrial environment and the attempts of space-weather forecasting (see for instance Baker and Lanzerotti (2016)). The question of modelling space plasmas using data provided by multi-spacecraft missions has been much developed during the Cluster era (Büchner et al., 1998). Concerning the magnetopause data, one of the key points concerns the mixing between magnetospheric and magnetosheath plasmas and the resulting non-Maxwellian shape of the distribution functions (hereafter d.f.) observed in these regions (Bosqued et al. (2001), Frey et al. (2003), Phan et al. (2005), Retinò et al. (2005)). These d.f. are often reminiscent of those observed in reconnection kinetic simulations (Nakamura and Scholer (2000), Tanaka et al. (2008), Aunai et al. (2011)). Some of these d.f. can be compared with simple analytic models as in the pioneering work by Cowley and Owen (1989). Since the populations coming from the two different sides of the magnetopause differ in density and in temperature, modeling the mixing requires at least the use of a multi-population model. In the perspective of investigating the dynamics of the magnetopause mixing layer by a three-fluid numerical simulation, the main target of this paper is to build up a three-fluid equilibrium as realistic as possible for initializing it.

Several multi-population models trying to simulate the plasma exchanges between magnetosheath and magnetosphere have been developed in the past. In particular kinetic models must provide a Vlasov equilibrium. Such models are very complicated so that the authors are lead to make simplistic mathematical assumptions for choosing the initial d.f., hopeless to get close to magnetopause observed profiles, as for instance the velocity and/or the magnetic field ones. Furthermore, these models involve many free parameters even in the simplest limit of a plane and tangential layer ($i.e.$ without a normal magnetic field: $B_n = 0$). There is no constraint, in particular for fixing the initial electric field profile of a tangential discontinuity in these approaches. Note also that all the equilibria built via d.f. that are functions of the particle invariants of motion only (Channell (1976)) cannot really be considered as "multi-population" models: they ignore the questions of accessibility and they can therefore not distinguish between particles of magnetospheric or magnetosheath origin. Some recent models (see Belmont et al. (2012) and Dorville et al. (2015) and references therein) allow to solve this problem only in part. Indeed in these models even if a few profiles can be fixed in a, let say, realistic way, all the other instead still depend on simple mathematical assumptions, which are largely arbitrary, so that they are still far from realistic.

In summary, the lack of realistic equilibria in the literature makes difficult, for kinetic simulations, the initialization of the magnetopause studies. Nevertheless, the multi-population character of the medium has been taken into account in a recent paper (Dargent et al., 2017) addressing the influence of cold and hot magnetospheric ions on the development of magnetic reconnection. In this paper, the magnetospheric plasma includes two populations with different temperatures in order to account for the presence of cold ions in the magnetosphere close to the magnetopause.

Multi-fluid models have been developed in various domains, but in general not for magnetopause studies. These studies address multi-species evolution involving chemical processes and collisions. They have been used to investigate planetary

atmospheres (Modolo et al. (2006), Ma et al. (2007)), the solar chromosphere (Alvarez Laguna et al., 2016), basic plasma physics problems (drift turbulence in Shumlak et al. (2011) for instance).

In this paper we present a new technique to build up a three fluid equilibrium that derives directly from satellite observations. The model assumes uni-dimensional gradients in the normal direction and a tangential boundary ($B_n = 0$) at the magnetopause. The magnetic and velocity shear are both taken into account in a realistic way. The profiles are chosen to fit at best data from the Magnetospheric MultiScale mission (MMS) (Burch et al., 2016b) for which the time-to-space conversion has been performed by means of recent techniques presented in (Manuzzo et al., 2019, under review). As it will be shown in section (4), the method provides a cold and a hot contributions in qualitative agreement with observations, even if the model uses, as inputs, only the global ion macroscopic moments.

2 Observations

We use MMS data during the period October 16th 2015, 13:05:34 + 40s UT, which embeds a magnetopause crossing. In Figure (1) we plot the experimental data that the equilibrium model attempts to reproduce. This interval shows the standard signatures of the region where magnetospheric and magnetosheath plasmas meet (magnetopause crossing): reversal of the magnetic field and change in the energy distributions.

In panels (a), (b) and (c) data are plotted as functions of a spatial coordinate $X_n = X_n(t)$ which is the projection of the spacecraft path along the direction normal to the magnetopause (units of $d_{i,MSh}$ with $d_{i,MSh} \simeq 70km$). $X_n(t)$ is obtained from the temporal integration of the magnetopause magnetic structure velocity by means of a combination of three distinct methods, STD+, SVF and MVF, optimized with a technique explained in a recent work presently under review on JGR (Manuzzo et al., submitted). Assuming a quasi-stationary structure for the magnetopause current sheet, the procedure gives the position of the probed data with respect to this structure. The main point of this technique is to allow one to recover the spatial profiles of quantities of interest when crossing the magnetosheath - magnetosphere boundary with a variable velocity. For the sake of completeness, we give also in the abscissa of panel (c) the time corresponding to each given value of $X_n(t)$.

In the two spectrograms (panels b and c), black points have been over-plotted to indicate their maxima. This allows one to individuate more easily where the magnetosheath and the magnetospheric plasma interact, as indicated by discontinuities in the curve joining the maxima. The mixing region, emphasised by a blue rectangle in panel (b), is located at $X_n \sim 3d_i$.

In panels (d), (e) and (f) we plot the 2D ion distribution functions (i.d.f.) in the plane tangential to the magnetopause. They are obtained by integration over the out-of-plane (normal) component of the velocity. Each plot is the average of 5 single i.d.f recorded within a $\sim 0.75s$ long interval (equivalent to $0.5d_i$). The radius of the distribution functions is 10^3 km/s and the purple full circle drawn at their centres determines the bottom limits in energy of the FPI instrument (10 eV $\sim$ 53 km/s for ions). The direction of the local magnetic field is indicated by a white arrow. In panel (e) (mixing region), one can observe that the i.d.f. contains two peaks emphasised by the over-plotted circles (blue and red dashed lines). These two circles have a diameter equal to the magnetosheath and magnetospheric thermal velocities, respectively. The same circles are shown for the magnetosheath and magnetospheric i.d.f.s, (f) and (d) panels. In these two asymptotic media, we see that there is only

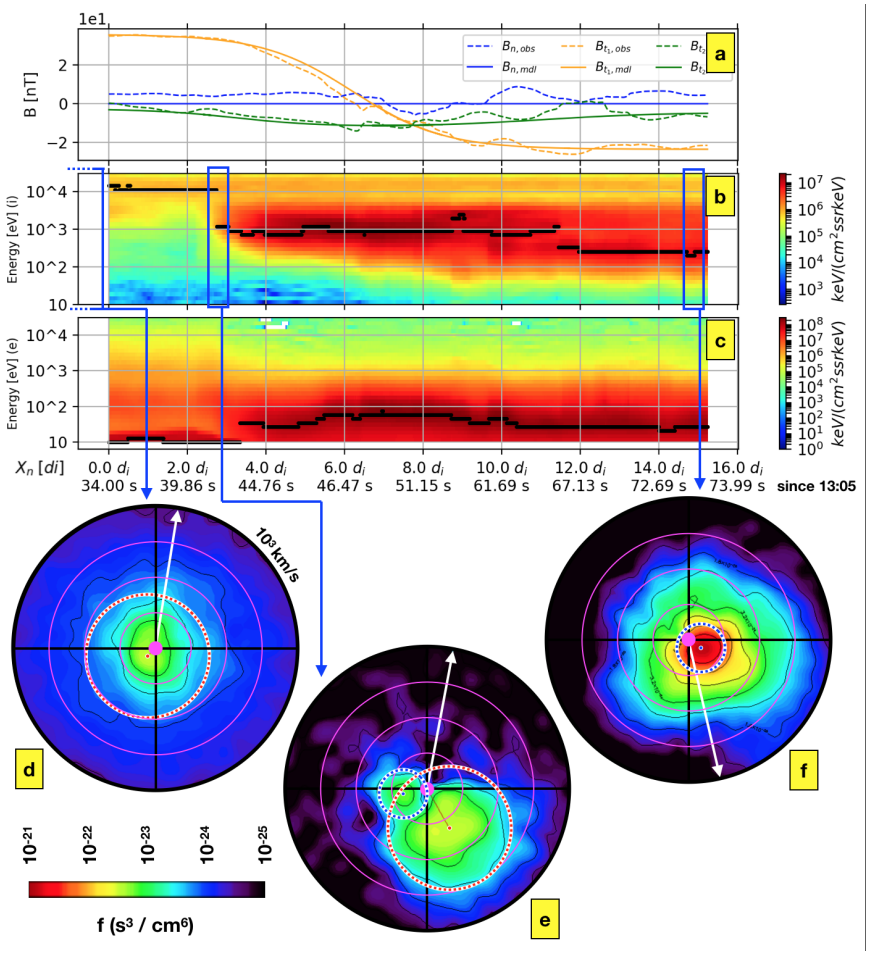

Figure 1. MMS data for the October 16th 2015, 13:05:34 UT + 40s event. Panel a: normal and tangential (to the magnetopause plane) components of the magnetic field. Panels b and c: ion and electron spectrograms. The first abscissa is the spatial coordinate normal to the magnetopause X_n (see text) and the second one is time. Panels d, e and f: ion distribution functions recorded by the FPI instruments, respectively in the magnetosphere, in the overlapping region and in the magnetosheath. These i.d.f.s are projected on the tangential plane by integration over the normal component of the velocity.

one single peak. Note that the i.d.f. shown in panel (d) has been recorded a little earlier (10:20:00 UT + 2s) during a "clear" observation of the magnetosphere allowing to avoid the presence of magnetosheath particles when the spacecraft is too close to the magnetopause. On the other hand panel (e) shows a mixture of the magnetosheath and magnetospheric populations at the same time. However, since the two peaks are close to each other and since the distributions of the two populations are partly superposed, it is not possible to clearly separate the hot/cold contributions, a necessary input for the multi-population model to be built by a direct fit of this region. We will explain in the next section a new method capable of separating the two particle components even in such complex situations. Note that, in the magnetospheric region ($X_n \leq 2d_i$) the electron spectrogram of panel (c) shows energy maxima that lay just at the bottom limit of the instrument ($\simeq 10\ eV$). This indicates the presence of cold electrons in the magnetosphere. The role of this poorly measured cold electron population is not relevant for the magnetopause pressure equilibrium, but in the electron bulk velocity it could be significant. However the electron population parameters will be not determined by a direct fit of the data, nor will those of the two ion populations (cold/hot). They will be determined instead by another method based on the equilibrium equations, which we will describe in the next section.

3 The three fluid model

3.1 Equilibrium equations

We present here a 3fluid collisionless model which includes two ion populations (one cold and one hot) and one electron population. The cold ion population models the ions of magnetosheath origin and disappears more and more on the magnetospheric side. Conversely, the hot population models the ions of magnetosphere origin and disappears on the magnetosheath side.

The continuity and ion momentum equations are derived from the first two moments of the Vlasov equation. We impose charge neutrality and the displacement current is neglected. We assume isotropic pressures and adopt a polytropic closure for all populations. These equations are coupled to the electromagnetic fields via the Faraday's equation and we use an Ohm's law taking into account the electron pressure gradient but neglecting electron inertial effects.

We normalise the 3fluid set of equations by using ion quantities, the proton mass and charge m_p and e, respectively, the ion cyclotron frequency $\Omega_{ci} = e\bar{B}/m_p c$, the ion inertial length $d_i = c/\omega_{pi}$ where $\omega_{pi} = (4\pi\bar{n}m_p/e)^{1/2}$. In particular the characteristic density $\bar{n}$ and mean magnetic field $\bar{B}$ are taken in the magnetosheath far from the central inhomogeneous region. Using index α when all plasma populations are concerned and β when only the ion populations are concerned, the non dimensional 3fluid system of equations reads:

$$
\begin{cases}
\sum_{\alpha} sign(q_\alpha) n_\alpha = 0 & \text{(1a)} \\
\sum_{\alpha} sign(q_\alpha) n_\alpha \mathbf{U}_\alpha = \overline{\nabla} \times \mathbf{B} & \text{(1b)} \\
\frac{\partial n_\beta}{\partial t} + \overline{\nabla} \cdot (n_\beta \mathbf{U}_\beta) = 0 & \text{(1c)} \\
\frac{\partial (n_\beta \mathbf{U}_\beta)}{\partial t} + \overline{\nabla} \cdot (n_\beta \mathbf{U}_\beta \mathbf{U}_\beta) + \overline{\nabla} (n_\beta T_\beta) = n_\beta \left(\mathbf{E} + \mathbf{U}_\beta \times \mathbf{B} \right) & \text{(1d)} \\
\frac{\partial (n_\alpha S_\alpha)}{\partial t} + \overline{\nabla} \cdot [\mathbf{U}_\alpha (n_\alpha S_\alpha)] = 0 \text{ with } S_\alpha = T_\alpha n_\alpha^{1-\gamma} & \text{(1e)} \\
\frac{\partial \mathbf{B}}{\partial t} = -\overline{\nabla} \times \mathbf{E} & \text{(1f)} \\
\mathbf{E} = -(\mathbf{U}_e \times \mathbf{B} + \frac{1}{n_e} \overline{\nabla} (n_e T_e)) & \text{(1g)}
\end{cases}
$$

3.2 Determination of the fluid profiles

We aim at establishing a tangential 1D equilibrium to mimic as close as possible the magnetopause observations previously presented. Assuming $\partial/\partial t$ = 0, this is done in three steps.

Step 1: We impose the magnetic field $\mathbf{B}$, the density n_i, temperature T_i and velocity $\mathbf{U}_i$ profiles these last without distinguishing the cold and hot populations. This is done by fitting the data using a combination of hyperbolic tangents as explained in section (4).

Step 2: We deduce the electron density n_e and velocity $\mathbf{U}_e$ by using the equilibrium equations (1a) and (1b). The temperature T_e is deduced from

$$P_e = P_{tot} - (P_B + n_i T_i) \quad (2)$$

where the total pressure, P_{tot}, is assumed to be a constant in order to fulfil the equilibrium conditions.

As far as P_e is concerned, we note that i) P_e is much smaller than $P_i + P_B$ (see Fig. 2) and that ii) it is difficult to estimate it precisely because of experimental uncertainties. As a consequence, we take for P_{tot} the maximum of the measured total pressure $P_i + P_B + P_e$ and we deduce the modeled P_e from equation 2; this ensures one to get only positive values for P_e.

Finally, the electric field $\mathbf{E}$ is deduced from the Ohm's Law, Equation (1g).

Step 3: We now split the global proton population into two different populations, cold and hot (hereafter "ic" and "ih", respectively) to distinguish the magnetospheric and magnetosheath populations. The densities (n_{ic} and n_{ih}), pressures (P_{ic} and P_{ih}) and currents ($\mathbf{J}_{ic}$ and $\mathbf{J}_{ih}$) of the two ion populations add to form the total ion density, pressure and current as follows

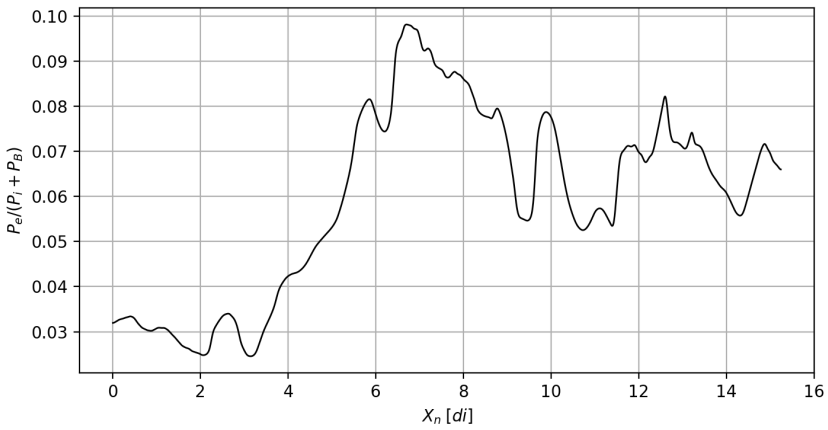

Figure 2. Comparison between P_e and the other pressure terms P_i and P_B. P_e is small everywhere, both within the magnetosphere ($X_n \leq 2.0d_i$) and in the magnetosheath ($X_n \geq 12.0d_i$).

$$n_i = n_{ic} + n_{ih} \tag{3a}$$

$$n_i T_i = n_{ic} T_{ic} + n_{ih} T_{ih} \tag{3b}$$

$$n_i \mathbf{U}_i = n_{ic} \mathbf{U}_{ic} + n_{ih} \mathbf{U}_{ih} \tag{3c}$$

The temperatures of the cold and hot ion populations, T_{ic} and T_{ih}, are assumed to be constant. Since the global ion temperature profile T_i is known, their values are obtained from the satellite data by the two limits:

$$\lim_{x \to MSph} T_{ih} = T_i\,; \quad \lim_{x \to MSh} T_{ic} = T_i$$

The temperature ratio between the two populations is set by the value of the dimensionless parameter:

$$\Upsilon \equiv \frac{T_{ih}}{T_{ic}} \tag{4}$$

Using Equation (3b), the contributions of each population to density and pressure are fully determined by the T_i profile and the temperature ratio Υ:

$$\Gamma \equiv \frac{n_{ic}}{n_i} = \frac{\Upsilon - \frac{T_i}{T_{ic}}}{\Upsilon - 1} \tag{5a}$$

$$\Pi \equiv \frac{P_{ic}}{P_i} = \left(1 + \frac{1-\Gamma}{\Gamma}\Upsilon\right)^{-1} \tag{5b}$$

The perpendicular currents and by consequence the corresponding velocities, are fully determined by Equations (1d). On the contrary, the parallel currents cannot be determined by the above system of equilibrium equations. We will set them by a reasonable choice for the parameter ϕ which is equal to the ratio of the cold parallel ion current to the total parallel ion current as seen in the electrons frame:

$$\phi \equiv \Gamma \frac{(\mathbf{U}_{ic} - \mathbf{U}_e) \cdot \mathbf{b}}{(\mathbf{U}_i - \mathbf{U}_e) \cdot \mathbf{b}} \tag{6}$$

The parallel components of the hot and cold ion velocities can have opposite directions, so that ϕ is defined in the $[-1, 1]$ range, while Γ and Π are defined in the $[0, 1]$ range. The reasonable choice for ϕ is suggested by the data and will be discussed in more details in the next section. In general, the asymptotic values of the cold and hot ion currents are chosen in agreement with the asymptotic values of n_{ic} and n_{ih}, in order that all the corresponding values of the velocities U_{ic} and U_{ih} have reasonable values, although one of the two densities n_{ic} or n_{ih} tends to nearly zero on each side.

In order to implement this model into a numerical simulation, a compromise is necessary since the multi-fluid code cannot deal with a population having a zero density somewhere in the domain. To avoid this problem, we introduce the parameters $\epsilon^{(c)} \ll 1$ and $\epsilon^{(h)} \ll 1$ and we modify the initialisation so that the cold and hot densities tend to $\epsilon^{(h)} n_i$ and $\left(1 - \epsilon^{(h)}\right) n_i$ on the magnetospheric side, and vice versa to $\left(1 - \epsilon^{(c)}\right) n_i$ and $\epsilon^{(c)} n_i$ on the magnetosheath side. The temperatures are changed according to:

$$T_{ic} = \frac{\epsilon^{(c)} T_i^{MSph} - \left(1 - \epsilon^{(h)}\right) T_i^{MSh}}{\epsilon^{(c)} + \epsilon^{(h)} - 1} \tag{7a}$$

$$T_{ih} = \frac{\epsilon^{(h)} T_i^{MSh} - \left(1 - \epsilon^{(c)}\right) T_i^{MSph}}{\epsilon^{(c)} + \epsilon^{(h)} - 1} \tag{7b}$$

where T_{ic} and T_{ih} indicate the observed values corresponding to the model, and T_i^{MSph} and T_i^{MSh} the temperatures corresponding to the magnetospheric and magnetosheath values of T_i. A similar correction is made for the ion velocities (see next sections).

4 Data vs analytic profiles

We apply the procedure to the case study introduced in section (2). In Figure (3) we compare the model field profiles with the ones obtained with the MMS data. The model profiles for the magnetic field, the ion temperature and density are obtained by a fit procedure, panels (a), (b), and (c), respectively, while the others are calculated from the equilibrium equations. The fits are obtained by means of analytic functions. For a given quantity Q, the fitting functions have the following form:

$$Q = \sum_j a_{Q,j} + b_{Q,j} tanh(\frac{X_n - c_{Q,j}}{d_{Q,j}}) \tag{8}$$

where X_n is the coordinate along the direction normal to the magnetopause (as discussed in section 2). The parameters $a_{Q,j}$, $b_{Q,j}$, $c_{Q,j}$, and $d_{Q,j}$ are the free parameters shaping the analytic profiles and j is the component index. The maximum value

of j depends on the fitted quantity: the analytic profiles are considered as good fits of the data if they correctly shape the large scale configuration, as well as the position and the length scale of the gradients within the magnetopause layer. An example of such a "good fit" is given in Fig. 3, panels (a), (b) and (c). It is worth noticing that the particle boundary, observed on density and temperature, has a length scale smaller than the magnetic boundary (by a ratio $\simeq 0.25$) and that its position is considerably shifted toward the magnetosphere with respect to the centre of the magnetic jump. This may indicate the presence of a boundary layer, possibly made of magnetosheath plasma observed on the magnetospheric side of the magnetopause (Hasegawa, 2012). Such features cannot be reproduced in the framework of a MHD equilibrium model. To the best of our knowledge, they have not been introduced even in the context of a kinetic model.

In panel (b) we show the temperature profiles as obtained with our model equilibrium. The total ion population temperature T_i has been obtained by fit, and it is superposed with the cold ion population temperature T_{ic} (blue curve) and the hot ion population one T_{ih} (red curve). The figure has been drawn using $\epsilon^{(h)} = 0.35$ and $\epsilon^{(c)} = 0.05$, which determines the values of T_{ic} and T_{ih} via Eqs.(7).

One observes that the global temperature is well fitted by the model outside the mixing region, but that the fit is less accurate in the $\sim 1.0 d_i \leq X_n \leq \sim 2.5 d_i$ interval. In this interval the real total ion temperature becomes actually larger than its magnetospheric asymptotic limit. Unfortunately this feature can not be reproduced by the present 3fluid model with constant hot and cold temperatures since the $\Gamma \geq 0$ constraint forces the T_i profile to be everywhere lower than T_{ih} (see Equation (5a)). This little deviation is acceptable since the model mainly aims at reproducing the asymptotic trends, the observed inner region probably being out of equilibrium.

In panel (c) we show the density profiles. As explained in the previous section, the hot and cold ion contribution to the total density n_i are computed by means of the Γ function which is fixed once the global T_i profile and the temperature ratio Υ are fixed (Equation (5a)). For all panels of Figure (3) the two vertical lines (dashed black) indicate the limits of the region where $1/4 \leq \Gamma \leq 3/4$. Note that the cold ion density falls rapidly to very low values in more or less $\sim 2\ d_i$ while the hot population density keeps nearly the same value over a longer interval (between 0 and 8 d_i).

The electron density and velocity profiles are obtained from the equilibrium equations. However these quantities are not plotted here since their experimental counterparts are likely to be biased in the magnetosphere by the cold electron population which is below the bottom threshold in energy of the FPI instrument (as mentioned in section 2). On the other hand, we plot in panel (d) the electric field, which is obtained from the 3fluid model, Equation (1g). We see that the electric field calculated by the model agrees quite well with the one measured by the instrument independently of the electron measurements.

The parallel components of the cold and hot ion currents are set by ϕ (Equation 6). As long as there are no cold ions on the magnetospheric side and no hot ions on the magnetosheath side, the asymptotic constraints on ϕ would be

$$\lim_{x \to MSph} \phi = 0\,; \quad \lim_{x \to MSh} \phi = 1$$

Nevertheless, because of the compromise necessary for implementing the model in the multi-population numerical simulation, the cold and hot densities actually take small but not strictly null values on both sides. To determine the corresponding parallel currents, corrections similar to Eqs. (7) are applied with the assumption that, on each side, the parallel velocities of the cold

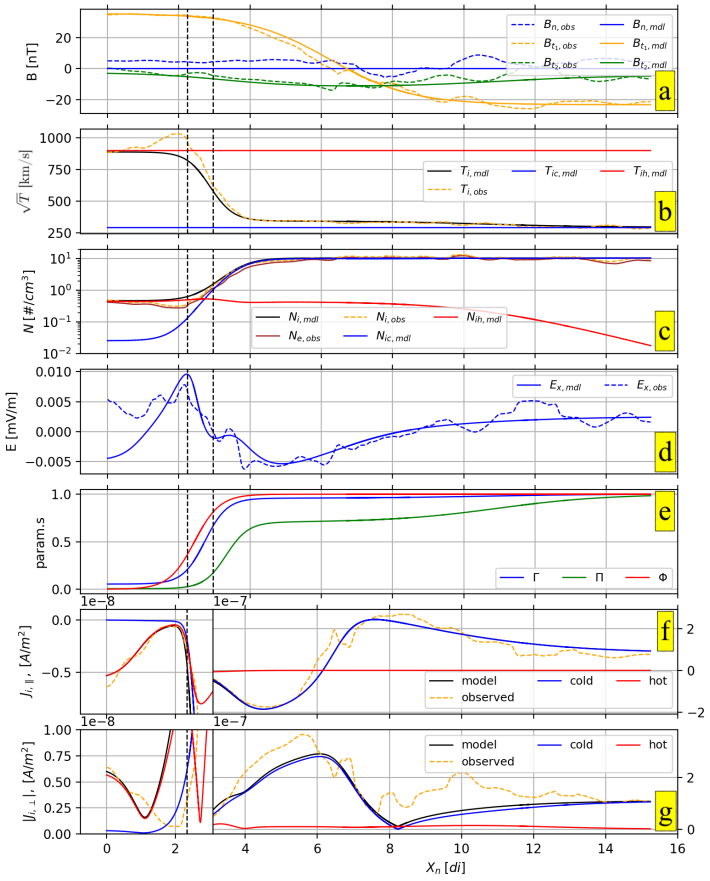

Figure 3. Comparison between the magnetopause profiles as observed by MMS during the 16 October 2015, 13:05:34 + 40s UT period and those used for the 3fluid model equilibrium. Satellite data are represented by dashed lines, the extrapolated profiles used in the model by continuous lines. The X_n coordinate represents the spatial coordinate normal to the magnetopause X_n. In the panels we show the magnetic field (a), the temperatures (b), the density (c), the electric field (d), the parameter Γ, Π and Φ (e), and the parallel and perpendicular components of the ion current (panels f and g respectively). The two vertical lines (black dashed) highlight the transition region ($1/4 \leq \Gamma \leq 3.4$). The blue and orange colours adopted for the electric and magnetic fields represent the normal and the tangential components of the fields. The square roots of the temperatures (panel b) are plotted in velocity units in order to make easier the comparison with i.d.f.s shown in Figure (1). For the sake of clarity, the curves shown in panels (f) and (g) have been multiplied by a factor 10 in the $0.0 \leq X_n \leq 3.0$ interval.

and hot populations, in the electron frame, are equal to each other and therefore equal to the global one. Under this assumption, it can be easily shown that the asymptotic values of Φ are equal to those of Γ:

$$\lim_{x \to MSph} \phi = \epsilon^{(h)}, ; \quad \lim_{x \to MSh} \phi = 1 - \epsilon^{(c)},$$

Note that for the particular MMS event considered, the global ion parallel velocities are observed to be quasi-null on each side, so that the same asymptotic property holds for the velocities of the two populations.

Between the two limits above, a reasonable choice for the ϕ profile is that the length of its gradients be of the same order as the scale length of the density and temperature gradients, $i.e. \sim 1 - 2d_i$. The position of the main gradient of ϕ is set in order to separate the magnetopause thickness in two parts, each of length proportional to the gyro-radii of the two populations (their ratio is $\simeq 2$).

In panel (e) of Figure (3) we show the model profiles for Γ, Π and Φ. Because of the differences of temperature between the two components, the profile in Π (concerning the pressures) noticeably differs from the profile in Γ (concerning the densities).

Finally, in panels (f) and (g) of Figure (3), we show the results concerning the parallel and perpendicular components of the ion currents. Once more, one observe that the global ion current is well fitted, at the exception of the perpendicular current in the mixing region, which is less accurate. This is due to the small inaccuracy already mentioned of the modeled ion temperature in this region.

5 Numerical simulations

5.1 Set up

Here we give an example of a 3fluid numerical simulation aiming at demonstrating the possibility of studying numerically the above system starting from an equilibrium not far from a real one, not only qualitatively but also quantitatively. A detailed numerical study relying on such approach will be the focus of future work.

The three-fluid model introduced in this paper has been used to initialize a 2D 3fluid numerical simulation of the interaction between the solar wind and the Earth's magnetopause. The numerical simulation is intended to mimic the October 16th 2015, 13:05:34 + 40s UT MMS crossing. This simulation has been performed by using a 3fluid numerical code that solves the set of Equations (1a-g). The code originates from a 2fluid 3D parallel code largely used for the study of the interaction of the solar wind with the Magnetosphere (see Fadanelli et al. (2018) and references therein). The 3fluid code adapts the new equations to the algorithm of the 2fluid code presented in Faganello et al. (2009). It advances in time with a standard third-order Runge-Kutta algorithm (Canuto, 1988). It uses sixth order explicit finite differences along the periodic y and z-direction and a sixth-order compact finite difference scheme with spectral like resolution for spatial derivative along the inhomogeneous x-direction. The numerical stability is guaranteed by means of a spectral filter along the periodic y and z directions and a spectral-like filtering scheme along the inhomogeneous x-direction. The code is parallelized along the periodic y and z directions (Lele, 1992). The code has been validated by standard numerical tests. In particular, by selecting separately the two cold and hot ion populations, we have reproduced the propagation of ion acoustic and Alfvén waves.

To initialize the simulation presented in this paper we take as initial equilibrium the model profiles represented in Figure (3), including the few modifications for the cold and hot ion density components (with respect to the basic model) because of the computational reasons discussed at the end of Section 3.

The simulation box dimensions are given by $L_x = 160d_i$, $L_y = 20\pi d_i$ and the box is discretized using $n_x = 800$ and $n_y = 320$ grid points corresponding to $dx = dy = 0.2d_i$. We have checked that the equilibrium configuration remains stable for several thousands of ion cyclotron times in the absence of an initial perturbation because of the very low values of the numerical noise and of the high accuracy of the numerical methods.

5.2 Results

The large scale equilibrium configuration used to initialize the simulation is unstable with respect to the reconnection mode. At $t = 0$ we add to the equilibrium an initial perturbation $\delta\mathbf{B} = \nabla \times \mathbf{A}$. The potential vector is given by a sum of random phase modes as follows:

$$A_l = \epsilon(x) \sum_{k_y} \sum_{k_x} \{cos\left[k_x x + k_y y + \phi_{1,l}(k_x, k_y)\right] +$$

$$cos\left[k_x x - k_y y + \phi_{2,l}(k_x, k_y)\right]\}/k; \quad l = x, y, z; \quad k = \sqrt{k_x^2 + k_y^2}; \quad i \neq j \tag{9}$$

where $\phi \in [0, 2\pi)$ are random phases and $\epsilon(x)$ is a Gaussian-like convolution profile in the inhomogeneous direction going to zero at both boundaries given by

$$\epsilon(x) = \epsilon_0 e^{-\left(\frac{x - x_{mp}}{2L_{mp}}\right)^2} \tag{10}$$

where $x_{mp} = L_x/2 = 60$ and $L_{mp} = 1.66$ are the position and the thickness of our magnetopause model.

The simulation is run for about 1500 ion cyclotron times. Very rapidly the initial perturbation reorganizes and sets up the reconnection eigenmodes that are identified by their wave-number in the y-periodic direction (each m wave-number is easily recovered by taking the Fourier Transform of the perturbation along the y-direction at a given time). Following the classical reconnection theory (Furth et al., 1963) (but ignoring the density inhomogeneity), we have checked that our equilibrium is Δ' unstable for the first five eigenmodes. We recall here that the Δ' parameter depends on the equilibrium magnetic shear and on the wavelength of the perturbation. It defines the instability threshold condition ($\Delta' \geq 0$). The unstable modes can be seen in Figure (4) where we plot Δ' as a function of the wave numbers m_y. We see that only the first five modes have a positive Δ', in agreement with the simulation where in the linear phase the $m_y \geq 6$ are stable (see discussion below). In Figure (5), panel (a), we plot the profile of the fastest growing eigenmode (corresponding to $m = 2$) of the x-component of the magnetic field fluctuation δb_x. The plot is along the inhomogeneous x-direction at five different times (see the legend) in log scale. The two red vertical dashed lines indicate the spatial window of the equilibrium represented in Figure (3). This picture shows that after an initial transient needed to set up the normal mode shape, the reconnection instability develops around the

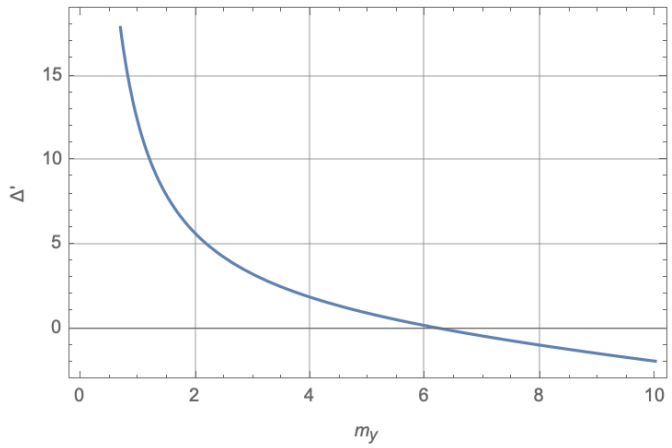

Figure 4. Δ' as a function of the wave numbers m_y for an equilibrium magnetic field $\sim tanh(x)$.

region where the magnetic field reverts, $0 \leq x \leq 16$ (see also Figure (3)). Since the equilibrium is asymmetric, in particular for what concerns the cold and hot ion density that vary in a different location with respect to the point where the magnetic field inverts, the eigenmode is not symmetric with respect to the point where the magnetic field inverts, $X_n \simeq 6.4$. To the best of our knowledge, this is the first time that one investigates the reconnection instability in the framework of a 3fluid approach in a non symmetric equilibrium representing directly the large-scale configuration taken from a satellite data event. Our goal here is to show the possibility to set up such a "realistic" large-scale initial equilibrium configuration to be simulated by a three-fluid approach. The non linear development of the system and in particular the mixing efficiency will be the object of future work. Still in Figure (5), panel (b), we plot the eigenmodes growth vs time in normalized units (log scale). We see the exponential growth of the first five modes, $m_y \equiv k_y L_y = 1, .., 5$. Modes with $m_y = 6, 7$ are instead stable. The orange curve corresponds to the most unstable mode, $m_y = 2$, the one plotted in panel (a). Despite the strong inhomogeneity of the system where, as discussed before, the magnetic inversion and the density variations occur at different locations, we see a very clear exponential growth with a constant growth rate. The linear phase last until about $t \simeq 1000$ after which the non linear phase begins. The values of the growth rates of the five unstable modes are reported in panel (c) confirming that $m_y = 2$ is the most unstable one. In Figure (6) we show at the beginning of the saturated phase, $t = 1455$ the shaded iso-contours of the cold ion population, $N_{i,c}$. We see the formation of a hole structure corresponding to the region where the cold ion density grows eventually reaching the asymptotic magnetosheath value. To show the cold density hole, we made a cut along the inhomogeneous x-direction at $y = 38$ (see dashed line) still in Figure (6) in the bottom frame. In Figure (7) we show the same quantities for the hot ion fluctuations. We see a "complementary" behavior in the sense that now a bump is generated more or less in correspondence of the cold ion hole. However, as already discussed, it is not the goal of this paper to study the non linear dynamics and mixing properties of the cold and hot ion populations. Our aim here is limited at presenting a method able to obtain a "realistic" 3fluid

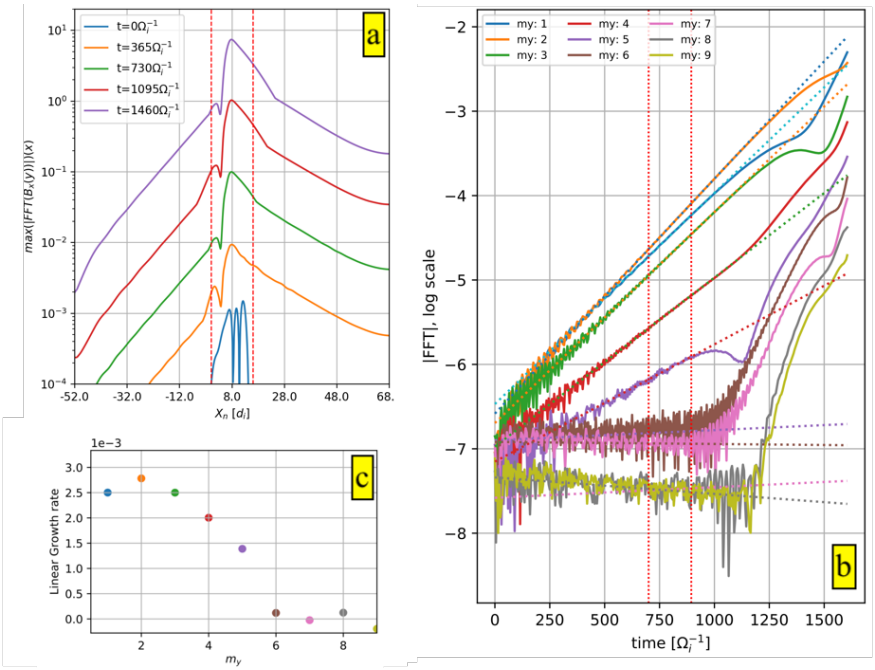

Figure 5. Development of the reconnection instability. Panel (a): the modulus of the Fourier Transform of δb_x along y vs x at five fixed time instant. The plots correspond to the fastest growing mode, $m = 2$, in log scale. The two red dashed vertical lines indicate the space interval of Figure (3). Panel (b): the first five eigenmodes growth vs time. The orange curve corresponds to the most unstable mode, $m = 2$, the one plotted in panel (a). Panel (c): the growth rate values vs k_y calculated by a best fit of the slopes in panel b. The colors correspond to those used in panel (b).

equilibrium starting from a set of satellite data that can be used as initial condition for the investigation of the dynamics in the framework of a three-fluid approach.

6 Conclusions

The huge amount of spacecraft data today available brings a lot of information about the magnetopause, especially those of the MMS mission with their high resolution particle data. The magnetopause modeling can now be improved in view of these observations, which show that this boundary is never the simple textbook boundary generally considered. Beyond the natural asymmetry in temperature and density between the magnetosphere and magnetosheath plasmas, the first important ingredient to consider is the strong velocity shear that arises at the boundary, in addition to the magnetic shear which is the defining property of the magnetopause. Furthermore, the gradients concerning the particles and those concerning the magnetic field

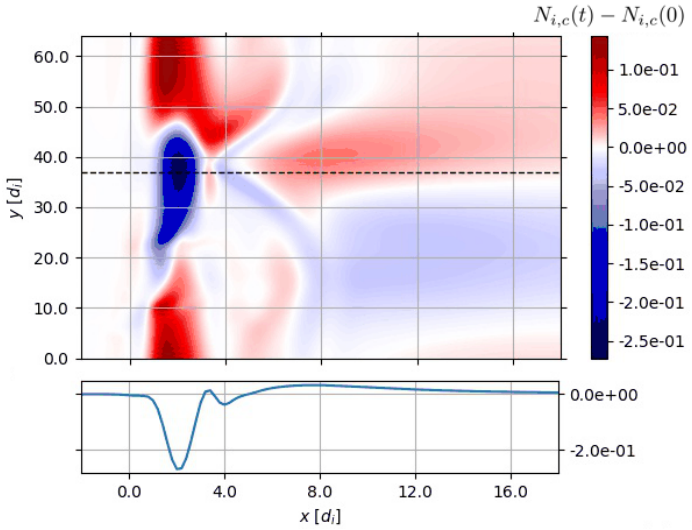

Figure 6. Shaded iso-contours of the cold ion fluctuations, $N_{i,c} - N_{i,c}(t=0)$ at $t = 1455\Omega_i^{-1}$. The bottom panel shows a plot of the same quantities vs x at $y \simeq 39$ corresponding to the horizontal dashed line in the shaded iso-contours. Numerical values are normalized to the magnetosheath density $N_{MSh} \sim 10cm^{-3}$.

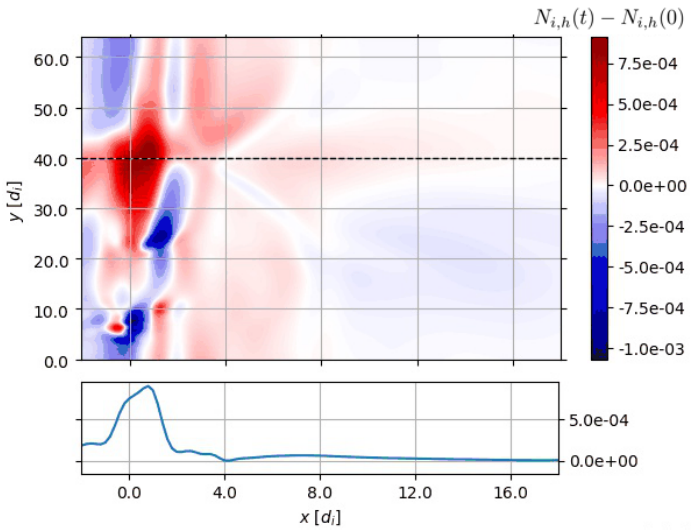

Figure 7. Same as Figure (6) for the hot ion fluctuations, $N_{i,h} - N_{i,h}(t=0)$.

most generally have different locations and show different scale-lengths. The model has also to be able to be take into account these characteristics.

In this paper, we present for the first time a three-fluid equilibrium directly derived from data, using a magnetopause crossing by MMS. The derivation of the model is based on a fit of the experimental data for the most reliable ones, completed by a "realistic" solution of the equilibrium fluid equations for the others. The relative densities of the hot and cold ion populations calculated using the equilibrium equations provide an $a\ posteriori$ check of our 3 fluid model. In particular, it helps understanding the different bulks observed on the ion distribution functions (see panel (d) in Figure (1)).

Furthermore, a preliminary study shows that the model can be implemented in a three-fluid numerical simulation, validating the correctness of the equilibrium solution. The detailed study of the long time evolution of the magnetopause instability will be the subject for future work.

Investigating the magnetopause stability and trying to understand, in particular, when and where reconnection phenomena can be triggered and how the plasmas of both sides can get mixed, is still nowadays a challenging issue to be attacked by numerical simulations. However, known that the stability of a physical system is given by the specific initial equilibrium state, it must be kept in mind that the resulting non linear dynamics, in particular the mixing properties, also strongly depend on the choice of the initial equilibrium. As a consequence it is very important to initialize a simulation with a configuration as much as realistic as possible. In most of the published literature, the simulations have been initialized with relatively simple configurations, Harris sheets, or modified Harris sheets with little relationship with the real magnetopause. The realistic 3fluid equilibrium presented in this paper should therefore allow for a step further. The same method could be applied to other experimental cases in the future.

Data availability. All the data used are available on the MMS data server: https://lasp.colorado.edu/mms/sdc/public/about/browse-wrapper/.

Competing interests. The authors declare that no competing interests are present.

Acknowledgements. This project (FC) has received funding from the European Union's Horizon 2020 research and innovation program under grant agreement No 776262 (AIDA). The French involvement on MMS is supported by CNES and CNRS.

References

Alvarez Laguna, A., Mansour, N., Lani, A., and Poedts, S.: MULTI-FLUID MODELING OF THE EARTH'S MAGNETOSPHERE, in: Comparative Heliophysics Program, Summer 2016 at NASA Ames Research Center, 2016.

Aunai, N., Belmont, G., and Smets, R.: Proton acceleration in antiparallel collisionless magnetic reconnection: Kinetic mechanisms behind the fluid dynamics, Journal of Geophysical Research: Space Physics, 116, https://doi.org/10.1029/2011JA016688, 2011.

Baker, D. N. and Lanzerotti, L. J.: Resource Letter SW1: Space Weather, American Journal of Physics, 84, 166–180, https://doi.org/10.1119/1.4938403, 2016.

Belmont, G., Aunai, N., and Smets, R.: Kinetic equilibrium for an asymmetric tangential layer, Physics of Plasmas, 19, 022 108, https://doi.org/10.1063/1.3685707, 2012.

Bosqued, J. M., Phan, T. D., Dandouras, I., Escoubet, C. P., Rème, H., Balogh, A., Dunlop, M. W., Alcaydé, D., Amata, E., Bavassano-Cattaneo, M. B., Bruno, R., Carlson, C., Dilellis, A. M., Eliasson, L., Formisano, V., Kistler, L. M., Klecker, B., Korth, A., Kucharek, H., Lundin, R., McCarthy, M., McFadden, J. P., Möbius, E., Parks, G. K., and Sauvaud, J. A.: Cluster observations of the high-latitude magnetopause and cusp: initial results from the CIS ion instruments, Annales Geophysicae, 19, 1545–1566, https://doi.org/10.5194/angeo-19-1545-2001, 2001.

Büchner, J., Kuska, J.-P., and Wiechen, H.: Numerical Modelling and Simulation for Multi-Spacecraft Data Analysis: Approaches and Examples, ISSI Scientific Reports Series, 1, 449–478, 1998.

Burch, J. L., Torbert, R. B., Phan, T. D., Chen, L.-J., Moore, T. E., Ergun, R. E., Eastwood, J. P., Gershman, D. J., Cassak, P. A., Argall, M. R., Wang, S., Hesse, M., Pollock, C. J., Giles, B. L., Nakamura, R., Mauk, B. H., Fuselier, S. A., Russell, C. T., Strangeway, R. J., Drake, J. F., Shay, M. A., Khotyaintsev, Y. V., Lindqvist, P.-A., Marklund, G., Wilder, F. D., Young, D. T., Torkar, K., Goldstein, J., Dorelli, J. C., Avanov, L. A., Oka, M., Baker, D. N., Jaynes, A. N., Goodrich, K. A., Cohen, I. J., Turner, D. L., Fennell, J. F., Blake, J. B., Clemmons, J., Goldman, M., Newman, D., Petrinec, S. M., Trattner, K. J., Lavraud, B., Reiff, P. H., Baumjohann, W., Magnes, W., Steller, M., Lewis, W., Saito, Y., Coffey, V., and Chandler, M.: Electron-scale measurements of magnetic reconnection in space, Science, 352, aaf2939, https://doi.org/10.1126/science.aaf2939, 2016b.

Canuto, C.: Spectral methods in fluid dynamics, Springer series in computational physics, Springer-Verlag, https://books.google.it/books?id=2TbvAAAAMAAJ, 1988.

Channell, P. J.: Exact Vlasov–Maxwell equilibria with sheared magnetic fields, The Physics of Fluids, 19, 1541–1545, https://doi.org/10.1063/1.861357, 1976.

Cowley, S. W. H. and Owen, C. J.: A simple illustrative model of open flux tube motion over the dayside magnetopause, Planetary and Space Science, 37, 1461–1475, https://doi.org/10.1016/0032-0633(89)90116-5, 1989.

Dargent, J., Aunai, N., Lavraud, B., Toledo-Redondo, S., Shay, M. A., Cassak, P. A., and Malakit, K.: Kinetic simulation of asymmetric magnetic reconnection with cold ions, Journal of Geophysical Research: Space Physics, 122, 5290–5306, https://doi.org/10.1002/2016JA023831, https://doi.org/10.1002/2016JA023831, 2017.

Dorville, N., B. G., Aunai, N., D. J., and Rezeau, L.: Asymmetric kinetic equilibria: Generalization of the BAS model for rotating magnetic profile and non-zero electric field, Physics of Plasmas, 22, 092 904, https://doi.org/10.1063/1.4930210, 2015.

Dungey, J. W.: Interplanetary Magnetic Field and the Auroral Zones, Phys. Rev. Lett., 6, 47–48, https://doi.org/10.1103/PhysRevLett.6.47, https://link.aps.org/doi/10.1103/PhysRevLett.6.47, 1961.

Fadanelli, S., Faganello, M., Califano, F., Cerri, S. S., Pegoraro, F., and Lavraud, B.: North-South Asymmetric Kelvin-Helmholtz Instability and Induced Reconnection at the Earth's Magnetospheric Flanks, Journal of Geophysical Research: Space Physics, 123, 9340–9356, https://doi.org/10.1029/2018JA025626, 2018.

Faganello, M. and Califano, F.: Magnetized Kelvin–Helmholtz instability: theory and simulations in the Earth's magnetosphere context, Journal of Plasma Physics, 83, 535830 601, https://doi.org/10.1017/S0022377817000770, 2017.

Faganello, M., Califano, F., and Pegoraro, F.: Being on time in magnetic reconnection, New Journal of Physics, 11, 063 008, https://doi.org/10.1088/1367-2630/11/6/063008, 2009.

Frey, H. U., Phan, T. D., Fuselier, S. A., and Mende, S. B.: Continuous magnetic reconnection at Earth's magnetopause, Nature, 426, 533–537, https://doi.org/10.1038/nature02084, 2003.

Furth, H. P., Killeen, J., and Rosenbluth, M. N.: Finite-Resistivity Instabilities of a Sheet Pinch, Physics of Fluids, 6, 459–484, https://doi.org/10.1063/1.1706761, 1963.

Hasegawa, H.: Structure and Dynamics of the Magnetopause and Its Boundary Layers, Monographs on Environment, Earth and Planets, 1, 71–119, https://doi.org/10.5047/meep.2012.00102.0071, 2012.

Labelle, J. and Treumann, R. A.: Plasma waves at the dayside magnetopause, Space Science Reviews, 47, 175–202, https://doi.org/10.1007/BF00223240, 1988.

Lee, L. C. and Roederer, J. G.: Solar wind energy transfer through the magnetopause of an open magnetosphere, Journal of Geophysical Research: Space Physics, 87, 1439–1444, https://doi.org/10.1029/JA087iA03p01439, https://agupubs.onlinelibrary.wiley.com/doi/abs/10.1029/JA087iA03p01439, 1982.

Lele, S. K.: Compact finite difference schemes with spectral-like resolution, Journal of Computational Physics, 103, 16 – 42, https://doi.org/https://doi.org/10.1016/0021-9991(92)90324-R, http://www.sciencedirect.com/science/article/pii/002199919290324R, 1992.

Ma, Y.-J., Nagy, A. F., Toth, G., Cravens, T. E., Russell, C. T., Gombosi, T. I., Wahlund, J.-E., Crary, F. J., Coates, A. J., Bertucci, C. L., and Neubauer, F. M.: 3D global multi-species Hall-MHD simulation of the Cassini T9 flyby, Geophysical Research Letters, 34, L24S10, https://doi.org/10.1029/2007GL031627, 2007.

Manuzzo, R., Belmont, G., Rezeau, L., Califano, F., and Denton, R.: Crossing of Plasma Structures by spacecraft: a path calculator, Journal of Geophysical Research: Space Physics, x, submitted.

Modolo, R., Chanteur, G. M., Dubinin, E., and Matthews, A. P.: Simulated solar wind plasma interaction with the Martian exosphere: influence of the solar EUV flux on the bow shock and the magnetic pile-up boundary, Annales Geophysicae, 24, 3403–3410, https://hal.archives-ouvertes.fr/hal-00330103, 2006.

Nakamura, M. and Scholer, M.: Structure of the magnetopause reconnection layer and of flux transfer events: Ion kinetic effects, Journal of Geophysical Research: Space Physics, 105, 23 179–23 191, https://doi.org/10.1029/2000JA900101, 2000.

Paschmann, G.: Observational Evidence for Transfer of Plasma Across the Magnetopause, Space Science Reviews, 80, 217–234, https://doi.org/10.1023/A:1004926004806, 1997.

Phan, T. D., Escoubet, C. P., Rezeau, L., Treumann, R. A., Vaivads, A., Paschmann, G., Fuselier, S. A., Attié, D., Rogers, B., and Sonnerup, B. U. Ö.: Magnetopause Processes, Space Science Reviews, 118, 367–424, https://doi.org/10.1007/s11214-005-3836-z, 2005.

Retinò, A., B. Bavassano-Cattaneo, M., Marcucci, M., Vaivads, A., André, M., Khotyaintsev, Y., Phan, T., Pallocchia, G., Rème, H., Möbius, E., Klecker, B., W. Carlson, C., McCarthy, M., Korth, A., Lundin, R., and Balogh, A.: Cluster multispacecraft observations

at the high-latitude duskside magnetopause: Implications for continuous and component magnetic reconnection, Annales Geophysicae, 23, https://doi.org/10.5194/angeo-23-461-2005, 2005.

Shumlak, U., Lilly, R., Reddell, N., Sousa, E., and Srinivasan, B.: Advanced physics calculations using a multi-fluid plasma model, Computer Physics Communications, 182, 1767–1770, https://doi.org/10.1016/j.cpc.2010.12.048, https://doi.org/10.1016/j.cpc.2010.12.048, 2011.

Tanaka, K. G., Retinò, A., Asano, Y., Fujimoto, M., Shinohara, I., Vaivads, A., Khotyaintsev, Y., André, M., Bavassano-Cattaneo, M. B., Buchert, S. C., and Owen, C. J.: Effects on magnetic reconnection of a density asymmetry across the current sheet, Annales Geophysicae, 26, 2471–2483, https://doi.org/10.5194/angeo-26-2471-2008, 2008.

23.3 Analyzing the Magnetopause Internal Structure: New Possibilities Offered by MMS Tested in a Case Study

AGU PUBLICATIONS

JGR

Journal of Geophysical Research: Space Physics

RESEARCH ARTICLE
10.1002/2017JA024526

Special Section:
Magnetospheric Multiscale (MMS) mission results throughout the first primary mission phase

Analyzing the Magnetopause Internal Structure: New Possibilities Offered by MMS Tested in a Case Study

L. Rezeau[1], G. Belmont[1], R. Manuzzo[1], N. Aunai[1], and J. Dargent[1,2]

[1]LPP, CNRS, Ecole polytechnique, UPMC Univ Paris 06, Univ. Paris-Sud, Observatoire de Paris, Université Paris-Saclay, Sorbonne Universités, PSL Research University, Paris, France, [2]IRAP, CNRS, Université de Toulouse, Toulouse, France

Key Points:
- The internal structure of the magnetopause is investigated, using new analysis tools allowed by the high-performance MMS instruments
- In a case study, the observed boundary is shown to be nonplanar and nonstationary
- Quasi 1-D thin sub layers are identified separated by regions that are mainly 2-D

Correspondence to:
L. Rezeau,
laurence.rezeau@upmc.fr

Citation:
Rezeau, L., Belmont, G., Manuzzo, R., Aunai, N., & Dargent, J. (2018). Analyzing the magnetopause internal structure: New possibilities offered by MMS tested in a case study. *Journal of Geophysical Research: Space Physics*, *123*. https://doi.org/10.1002/2017JA024526

Received 28 JUN 2017
Accepted 8 DEC 2017
Accepted article online 15 DEC 2017

Abstract We explore the structure of the magnetopause using a crossing observed by the Magnetospheric Multiscale (MMS) spacecraft on 16 October 2015. Several methods (minimum variance analysis, BV method, and constant velocity analysis) are first applied to compute the normal to the magnetopause considered as a whole. The different results obtained are not identical, and we show that the whole boundary is not stationary and not planar, so that basic assumptions of these methods are not well satisfied. We then analyze more finely the internal structure for investigating the departures from planarity. Using the basic mathematical definition of what is a one-dimensional physical problem, we introduce a new single spacecraft method, called LNA (local normal analysis) for determining the varying normal, and we compare the results so obtained with those coming from the multispacecraft minimum directional derivative (MDD) tool developed by Shi et al. (2005). This last method gives the dimensionality of the magnetic variations from multipoint measurements and also allows estimating the direction of the local normal when the variations are locally 1-D. This study shows that the magnetopause does include approximate one-dimensional substructures but also two- and three-dimensional structures. It also shows that the dimensionality of the magnetic variations can differ from the variations of other fields so that, at some places, the magnetic field can have a 1-D structure although all the plasma variations do not verify the properties of a global one-dimensional problem. A generalization of the MDD tool is proposed.

1. Introduction

The magnetopause boundary separates two magnetized plasmas of different origins: the solar wind and the magnetosphere. Its existence is due to the frozen-in property that prevails at large scale and which would fully prevent the two plasmas to reconnect if it was valid always and everywhere. As the magnetopause is accessible to in situ spacecraft measurements, it provides a unique occasion to study the internal structure of such a boundary and understand how the two plasmas interpenetrate each other via the kinetic effects. However, this study is made difficult by the fact that the boundary is always perturbed by nonstationary effects, due to the nonstationary incident solar wind and/or to surface wave instabilities such as tearing and Kelvin-Helmholtz instabilities (Chen et al., 1997; Faganello et al., 2008). It is worth noticing that if purely planar and stationary, the magnetopause layer should obey the classical theory of discontinuities (Belmont et al., 2013), that is, be purely tangential ($B_N = 0$) or, if not, either purely rotational or purely compressional. This is in contradiction with observations since compressional and rotational variations are always observed in a close vicinity of each other in the magnetopause layer, often mixed but with sometimes a clear separation between both (Dorville et al., 2014). Thanks to its unprecedented high quality and high time resolution experiments, the Magnetospheric Multiscale (MMS) spacecraft (Pollock et al., 2016; Russell et al., 2016) nowadays allow significant advances in the study of the internal structure of the magnetopause layer. This paper shows the new methods that can be used for that purpose.

The date 16 October 2015 was a day with multiple magnetopause crossings by MMS. Figure 1 shows that it is due to the fact that the orbit of the spacecraft grazes the magnetopause for about 4 h between 09:00 and 13:00 UTC. The expected position of the magnetopause is calculated with the Shue et al. (1997) model using ACE data (Stone et al., 1998). The figure evidences that many crossings are expected to happen. This is what is observed, and these multiple crossings can be expected to be complex, with possible back and forth motions and partial penetration in the current layer. We choose to study the crossing around 13:06

AGU Journal of Geophysical Research: Space Physics 10.1002/2017JA024526

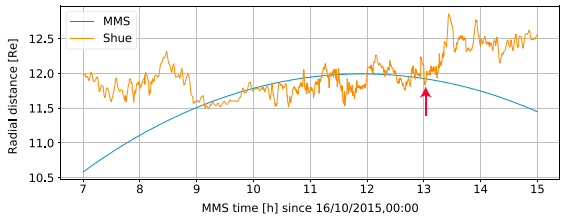

Figure 1. Radial distance from the Earth as a function of time: comparison between MMS orbit (blue line) and Shue magnetopause position computed with ACE data.

(which is shown by a red arrow) because this period has already been studied by Burch et al. (2016), Torbert et al. (2016), and Le Contel et al. (2016), with a main emphasis put on its relationship with the reconnection event identified at 13:07.

Figure 2 displays the magnetic field measured by the MMS magnetometers (Russell et al., 2016) during a 1 min interval around the crossing investigated. In this figure as in all the others unless specified, the times are counted for convenience from $t_0 = 13:05:30$. The magnetic field is smoothed using a Gaussian filter, with a standard deviation of the Gaussian kernel equal to 70 points, which makes an effective smoothing window of about 1.6 s. All the data used in the study are resampled to the magnetic field sampling time and then smoothed in the same way as the magnetic field.

One can see that the crossing is complex. The spacecraft come from a clear magnetospheric field at the beginning of the interval ($B_z \approx 35$ nT); a reversal is seen around $t \approx 15$ s, showing the crossing of the main magnetopause current layer; the magnetic field is not completely stationary afterward, which can be interpreted, as done by Torbert et al., by the fact that the spacecraft do not progress further in the normal direction with respect to the magnetopause, so remaining inside it ("stagnation"), with even a backward motion around $t = 28$ s.

Figure 3 summarizes the evolution of the main physical parameters during the interval under study, where it can be seen that the region where the plasma properties change is not identical to the magnetic field reversal region but is close to the first part of it, and slightly before.

2. The Magnetopause is Nonstationary and Nonplanar

2.1. Comparison of Normals

The most common method to analyze a magnetopause crossing is the minimum variance analysis (MVA), which has been introduced with the first measurements of the magnetic field in space (Sonnerup & Cahill, 1967; Sonnerup & Scheible, 1998). It is based on the assumption that the boundary is perfectly 1-D, that is, that all isosurfaces are parallel planes, and it provides a single boundary normal based on the magnetic field measurements across the "whole crossing." Years of study of experimental results have shown that this assumption is acceptable as long as sufficiently large scales are considered and ultimately amount to finding out the normal of the magnetopause boundary itself and compare it to a model (e.g., Shue et al. (1997)). But they have also shown that the magnetopause itself has an internal structure which can be complex (Burch et al., 2016; Dorville et al., 2014).

MVA relies on the Maxwell equation $\nabla \cdot \mathbf{B} = 0$, and on the constancy of the normal component that follows from it for a strictly 1-D geometry. This property is sufficient to determine the normal direction as long as this component is the only that does not vary, that is, when the $\mathbf{B_T}$ tangential hodogram has a certain curvature: otherwise, two components are constant and $B_N = \text{const}$ is not a sufficient condition to identify the normal direction (this excludes the coplanar case of shocks). If the magnetopause conformed to the simple classical image of a boundary made of a monotonous ramp connecting two homogeneous regions, the strict B_N conservation would be valid on any interval, whatever the number of points. The existence of different sublayers that can move with respect to each other would not invalidate this property, at the condition that these sublayers are all planar and strictly parallel to each other. The existence of nonstationarity should not bring difficulties either, at the condition that the boundary remains strictly planar everywhere and that its normal direction does not vary in time. The main difficulties therefore come from the departures from planarity and from the absence of time stationarity of the normal direction. Such departures are likely to occur often at the magnetopause, even if only due to the small scales waves and turbulence that are always present. To fix this difficulty, MVA is usually used on a statistical basis and applied over a sufficiently long interval between two points around the crossing, one considered as assuredly in the magnetosphere and one as assuredly

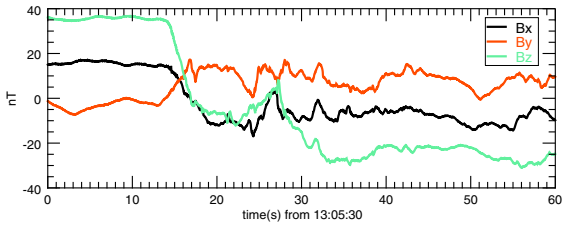

Figure 2. GSE magnetic field components observed on MMS1, 16 October 2015, beginning time at 13:05:30.

AGU Journal of Geophysical Research: Space Physics 10.1002/2017JA024526

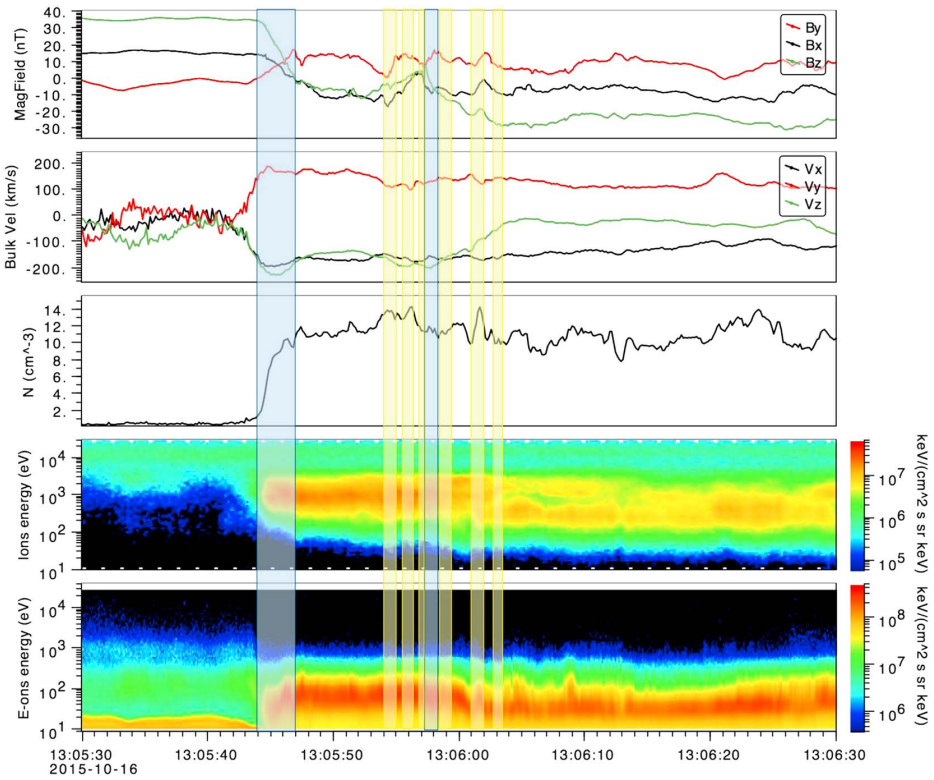

Figure 3. From top to bottom: magnetic field, electron velocity, density, and spectrograms of ions and electrons for the global period studied in the paper. The blue boxes select the regions where the geometry is 1-D and the yellow ones the regions where it is 2-D (see the discussion at the end of the paper).

in the magnetosheath. This actually transforms the condition that B_N is constant into the condition that its variance is less than the variance of the other components. A necessary condition for applying safely this condition is that the ratio between the minimum and intermediate variances is sufficiently small. Another condition that should be checked is that these two variances are really characteristic of the large-scale variation related with the current layer under study and not mainly due to the parasitic small-scale turbulence. When these conditions are not fulfilled, the result actually depends on the position and the size of the "global" interval chosen. The stability of the result is sometimes tested a posteriori, by checking the variations of the observed B_N and by using nested intervals (see, for instance, Zhang et al., 2005). When contradictions occur in one of these two tests, the results are rejected, under the assumption that the real local normal should not depend on time inside the crossing. Beyond this constraint of a strictly constant normal direction, MVA also suffers from another limitation that prevents people from using it on short intervals and therefore analyzing the substructure of the layer: the interval used must be long enough to evidence the curvature of the $\mathbf{B}_T$ tangential hodogram. Any variation obviously tends toward a straight line when the interval duration decreases, so increasing the inaccuracy of the result in the *M*-*N* plane.

These limitations encouraged scientists to develop more elaborate methods (a review can be found in Haaland et al., 2004). They are not all used nowadays, probably because they require more high time resolution data and are more difficult to apply than MVA. Let us cite in particular the different GRA methods (generic residue analysis; Sonnerup et al., 2006). These are generalizations of MVA to other parameters other than just **B**. Although generally more efficient than MVA, these methods rely on conservation laws (fields and plasma) that require also planarity (1-D variations) to be valid. They therefore suffer from most of the limitations of MVA for investigating sublayers. In addition, they require stationarity ($\partial_t = 0$). The BV method (Dorville et al., 2014) mixes magnetic field (*B*) and velocity (*V*) data and is based on different grounds but still in the same

AGU Journal of Geophysical Research: Space Physics 10.1002/2017JA024526

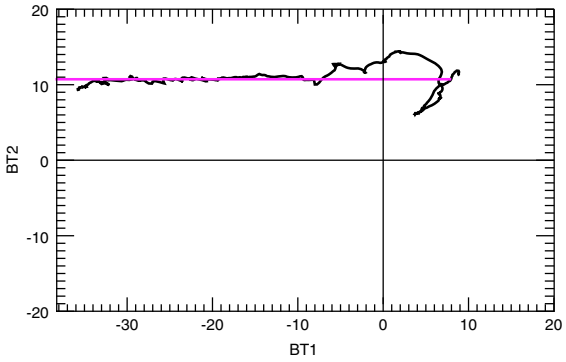

Figure 4. Hodogram of the magnetic field in the plane tangential to the magnetopause obtained by BV, and its fit. The tangential directions BT1 and BT2 chosen for the plot are those of intermediate and largest variances, but any rotation would not change the interpretation. The axis scales are in nanoteslas.

"global layer" spirit. It has been shown to give accurate normal determinations in a statistical study (Dorville et al., 2015). Nevertheless, it is not either perfectly suited for analyzing intervals much shorter than the global width of the current layer (in spite of the excellent time resolution of the MMS data). In any case, all the methods mentioned here assume that the boundary is locally a plane. This assumption may be questionable due to local deformations of the surface, such as surface waves. Confirmation is given by all the numerical simulations of reconnection or Kelvin-Helmholtz instability (Aunai et al., 2016; Chen et al., 1997; Dargent et al., 2017; Miura and Pritchett, 1982) and also by some experimental observations (Blagau et al., 2010).

For the crossing investigated in the present paper, MVA has been first applied on the global interval. It shows that the three eigenvalues are not well separated, the maximum variance being clearly larger than the two others, but these two others being rather similar (ratio 1.9). This means that the normal might not be precisely determined. Nevertheless, we obtain $\mathbf{N}_{MVA} = [0.811, 0.536, -0.234]$ which is close to the normal obtained with the (Shue et al., 1997) model which is $\mathbf{N}_{Shue} = [0.854, 0.519, -0.043]$. The angle between the two normals is 11° indicating that in this case the global magnetopause is probably not far from the standard paraboloid shape assumed by Shue et al. As MVA, as we use it, is a single-spacecraft technique, one can compare the MVA normals derived from the data on each of the four spacecraft. As they are actually very near, they measure very similar magnetic fields and the angle between each normal and the average normal is indeed less than 1°.

Looking at the magnetic data in Figure 2, the global crossing can be guessed to consist of a first current layer between, typically, $t = 10$ s and 20 s, followed by a backward motion later, with only a partial entrance in the magnetopause between $t = 25$ s and 30 s. For confirming or disproving such a guess, one has to investigate the internal structure of the magnetopause layer in more details and look for possible substructures. For this purpose, let us first compute MVA on shorter intervals. Between $t = 10$ s and 20 s, we obtain (on MMS1) $\mathbf{N}_{MVA} = [0.591, -0.591, -0.548]$, which is very different from the previous normal, the angle between both being 73°. Let us note that changing slightly the choice of the beginning and ending times of this MVA interval does not change much this conclusion. As the ratio between minimum and intermediate eigenvalues is again not much larger than 1 (2.6), MVA is quite questionable and one can wonder whether this determination is just erroneous or if such a large difference can actually exist between the local and the global normals. Taking advantage that, beyond **B**, all the other physical parameters are measured at the same time, it is possible to use the particle data (Pollock et al., 2016) to analyze the crossing with the BV technique (Dorville et al., 2014). The hodogram (Figure 4) is almost a straight line, without a clear curvature, but this does not prevent the BV method from working, the fit of this hodogram by a very elongated ellipse remaining quite acceptable. The BV program automatically determines the optimum interval for its fitting procedure, which is between, unsurprisingly, t =14 s and 18 s. The normal obtained is then (on MMS1) $\mathbf{N}_{BV} = [0.838, 0.506, -0.205]$, which is only 9° from the Shue et al. normal. This result is much more likely than the MVA one.

2.2. Thickness of the Magnetopause

A possible byproduct of the BV method is an estimation of the thickness of the current layer of the magnetopause and of its normal velocity, but it is worth noticing that these estimations have to be taken with caution. The BV program provides in its present version an estimated thickness of 30 km on MMS1 and MMS2 and 40 km on MMS3 and MMS4, which is smaller than the thermal ion Larmor radii (which vary from ≈140 km in the magnetosphere to ≈110 km in the magnetosheath). It also provides an estimated normal velocity of 8 km s^{-1} for MMS1 and MMS2 and 10 km s^{-1} for MMS3 and MMS4, which is much smaller than the normal Alfvén velocity (36 to 170 km s^{-1}). These results being noticeably smaller than the values commonly observed, we have used other methods to check them. These methods provide more likely results of about 200 km for the thickness and 50 km s^{-1} for the normal velocity.

The first calculation is the same as done in the BV method, and also similar to those used in Paschmann et al. (1990) and De Keyser et al. (2002), which consists in integrating the normal ion velocity V_{in} over time to obtain the abscissa $x(t)$, but using a different normal which is likely to be more precise (see in further sections how we

AGU Journal of Geophysical Research: Space Physics 10.1002/2017JA024526

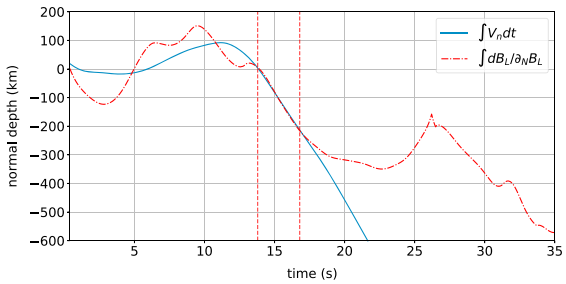

Figure 5. Abscissas $x(t)$ along the magnetopause normal, as determined by two different methods (see text). The origin is arbitrary.

have obtained this normal). The second calculation makes use of the four-spacecraft gradient determination. The abscissa along the normal is obtained by integrating the quantity $\delta x = Y/Y'$, where Y is a scalar variable and where Y' represents the projection of ∇Y on the normal direction (the normal direction being determined in the same way as above). The spatial derivatives in the different directions are estimated by linear interpolations from the multipoint measurements (here four spacecraft). This can be done by methods similar to the well-known "curlometer," which is very often used to calculate the electric current density (Chanteur, 1998). We have taken here $Y = B_L$, which is the component of **B** that varies most during the crossing. Figure 5 shows the comparison between the two results. Both results look quite compatible during the crossing of the main current layer and lead to the same value of ≈200 km for its thickness. This similarity validates the hypothesis which is done in the BV method that the flow through the boundary is negligible. Nevertheless, the two results clearly depart at later times. This is due to a very strong dependence of the result, with the BV method, on the quality of the normal determination (Dorville et al., 2014). A small uncertainty in the normal direction determination can draw a large variation of the V_n component because the tangential component of the velocity is much larger than the normal one (see Figure 3). With a magnitude of the velocity of about ≈300 km s^{-1}, an uncertainty of 10° on the normal direction corresponds to an uncertainty of ≈50 km s^{-1} for the normal velocity, and an uncertainty of about ≈200 km for the thickness. It is so quite understandable that with a normal valid in the 14–18 s interval, the inaccuracy increases very fast at later times where this normal is no more valid. The method based on gradients does not present this difficulty: it is much less sensitive to the accuracy of the normal determination. Nevertheless, we had also to add a caution to make it work correctly: because of various small accuracy issues, the denominator Y' may cancel at a time slightly different from the numerator, which results in short divergences in the result and jumps in the $x(t)$ curve. This has to be corrected by adding adequate small shifts in the denominator. In addition, Figure 5 clearly gives the confirmation that the spacecraft is going backward inside the magnetopause around $t = 27$ s, as was guessed before. Due to its importance, this technique is under review for further improvements and will be applied to other cases in next studies.

In Figure 6, we have plotted the projection of the ion velocity along the normal obtained by BV, together with the density profile. This evidences an internal structure inside the magnetopause. Two main parts can be observed in the interval $t = 14–18$ s, where the main plasma gradients are located and which is emphasized by a thick line: in interval (a) a sharp density gradient, with an almost constant V_n, followed in interval (b) by a smoother gradient with a normal velocity close to zero. This is in agreement with the sketch drawn in Figure 3 of (Burch et al., 2016) which is a possible interpretation of this crossing (although assuming a stationary boundary): a rather straight crossing, followed by a stagnation of the spacecraft inside the boundary. This is confirmed by the observation of energetic ions continuously after 13:05:42 (Le Contel et al., 2016). Out of the central interval $t = 14–18$ s, the curve $V_n(t)$ is plotted with a dashed line, to warn the reader that the projection of the velocity is obtained using the BV normal based on this interval and that the validity of this projection, even if correct in the magnetic ramp itself, remains questionable outside of it.

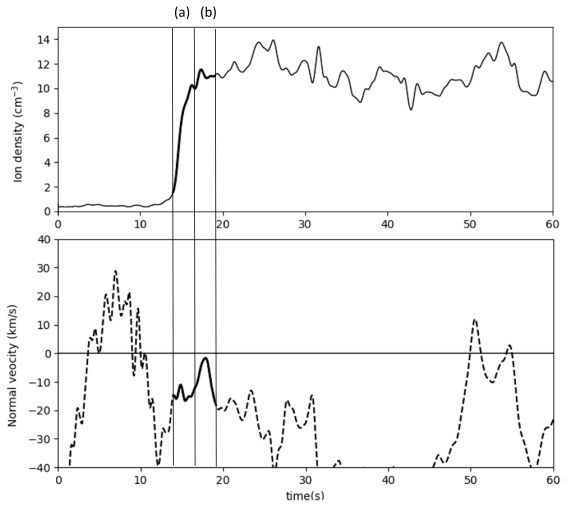

Figure 6. Comparison of the normal component of the velocity and the density variation (MMS1). The thick lines correspond to the $t = 14–18$ s interval. The vertical thin lines indicate the limits of the two periods described in the text.

2.3. Nonstationarity

Using timing methods is another classical way for getting information on the boundary properties from multispacecraft measurements. We tested CVA (constant velocity analysis), which assumes that the boundary is a planar structure encountered by the four spacecraft with a constant velocity (Sonnerup, Teh, & Hasegawa, 2008; Sonnerup, Haaland, & Paschmann, 2008). As in any other timing method, the analysis is based on the knowledge of the positions of the spacecraft and the measurements of the delays between the signatures of the crossing seen by the four spacecraft.

AGU Journal of Geophysical Research: Space Physics 10.1002/2017JA024526

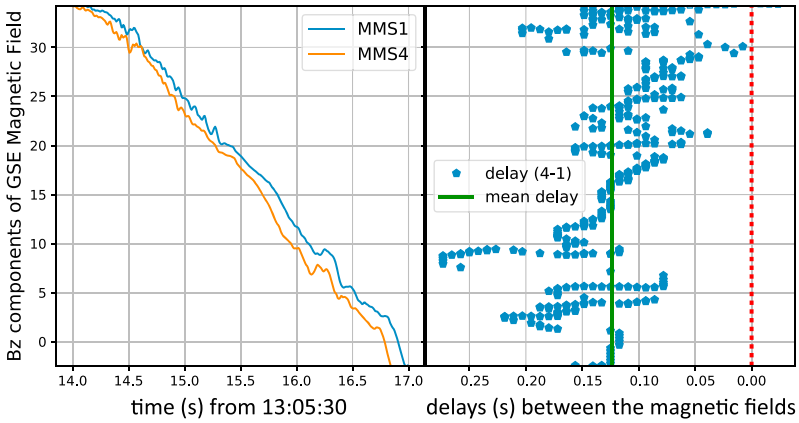

Figure 7. Comparison of the main component (B_z) of the (left) magnetic field and (right) computation of the delay between points having the same B_z value. The green vertical line is the average delay.

As shown in Figure 7, these delays are very short with respect to the parasitic variations due to the intrinsic nonstationarities, in particular waves and turbulence. If the boundary was stationary, we should find a constant delay between the fields observed by MMS1 and MMS4. On the contrary, it is obvious that the dispersion of the points is not negligible at all with respect to the delay itself. It is worth noticing that we have plotted here the B_z component, which is the component that varies most, and for the MMS1-MMS4 pair, for which the delay is maximum. The situation is worst when using the other components and the other spacecraft pairs. This results in a very inaccurate determination of the delays and therefore in a bad determination of the normal direction. The first conclusion is therefore that in this case, the CVA method cannot be used without much caution.

Looking at Figure 7, we can also derive some hints on the nonstationarity of the boundary at different scales. In the beginning of the crossing there are oscillations, evoking the presence of waves, superimposed to the magnetopause variation. This induces variations of the delay on the top of the figure. But there is also a large-scale variation of the delay: on the top of the figure (beginning of the crossing) its mean value is about −0.07 s and afterward it goes to −0.15 s: the delay is not constant through the crossing. Similar conclusions are obtained with the two other spacecraft. Using an averaging of the delays, one could interpret the large-scale variation as a constant acceleration of the boundary, which would help improving this result (Dunlop et al., 2002). Results of other timing methods, such as CTA (constant thickness analysis) are not presented here, but the same difficulty (small delays with respect to the intrinsic fluctuations) would lead, on this example, to the same difficulties.

The conclusion of these observations is that the magnetic field is not stationary during the crossing by the four MMS spacecraft, and therefore, the boundary is not the planar stationary discontinuity which is the most simple model for the magnetopause. It is necessary to investigate in more details the geometry and behavior of the magnetopause.

3. Internal Structure: Departures From Planarity

When analyzing a boundary crossing, one most often assumes that this boundary is 1-D, that is, that all parameters vary only in one direction, which is its normal. When this hypothesis of planarity is fully verified, the normal component B_n of the magnetic field is strictly constant and this property is used in MVA method to determine a single global normal direction (if no other **B** component is constant in the interval). Nevertheless, when the boundary is shaken by some nonstationary effect (either due to varying incident conditions or due to surface instability such as tearing mode or Kelvin Helmholtz), it generally does not remain fully 1-D. Such departures to planarity can easily be observed in numerical simulations of reconnection (see, for instance, Dargent et al., 2017, which will be used afterward in the paper) or, less easily, it can be guessed from data (see the magnetopause reconstructions in De Keyser, 2008; Hasegawa et al., 2005). These departures result

AGU Journal of Geophysical Research: Space Physics 10.1002/2017JA024526

in the fact that MVA is not suitable to this case, and the meaning a global normal direction becomes unclear. One way for dealing with these cases is to try to determine, when possible, a "local normal," possibly varying along the crossing, instead of a single global one.

3.1. Local Normal Analysis

We introduce here a new method, which we call LNA (local normal analysis), based on the independent measurements of **B** (from field data) and **j** (from particle data), and which allows determining a normal that can vary along the crossing. Mathematically speaking, a local normal direction can be defined wherever all plasma parameters depend on space only through a single scalar function $s(x, y, z)$ of the three coordinates. This ensures that the gradients of all parameters are parallel to each other at any point, this common "normal" direction possibly depending on the point considered. The direction **N** is given by

$$\mathbf{N} = \frac{\nabla s}{|\nabla s|} \tag{1}$$

In a cylindrical geometry for instance, all quantities depend on space only through the radius r, so that all gradients are everywhere parallel to the radial direction. Of course, this direction is variable from one point to another in the azimuthal direction.

For any vectorial field **U** verifying this property, one can write the curl as

$$\nabla \times \mathbf{U} = \nabla s \times d_s \mathbf{U} = \mid \nabla s \mid \mathbf{N} \times d_s \mathbf{U} \tag{2}$$

where $d_s\mathbf{U}$ stands for the derivative of **U** with respect to s. Therefore, when it is applied to the magnetic field it shows that the current density is perpendicular to the normal (neglecting the displacement current). When applied to the electric field, it shows that $\partial_t \mathbf{B}$ is perpendicular to the normal, using Maxwell-Faraday equation. A simple cross product between these two vectors is then a priori sufficient to provide the normal direction

$$\mathbf{N} = \frac{\mathbf{j} \times \partial_t \mathbf{B}}{|\mathbf{j} \times \partial_t \mathbf{B}|} \tag{3}$$

When both parameters **j** and **B** are independently determined with a sufficient accuracy, this expression can provide a simple and efficient way for determining the local normal **N** at each time and for a single spacecraft. It is worth noticing that this method does not rely on $\nabla \cdot \mathbf{B} = 0$ and thus on the fact that one component (and only one) is constant: it is therefore not limited to sufficiently rotational cases. For the first time in space history, MMS provides independent — and generally reliable — measurements for **j** and **B** (Torbert et al., 2016), since we can compute a high-resolution current density from the particle data (Pollock et al., 2016). On previous space observations we used to work only with current density obtained from the magnetic field, with the well-known curlometer technique, because the particle instruments had neither the necessary accuracy nor the necessary time resolution to do it. On MMS it has been shown that both calculations of the current show a global fairly good agreement (see Le Contel et al., 2016 who computed the currents for the same time period).

It is worth noticing that this new method has to be scale dependent: in the present program, this dependence is crudely controlled by the way the variables are smoothed before use. Since the method relies on time derivatives, this smoothing has an important role in the result. Here the components of the magnetic field are smoothed with a local cubic fit, which is convenient for getting the time derivatives analytically (The smoothing is performed on the same time scale as the previous Gaussian filtering). Going to large-scale smoothing should allow retrieving the classical notion of global normal. On the contrary, going to very short scale smoothing would provide the wave vectors of the different waves encountered (which can be considered as "parasitic" for the present kind of study). This step could be improved in the future (by using for instance a Fourier filtering instead of a smoothing).

Figure 8 shows what the results look like when running the "local normal analysis" (LNA) method on the case presented in Figure 2 without further precaution. The data have been smoothed over 1.6 s (the global interval being of 1 min). This time scale is a good compromise for this case: it is significantly shorter than the global crossing time (so giving access to the internal structure), and long enough to get rid of most high frequency turbulence. One can see that this figure appears almost unintelligible in these conditions: apart from a short period about $t = 15$ s where the normal appears relatively stable (and where its direction will be confirmed by another method hereafter), it appears highly fluctuating and apparently random. The reason can easily be understood: the method provides the local normal under the hypothesis that this normal exists, that is,

AGU Journal of Geophysical Research: Space Physics 10.1002/2017JA024526

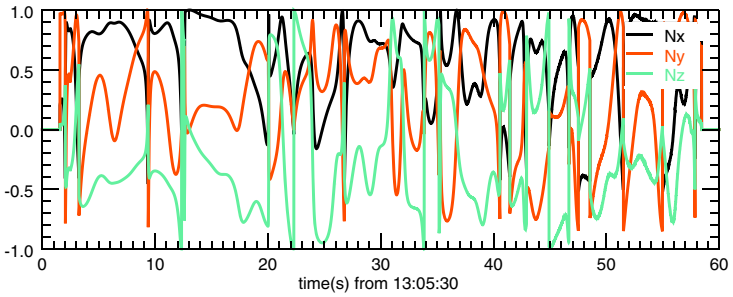

Figure 8. The three components of the vector $\mathbf{N}_{LNA}$ as determined by LNA without 1-D selection in GSE frame, with no test of the significance of the result.

that the variations are locally 1-D. As, at this stage, there is no test of this hypothesis, one gets a result everywhere, even where it is not verified and where the result is thus meaningless. An additional test of locally 1-D variations is therefore necessary to make the LNA method complete. It will be the subject of the next sections.

3.2. Test of the Local Planarity

The best test for determining the dimensionality of observed variations demands multipoint measurements. It has been proposed by Shi et al. (2005) for Cluster data. This method, called MDD (minimum directional derivative), analysis makes use of magnetic field data, although it is not based on specific properties of this field. It actually has been little used with Cluster, most of the authors preferring to stay in the purely 1-D hypothesis and the simple notion of a global normal supposed to be determined by MVA. But it is nowadays attracting increasing interest for analyzing the MMS data (see, for instance, Chen et al., 2017) because of the short separation between spacecraft that allows a better determination of the local gradients. In a recent paper, Denton et al. (2016) have even applied this MDD method on a magnetopause crossing in the same global interval shown in Figure 1 as the crossing analyzed here, but a bit later.

The MDD method consists in diagonalizing the matrix $\mathbf{L} = \mathbf{G} \cdot \mathbf{G}^T$, where $\mathbf{G} = \nabla\mathbf{B}$ and the superscript T indicates matrix transposition and where the spatial derivatives are computed as explained before. The largest eigenvalue λ_1 corresponds to the largest derivative for the ensemble of the **B** components. When this eigenvalue is much larger than the two other eigenvalues, it means that all **B** components vary in one single direction, which is given by the corresponding eigenvector $\boldsymbol{\alpha}_1$, that is, that it is 1-D, with the normal direction $\mathbf{N} = \boldsymbol{\alpha}_1$. When the two largest values λ_1 and λ_2 have the same order of magnitude, while the third one λ_3 is much smaller, it means that the problem is 2-D, the variations occurring in the plane $(\boldsymbol{\alpha}_1, \boldsymbol{\alpha}_2)$, $\boldsymbol{\alpha}_3$ so being the direction of invariance. When the three eigenvalues have the same order of magnitude, it means that the **B** variations are fully 3-D. A modified MDD method has been proposed by Denton et al. (2010) (see also a test in simulation in Denton et al., 2012) to avoid the effects of possible offsets and calibration errors in the data. These errors might have a noticeable impact when the method is used to compute the velocity of a structure, (Denton et al., 2010) but, as it is not what we do here, we use only the original version of MDD in the present paper. Nevertheless, this point of view may have to be reconsidered for the generalized MDD method that we propose hereafter because such errors have certainly a much larger effect when using the electric field data than with the only magnetic field ones.

In order to visualize more easily the effective dimensionality of the variations, we have introduced three parameters, which can be used as proxies:

$$D_1 = \frac{\lambda_1 - \lambda_2}{\lambda_1} \tag{4}$$

$$D_2 = \frac{\lambda_2 - \lambda_3}{\lambda_1} \tag{5}$$

$$D_3 = \frac{\lambda_3}{\lambda_1} \tag{6}$$

These three parameters vary between 0 and 1 and their sum is equal to 1. For $D_1 = 1$ and $D_2 = D_3 = 0$, variation happens only in one direction: the geometry can be told "purely 1-D variation." For $D_2 = 1$ and $D_1 = D_3 = 0$,

AGU Journal of Geophysical Research: Space Physics 10.1002/2017JA024526

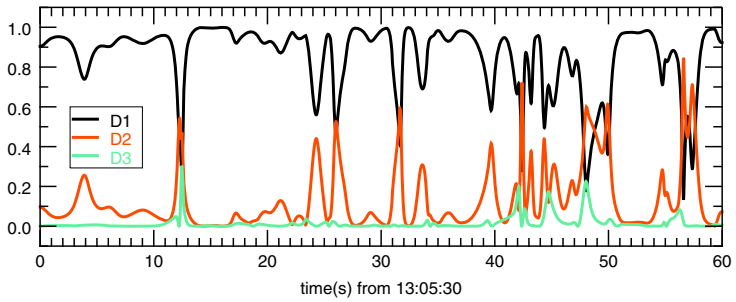

Figure 9. The three dimensions resulting of the MDD analysis as functions of time for the same interval as Figure 8.

the amplitudes of the variations are equal in two directions: it is what we call the case "purely 2-D." For $D_3 = 1$ and $D_1 = D_2 = 0$, the amplitudes of the variations are equal in the three directions: it is what we call it "purely 3-D." Of course, all intermediate situations are possible. Let us consider, for instance, a flux rope with $\lambda_1 = 5$, $\lambda_2 = 1$, and $\lambda_1 = 0.1$, which gives the dimensions $D_1 = 0.8$, $D_2 = 0.18$, and $D_3 = 0.02$. The structure has a slightly 2-D character since D_2 is not negligible, but $D_1 > D_2$ indicates that the tube is strongly flattened in one direction: this makes the transition between 2-D (circular tube) and 1-D (tube infinitely flattened). Such structures have been observed and studied by Shi et al. (2009) and Shi et al. (2013) on Cluster and Yao et al. (2017) on MMS.

When applying the MDD Analysis to the interval under study, the three eigenvalues obtained are quite similar to those of the Figure 1 of Denton et al. (2016). These results are plotted in Figure 9 using the three D_i parameters. It must be kept in mind that the D_i coefficients deriving from MDD give a local measurement of the dimensionality at the scale which has been selected by the smoothing. Our data have been smoothed on 1.6 s; therefore, the wave structures superimposed on the magnetopause crossing are mostly removed. It can be observed that the 1-D variations are generally dominant but that 2-D and 3-D variations are also present in the interval. It is worth noticing that in the regions of 2-D variations, the direction of invariance $\boldsymbol{\alpha}_3$ is determined by the MDD method, which may be an important information for numerical modeling purposes.

In the regions where $D_1 \approx 1$, the normal can be determined by $\mathbf{N}_{\mathrm{MDD}} = \boldsymbol{\alpha}_1$. In Figure 10, the angular distance of this MDD normal with the reference $\mathbf{N}_{\mathrm{Shue}}$ normal is plotted, for the regions where $D_1 > 0.9$ (thin line) and for $D_1 > 0.98$ (thick line). An additional caution has been taken in this figure: we have discarded the regions where there are no significant magnetic field variations ($\left|\partial_t(\mathbf{B})\right|^2$ less than one tenth of its maximum value) because we are not interested in the direction of the gradients for these small variations: they are more likely related to wave and turbulence rather than to the large-scale current layers. In the remaining regions, the results of our LNA have been overplotted for comparison (in blue). One can observe that, as expected, the results obtained by the two methods are generally close to each other when $D_1 \approx 1$ and that they diverge from each other for smaller values of D_1. For the sake of clarity, we have isolated the two intervals, limited by dashed lines in the figure, where $D_1 > 0.98$ and which are long enough: interval 1 from 13.8 to 16.8 and interval 2 from 27.4 to 28.4. If we compute the averaged normals on these intervals, we find that the two normals make a 4° angle in interval 1 and 7° angle in interval 2. Considering, for instance, the normal determined with MDD, it is $\mathbf{N}_1 = [0.925, 0.124, -0.355]$ for interval 1 and $\mathbf{N}_2 = [0.872, 0.473, -0.121]$ for interval 2. Therefore, during the small incursion into the magnetopause which is observed around $t = 28$ s, the normal is different from the normal observed during the large crossing. The two normals are separated by 25°, and the interval 2 normal is closer to the nominal Shue model (which assumes the magnetopause is a paraboloid) than the interval 1 normal.

Nevertheless, one can also observe that at some points (see $t \approx 22$ or $t \approx 29$), the results can be significantly different (with fast variations for LNA), while D_1 is not much smaller than unity. A possible reason for these differences may be the use of different current densities: LNA uses the particle current density, whereas MDD is based on the magnetic field. These departures may also indicate that sometimes, the layer is 1-D in the sense of MDD, but not in the sense of LNA. The physical reasons for these discrepancies will be investigated in the next subsection, where the two analysis methods have been tested in a numerical simulation.

AGU Journal of Geophysical Research: Space Physics 10.1002/2017JA024526

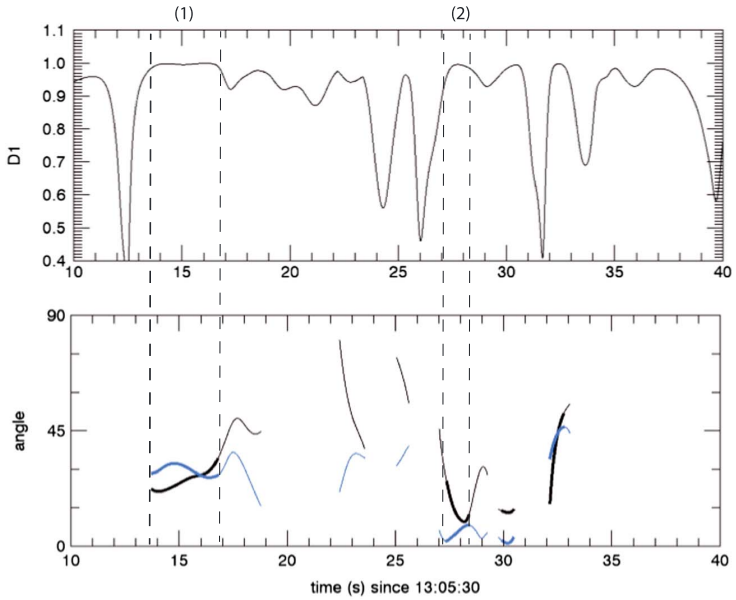

Figure 10. On top, the D_1 parameter. Below the angle between the normal determined by MDD (in blue) and the reference normal given by the Shue model. The thin lines correspond to $D_1 > 0.9$. The thick lines correspond to $D_1 > 0.98$. In black, the results of the LNA method have been overplotted for comparison, with the same convention. The intervals selected by dotted lines refer to the text.

3.3. Tests of the MDD and LNA Methods on a Numerical Simulation and Generalization of MDD

For testing the MDD and LNA methods, we use a 2-D numerical particle-in-cell simulation published in Dargent et al. (2017). Note that this simulation of reconnection has no relation with the above experimental case. In this simulation, we have mimicked various spacecraft crossings of the magnetopause layer and treated the data by both the MDD and LNA methods. The crossing used in this paper is shown in Figure 11 where a map of the magnetic field in the simulation is plotted. The only difference with the real spacecraft data is that the spatial derivatives have been estimated directly from the simulation grid instead of being estimated from the 4-point measurements of the MMS irregular tetrahedron.

Figure 12 shows the results for the crossing shown in Figure 11, in the same format as Figure 10, with the same criterion on $|\partial_t(\mathbf{B})|^2$. It can be seen that MDD determines a normal which is, as expected, close to the y direction, with a clear regular variation which finely fits the shape of the exhaust region in the simulation. It is worth noticing that the **B** variations are shown to be almost 1-D everywhere in the layer, even in the region relatively close to the X point where the field lines are clearly not straight lines. Our LNA result is quite consistent, in general, with this one. Nevertheless, one can once again observe that the two results are not perfectly identical: at some points (see $t = 41-43$) where D_1 is very close to unity, the difference between the two results is significant. The LNA result can even include a nonnegligible z component (not shown),

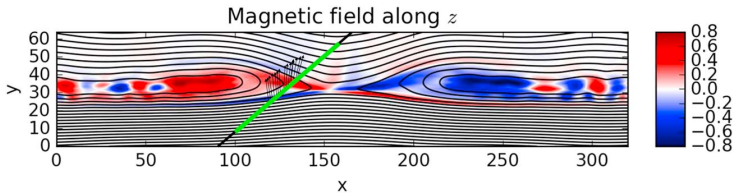

Figure 11. B_z component in the numerical simulation superimposed to the magnetic field lines in the simulation plane. The (x, y) components are those of the 2-D simulation box. The straight line indicates the simulated crossing trajectory, with the period of time which is studied below overlined in green, beginning at the bottom of the simulation box and going in the direction of the increasing y. The small arrows are the MDD local normals determined along the trajectory.

AGU Journal of Geophysical Research: Space Physics 10.1002/2017JA024526

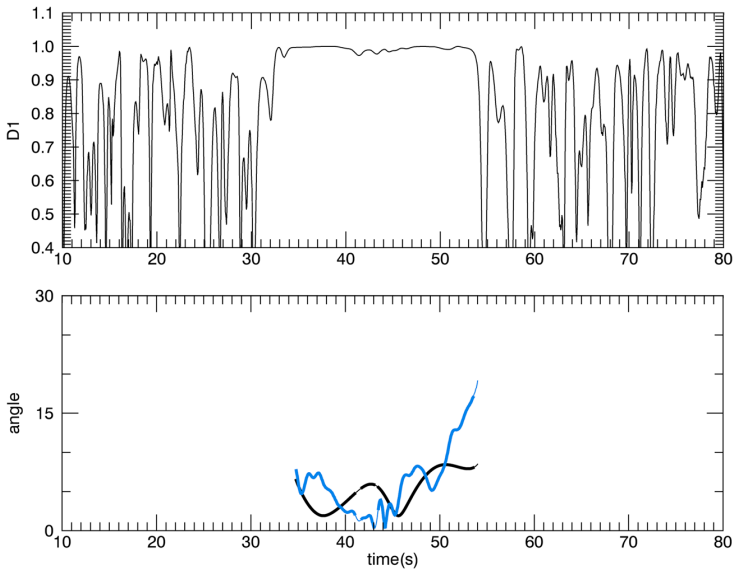

Figure 12. Same as Figure 10 for the crossing in the simulation box shown in Figure 11. The time is counted from the entrance of the spacecraft in the simulation box which is crossed at constant velocity. The angle is measured with respect to the reference direction, which is here the *y* direction of the simulation box. The thin lines correspond to $D_1 > 0.9$. The thick lines correspond to $D_1 > 0.98$.

which is inconsistent with the 2-D simulation. Although the discrepancies remain generally small, they are to be understood because, for a fully 1-D variation, it is clear that **j** and $\partial_t(\mathbf{B})$ should be strictly tangential and the LNA method should work perfectly. The MDD local normals are plotted also in Figure 11, where it is clear that the local normal varies along the crossing.

These discrepancies point out a weak point in the basic MDD method, which is based on the magnetic field only: when $D_1 \approx 1$, it indeed guarantees that the **B** variations are 1-D, so that **j** is tangential, but it does not guarantee that the other plasma variations are also 1-D. In particular, if **E** variations are not 1-D, there is no reason why $\partial_t\mathbf{B}$ should be strictly tangential, which is necessary for LNA to work. In low beta regions, one can guess that the magnetic field controls all the other plasma parameters, so that everything is likely to be 1-D when the magnetic field is 1-D. It is probably the reason why the discrepancies remain quite limited. But in the regions where pressure effects are important (in the central part of the exhaust, for instance, in reconnection geometries), it is not certain that the 1-D variations of **B** actually ensure the planarity for all the plasma parameters. The fluid equations of momentum, for ions and electrons, clearly show in particular that the variations of the parallel components of the fluid velocities $\mathbf{u}_i$ and $\mathbf{u}_e$ are determined by the pressure forces. When these pressure effects are not negligible, the parallel velocities are therefore not constrained by the geometry of the magnetic field variations.

Fortunately, the MDD can easily be generalized. Instead of considering the 3*3 matrix $\mathbf{G} = \nabla\mathbf{B}$, one can introduce variations of all the needed parameters $\mathbf{G}' = \nabla\mathbf{S}$, where **S** is a vector of dimension *N*, including not only the three components of **B** but also any of the other available parameters: the components of the electric field, those of the ion and electron velocities, those of the pressure tensors, and the scalars as the density, etc. In these conditions, $\mathbf{G}'$ is a 3 by *N* tensor, but **L** remains $3 * 3$ and the rest of the method can remain unchanged. A normalization has to be introduced in the computation so that the weight of the different physical quantities is equivalent: the Frobenius norm of $\nabla\mathbf{B}$ is computed as a function of time, and the magnetic field is normalized by the maximum of the norm over all the interval. And the same is done for the electric field.

In the simulation data, such a generalization has been done by just introducing the electric field vector in addition to the magnetic one. The result, which can be compared with the result of Figure 12, is presented in Figure 13. One can see that the generalized MDD method allows evidencing a 2-D character of the plasma

AGU Journal of Geophysical Research: Space Physics 10.1002/2017JA024526

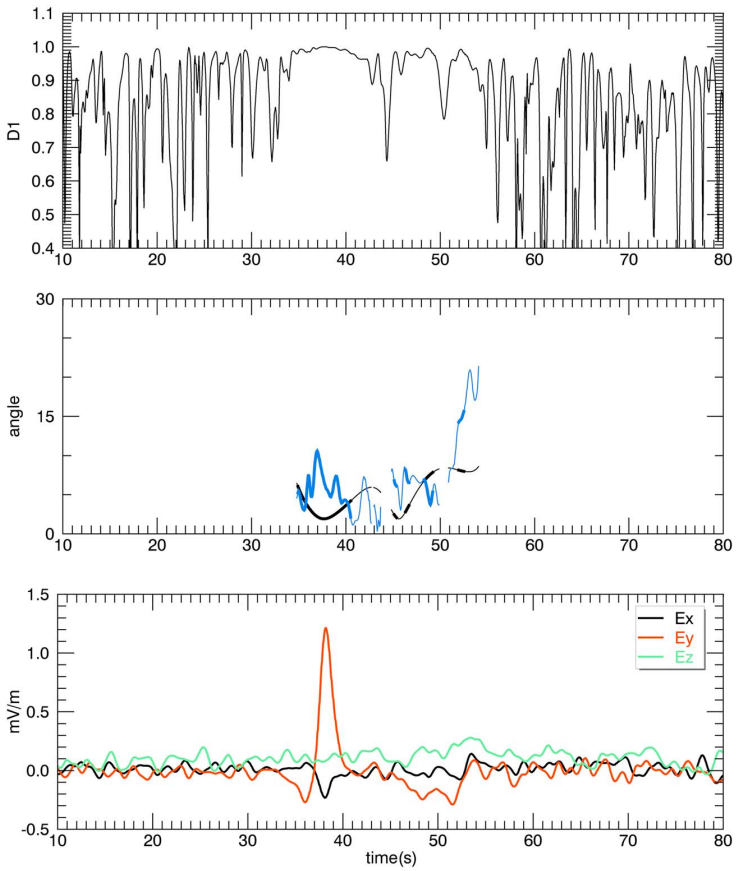

Figure 13. Same as Figure 12 for the crossing in the simulation box shown in Figure 11 when MDD is replaced by MDD generalized to *E* field. The three components of the electric field are plotted in the bottom panel for reference.

in a small region in the current layer, close to the *X* point, that was not evidenced by the only **B** variations. D_1 has more contrasted variations than with the nongeneralized method, so that the same threshold is now more demanding. This leads to reject some normal determinations in the regions where the discrepancy between the LNA and MDD normals was the most important (with a noticeable *z* component for the LNA normal in particular) and where D_1 has now smaller values.

Concerning the magnetopause crossing presented in this paper, preliminary tests have been done of the generalization of MDD. They are not presented here because they have not proved yet to be efficient. When applying the same generalization as in the simulation (addition of the **E** data), the result is not conclusive. The reason seems to be purely experimental: as the calibration of electric antennas is a difficult issue, the precision on the different components of **E** (Ergun et al., 2016) is not sufficient to calculate safely the tensor $\nabla\mathbf{E}$ from the four spacecraft measurements: even the basic Maxwell-Faraday law cannot be verified from the data because the differences between spacecraft are dominated by the differences between offsets rather than by the physical differences. The problem is still complicated by the presence, on the magnetospheric side, of very strong electrostatic bursts of short period, which can hardly be eliminated by the smoothing process and which make difficult obtaining the small transverse field induced by the current layers we are interested in. The attempts to use the MDD method modified by Denton et al. (2010) have not allowed hitherto to overcome this difficulty.

Generalizing with the ion velocity $\mathbf{V}_i$ does not pose similar problems. This has been done, but this test did not lead to conclusive results either: introducing the $\mathbf{V}_i$ variations does not change significantly the result

AGU Journal of Geophysical Research: Space Physics 10.1002/2017JA024526

Table 1
Comparison of the Normals Obtained by MDD and LNA on the Periods Given on the Left (the Duration is Indicated in Parentheses)

Date	$\theta_{LNA/MVAB}$	$\theta_{MDD/MVAB}$	$\theta_{LNA/MDD}$
2015-10-16 10:20:00 (+120)	20 ± 3	17 ± 8	9 ± 6
2015-10-16 10:29:30 (+120)	56 ± 0.5	44 ± 3	12 ± 4
2015-10-16 10:36:30 (+120)	33 ± 0.8	21 ± 0.9	12 ± 0.4
2015-10-16 10:55:00 (+60)	12 ± 1	11 ± 4	3 ± 1
2015-10-16 13:05:30 (+60)	24 ± 2	20 ± 3	7 ± 3
2017-01-27 12:05:23 (+70)	35 ± 19	39 ± 14	9 ± 6

Note. The table provides the angles (in degrees) of the two types of normals with respect to MVAB and the angle between them. The statistics are done over all the local normals that satisfy $D_1 > 0.99$ and $\partial_t(B)^2 > 0.5$ of its maximum value. The first number corresponds to the mean value, and the second one (after $\pm$) corresponds to the standard deviation.

obtained with **B** alone. Improving the generalized MDD method to make it efficient with the experimental observations is still a work in progress.

4. Conclusion and Perspectives

For investigating the magnetopause internal structure, one cannot be satisfied with the simplest hypothesis of a perfectly stationary and monodimensional layer. We give here evidence of departures from these two simple hypotheses on a magnetopause crossing by MMS. The departure from planarity is particularly investigated, introducing a new single spacecraft method, called LNA, used together with an existing multispacecraft method called MDD (Shi et al., 2006). As LNA can give a reliable result only when the variations are locally 1-D, it can indeed be usefully combined with MDD, which allows selecting the intervals where this local 1-D hypothesis is verified. We have shown that the basic MDD method, which is based on the **B** variations only, is not always sufficient for that: even when it indicates variations close to perfectly 1-D, the normal provided by LNA can show small but significant differences with the corresponding normal coming from MDD itself. We therefore propose a generalization of MDD using more data. The idea has been tested by adding the **E** variations to the **B** ones, with data coming from a numerical simulation: the test has shown that this addition is sufficient for solving, at least partly, the problem. It remains to be investigated more thoroughly with spacecraft data. It is worth emphasizing once again that this paper presents the different methods accessible by MMS for investigating the internal structure of the magnetopause only from a case study: benchmarking these methods and comparing their performances on a statistical basis remain to be done in future studies.

Pending these studies, Table 1 shows that the case presented here is not exceptional and seems rather typical. We analyze six cases in the same way as above, six of them being in the same day as the example of this paper. And we show that the two determinations, LNA and MDD, when restricted to strong criteria for D_1 and for the amplitude of the B variation, are globally consistent, even though they both vary with respect to the global MVAB normal (determined in a short interval including the main magnetic gradient). They both show to be often clearly different from this global MVAB determination. The choice of severe criteria has been done here in order to limit as much as possible the effects of nonplanarity and the role of the superposed turbulence and therefore make the different cases more comparable. However, the results are not perfect in the sense that the distance between the LNA and MDD determinations, which could be expected to be negligible, are generally not smaller than the local variations of each determination, as estimated by the standard deviation of their direction with respect the global MVAB result. This imperfection is likely to be due to the same reason as explained above: using MDD only on the magnetic field does not guarantee the real monodimensionality of the physics. Generalizing the method to the electric field should solve this problem if the electric field measurement was accurate enough to allow such a generalization.

The MDD method, contrary to LNA, does not make use of Maxwell equations. In return, it loses the single-spacecraft character of LNA and so part of its locality. There is a priori no method that would be strictly single spacecraft and which would allow to test the local 1-D hypothesis with a comparable reliability. Nevertheless, some simplifying hypotheses could be used, in the future, to discard the non-1-D regions with some confidence. If one assumes, for instance, that the observed **B** variations can be approximated locally as stationary in some frame, we must have, in the observation frame,

$$\partial_t(\mathbf{B}) = -\mathbf{V} \cdot \nabla \mathbf{B} \tag{7}$$

where **V** is the local propagation velocity of the structure. The same property has already been assumed in Shi et al. (2006), where the propagation velocity of the structures could so be determined. It can be noticed that the red curve plotted in Figure 5 is an integration of the velocity obtained by this method. The change of slope in the curve around $t = 27$ indicates a change of the velocity of the boundary and therefore gives a confirmation of the relative back and forth motion of the boundary that was guessed at the beginning of the paper. It seems to also confirm the hypothesis that the flow across the structure is negligible. If true, this may justify equation (7), the propagation velocity simply being the normal flow velocity.

AGU Journal of Geophysical Research: Space Physics 10.1002/2017JA024526

As soon as the property of equation (7) is valid, it can easily be shown that the two vectors $\partial_t(\mathbf{B})$ and $\mathbf{j}$ are perpendicular to each other when the local variation is 1-D, since $\mathbf{j} = \mathbf{n}\times\partial_N(\mathbf{B})$ and $\partial_t(\mathbf{B}) = -V_N\partial_N(\mathbf{B})$. Checking where the two vectors are perpendicular may provide a test of planarity. This is left for further studies.

As discussed before, the MDD method gives the normal to a one-dimensional boundary, but it can also give information when the problem is 2-D. In this case, the eigenvector associated with the largest eigenvalue $\boldsymbol{\alpha}_1$ does not give much information, but the eigenvector associated with the smallest eigenvalue, $\boldsymbol{\alpha}_3$, indicates the direction in which the problem is quasi-invariant. This direction will have to be compared with the direction obtained by other methods such as De Keyser et al. (2005). Knowing experimentally the invariant direction may be important for comparing the data with 2-D numerical simulations. Of course, $\boldsymbol{\alpha}_3$ is approximately in the plane perpendicular to $\mathbf{N}_{\text{Shue}}$, since the effective normal, given by $\boldsymbol{\alpha}_1$, is not much different from $\mathbf{N}_{\text{Shue}}$. In this plane, investigating the actual direction of $\boldsymbol{\alpha}_3$ deserves to be explored further. It may provide information, for instance, on the local fluctuations at different scales, whatever their cause: reconnection (Aunai et al., 2016), Kelvin-Helmholtz (Belmont & Chanteur, 1989; Miura & Pritchett, 1982), or any other phenomenon.

Finally, we have reported in Figure 3 the intervals where the $\mathbf{B}$ variations are mainly 1-D ($D_1 > 0.98$) or 2-D ($D_3 < 0.05D_2$) with a color code. Of course these criteria leave many intervals where the dimension of the problem is not determined, either because the variations are too weak and the concept of dimension is meaningless or because the dimension of the problem is not close to 1-D or 2-D. The 2-D intervals are concentrated in the region where the spacecraft go back into the magnetopause layer which is reached only in the very small interval around $t = 28$ s. It seems that this incursion is made in a region which is much more complex than the "clean" magnetopause crossing observed at the beginning of the period. The "oscillations" that are seen in the dimension may correspond to the oscillations that are observed on the density. The reason remains to be investigated.

Acknowledgments
The authors thank Olivier Le Contel and Laurent Mirioni for their help in dealing with the MMS data and for fruitful discussions. The French involvement on MMS is supported by CNES and CNRS. All the data used are available on the MMS data server: https://lasp.colorado.edu/mms/sdc/public/about/browse-wrapper/.

References

Aunai, N., Hesse, M., Lavraud, B., Dargent, J., & Smets, R. (2016). Orientation of the X-line in asymmetric magnetic reconnection. *Journal of Plasma Physics*, *82*(4), 535820401. https://doi.org/10.1017/S0022377816000647

Belmont, G., & Chanteur, G. (1989). Advances in magnetopause Kelvin-Helmholtz instability studies. *Physica Scripta*, *40*(1), 124–128.

Belmont, G., Grappin, R., Mottez, F., Pantellini, F., & Pelletier, G. (2013). *Collisionless plasmas in astrophysics*. Hoboken, NJ: Wiley.

Blagau, A., Klecker, B., Paschmann, G., Haaland, S., Marghitu, O., & Scholer, M. (2010). A new technique for determining orientation and motion of a 2-D, non-planar magnetopause. *Annales Geophysicae*, 753–778. https://doi.org/10.5194/angeo-28-753-2010

Burch, J. L., Torbert, R. B., Phan, T. D., Chen, L.-J., Moore, T. E., Ergun, R. E., & Chandler, M. (2016). Electron-scale measurements of magnetic reconnection in space. *Science*, *352*, AAF2939. https://doi.org/10.1126/science.aaf2939

Chanteur, G. (1998). Spatial interpolation for four spacecraft: Theory. *ISSI Scientific Reports Series*, *1*, 349–370.

Chen, L.-J., Hesse, M., Wang, S., Gershman, D., Ergun, R. E., Burch, J., … Avanov, L. (2017). Electron diffusion region during magnetopause reconnection with an intermediate guide field: Magnetospheric multiscale observations. *Journal of Geophysical Research: Space Physics*, *122*, 5235–5246. https://doi.org/10.1002/2017JA024004

Chen, Q., Otto, A., & Lee, L. C. (1997). Tearing instability, Kelvin-Helmholtz instability, and magnetic reconnection. *Journal of Geophysical Research*, *102*(A1), 151–161. https://doi.org/10.1029/96JA03144

Dargent, J., Aunai, N., Lavraud, B., Toledo-Redondo, S., Shay, M. A., Cassak, P. A., & Malakit, K. (2017). Kinetic simulation of asymmetric magnetic reconnection with cold ions. *Journal of Geophysical Research: Space Physics*, *122*, 5290–5306. https://doi.org/2016JA023831

De Keyser, J., Darrouzet, F., & Roth, M. (2002). Trying to bring the magnetopause to a standstill. *Geophysical Research Letters*, *29*, 1453. https://doi.org/10.1029/2002GL015001

De Keyser, J., Roth, M., Dunlop, M. W., Rème, H., Owen, C. J., & Paschmann, G. (2005). Empirical reconstruction and long-duration tracking of the magnetospheric boundary in single- and multi-spacecraft contexts. *Annales Geophysicae*, *23*, 1355–1369. https://doi.org/10.5194/angeo-23-1355-2005

De Keyser, J. (2008). Empirical reconstruction. *ISSI Scientific Reports Series*, *8*, 91–98.

Denton, R. E., Sonnerup, B. U. Ã., Birn, J., Teh, W.-L., Drake, J. F., Swisdak, M., … Baumjohann, W. (2010). Test of methods to infer the magnetic reconnection geometry from spacecraft data. *Journal of Geophysical Research*, *115*, A10242. https://doi.org/10.1029/2010JA015420

Denton, R. E., Sonnerup, B. U. O., Hasegawa, H., Phan, T. D., Russell, C. T., Strangeway, R. J., … Torbert, R. B. (2016). Motion of the MMS spacecraft relative to the magnetic reconnection structure observed on 16 October 2015 at 1307 UT. *Geophysical Research Letters*, *43*, 5589–5596. https://doi.org/2016GL069214

Denton, R. E., Sonnerup, B. U. Ö., Swisdak, M., Birn, J., Drake, J. F., & Hesse, M. (2012). Test of Shi et al. method to infer the magnetic reconnection geometry from spacecraft data: MHD simulation with guide field and antiparallel kinetic simulation. *Journal of Geophysical Research*, *117*, A09201. https://doi.org/10.1029/2012JA017877

Dorville, N., Belmont, G., Rezeau, L., Aunai, N., & Retinò, A. (2014). BV technique for investigating 1-D interfaces. *Journal of Geophysical Research: Space Physics*, *119*, 1709–1720. https://doi.org/10.1002/2013JA018926

Dorville, N., Belmont, G., Rezeau, L., Grappin, R., & Retinò, A. (2014). Rotational/compressional nature of the magnetopause: Application of the BV technique on a magnetopause case study. *Journal of Geophysical Research: Space Physics*, *119*, 1898–1908. https://doi.org/10.1002/2013JA018927

Dorville, N., Haaland, S., Anekallu, C., Belmont, G., & Rezeau, L. (2015). Magnetopause orientation: Comparison between generic residue analysis and BV method. *Journal of Geophysical Research: Space Physics*, *120*, 3366–3379. https://doi.org/2014JA020806

Dunlop, M. W., Balogh, A., & Glassmeier, K.-H. (2002). Four-point Cluster application of magnetic field analysis tools: The discontinuity analyzer. *Journal of Geophysical Research*, *107*, 1385. https://doi.org/10.1029/2001JA005089

Ergun, R. E., Tucker, S., Westfall, J., Goodrich, K. A., Malaspina, D. M., Summers, D., … Cully, C. M. (2016). The axial double probe and fields signal processing for the MMS mission. *Space Science Reviews*, *199*(1), 167–188. https://doi.org/10.1007/s11214-014-0115-x

Faganello, M., Califano, F., & Pegoraro, F. (2008). Competing mechanisms of plasma transport in inhomogeneous configurations with velocity shear: The solar-wind interaction with Earth's magnetosphere. *Physical Review Letters*, *100*, 015001. https://doi.org/10.1103/PhysRevLett.100.015001

Haaland, S., Sonnerup, B., Dunlop, M., Balogh, A., Georgescu, E., Hasegawa, H., … Vaivads, A. (2004). Four-spacecraft determination of magnetopause orientation, motion and thickness: Comparison with results from single-spacecraft methods. *Annales Geophysicae*, *22*, 1347–1365. https://doi.org/10.5194/angeo-22-1347-2004

Hasegawa, H., Sonnerup, B. U. O., Klecker, B., Paschmann, G., Dunlop, M. W., & Rème, H. (2005). Optimal reconstruction of magnetopause structures from Cluster data. *Annales Geophysicae*, *23*, 973–982. https://doi.org/10.5194/angeo-23-973-2005

Le Contel, O., Retinò, A., Breuillard, H., Mirioni, L., Robert, P., Chasapis, A., … Saito, Y. (2016). Whistler mode waves and Hall fields detected by MMS during a dayside magnetopause crossing. *Geophysical Research Letters*, *43*, 5943–5952. https://doi.org/10.1002/2016GL068968

Miura, A., & Pritchett, P. L. (1982). Nonlocal stability analysis of the MHD Kelvin-Helmholtz instability in a compressible plasma. *Journal of Geophysical Research*, *87*(A9), 7431–7444. https://doi.org/10.1029/JA087iA09p07431

Paschmann, G., Baumjohann, W., Sckopke, N., Sonnerup, B., & Papamastorakis, I. (1990). The magnetopause and boundary layer for small magnetic shear—Convection electric fields and reconnection. *Geophysical Research Letters*, *17*, 1829–1832. https://doi.org/10.1029/GL017i011p01829

Pollock, C., Moore, T., Jacques, A., Burch, J., Gliese, U., Saito, Y., … Zeuch, M. (2016). Fast Plasma Investigation for Magnetospheric Multiscale. *Space Science Reviews*, *199*(1), 331–406. https://doi.org/10.1007/s11214-016-0245-4

Russell, C. T., Anderson, B. J., Baumjohann, W., Bromund, K. R., Dearborn, D., Fischer, D., … Richter, I. (2016). The Magnetospheric Multiscale Magnetometers. *Space Science Reviews*, *199*(1), 189–256. https://doi.org/10.1007/s11214-014-0057-3

Shi, Q. Q., Pu, Z. Y., Soucek, J., Zong, Q.-G., Fu, S. Y., Xie, L., … Reme, H. (2009). Spatial structures of magnetic depression in the Earth's high-altitude cusp: Cluster multipoint observations. *Journal of Geophysical Research*, *114*, A10202. https://doi.org/10.1029/2009JA014283

Shi, Q. Q., Shen, C., Dunlop, M. W., Pu, Z. Y., Zong, Q.-G., Liu, Z. X., … Balogh, A. (2006). Motion of observed structures calculated from multi-point magnetic field measurements: Application to Cluster. *Geophysical Research Letters*, *33*, L08109. https://doi.org/10.1029/2005GL025073

Shi, Q. Q., Shen, C., Pu, Z. Y., Dunlop, M. W., Zong, Q.-G., Zhang, H., … Balogh, A. (2005). Dimensional analysis of observed structures using multipoint magnetic field measurements: Application to Cluster. *Geophysical Research Letters*, *32*, L12105. https://doi.org/10.1029/2005GL022454

Shi, Q. Q., Zong, Q.-G., Fu, S. Y., Dunlop, M. W., Pu, Z. Y., Parks, G. K., … Lucek, E. (2013). Solar wind entry into the high-latitude terrestrial magnetosphere during geomagnetically quiet times. *Nature Communications*, *4*, 1466.

Shue, J.-H., Chao, J. K., Fu, H. C., Russell, C. T., Song, P., Khurana, K. K., & Singer, H. J. (1997). A new functional form to study the solar wind control of the magnetopause size and shape. *Journal of Geophysical Research*, *102*(A5), 9497–9511. https://doi.org/10.1029/97JA00196

Sonnerup, B. U. O., & Cahill, L. J. (1967). Magnetopause structure and attitude from Explorer 12 observations. *Journal of Geophysical Research*, *72*, 171–183. https://doi.org/10.1029/JZ072i001p00171

Sonnerup, B. U. O., Haaland, S. E., & Paschmann, G. (2008). Discontinuity orientation, motion, and thickness. *ISSI Scientific Reports Series*, *8*, 1–16.

Sonnerup, B. U. O., Haaland, S., Paschmann, G., Dunlop, M. W., Rème, H., & Balogh, A. (2006). Orientation and motion of a plasma discontinuity from single-spacecraft measurements: Generic residue analysis of Cluster data. *Journal of Geophysical Research*, *111*, A05203. https://doi.org/10.1029/2005JA011538

Sonnerup, B. U. Ö, & Scheible, M. (1998). Minimum and maximum variance analysis. *ISSI Scientific Reports Series*, *1*, 185–220.

Sonnerup, B. U. O., Teh, W.-L., & Hasegawa, H. (2008). Grad-Shafranov and MHD reconstructions. *ISSI Scientific Reports Series*, *8*, 81–90.

Stone, E. C., Frandsen, A. M., Mewaldt, R. A., Christian, E. R., Margolies, D., Ormes, J. F., & Snow, F. (1998). The Advanced Composition Explorer. *Space Science Reviews*, *86*, 1–22. https://doi.org/10.1023/A:1005082526237

Torbert, R. B., Burch, J. L., Giles, B. L., Gershman, D., Pollock, C. J., Dorelli, J., … Bounds, S. (2016). Estimates of terms in Ohm's law during an encounter with an electron diffusion region. *Geophysical Research Letters*, *43*, 5918–5925. https://doi.org/2016GL069553

Yao, S. T., Wang, X. G., Shi, Q. Q., Pitnen, T., Hamrin, M., & Yao, Z. H. (2017). Observations of kinetic-size magnetic holes in the magnetosheath. *Journal of Geophysical Research: Space Physics*, *122*, 1990–2000. https://doi.org/2016JA023858

Zhang, T. L., Baumjohann, W., Nakamura, R., Volwerk, M., Runov, A., Vörös, Z., … Balogh, A. (2005). Neutral sheet normal direction determination. *Advances in Space Research*, *36*(10), 1940–1945. https://doi.org/10.1016/j.asr.2004.08.010

23.4 Poster presented during the American Geophysical Union 2017

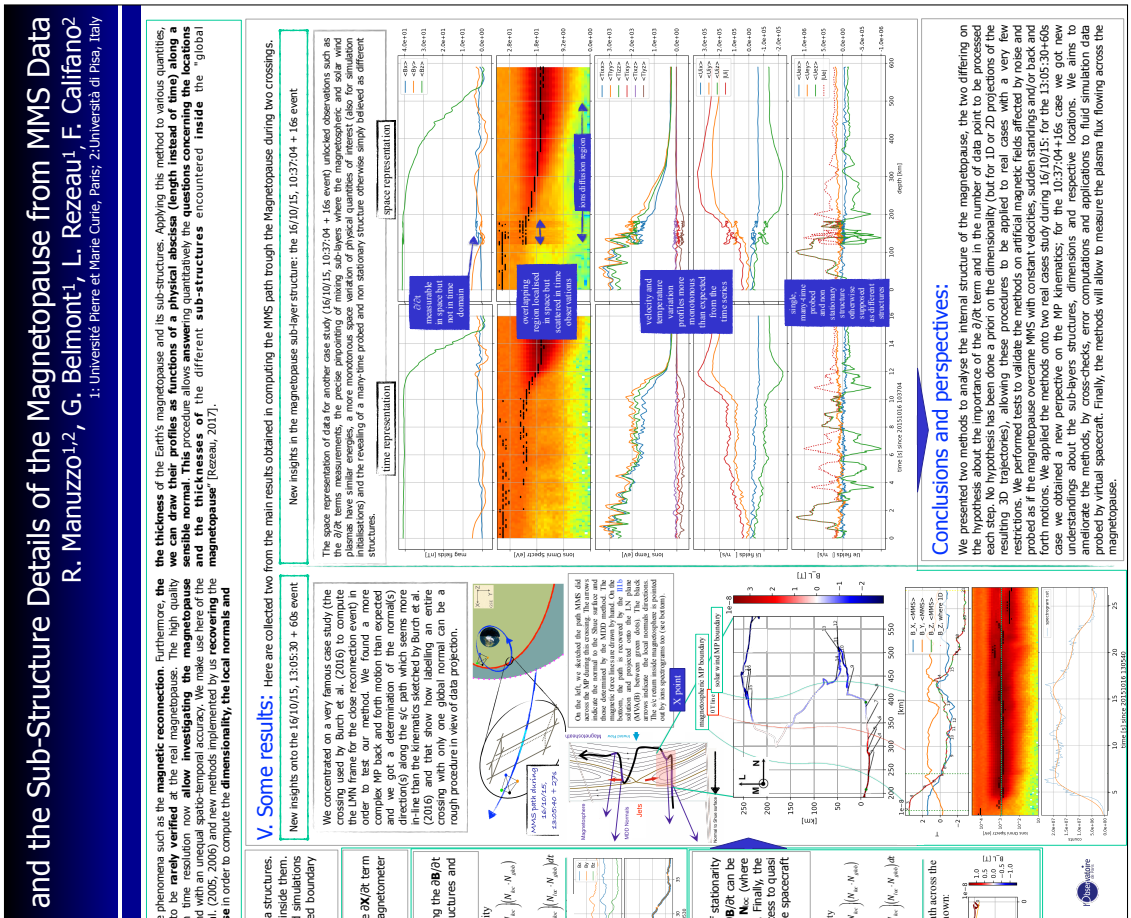

23.5 Poster presented during the European Geosciences Union 2018

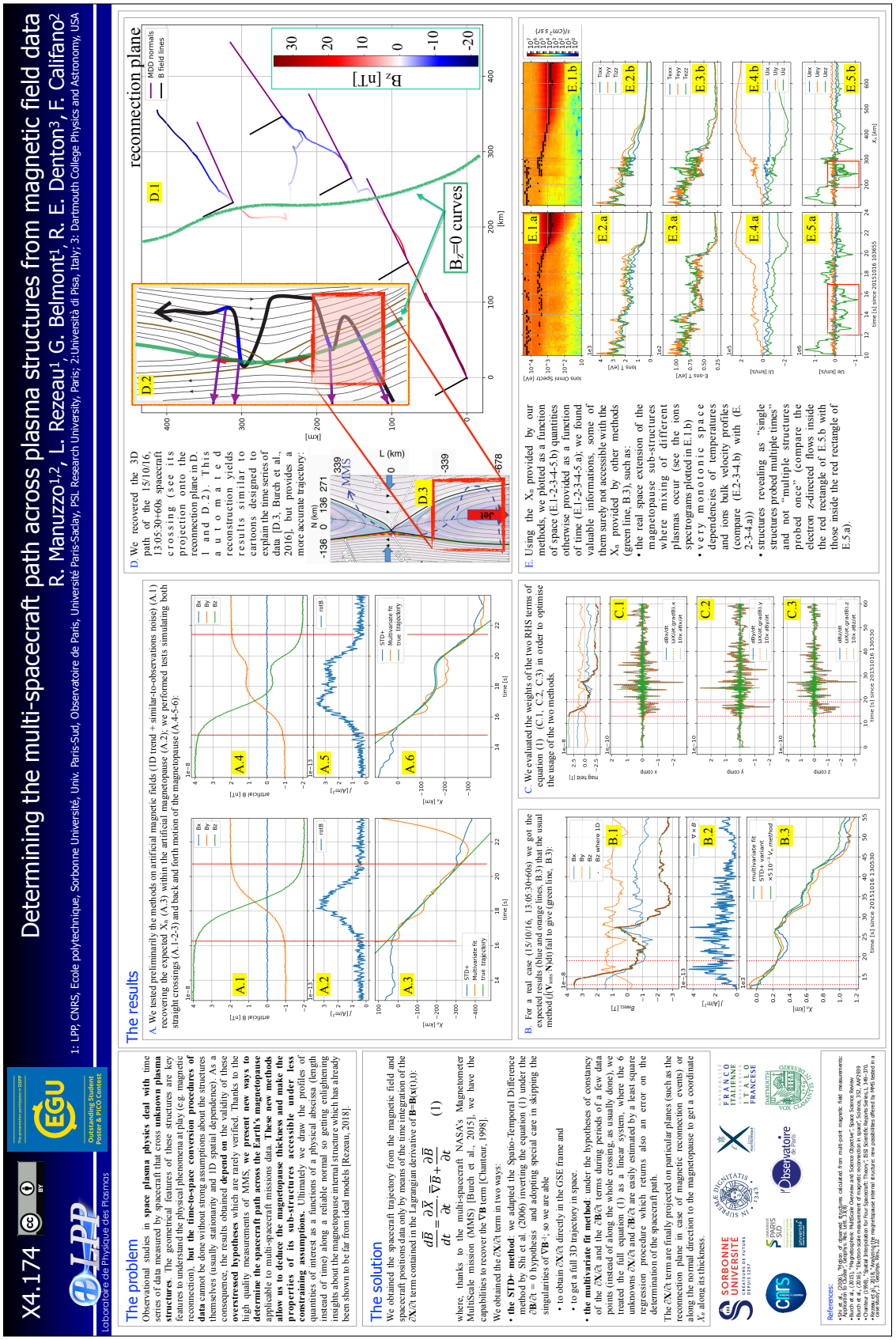

23.6 Poster presented during the American Geophysical Union 2018

SM11C-2792

NO PHOTOS

A new multi-fluid model for space plasma simulations

R. Manuzzo[1,2], F. Califano[2], G. Belmont[1], L. Rezeau[1], N. Aunai[1]

1: LPP, CNRS, Ecole polytechnique, Sorbonne Université, Univ. Paris-Sud, Observatoire de Paris, Université Paris-Saclay, PSL Research University, Paris; 2:Università di Pisa, Italy

Laboratoire de Physique des Plasmas

Do you want
to know how we localise data in space? Are you interested in knowing the spacecraft path or in studying the minute sub-structure details of the magnetopause? Come to see our E-lighting poster on Wednesday, 12 December 2018, 08:40 - 08:43 Convention Ctr - eLightning Theater I

Abstract

We propose a new numerical code based on a new multi-species theoretical model to study the mass, momentum and energy exchanges (MMEE) that happen across the magnetospheric boundaries. We use two distinct populations for ions, one cold and one hot (plus one neutralising electron population), to take into account the differences between the properties of the plasmas coming from the magnetosphere and from the solar wind. This approach represents a step forward in the context of the study of coupled large-scale plasma systems being a new and efficient compromise between fluid and kinetic codes in tracing the different plasma contributions during MMEE. Due to the very important role that magnetic reconnection plays in connecting the shocked Solar Wind to the Earth's magnetosphere, we show and discuss the very preliminary results we obtained about the simulations of the tearing mode instability occurring across an Earth's magnetopause that we modelled thanks to our most recents MMS observations about the 16/10/15, 13:05:30+60s crossing [Rezeau 2018].

Theoretical and computational methods employed: the three fluid code

The plasma region we intend to simulate is of the order of about a thousand of ion inertial length d_i (where d_i ~ 100 km in the MP) and we must follow the plasma dynamics down to, at least, a fraction of d_i. In order to simulate such a large scale structure and, at the same time, in order to resolve the length scales at which the plasma mixing occurs (around 1 d_i), we make use of a performant, parallelised numerical multi-fluid code recently builded up onto the skeleton of a bi-fluid code that has already successfully used by our group to study the solar wind/magnetosphere interaction [Faganello et al., 2009; Faganello & Califano, 2017].
The new code evolves in time a set of fluid quantities (density, velocities, etc...) by means of a set of equations (very similar to MHD equations) for three charged fluids representing two ions and one electron population. The set of equations is self-consistently coupled to the Maxwell equations via the charge and current densities. Two directions, y and z, are periodic while the x direction, corresponding to the inhomogeneity direction (i.e. transition layer) has transparent boundary conditions (or numerical open boundary conditions). The code has been massively parallelised along directions y and z with MPI in collaboration with the HPC center CINECA (Italy); it advances in time with a standard Runge-Kutta algorithm; it uses sixth order explicit finite difference stencils along the periodic y and z-direction and a sixth-order compact finite difference scheme with spectral like resolution for spatial derivative along the inhomogeneous x-direction. The numerical stability is guaranteed by means of a spectral filter along the periodic y and z directions and a spectral-like filtering scheme along the inhomogeneous x-direction [Canuto et al., 1988 and Lele, 1992].

References:

- Rezeau L., Belmont, G., Manuzzo, R., Aunai, N., & Dargent, 2018, "Analyzing the magnetopause internal structure: new possibilities offered by PWS tested in a case study", J. Geophys. Res., 123.
- Canuto, et al., "Spectral Methods in Fluid Dynamics", Springer Series In Computational Physics, New York, Springer, 1988
- Lele, J. Comput. Phys. 103, 16, 1992
- Faganello, M., & Califano, F. (2017). Magnetized Kelvin-Helmholtz instability: Theory and simulations in the Earth's magnetosphere context. Journal of Plasma Physics, 83(6), 535830601. doi:10.1017/S0022377817000770
- Faganello, M.et al. (2009) Being on time in magnetic reconnection.New J. Phys.11, 063008.
- Burch et al., (2016), "Electron-scale measurement of magnetic reconnection in space", Science, 352, AAF2939
- Furth, J. Killeen, and M. N. Rosenbluth, Phys. Fluids 6, 459, 1963

The analytical equations for a 3fluid equilibrium

The model assumes a minimum set of *known quantities* to recover firstly a *i-e* equilibrium, and subsequently a *cold ions - hot ions - electrons* equilibrium:

$$i-e:\begin{cases} n_e = n_i \\ \mathbf{U}_e = \mathbf{U}_i - \frac{1}{n_i}\frac{(\nabla\times\mathbf{B})}{e\mu_0} \\ P_e = P_{tot} - (P_B + n_i T_i) \\ \mathbf{E} = -\frac{1}{en_e}\nabla P_e - (\mathbf{U}_e\times\mathbf{B}) \end{cases}$$

$$ic-ih-e:\begin{cases} n_{ic}+n_{ih}=n_i \\ P_{ic}+P_{ih}=P_{tot}-(P_B+P_e) \\ n_{ic}\mathbf{U}_{ic}+n_{ih}\mathbf{U}_{ih}=n_e\mathbf{U}_e+\frac{1}{e\mu_0}\nabla\times\mathbf{B} \\ \nabla P_{ic}-\left[q_{ic}n_{ic}\mathbf{E}+q_{ic}n_{ic}\mathbf{U}_{ic}\times\mathbf{B}\right]=0 \\ \nabla P_{ih}-\left[q_{ih}n_{ih}\mathbf{E}+q_{ih}n_{ih}\mathbf{U}_{ih}\times\mathbf{B}\right]=0 \end{cases}$$

Analytical model vs MMS Data

The *known quantities* are mimed by analytical functions fitting MMS data (16/10/15, 13:05:30+60s) plotted as a function of space; the remaining unknowns, which are derived by the 3fluid equations, partially recover the observations (the differences are due to very close non-stationary phenomena affecting the examined data [Burch et al., 2016]).

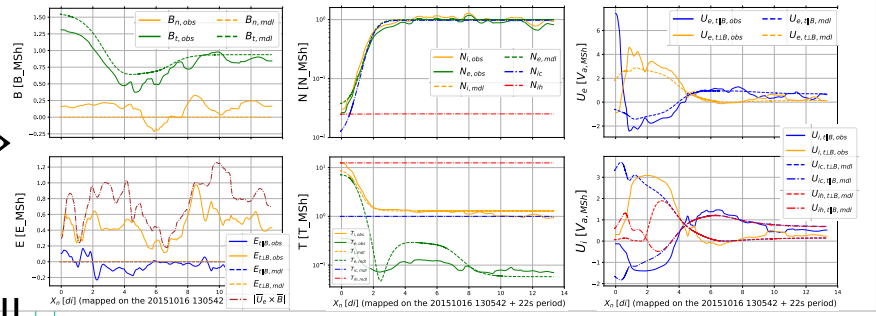

Preliminary results

A deeper look at data due to a theoretical suggestion

For particular parameters adopted in shaping the 3fluid equilibrium model, the theoretical curves of the cold and the hot ions bulk flows show counter-ward directed peaks (U_y, B.2) at the magnetospheric side of the magnetopause (red vertical dashed line, B.1-B.3). At the time corresponding to this location, the ions distribution function provided by MMS shows two beams, one hot and one cold, having nearly the same amplitude of the theoretical one (the red horizontal dashed lines of B.4 corresponds to +1, -1 and -2 $V_{a,MSh}$).

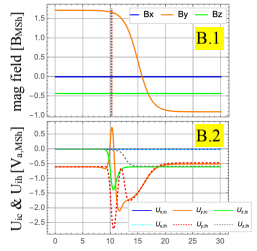

The tearing instability

By means of a magnetic perturbation, we trigger a tearing mode instability that shows magnetic field/ions velocity eigenfunctions (C.1 - C.2), FGM wave numbers (cfr. C.3 with C.4) and FGM growth rates (C.4) that agree with the theory [Furth et al., 1963].

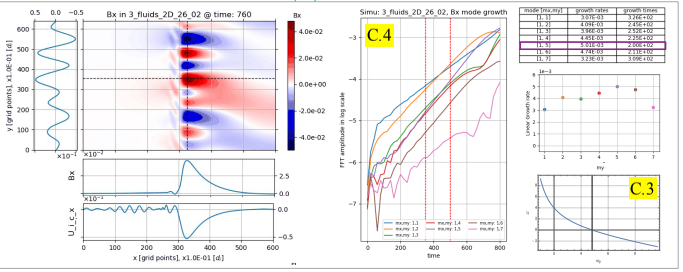

The 3fluid numerical scheme

1. Transport of the density of ions and electrons entropies ($nS \equiv Pn^{1-\gamma}$), $\alpha = \{ic, ih, e\}$:
$$\frac{\partial(n_\alpha S_\alpha)}{\partial t} + \nabla\cdot[\mathbf{U}_\alpha(n_\alpha S_\alpha)] = 0 \quad (1)$$
2. Ions densities, $\alpha = \{ic, ih\}$:
$$\frac{\partial n_\alpha}{\partial t} + \nabla\cdot(n_\alpha\mathbf{U}_\alpha) = 0 \quad (2)$$
3. Electron density from updated ions densities[1], $\alpha = \{ic, ih\}$:
$$n_e^* = \sum_\alpha n_\alpha^* \quad (3)$$
4. Ions momenta, $\alpha = \{ic, ih\}$:
$$\frac{\partial(n_\alpha\mathbf{U}_\alpha)}{\partial t} + \frac{1}{n_\alpha}\nabla P_\alpha + \nabla\cdot(n_\alpha\mathbf{U}_\alpha\mathbf{U}_\alpha) - \frac{q_\alpha n_\alpha}{m_\alpha}(\mathbf{E}+\mathbf{U}_\alpha\times\mathbf{B}) = 0 \quad (4)$$
5. Ions and electrons pressures, $\alpha = \{ic, ih, e\}$:
$$P_\alpha^* = [n_\alpha S_\alpha]^*(n_\alpha^*)^{\gamma-1} \quad (5)$$
6. Ions velocities, $\alpha = \{ic, ih\}$:
$$\mathbf{U}_\alpha^* = (n_\alpha\mathbf{U}_\alpha)^*/n_\alpha^* \quad (6)$$
7. Magnetic field
$$\frac{\partial\mathbf{B}}{\partial t} + \nabla\times\mathbf{E} = 0 \quad (7)$$
8. Electronic velocities, $\alpha = \{ic, ih\}$:
$$\mathbf{U}_e^* = \left[\sum_\alpha(n_\alpha^*\mathbf{U}_\alpha^*) + \frac{1}{q_e\mu_0}\nabla\times\mathbf{B}^*\right]/n_e^* \quad (8)$$
9. Electric field
$$\mathbf{E}^* = -\mathbf{U}_e^*\times\mathbf{B}^* + \frac{1}{q_e n_e^*}\nabla P_e^* \quad (9)$$

23.7 Electronic Poster presented during the American Geophysical Union 2018